On the rupture processes of large earthquakes using three-dimensional data-integrated dynamic rupture simulations

Thomas Ulrich

München 2019

On the rupture processes of large earthquakes using three-dimensional data-integrated dynamic rupture simulations

Thomas Ulrich

Dissertation zur Erlangung des
Doktorgrades an der Fakultät für Geowissenschaften
der Ludwig–Maximilians–Universität
München

vorgelegt von
Thomas Ulrich

München, den 17.12.2019

Erstgutachter: Prof. Dr. Heiner Igel
Zweitgutachter: Dr. Alice-Agnes Gabriel
Tag der mündlichen Prüfung: 25.05.2020

Summary

In this dissertation, I use 3D dynamic rupture modeling to understand the dynamics of previous large earthquakes and, more generally, to advance the physical understanding of coseismic processes on natural faults. I focus on a set of large and destructive earthquakes, characterized by puzzling features, and I conduct additional numerical analyses to investigate the scale-dependence of fault roughness effects.

I first study the complex dynamics of the 2016 M_w 7.8 Kaikōura earthquake. I present a highly realistic 3D dynamic rupture scenario that reproduces key characteristics of the event and constrains puzzling features. I show that the observed rupture cascade is dynamically consistent with regional stress estimates and a crustal fault network geometry inferred from seismic and geodetic data. In the model, overpressurized fluids, low dynamic friction and stress concentrations induced by deep fault creep result in low apparent friction. I then present a coupled scenario of the 2018 Palu, Sulawesi earthquake and tsunami. The model, constrained by rapidly available observations, suggests that the primary tsunami source, a key riddle of the event, may have been direct earthquake-induced uplift and subsidence. This study demonstrates that physics-based interpretations can be an important part of the rapid earthquake response toolset. Next, I explore the dynamics of the 2004, M_w 9.1 - 9.3 Sumatra-Andaman earthquake. My models suggest that along-depth variation of trench sediments, off-fault plastic yielding, and along-arc variations of regional stresses and tectonic convergence rates are the dominant factors controlling the event's dynamics and kinematics. I demonstrate that 3D dynamic rupture modeling of megathrust earthquakes is now feasible and is critical for understanding the interplay of subduction mechanics, megathrust earthquakes and tsunami genesis. Finally, I investigate the scale-dependence of fault roughness effects on earthquake kinematics, dynamics and ground motion. The models on fractal strike-slip rough faults do not reveal systematic wavelength dependence of these effects. Nevertheless, the characteristic length scale posed by rupture process zone width affects rupture dynamics locally. In this study, I also propose strategies to capture fault roughness effects on coarser geometric fault representations, which offer an interesting compromise between computational efficiency and accuracy.

Overall, this work advances the physical understanding of earthquake rupture processes. The developed models shed light on the physical mechanisms of cascading ruptures in complex fault systems and of megathrust earthquakes. In particular, they pose constraints on the conditions leading to such large earthquakes. This work contributes to advancing the current state-of-the-art of modeling earthquake source dynamics, by bridging the gap between rupture dynamic modeling and seismic observations.

Acknowledgements

Firstly, I thank my advisor, Dr. Alice-Agnes Gabriel, for her continuous support and for successfully guiding me through this Ph.D. She shaped in the best way the overall direction of my research while leaving me lots of freedom, and she put me in optimal conditions for learning, progressing, and becoming a better scientist.

I also thank the rest of my thesis committee: Prof. Claudia Trepmann, Prof. Jean-Paul Ampuero, Prof. Heiner Igel, Prof. Ralf Ludwig, and Prof. Martin Mai, for the time they dedicated to assess my work, for their insightful comments and their positive feedbacks and encouragements. In particular, I would like to thank Heiner Igel, for his support, and for his motivating seminars, which promote discussion and expend our scientific horizon, Prof. Pablo Ampuero, for the fruitful exchanges we had when working on the Kaikoura study, and Prof. Martin Mai, for the constructive discussions we had regarding rough faults and ground motion.

I also thank Prof. Michael Bader and his scientific computing group at TUM. In particular, special thanks to Carsten, Sebastian, and Leonhard, and the newest team members, Lukas, Sebastian, and Ravil. This dissertation would have looked much different without all their developments, and I'm very grateful we have such a fruitful collaboration.

A big thanks to my colleagues, Ph.D. students, and postdocs of the geophysics group, for stimulating discussions, and for the good atmosphere we had in the last five years. In particular, special thanks to the earthquake physics group, Stephanie, Betsy, Kenneth, Duo, Taufiq, Sebastian, Bo, and Aniko, and to Lion, Lorenzo, Kasra, Sia, Martin, Simon, Djamel, Chris, Dave, and Shihao. I also thank the administrative and IT staff for their support, in particular, Rosa, Elena, Jens, Alex, and Hosna.

Thank you also to the member of the ASCETE project I did not cite yet: Stefan, Joern, Ylona, and Iris.

Thank you to my former colleagues at BRGM, in particular John, Hideo, Caterina, Pierre, and many others, who introduced me to science and inspired me into this Ph.D.

I also thank my friends in Munich, Nicky, Martin, Magda, Kike, Manu, Florin, Isabel, Theo, Stefania, Stefan, and their family, for bringing me out every weekend.

Finally, my special thank goes to Andreea, Clovis, and Félix, for their support and understanding.

Contents

List of Figures

List of Tables

1
Introduction

Earthquakes result from the sudden release of accumulated tectonic stress through slip along faults on plate boundaries and within plate interiors, in- and off-fault damage of the fault zone rocks, heat, and seismic radiation. Earthquake hazards are manifold. Direct hazards include ground displacements and shaking. Secondary hazards, such as tsunami, landslides, fires and soil liquefaction, can multiply the consequences of an earthquake. Recent events confirmed that earthquakes can have devastating consequences. Such consequences can be strongly increased by the unpreparedness and vulnerability of populations and structures. The aftermath of the 2010 Haiti earthquake (e.g., Hayes et al, 2010; Douilly et al, 2015), which killed more than 310 thousand people, was for example increased by the existing poverty and poor housing condition in this country (e.g., DesRoches et al, 2011). Also, many of the more than 220 thousand fatalities caused by the 2004 Indian Ocean earthquake and tsunami could have been prevented by an efficient tsunami early warning system (e.g., Shearer and Bürgmann, 2010). The tsunami reached Sri Lanka and Somalia respectively more than 2 and 7 hours after the mainshock and yet killed about 35 000 and 300 people, respectively in these countries.

In spite of constant progress, new events regularly challenge our understanding of earthquakes. For instance, the unexpectedly large moment magnitude of the 2004 Sumatra-Andaman earthquake (Chapter 4) challenged the established concepts (e.g., Ruff and Kanamori, 1980) of convergence rate and age of the oceanic lithosphere controlling the largest earthquake size observed on subduction interfaces (e.g., Kanamori, 2006). More recently, an apparent gap of 15–20 km in the mapped surface rupture of the 2016 Kaikōura earthquake, suggesting a possible rupture transfer between these faults, challenged the state-of-the-art. The Third Uniform California Earthquake Rupture Forecast (e.g., Field et al, 2014),for example, which considers ruptures across stepovers, with a probability of step over jump that decays with distance in a way that is consistent with observations (e.g., Wesnousky, 2006), predicts a near-zero likelihood for step over larger than 5 km. In Chapter 2, I show that the presence of a blind fault may have connected these distant surface faultings without contradicting the established theory. The unexpectedly large size of the 2011 Tōhoku earthquake (e.g., Lay and Kanamori, 2011), which in turn triggered a tsunami of unanticipated magnitude killing about 16 thousand people in the arguably most prepared country to deal with earthquakes, reminds us that better understanding the nature of earthquake faulting processes remains a key undertaking towards a better seismic hazard characterization, disaster prevention, and mitigation.

The aim of this work is therefore to advance the physical understanding of the coseismic processes on natural faults. This is done by designing data-integrated numerical models of previous large earthquakes. In particular, I try to constrain the conditions leading to such events and to understand more generally how fault systems operate. This work contributes to advancing the current state-of-the-art of modeling earthquake source dynamics, by bridging the gap between rupture dynamic modeling and seismic observations.

1.1 Some geophysical background

Earthquakes are the results of processes occurring along a wide range of temporal and spatial scales. The lithosphere, which consists of the crust and the upper layer of earth's mantle is the rigid skin on our planet (e.g., White, 1988). Within the lithosphere, rocks are fragile and can break seismically, as opposed to the ductile rheology of rocks in the mantle. The lithosphere can be divided into tectonic plates, which move one respect to each other. The dynamics of tectonic plates is the outcome as a gravity-driven convection system (e.g., Conrad and Lithgow-Bertelloni, 2002; Iaffaldano and Bunge, 2009; Stadler et al, 2010), in which young and therefore hot plates are pushed away from spreading ridges, and old cold plates are pulled down into subduction zones. Shallow interplate earthquakes, which occur at the boundary between tectonic plates, account for more than 95 % of the total worldwide seismic energy released (e.g., Bormann et al, 2002).

The relative motion at plate boundaries, convergent, divergent or parallel lead to various styles of faulting: thrust, normal,strike-slip or mixed faulting. Strike-slip ruptures are usually segmented (e.g., Klinger, 2010). Faults segments can be separated by step over and fault bends. Fault segmentation often controls the rupture extend of large-strike slip earthquakes (e.g., Wesnousky, 2006), and may lead to complex rupture processes (e.g., Douilly et al, 2015; Wollherr et al, 2019; Ross et al, 2019). Examples of such complex ruptures are the 2016 Kaikōura and the 2018 Palu earthquakes, which are the subject of Chapters 2 and 3 of this dissertation. Subduction zones are convergent plate boundaries where two plates move one under another. Subduction zones account for about 85 % of the total worldwide seismic moment release (e.g., Bormann et al, 2002), and host the largest earthquakes on Earth. This is because the brittle-ductile transition zone, below which brittle faulting processes are supplanted by ductile aseismic creep, and which controls the depth extent of earthquakes, is deeper in subduction area than elsewhere. The temperature of the cold subducting slab, which is progressively warmed up by the mantle, controls the depth of the brittle-ductile transition. The largest megathrust earthquakes are sometimes associated with a devastating tsunami. These rare and extremely damaging events affect deeply our society. Recent examples of such tsunamigenic mega earthquakes are the 2004 Sumatra-Andaman, that I study in Chapter 4 of this dissertation, and the 2011 Tōhoku earthquakes.

During the interseismic period, faults are locked, that is they are prevented from slipping and elastic potential energy is stored in the rock (e.g., Reid, 1911). The accumulation of tectonic strain and stress at the plate boundary of a few mm or cm a year can last for hundreds or thousands of years until the fault frictional resistance is locally overcome. This triggers the earthquake rupture, which spontaneously propagates along faults until getting arrested. Because pre-fractured rocks are much weaker than unbroken rocks, ruptures usually break existing faults. During the earthquake rupture, the on-fault friction weakens dramatically (e.g., Noda et al, 2009; Di Toro et al, 2011). The rupture results in a stress drop and permanent offset. The earthquake process, lasting seconds to minutes is then followed by a postseismic phase, which can last several years, in which postseismic processes, including afterslip, viscoelastic relaxation and aftershocks occur.

The recent development of dense seismological and geodetic networks, combined with modern remote sensing techniques allow a finer characterization of faulting processes but also challenge the current understanding of these processes. The most recent earthquakes may be recorded by dozens of strong-motion and high-rate GPS sensors. Such near-source observations enable the characterization of smaller-scale features of the source. Dense seismic arrays also allow characterizing the kinematics of remote events through back-projection techniques (e.g., Ishii et al, 2005). Satellite remote sensing techniques, based on radar interferometry (e.g., Massonnet and Feigl, 1998) or optical imaging (e.g., Van Puymbroeck et al, 2000), allow mapping surface rupturing and capturing the coseismic ground displacement field of remote large earthquakes over broad areas and to a fantastic level of detail. Recent advances in machine learning (e.g., Ross et al, 2018) allow mapping aftershock sequences to an unprecedented resolution (e.g., Ross et al, 2019). Generating models able to unify all observables is becoming a real challenge.

In spite of more diverse and numerous data available to characterize earthquakes, our state of knowledge of faulting processes remains limited. In particular, fault stress and strength conditions are crucial in understanding earthquake faulting processes but are poorly constrained (e.g., Hardebeck, 2015). Faulting processes occur at great depth, while most boreholes are limited to much shallower depths, preventing direct observation of these conditions. Also, reproducing the typical conditions of faulting in the laboratory is complicated, and it is not clear how results can be extrapolated from the laboratory to a natural scale. Earthquake kinematics can be inferred from the multitude of data available and can inform us about the complexity of earthquake faulting processes. Unfortunately, such data-driven inversion processes are often characterized by a limited resolution and a high non-uniqueness (e.g., Mai et al, 2016). Kinematics models may not be able to resolve subtle features, such as the existence of multiple rupture fronts or limited slip on a connecting fault, which may be crucial in the propagation of the earthquake source process.

Natural fault systems are complex. The propagation of seismic waves in the Earth is a well-understood phenomenon, which can be modeled by solving the equation of motion combined with a stress-strain relation, which described the intrinsic properties of rocks. In contrast, faulting processes cannot be modeled by such elastic laws. In fact, fault rheology is typically described by a non-linear constitutive law, which specifies how fault weakens. These include the linear-slip weakening law (e.g., Andrews, 1976), in which fault weakens linearly with fault slip until a characteristic slip distance, and more complex (rate-and-state) friction laws (Dieterich, 1979; Ruina, 1983), derived from laboratory experiments, which provide empirical relations between the measured coefficient of friction, rate of deformation (slip rate), and a state variable, which characterizes the physical state of the surface or shearing zone, and therefore allows accounting for time-dependent evolution/memory effects. Derived forms of the classical rate-and-state friction laws (e.g., Dunham et al, 2011a; Bizzarri and Cocco, 2006) allow reproducing the dramatic frictional weakening at coseismic slip rates observed in laboratory experiments (e.g., Noda et al, 2009; Di Toro et al, 2011), and some secondary features, such as fault reactivation which may play an important role in the overall rupture dynamics (e.g., Gabriel et al, 2012). In the Chapters 2 and 3 of this dissertation, I demonstrate that realistic 3D earthquake scenarios can be achieved using such modern constitutive laws. Depending on the initial condition, faults can exhibit a wide variety of behavior, including conventional earthquakes that rupture at great speeds and slow earthquakes (e.g., Miller, 2002) that involve anomalously slow ruptures, radiating either seismic tremor (e.g., Rogers, 2003; Hirose and Obara, 2005) or not radiating any detectable seismic waves. Such non-conventional earthquakes may have a fundamental importance in triggering and modulating conventional earthquake ruptures (e.g., Ito et al, 2013). Conventional earthquakes themselves can exhibit a wide range of rupture styles: slow and fast rupture, subshear and supershear (e.g., Andrews, 1985; Dunham, 2007; Socquet et al, 2019; Bao et al, 2019), crack-like rupture (e.g., Yomogida, 1988), in which the duration of slip at each point on the fault is comparable to the overall rupture duration, and pulse-like rupture (e.g., Heaton, 1990; Gabriel et al, 2012), in which the duration of slip is much shorter.

Numerical models offer a valuable way to study and understand faulting mechanisms, especially given the fact that faulting processes on natural fault cannot be easily observed directly. Numerical models typically use a set of physical equations to model a process numerically using computational resources.

Dynamic rupture models aim at reproducing the physical processes that govern the way faults yield and slide and interact with the earth that surrounds them. The kinematics of the simulated earthquake is not predetermined but results from the physical conditions at the beginning of the simulation and the time-dependent processes occurring during earthquake rupture. The results of dynamic rupture modeling depend on initial assumptions, such as the geometry of the faults, the initial stress state within the hosting rock, the rock rheology and properties and the choice of a constitutive law for modeling the fault. Previous studies have identified many ingredients that may strongly affect rupture dynamics. These include stress and strength heterogeneities (e.g., Ripperger et al, 2007), fault roughness (e.g., Dieterich and Smith, 2009; Dunham et al, 2011b; Shi and Day, 2013), bi-material effects (e.g., Ampuero and Ben-Zion, 2008), low-velocity zone (e.g., Harris and Day, 1997;

Huang and Ampuero, 2011), off-fault damage (e.g., Templeton and Rice, 2008; Gabriel et al, 2013), thermal pressurization (e.g., Andrews, 2002; Bizzarri and Cocco, 2006), flash heating, frictional melting (e.g., Rice, 2006), etc. Given the cost of including each process, it is essential to identify the first-order processes that have the most influence of earthquake dynamics, to achieve a realistic model of minimum complexity. Dynamic rupture modeling allows describing in detail the spontaneous evolution of slip and traction on the fault, as well as the seismic waves it radiates and the subsequent ground motion. Dynamic rupture modeling have been used to understand previous earthquakes (e.g., Olsen et al, 1997; Ma et al, 2008), to assess earthquake hazard (e.g., Hok et al, 2011; Aochi and Ulrich, 2015) and to study fundamental aspects of earthquake physics (e.g., Gabriel et al, 2012; Shi and Day, 2013). Collective earthquake behavior can be investigated using a wide range of models (e.g., Fang and Dunham, 2013), while singular earthquake can be explained using only a few scenarios (e.g., Olsen et al, 1997; Douilly et al, 2015). Dynamic rupture modeling can provide a valuable complement to the data-driven state-of-the-art method of assessing the seismic hazard (e.g. PSHA, probabilistic seismic hazard assessment). In fact, dynamic rupture simulations can assess source, path and site complexity such as directivity effects, off-fault plastic reduction of peak shaking levels, asymmetric ground motions from normal/thrust faulting, subshear vs supershear rupture speeds, buried vs non-buried ruptures, as well as providing non-ergodic recurrence and fault interaction inferences for PSHA leading up to physics-based maximum magnitude scenarios. Dynamic rupture models incorporating small-scale fault roughness effects can produce reliable synthetics at the frequency range relevant for performance-based design because they capture the high-frequency radiation emitted by natural faulting processes (e.g., Dunham et al, 2011b; Withers et al, 2019a,b).

In this dissertation, I rely on SeisSol, a high-order numerical method based on the arbitrary high-order derivative discontinuous Galerkin (ADER-DG) scheme (e.g., Dumbser and Käser, 2006; Pelties et al, 2012), which utilizes unstructured tetrahedral element discretizations to account for 3D, geometrically complex structures, such as high-resolution topography and subsurface structures, curved subduction interfaces and splay faults (e.g., Uphoff et al, 2017) and complex fault networks (e.g., Wollherr et al, 2018; Ulrich et al, 2019a,b). SeisSol is empowered by recent computational optimizations targeting strong scalability on many-core CPUs such as an efficient local time-stepping algorithm (e.g., Breuer et al, 2014; Heinecke et al, 2014; Rettenberger et al, 2016; Uphoff et al, 2017). It can handle nonlinear rheologies (e.g., Wollherr et al, 2018) and propagate seismic waves with high-order accuracy.

In this work, I focus on the dynamics of a set of large and destructive earthquakes, characterized by puzzling features. Large events receive a great interest of seismologists because they contribute a large percentage of the death toll and damage caused overall by earthquakes. Also, their spatial and temporal scale facilitate their characterization. Finally, large earthquakes are rare, which limits our understanding of their mechanisms.

1.2 Thesis outline

This dissertation is subdivided into four major parts, which are fairly independent one from each other. They are arranged as follows:

In Chapter 2, I present a dynamic rupture model of the 2016 M_w 7.8 Kaikōura earthquake. This event, which can be arguably considered the most complex rupture observed to date, caused surface rupture of at least 21 segments of the Marlborough fault system, in New Zealand's South Island (e.g., Hamling et al, 2017). The proposed scenario reproduces key characteristics of the event, including a large gap separating surface rupture traces, the possibility of significant slip on the subduction interface, the non-rupture of the fast-slipping Hope fault, and slow apparent rupture speed. This study demonstrates that dynamic rupture models can provide insight into the mechanical viability of competing hypotheses proposed by data-driven seismic inversion to explain the earthquake. The model suggests that the complex fault system operates at low apparent friction, thanks to the combined effects of overpressurized fluids, low dynamic friction and stress concentrations induced by deep fault creep.

In Chapter 3, I present an earthquake scenario of the September 2018, M_w 7.5 Sulawesi earthquake. This earthquake which occurred on the Palu-Koro strike-slip fault system was followed by an unexpected localized tsunami. By coupling the time-dependent, 3D seafloor displacements output of the earthquake scenario into a tsunami simulation, I show that direct earthquake-induced uplift and subsidence could have sourced the observed tsunami within Palu Bay. In fact, the remote stress regime reflecting regional transtension applied in the model produces some oblique faulting within the bay, which generates sufficient vertical ground displacement to reproduce tsunami and inundation observations. These results have important implications for submarine strike-slip fault systems worldwide, as the tsunami hazard of strike-slip faulting may be underestimated. This study, which was released on a preprint server only a few months after the event, demonstrates that physics-based interpretations can be an important part of the rapid earthquake response toolset.

Chapter 4 is focused on the 2004, M_w 9.1 Sumatra-Andaman earthquake. The sheer dimensions and tectonic complexity of this event challenged data collection and analysis capabilities. I present scenarios, constrained by the available globally acquired observations, that identify the key mechanisms controlling this enormous and devastating series of natural disasters. The models suggest that the along-depth variation in rock rigidity due to the presence of near-trench sediments, the off-fault yielding of these sediments during the rupture and the along-arc variation in the regional driving stress, are dominant factors which may have controlled the earthquake's dynamics and kinematics. This study demonstrates that 3D dynamic rupture modeling of megathrust earthquakes is now feasible and is critical to understanding the interplay of subduction mechanics, megathrust earthquakes and tsunami genesis, particularly when observations are sparse.

In Chapter 5, I investigate if fault roughness effects on earthquake kinematics, dynamics, and ground motion are scale-dependent, that is if specific wavelengths of fault roughness impact more earthquake dynamics than others. The models on fractal strike-slip rough faults do not reveal systematic wavelength dependence of these effects. Nevertheless, the characteristic length scale posed by rupture process zone width affects rupture dynamics locally. In this chapter, I also propose strategies to capture fault roughness effects on coarser geometric fault representations, which offer an interesting compromise between computational efficiency and accuracy.

A final Outlook (Chapter. 6) summarizes the key results of this thesis as well as ideas for future research.

1.3 Publications

Chapters 2 and 3 have been published in slightly altered form as:

- Ulrich T, Gabriel AA, Ampuero JP, Xu W (2019) Dynamic viability of the 2016 Mw 7.8 Kaikōura earthquake cascade on weak crustal faults. Nature Communications 10(1):1213, DOI 10.1038/s41467-019-09125-w

- Ulrich T, Vater S, Madden EH, Behrens J, van Dinther Y, van Zelst I, Fielding EJ, Liang C, Gabriel AA (2019) Coupled, Physics-Based Modeling Reveals Earthquake Displacements are Critical to the 2018 Palu, Sulawesi Tsunami. Pure and Applied Geophysics DOI 10.1007/s00024-019-02290-5

The work in Chapter 4 extends the Best Paper Award-winning publication:

- Uphoff C, Rettenberger S, Bader M, Madden E, Ulrich T, Wollherr S, Gabriel AA (2017) Extreme scale multi-physics simulations of the tsunamigenic 2004 Sumatra megathrust earthquake. In: Proceedings of the International Conference for High Performance Computing, Networking, Storage and Analysis, SC 2017, DOI 10.1145/3126908.3126948

An extended version of Chapter 4 has also been submitted as:

- Ulrich T, Gabriel AA, Madden E (2019) Stress, rigidity and sediment strength control megathrust earthquake and tsunami dynamics, DOI 10.31223/osf.io/s9263

The Chapter 5 will be submitted for publication shortly as well. During my Ph.D. thesis, I've also be involved in many collaborations, which are not detailed in this dissertation. In particular, my name is associated with 4 further submitted/published articles:

- Aochi H, Douglas J, Ulrich T (2017) Stress accumulation in the Marmara Sea estimated through ground-motion simulations from dynamic rupture scenarios. Journal of Geophysical Research: Solid Earth 122(3):2219–2235, DOI 10.1002/2016JB013790

- Madden E, Bader M, Behrens J, van Dinther Y, Gabriel AA, Rannabauer L, Ulrich T, Uphoff C, Vater S, Wollherr S, van Zelst I (2019) Linked 3D modeling of megathrust earthquake-tsunami events: from subduction to tsunami run up, submitted to GJI, reference GJI-20-0891

- Harris RA, Barall M, Aagaard B, Ma S, Roten D, Olsen K, Duan B, Liu D, Luo B, Bai K, Ampuero J, Kaneko Y, Gabriel A, Duru K, Ulrich T, Wollherr S, Shi Z, Dunham E, Bydlon S, Zhang Z, Chen X, Somala SN, Pelties C, Tago J, Cruz-Atienza VM, Kozdon J, Daub E, Aslam K, Kase Y, Withers K, Dalguer L (2018) A Suite of Exercises for Verifying Dynamic Earthquake Rupture Codes. Seismological Research Letters 89(3):1146–1162, DOI 10.1785/0220170222

- Palgunadi KH, Gabriel AA, Ulrich T, Lopéz-Comino JA, Mai PM (2020). Dynamic fault interaction during a fluid-injection induced earthquake: The 2017 Mw 5.5 Pohang event. Bull. Seismol. Soc. Am., DOI 10.1785/0120200106

2

Dynamic viability of the 2016 Mw 7.8 Kaikōura earthquake cascade on weak crustal faults

2.1 Abstract

We present a dynamic rupture model of the 2016 M_w 7.8 Kaikōura earthquake to unravel the event's riddles in a physics-based manner and provide insight on the mechanical viability of competing hypotheses proposed to explain them. Our model reproduces key characteristics of the event and constraints puzzling features inferred from high-quality observations including a large gap separating surface rupture traces, the possibility of significant slip on the subduction interface, the non-rupture of the Hope fault, and slow apparent rupture speed. We show that the observed rupture cascade is dynamically consistent with regional stress estimates and a crustal fault network geometry inferred from seismic and geodetic data. We propose that the complex fault system operates at low apparent friction thanks to the combined effects of overpressurized fluids, low dynamic friction and stress concentrations induced by deep fault creep.

This chapter has been published in slightly altered form as Ulrich T, Gabriel AA, Ampuero JP, Xu W (2019) Dynamic viability of the 2016 Mw 7.8 Kaikōura earthquake cascade on weak crustal faults. Nature Communications 10(1):1213, DOI 10.1038/s41467-019-09125-w

2.2 Introduction

The M_w 7.8 Kaikōura earthquake struck New Zealand's South Island on November 14, 2016. This event, considered the most complex rupture observed to date, caused surface rupture of at least 21 segments of the Marlborough fault system, some of them previously unknown. Here we develop a dynamic rupture model to unravel the event's riddles in a physics-based manner. Our model reproduces involves strike and thrust faulting and requires a linking low-dipping shallow thrust fault, but not slip on an underlying megathrust. The apparent rupture slowness is explained by a zigzagged propagation path and rupture delays at the transitions between faults. The complex fault system operates at low apparent friction thanks to the combined effects of overpressurized fluids, low dynamic friction and stress concentrations induced by deep fault creep. Our results associate the non-rupture of the Hope fault, one of the fundamental riddles of the event, with unfavourable dynamic stresses on the restraining step-over formed by the Conway-Charwell and Hope faults.

Studies of the Kaikōura earthquake based on geological, geodetic, tsunami and seismic data reveal puzzling features as well as observational difficulties. An apparent gap of 15–20 km in surface rupture between known faults (Hamling et al, 2017) may suggest a rupture jump over an unexpectedly large distance or the presence of deep fault segments connecting surface rupturing faults. Rupture duration is long, more than twice the average duration of past earthquakes of same magnitude (Duputel and Rivera, 2017). Finite-fault source inversion models inferred from strong motion and other data (Bradley et al, 2017; Holden et al, 2017; Wang et al, 2018) present unconventional kinematic features, such as unusually large delays between segments (Bradley et al, 2017) or strong scatter in the distribution of rupture time (Wang et al, 2018). The rupture may include simultaneous slip on the Hikurangi subduction interface (Wang et al, 2018) and several segments slipping more than once (Holden et al, 2017). Teleseismic back-projection studies (Hollingsworth et al, 2017; Xu et al, 2018; Zhang et al, 2017) agree on general earthquake characteristics (e.g. an overall SW-NE propagation direction) but not on the space-time evolution of the rupture.

Competing views of the role played by the Hikurangi subduction interface during the Kaikōura earthquake have emerged from previous studies. Whereas far-field teleseismic and some tsunami data inferences require thrust faulting on a low dipping fault, interpreted as the subduction interface beneath the Upper Kowhai and Jordan Thrust faults (Duputel and Rivera, 2017; Wang et al, 2018; Hollingsworth et al, 2017; Bai et al, 2017), analysis of strong motion, aftershocks, geodetic and coastal deformation observations find little or no contribution of the subduction interface (Holden et al, 2017; Xu et al, 2018; Clark et al, 2017; Cesca et al, 2017). The geometry of the Hikurangi megathrust is not well constrained in its Southern end (Williams et al, 2013): dipping angles assumed in previous studies range from 12 to 25 degrees (Hamling et al, 2017; Wang et al, 2018). Large-scale ground-deformations have then been explained by either slip on the subduction interface (e.g. Hamling et al, 2017; Wang et al, 2018) or by crustal models featuring listric fault geometries (Xu et al, 2018) or shallow thrust faults (Clark et al, 2017).

Incorporating the requirement that the rupture should be dynamically viable can help constrain the unexpected features and competing views of this event. Analyses of static Coulomb failure stress changes during rupture provides some mechanical insight on the rupture sequence (Hamling et al, 2017; Xu et al, 2018), but do not account for dynamic stress changes, which are an important factor in multi-fault ruptures (e.g. Bai and Ampuero, 2017). Dynamic rupture simulations provide physically self-consistent earthquake source descriptions, and have been used to study fundamental aspects of earthquake physics (e.g. Gabriel et al, 2012; Shi and Day, 2013), to assess earthquake hazard (e.g. Aochi and Ulrich, 2015) and to understand previous earthquakes (e.g. Olsen et al, 1997; Ma et al, 2008). The dynamic rupture modelling presented here provides physical arguments to discriminate between competing models of the fault system geometry and faulting mechanisms.

Mature plate boundary faults are, in general, apparently weak (Zoback et al, 1987; Behr and Platt, 2014; England, 2018), a feature that is required also by long-term geodynamic processes (e.g. Duarte et al, 2015; Osei Tutu et al, 2018) but that seems incompatible with the high static frictional strength of rocks (Byerlee, 1978). These two observations can be reconciled by considering dynamic weakening, which allows faults to operate at low average shear stress (Noda et al, 2009). However, low background stresses are generally unfavourable for rupture cascading across a network of faults. For instance, rupture jumps across fault stepovers are hindered by low initial stresses (Bai and Ampuero, 2017). This is one reason why finding a viable dynamic rupture model is non-trivial. The modelled fault system presented here features a low apparent friction while being overall favourably oriented with respect to the background stress. We demonstrate that fault weakness is compatible with a multi-fault cascading rupture. Our models suggest that such a weak-fault state is actually required to reproduce the Kaikōura cascade (see Methods sec. Apparent fault weakness).

Our dynamic model of the Kaikōura earthquake is tightly determined by integrating knowledge and data spanning a broad range of scales. It combines an unprecedented degree of realism, including a modern laboratory-based friction law, off-fault inelasticity, seismological estimates of regional stress, a realistic fault network geometry model, a 3D subsurface velocity model and high-resolution topography and bathymetry. High resolution 3D modeling is enabled by the SeisSol software package that couples seismic wave propagation with frictional fault failure and off-fault inelasticity, and is optimized for high-performance computing (see Methods sec. Numerical method).

The resulting dynamic model of the Kaikōura earthquake sheds light on the physical mechanisms of cascading ruptures in complex fault systems. Our model reproduces key characteristics of the event and constraints puzzling features including a large gap separating surface rupture traces, the possibility of significant slip on the subduction interface, the non-rupture of the Hope fault, and slow apparent rupture speed. We show that the observed rupture cascade is dynamically consistent with regional stress estimates and a crustal fault network geometry inferred from seismic and geodetic data under the assumption of low apparent friction.

2.3 Results

2.3.1 Fault geometry

We construct a model of the non-planar, intersecting network of crustal faults (Fig.2.1) by combining constraints from previous observational studies and from dynamic rupture modeling experiments. Fault geometries and orientations have been constrained by geological and geodetic data (e.g. Xu et al, 2018; Litchfield et al, 2014; Nicol et al, 2018). Our starting point is a smoothed version of the fault network geometry model III inferred from field and remote sensing data by Xu et al. It comprises three strike-slip faults: Humps and Stone Jug faults and a long segment with listric geometry (flattening at depth) resembling jointly the Hope-Upper Kowhai-Jordan Thrust, Kekerengu and Needles faults; and four thrust faults: Conwell-Charwell, Hundalee, Point Kean and Papatea faults. The model does not include the subduction interface but is sufficient to explain the observed static ground deformations in the near-field and far-field.

We extend this simplified model to capture the complexity of the southern part of the fault network. The western tip of the Humps segment is slightly rotated (azimuth direction from WSW to W) in our model. The improved agreement with the mapped surface rupture enables spontaneous termination of the westward rupture front. We substitute the Conway-Charwell fault zone by the distinct Leader and Conway-Charwell faults (Nicol et al, 2018). The geometry of the Leader fault is similar to the Conway-Charwell fault zone of Xu et al's model, however the former is increasingly steeper to the North. Surface rupture mapping suggests a segmentation of the Leader fault in at least two segments (Nicol et al, 2018). Yet the continuity of the inferred ground-deformations in that region (Nicol et al, 2018) suggests a unified segment. Dynamic rupture experiments accounting for a large step-over within the Leader fault also suggest that a segmented geometry is not viable. The Conway-Charwell fault steps over the Leader fault. It runs roughly parallel to the Hope fault to the North. The Southernmost part of the long listric segment of Xu et al's geometry, representing the Hope fault, is replaced here by the Hope fault geometry proposed by Hamling et al (2017), which is more consistent with the mapped fault trace and inferred dip angle (Litchfield et al, 2014). The 60° dipping Stone Jug fault of Xu et al is replaced by a steeper fault, as suggested by Nicol et al (2018). The Hundalee segment is shortened at its extremities, to limit its slip extent according to Xu et al's inversion results.

Based on experimental dynamic rupture simulations, we remove the Upper Kowhai fault. Instead, we postulate that the previously unknown Point Kean fault(Clark et al, 2017) acted as a crucial link between the Hundalee fault and the Northern faults. The Upper Kowhai fault is well oriented relative to the regional stress and, when included, experiences considerable slip in contradiction with observations. Although geodetic data suggest a moderate amount of slip on this fault at depth(Hamling et al, 2017; Xu et al, 2018), we hypothesize that such slip is not crucial for the continuation of the main rupture process. This is supported by recent evidence suggesting the rupture propagated from the Papatea fault to the Jordan thrust (more details in sec. Strong ground motion and continuous GPS data), rather than a Jordan thrust - Papatea fault sequence mediated by slip on the

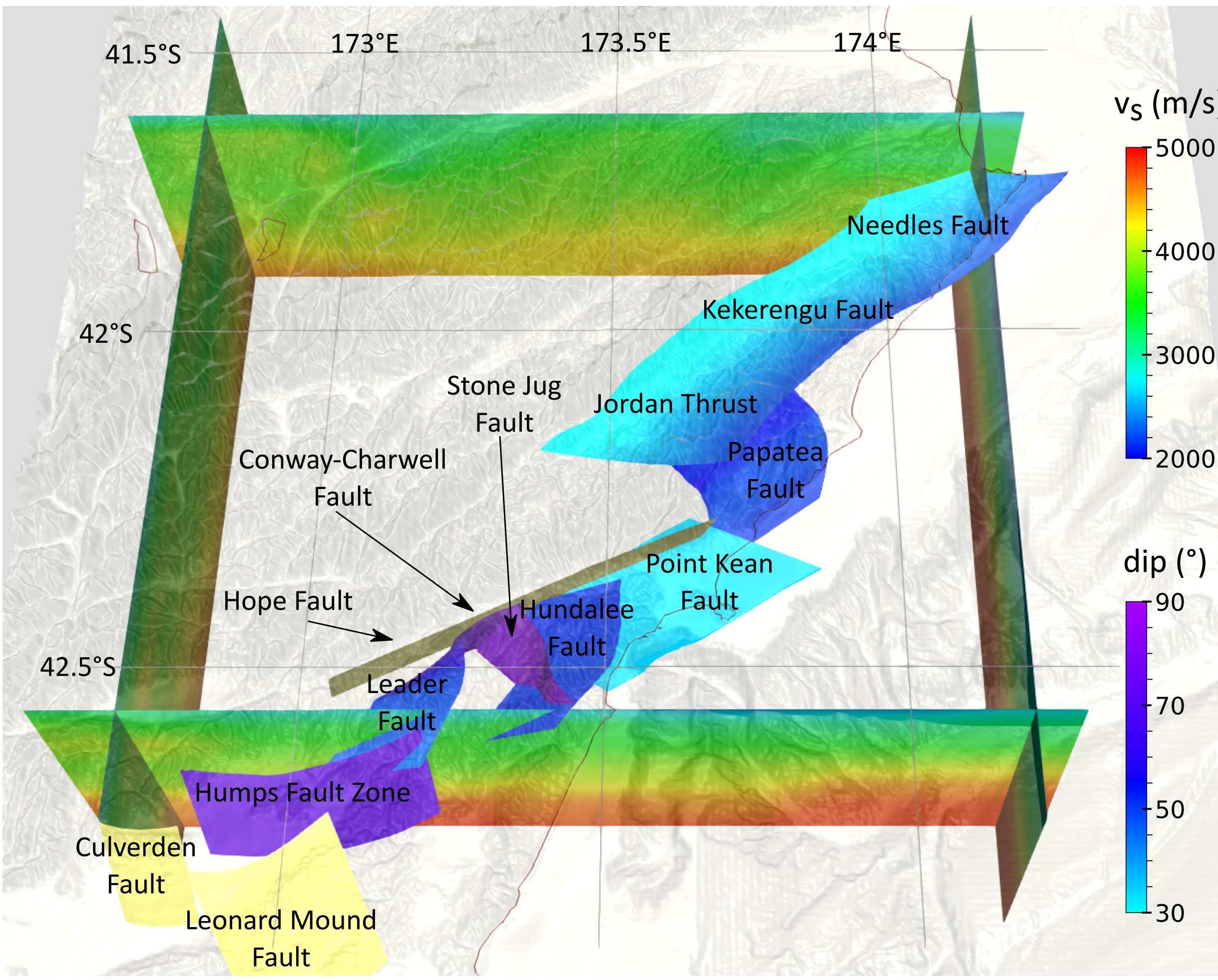

Figure 2.1: Fault network geometry prescribed for dynamic earthquake rupture modeling. Colors on fault surfaces indicate dipping angle (dip), highlighting the flattening with depth of the Jordan Thrust, Kekerengu and Needles faults. All segments dip westwards, except for the Humps Fault Zone. The Hope, Culverden and Leonard Mound faults, dipping respectively 70° toward NorthWest, 70° toward South and 50° toward SouthEast, are displayed in yellow. These faults do not rupture in our dynamic rupture model. Also shown are the high-resolution topography and bathymetry (Mitchell et al, 2012), and S-wave speeds (Vs) on four cross-sections of the 3D subsurface structure (Eberhart-Phillips et al, 2010) incorporated in the model.

Upper Kowhai fault. Moreover, localized slip at depth on the Upper Kowhai fault would be difficult to reproduce without additional small scale features in the fault geometry or fault strength heterogeneities.

2.3.2 Friction

We constrain our model parameters based on findings from laboratory to tectonic scale. Specifically, incorporating realistic levels of static and dynamic frictional resistance and stress drop is an important goal in our model design.

In our model, adopting a friction law with severe velocity- weakening friction law enables full cascading rupture and realistic amounts of slip, in contrast with simplified friction laws. We adopt a friction law featuring rapid weakening at high slip velocity (adapted from Dunham et al (2011a) as detailed in Methods sec. Fault friction) which reproduces the dramatic friction decrease observed in laboratory experiments at co-seismic slip rates (Di Toro et al, 2011). Comparing to results of our numerical experiments with linear slip-weakening friction (e.g. Andrews, 1976) on the same fault geometry, we find that strong velocity-weakening facilitates rupture cascading because it yields a smaller critical size to initiate self-sustained rupture by dynamic triggering.

2.3.3 Initial Stresses

The stresses acting on natural faults and their strength are difficult to quantify. Although strength parameters are measured in laboratory friction experiments (Di Toro et al, 2011) and estimated from different types of observations (Copley, 2018), little consensus about the actual strength of faults exists (Hardebeck, 2015). We introduce new procedures to constrain the initial fault stress and relative strength. This systematic approach, detailed in Methods sec. Initial stresses and Supplementary Fig. 2.A.7, is constrained by observations and simple theoretical analysis, including seismo-tectonic observations, fault slip inversion models, deep aseismic creep, fault fluid pressurization, Mohr-Coulomb theory of frictional failure and strong dynamic weakening. In addition to static analysis, it requires only few trial simulations to ensure sustained rupture propagation. By efficiently reducing the non-uniqueness in dynamic modeling, this approach is superior to the common trial-and-error approach.

Our initial stress model is fully described by seven independent parameters (Supplementary Fig. 2.A.7): four parameters related to regional stress and seismogenic depth, which are directly constrained by observations, and three unknown parameters related to fluid pressure, background shear stress and the intensity of deep stress concentration. A stress state is fully defined by its principal stress magnitudes and orientations. The orientations of all components and the relative magnitude of the intermediate principal stress are constrained by seismological observations (Townend et al, 2012). In addition, the smallest and largest principal stress components are constrained by prescribing the prestress relatively to strength drop on optimally-oriented fault planes (Aochi and Madariaga, 2003). To determine the preferred initial stresses, we first ensure compatibility of the stress state with the prescribed fault geometry and the slip rakes inferred from static source inversion. In this purely static step, we determine optimal stress parameters, within their identified uncertainties, that maximize the ratio of shear to normal stress all over the fault and maximize the alignment between fault shear tractions and inferred slip (Xu et al, 2018). We then use a set of dynamic rupture simulations to determine the depth-dependent initial shear stress and fluid pressure that lead to subshear rupture and slip amounts consistent with previous source inversion studies. The resulting model incorporates over-pressurized fault zone fluids (Suppe, 2014; Sutherland et al, 2017; Uphoff et al, 2017) with a fluid pressure considerably higher than hydrostatic stress but well below lithostatic level (see Methods sec. Initial stresses).

A favourable stress orientation on all segments, including thrust and strike-slip faults, is promoted by an intermediate principal stress close to the minimum principal stress (Aochi et al, 2006) representing a transpressional regime. This configuration promotes thrust faulting on faults dipping at approximately 60 degrees and striking perpendicularly to the direction of maximum compression, which roughly corresponds with the thrust fault geometries of our model.

In our model, dynamic rupture cascading is facilitated by deep stress concentrations (Fig. 2.2). The presence of stress concentrations at depth near the rheological transition between the locked and steady sliding portions of a fault is a known mathematical result of the theory of dislocations in elastic media (e.g. Kato, 2012; Bruhat and Segall, 2017). Such stress concentrations are also a typical result of interseismic stress calculations based on geodetically-derived coupling maps (Ader et al, 2012) or long-term slip rates (Mildon et al, 2017). Stress concentrations due to deep creep on the megathrust have been proposed to determine the rupture path independent of crustal fault characteristics (Lamb et al, 2018). Stress concentration is introduced in our model by two independent modulation functions (Supplementary Fig. 3.7).

Our initial stress model leads to low values of the initial shear to normal stress ratio over most of the seismogenic zone (the median value over the rupture area is 0.09, see Supplementary Fig. 2.A.9) in consistence with the apparent weakness of faults (Copley, 2018) (see Methods sec. Apparent fault weakness). Yet, most faults of our model are relatively well oriented with respect to the regional stress, and are therefore not weak in the classical sense. The classical Andersonian theory of faulting may be challenged in transpressional tectonic stress regimes resulting in non-unique faulting mechanisms. In the framework of dynamic rupture modeling, faults can be stressed well below failure almost everywhere and yet break spontaneously if triggered by a small highly stressed patch. Under the assumption of severe velocity-weakening friction (detailed in the previous section), a low level of prestress is required to achieve a reasonable stress drop. To this end, we have considered here two effects rarely taken into account together in dynamic rupture scenarios: 1) increased fluid pressure and 2) deep stress concentrations. We discuss their trade offs in more detail in Methods sec. Initial stresses. We infer that the interplay of deep creep, elevated fluid pressure and frictional dynamic weakening govern the apparent strength of faults and that these factors cannot be treated in isolation for such complex fault systems.

Further minor adjustments of the initial stresses are motivated by observations. To

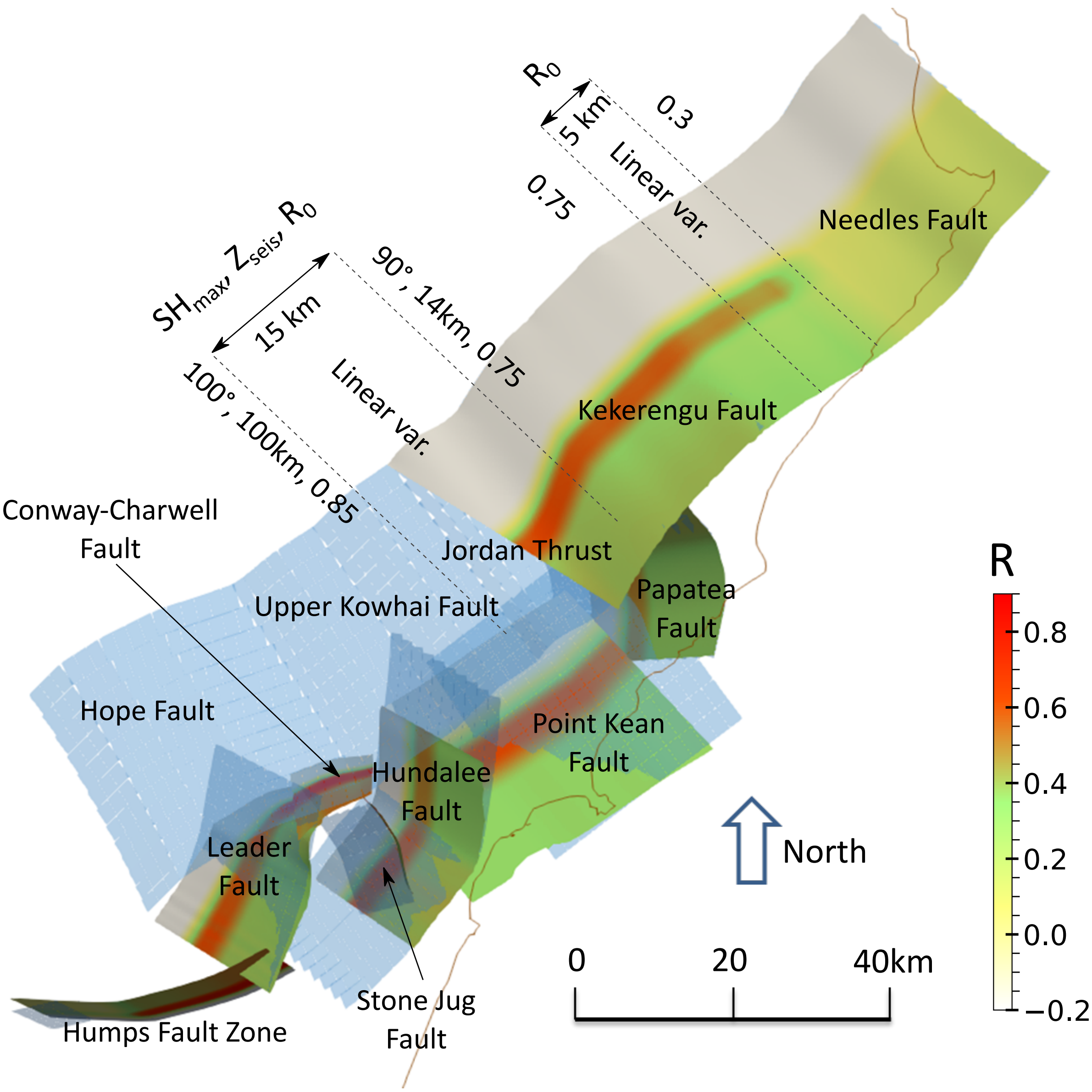

Figure 2.2: Adaptations made on the geodetically inferred fault geometry to develop a realistic dynamic rupture model. Changes made to the fault geometry are highlighted by plotting the here used geometry over the fault geometry of Xu et al (2018), shown in transparent blue. The distribution of initial fault stress ratio (eq. 1) along the fault network is also shown. The spatial distributions of parameters defining the stress (, and defined in Methods sec. Initial stresses) are indicated. The magnitude of the initial stress loading is decreased in the Needle fault region to prevent large slip on this optimally oriented segment (such decrease is modeled by decreasing by 60% and suppressing the deep stress concentrations in that region).

prevent excessive thrust faulting of the Kekerengu fault, we introduce a rotation of the maximum compressive stress orientation, within its range of uncertainty, from 100° in the South to 90° in the North. We also introduce a North-South increase of the seismogenic depth to allow deeper slip on the Papatea and Kekerengu faults, and a slight decrease of initial stress magnitude. Collectively both measures improve the model agreement with observed far-field ground deformations and rupture speed (they prevent shallow supershear rupture). Finally, we locally reduce the initial stresses on the Northernmost part of the Needles fault to prevent the occurrence of large slip in this area. We find that the Needles fault would otherwise host more than 10 m of slip, which is not supported by inversion results (Hamling et al, 2017; Xu et al, 2018).

2.3.4 A dynamically viable, cascading rupture

In our dynamic model rupture propagates spontaneously across eight fault segments (Fig. 2.1, which also shows three non-activated fault segments). The combined rupture length exceeds 240 km. The rupture successively cascades from South to North, directly branching at variable depths from the Humps to the Leader, Conwell-Charwell, Stone Jug, Hundalee and Point Kean faults. It then jumps to the Papatea fault via dynamic triggering at shallow depth, and finally branches to the Jordan Thrust (Fig. 2.3), Kekerengu and Needles faults (Fig. 2.4). This rupture cascade is dynamically viable without slip on the underlying subduction interface.

2.3.5 Fault slip

The modeled slip distributions and orientations are in agreement with the existing results (Xu et al, 2018; Clark et al, 2017). We observe an alternation of right-lateral strike-slip faulting (Humps, Conwell-Charwell, Jordan Thrust, Kekerengu and Needles faults) and thrusting (Leader, Hundalee and Papatea faults), as well as left-lateral strike-slip rupture of the Stone Jug fault and oblique faulting of the Point Kean fault (Fig. 2.5). Due to the smoothness of our assumed initial stresses, the final slip distribution is less patchy than in source inversion models. However, the moment magnitude of 7.9 is in excellent agreement with observations (Fig. 2.5f).

2.3.6 Apparent rupture speed

The complexity of the rupture cascade contributes to its apparently slow rupture speed. The ratio of rupture length to rupture duration (inferred from moment rate functions estimated by various authors; Fig. 2.5f, (Zhang et al, 2017; Bai et al, 2017; Vallée et al, 2011) indicates a slow average rupture velocity of about 1.4 km/s (Xu et al, 2018). In our model, rupture along each segment propagates twice as fast, at 2.9 km/s on average. Nevertheless, the observed rupture duration of approximately 90 s is reproduced thanks to a zigzagged propagation path accompanied by rupture delays at the transitions between segments (see Supplementary movies 1 and 2). Specifically, the modeled rupture sequence

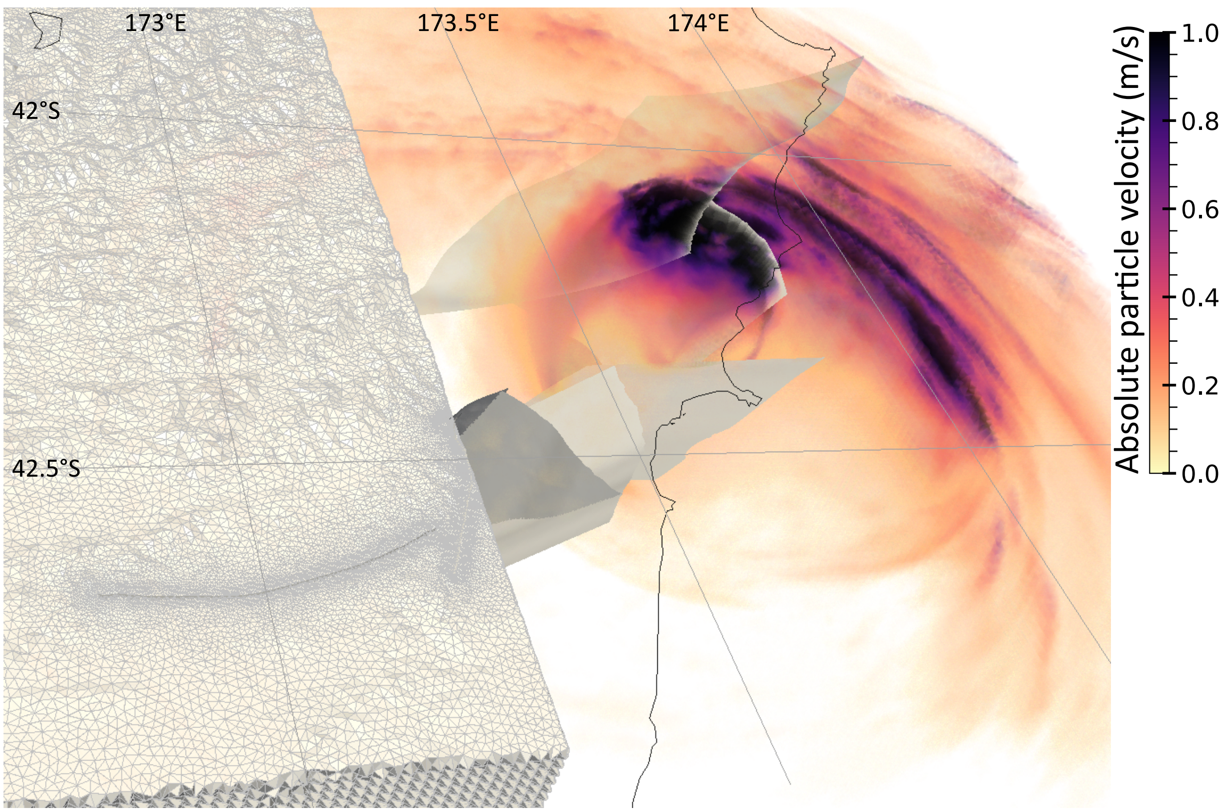

Figure 2.3: Snapshot of the wavefield (absolute particle velocity in m/s) across the fault network at a rupture time of 55 s. The model is discretized by an unstructured mesh accounting for 3D subsurface structure and high-resolution topography and featuring refined resolution in the vicinity of the faults. It incorporates the non-linear interactions between frictional on-fault failure, off-fault plasticity and wave propagation.

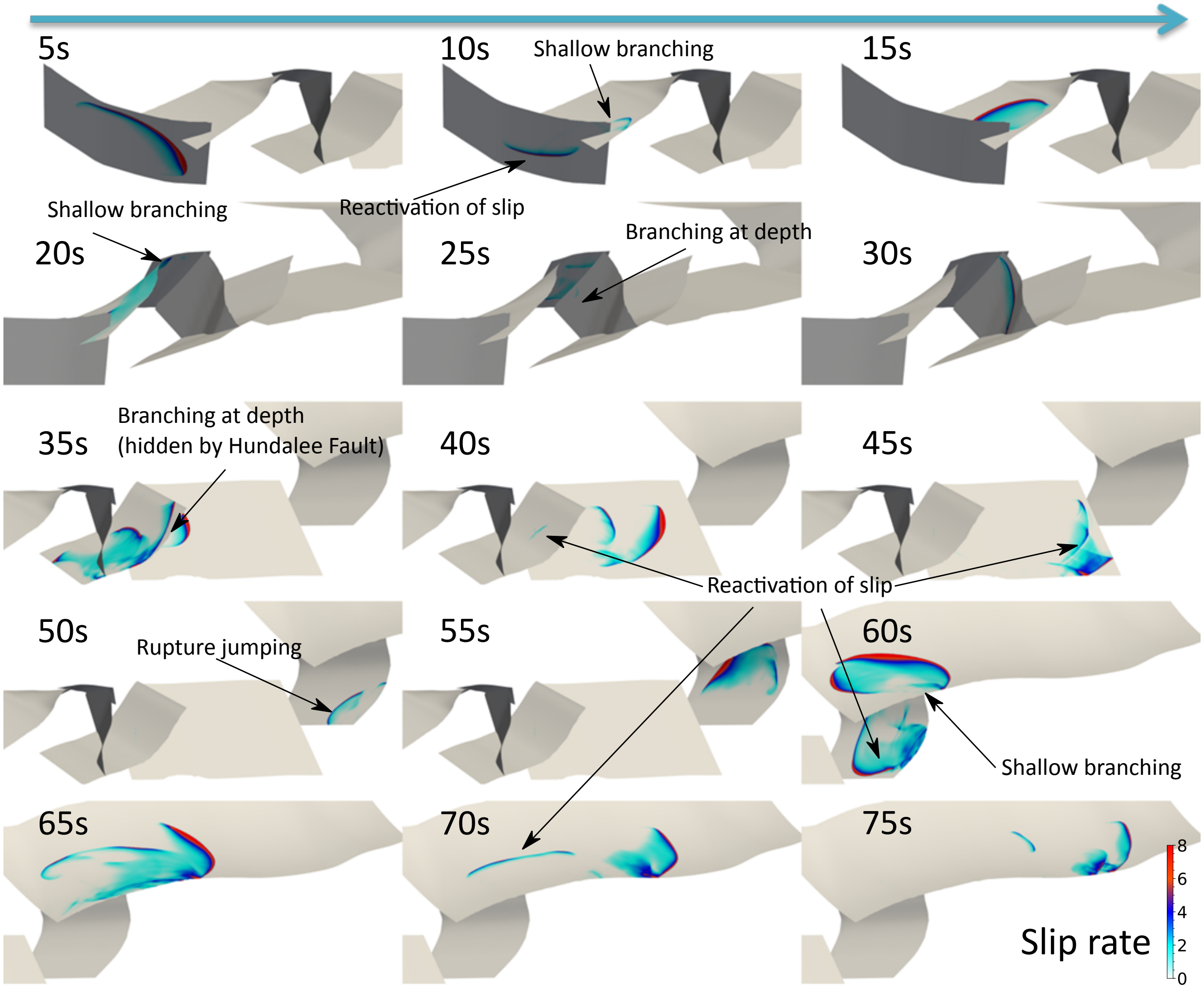

Figure 2.4: Overview of the simulated rupture propagation. Snapshots of the absolute slip rate are shown every 5 s. The figure focuses on four different portions of the fault system, following the rupture front as it propagates from South to North. Labels indicate remarkable features of the rupture discussed in the text.

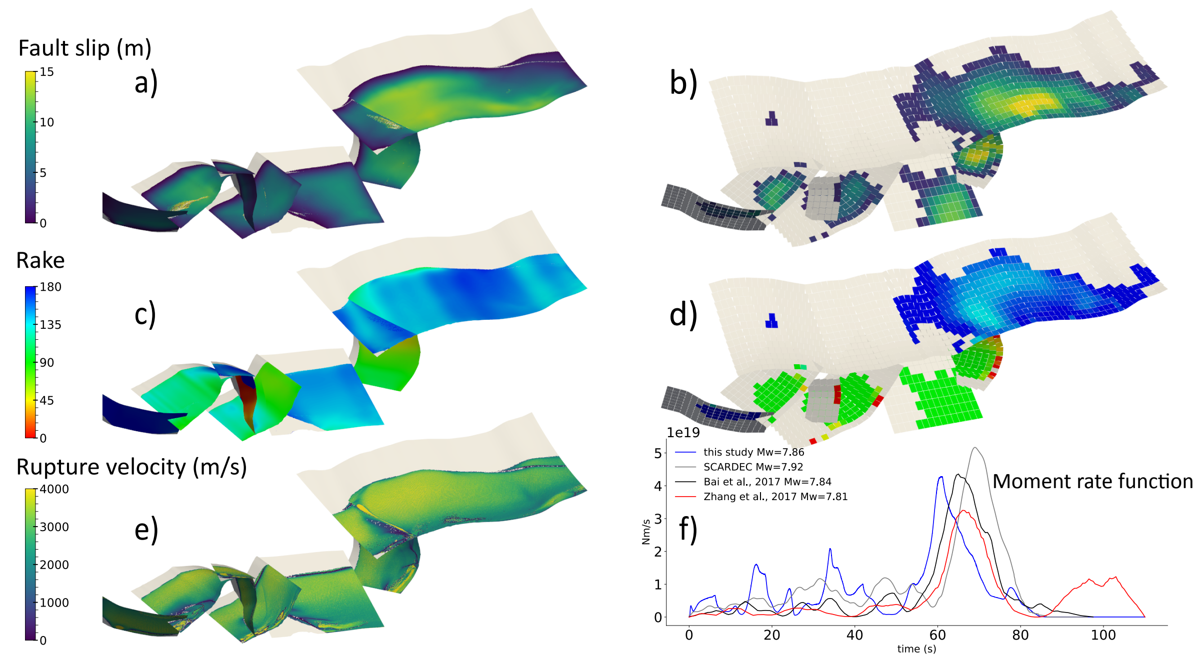

Figure 2.5: Source properties of the dynamic rupture model and comparison to observational inferences. Final slip magnitude (a) modeled here and (b) inferred by Xu et al.7. Final rake angle (c) modeled and (d) inferred by Xu et al (2018). (e) Modeled rupture velocity. (f) Modeled moment rate function compared with those inferred by Bai et al (2017) from teleseismic and tsunami data, byZhang et al (2017) from seismic waveform inversion and from teleseismic data by the SCARDEC method (Vallée et al, 2011).

takes about 30 s to reach the Hundalee fault after nucleation, whereas a hypothetical, uninterrupted rupture propagating at a constant speed of 3 km/s from the Humps to Hundalee faults would take only half this duration. The geometrical segmentation of the Leader and Conway-Charwell faults delays rupture by more than 5 s. Rupture across the Conway-Charwell fault is initiated at shallow depth. The Stone Jug fault can subsequently only be activated after rupture reached the deep stress concentration area and unleashed its triggering potential, causing further delay.

2.3.7 Moment release

Specific episodes of the dynamic rupture model can be associated to prominent phases of moment release and high-frequency radiation observed in the Kaikōura earthquake. Abrupt changes in rupture velocity during the entangled Leader - Charwell-Conwell - Stone Jug fault transition 20 seconds after rupture onset may correspond to a burst of high-frequency energy (Madariaga, 1977) noted by back-projection studies (Xu et al, 2018; Zhang et al, 2017). Around 60 s after rupture onset, a distinct moment release burst lasting 20 s corresponds to the simultaneous failure of the Papatea and Kekerengu faults and is well aligned with observations (Zhang et al, 2017; Bai et al, 2017; Vallée et al, 2011).

2.3.8 Ground deformation

The static ground deformation in our model is in good agreement with that inferred from geodetic data (Hamling et al, 2017; Xu et al, 2018) (figs. 2.6 and 2.7). In particular, the maximum horizontal deformation along the Kekerengu fault and the substantial uplift near the intersection between the Papatea and Kekerengu faults are captured, and the observed ground deformation near the epicenter is reasonably replicated.

2.3.9 Strong ground motion and continuous GPS data

Strong ground motion and continuous GPS data provide valuable constraints on the rupture kinematics. We compare our simulation results to these data with a focus on the timing of pulses, because our model does not account for small scale heterogeneities which could significantly modulate waveforms. Due to the close distance of some of the stations to the faults (Fig. 2.8) a close match of synthetic and observed waveforms is not expected. Yet, the dynamic rupture model is able to reproduce key features of the strong ground-motion and GPS recordings (Fig. 2.9). Our model captures the shape and amplitude of some pronounced waveform pulses, e.g. of the first strong pulse recorded along the NS direction at GPS station MRBL, which is situated in the nucleation area. A time shift of around 2 s hints at a nucleation process slower than modeled. At near-fault station KEKS two dominant phases are visible on both observed and synthetics waveforms (at 52 s and 63 s after rupture onset in the NS synthetics of Fig. 2.9 and in the fault-parallel-rotated waveforms of Supplementary Fig. 2.A.3). These dominant phases were attributed to a slip reactivation process on the Kekerengu fault by Holden et al (2017). However, our

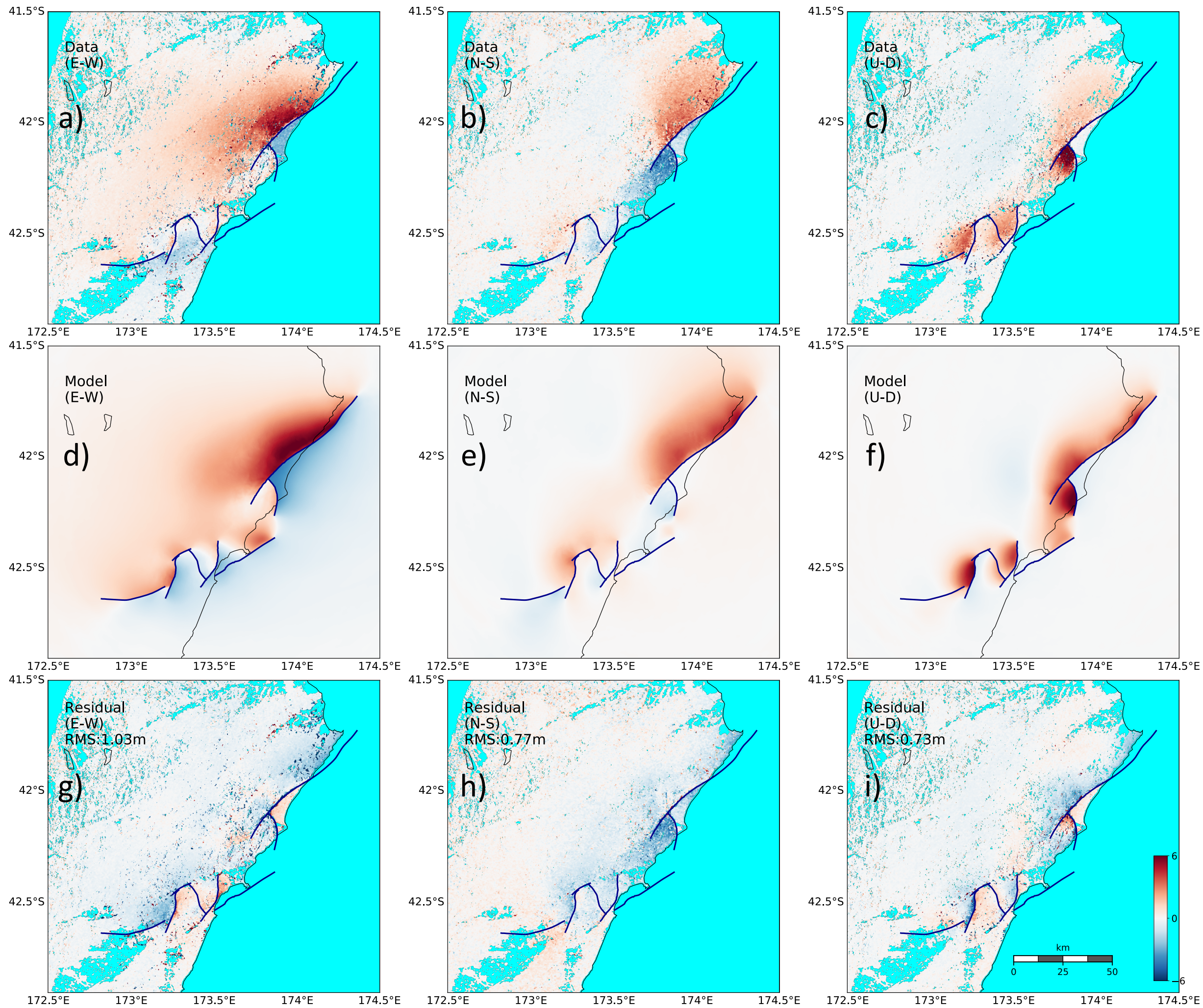

Figure 2.6: Comparison of observed and modeled coseismic surface displacements. 3D ground displacement (first row, panels a, b, c) inferred by space geodetic data (Xu et al, 2018), (second row, panels d, e, f) generated by the dynamic rupture model and (third row, panels g, h, i) their difference, all in meters. Columns from left to right are EW, NS and UD components. Root-mean-square (RMS) misfits are provided in the third row for each component.

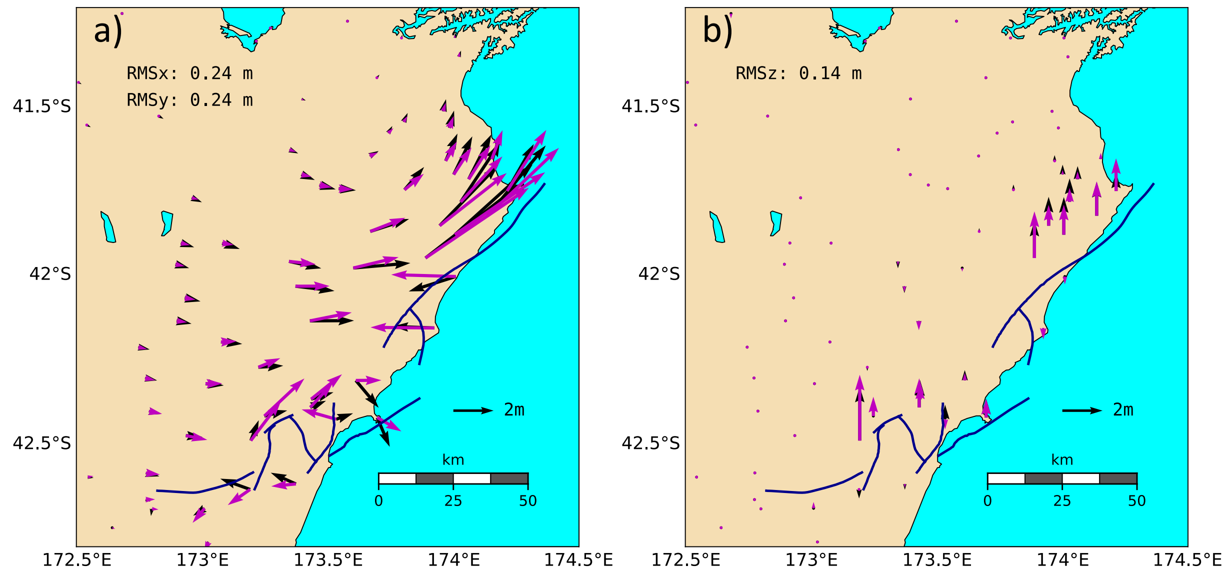

Figure 2.7: Comparison of observed and synthetic static ground deformation. Shown are observed (black) and modeled (magenta) horizontal (panel a) and vertical (panel b) ground displacement at GPS stations. Root-mean-square (RMS) misfits are provided for each component. The observed ground displacements at the locations of the GPS stations are taken from Hamling et al (2017)

model suggests that the first peak stems from the earlier rupture of the Papatea segment (see Supplementary movie 2). The ground motions recorded at station KEKS are thus consistent with a sequential rupture from the Papatea to Kekerengu faults. Strong evidence for a rupture sequence from Papatea to Kekerengu is further provided by the teleseismic back-projection results of Xu et al (2018). More recently, comparing remote sensing and field observations to 2D dynamic simulation results, Klinger et al (2018) showed that observed patterns of surface slip and off-fault damage support this scenario.

2.3.10 Teleseismic data

Our model without slip on the subduction interface satisfactorily reproduces long-period teleseismic data. Synthetics are generated at 5 teleseismic stations around the event (Fig. 2.8). We translate the dynamic fault slip time histories of our model into a subset of 40 double couple point sources. From these sources, broadband seismograms are calculated from a Green's function database using Instaseis (Krischer et al, 2017) and the PREM model for a maximum period of 2 s including anisotropic effects. In the long period range considered (100 to 450 s) the fit to observations is satisfying (Fig. 2.10). The effect of gravity, significant for surface waves at those periods, is not accounted for in the synthetics due to methodological limitations of Instaseis. In conjunction with our restriction to the 1D PREM model instead of incorporating 3D subsurface information, remaining differences between synthetics and observed records are expected. Following the same approach but

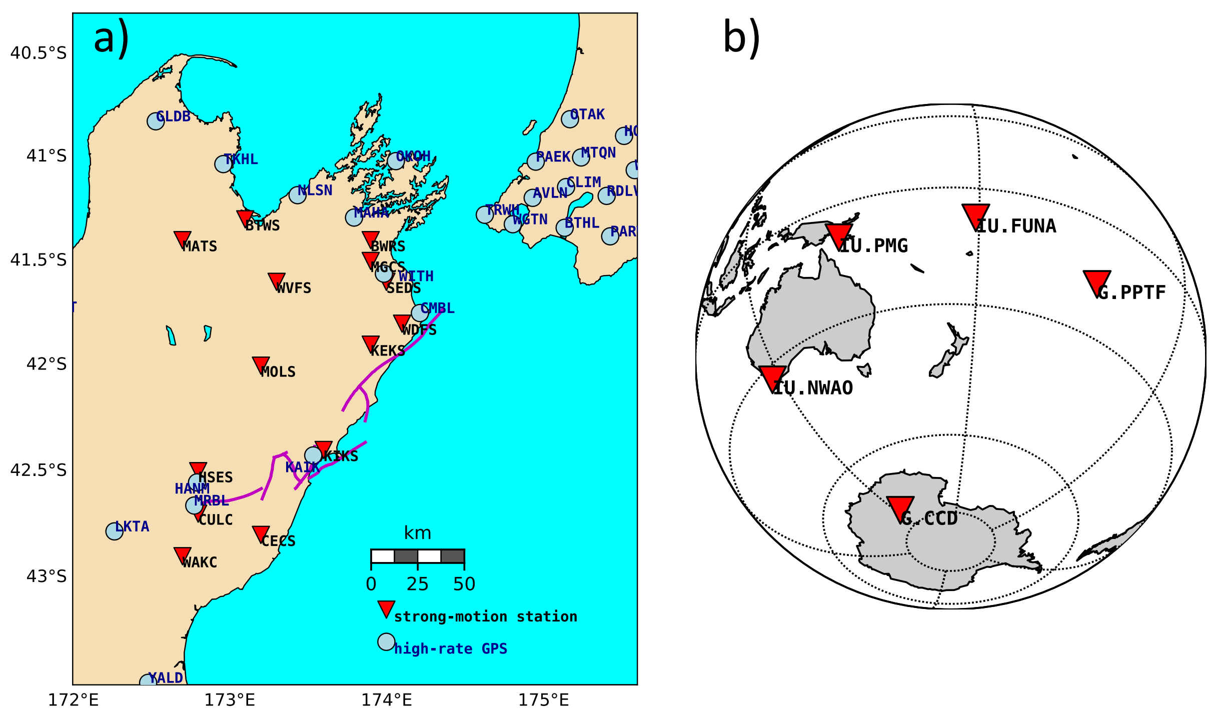

Figure 2.8: Locations of seismic and geodetic observations used for model verification. Near-fault high-rate GPS and strong-motion stations (on South Island) actively recording during the Kaikōura earthquake (a). Teleseismic stations at which synthetic data is compared with observed records (b).

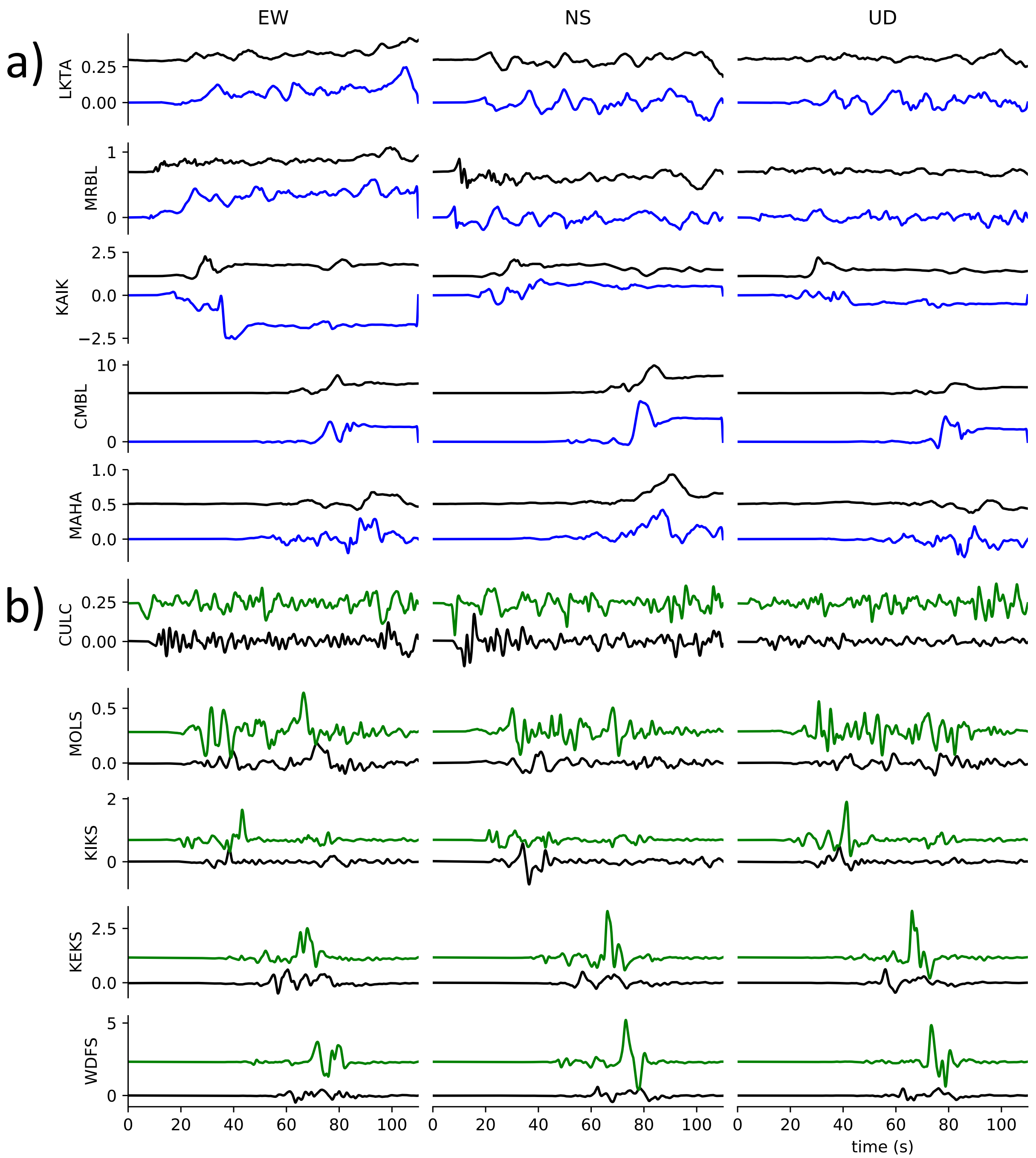

Figure 2.9: Comparison of modelled and observed ground motions. Five top rows (a): synthetic (blue) and observed (black) ground displacements at selected GPS stations. A 1 s low-pass filter has been applied to both signals. Five bottom rows (b): synthetic (green) and observed (black) ground velocities at selected strong-motion stations. A 0.005-1 s band-pass filter has been applied to both signals. The station locations are shown in Figure 2.8.

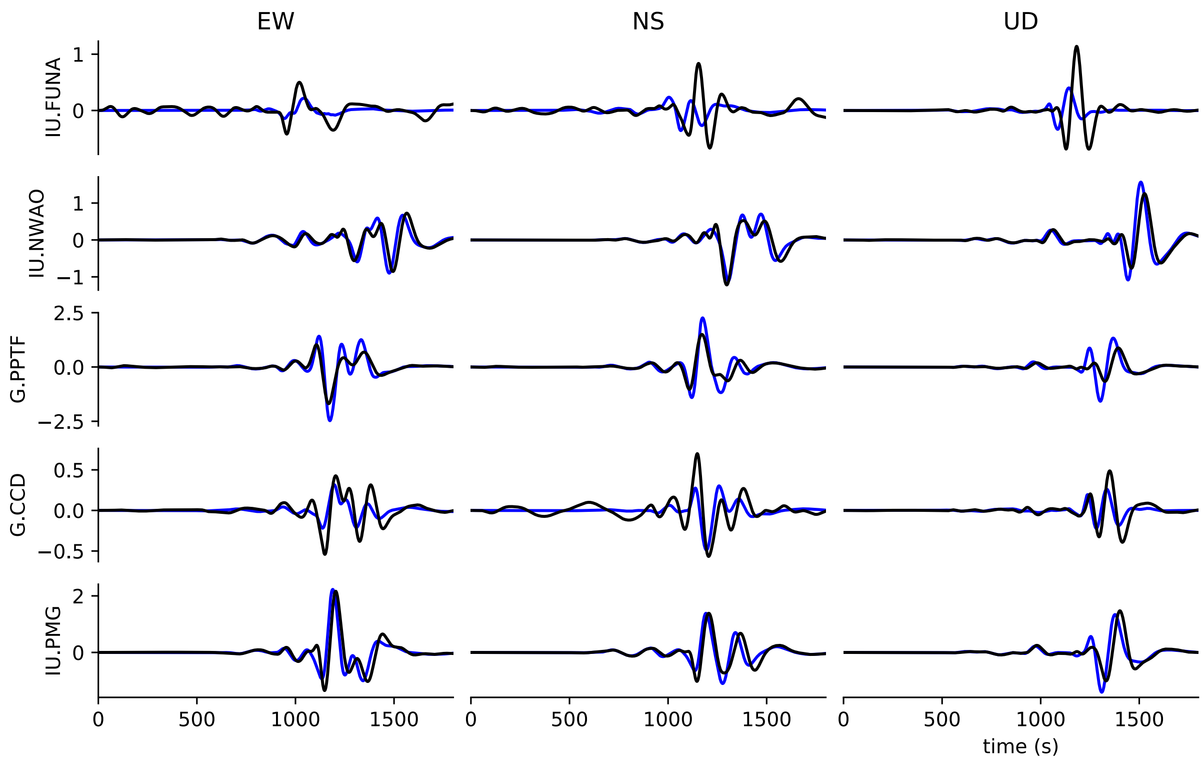

Figure 2.10: Comparison of modeled (blue) and observed (black) teleseismic waveforms. A 100-450 s band-pass filter is applied to all traces. Synthetics are generated using Instaseis (Krischer et al, 2017) and the PREM model including anisotropic effects and a maximum period of 2 s.

based on Duputel and Rivera's kinematic source model inferred from teleseismic data, indeed yields similar discrepancies. Overall, our results imply that slip on the subduction interface is not required to explain teleseismic observables.

2.3.11 Uniqueness of the dynamic model

There is a high level of uniqueness in the outcome of our dynamic model. Slight variations on the initial conditions, for instance a subtle change in the maximum principal stress direction of 10 degrees or a less transpressional regime (e.g. a 10% increase of the stress shape ratio defined in eq. 9 of Methods sec. Initial stresses), lead to early spontaneous rupture arrest. Changes in fault geometry (orientation, size and separation distance of fault segments) also affect the dynamics considerably. Moreover, ad hoc abrupt lateral changes in initial fault stress or strength are not required to steer the rupture along its zigzagged path. We nevertheless acknowledge the possibility of alternative models yielding similar rupture dynamics. Such models can be readily designed based on the trade-offs we define in Methods sec. Initial stresses, e.g. by decreasing or increasing the effects of deep stress concentrations, fluid pressure or frictional weakening. In Methods sec. Apparent fault weakness, we accordingly ensure the robustness of important modelling choices of the preferred model.

2.3.12 Linking fault segments

Two segments, the Stone Jug and the Point Kean faults, are crucial for the successful propagation of the rupture to the North. The Stone Jug fault hosts little slip but allows the earthquake to branch towards the Hundalee fault. The offshore Point Kean fault links at depth the seemingly disconnected Southern and Northern parts of the fault system (as proposed by Clark et al), whose surface traces are separated by a large gap of 15 km. Our model matches the observed (horizontal) surface rupture in the Northern part (Litchfield et al, 2017), the inferred slip amplitude and the northwards rupture propagation on the Point Kean fault, by dominantly oblique faulting. It supports a previous suggestion that rupture of the Point Kean fault was responsible for the observed on-shore coastal uplift extending 20 km north of Kaikōura Peninsula (Clark et al, 2017). On the other hand, a stronger dip-slip component would be required to explain the northeastward GPS displacements around this thrust fault. According to the dynamic rupture model, this could only be achieved by an (unlikely) local prestress rotation of about 30 degrees towards South, or by considering a fault geometry with lower strike.

2.3.13 Rupture complexity

The dynamic model shows rupture complexity also at a fine scale. Rupture takes the form of slip-pulses (Fig. 2.4) of various origins: fast-velocity weakening friction promotes self-healing slip pulses (Gabriel et al, 2012; Heaton, 1990) which can propagate at lower background stress levels and with smaller slip than crack-like ruptures. The nonlinear interaction between frictional failure and the free surface causes interface waves that bounce back from the surface, fault ends and branching points lead to rupture front segmentation, unloading stresses carried by seismic waves reflected from subsurface impedance contrasts cause healing fronts. The Hundalee, Point Kean, Papatea and Kekerengu segments slip more than once.

Rupture complexity can affect seismological inferences of fault friction properties. Frictional parameters are typically adopted from laboratory experiments. However, it is uncertain how valid it is to extrapolate results from the laboratory scale to the field scale. For the Kaikōura earthquake, a large slip-weakening distance D_c, the amount of slip over which frictional weakening occurs, has been estimated from a strong-motion record (Kaneko et al, 2017). Despite the much smaller on-fault Dc values (0.2 to 0.5 m) in our model, the apparent Dc value inferred from the resulting off-fault ground motions is large (5.6 m, Supplementary Fig. 2.A.3), which can be attributed to intertwined waveforms from multiple slip fronts.

2.4 Discussion

The physics-based dynamic source modeling approach in this study has distinct contributions compared to the data-driven kinematic source modeling approach. In the latter, a large number of free parameters enables close fitting of observations at the expense of mechanical consistency. Furthermore, the kinematic earthquake source inversion problem is inherently non-unique (many solutions fit the data equally well). In contrast, our dynamic model is controlled by a few independent parameters. Its main goal is to understand the underlying physics of the cascading rupture sequence. Adopting fault geometries and a regional stress state consistent with previous studies, our dynamic rupture model reproduces major observations of the real event, reveals unexpected features and constrains competing hypotheses.

Our results provide insight on the state of stress under which complex fault systems operate. In our model, strong frictional weakening, fluid overpressure and deep stress concentrations result in a remarkably low apparent friction. Yet the low average ratio of initial shear stress to normal stress does not hinder dynamic rupture cascading across multiple fault segments. Instead, it is crucial to achieve the full cascading rupture with realistic stress drop and slip. In Methods sec. Apparent fault weakness we discuss fault strength based on the orientation of the fault system, apparent fault strengths in the static and dynamic sense and explore additional model setups demonstrating the robustness of our preferred model. We conclude by quantifying the relative contributions of our modeling assumptions to the apparent weakness of faults.

The effects of overpressurized fault fluids and deep stress concentrations and the additional effect of a low dynamic friction result in an overall low apparent friction coefficient. We find that reproducing all aspects of the rupture cascade requires all three effects. The combined effect of strong frictional weakening, fluid overpressure and deep stress concentrations and the fundamental impact of fault weakness on the existence of subduction and tectonics (e.g. Osei Tutu et al, 2018) show the importance of mechanical feedbacks across multiple time scales, from the short-term processes of dynamic rupture and earthquake cycles to the long-term geodynamic processes that shape and reshape the Earth.

Dramatic frictional weakening is one of the key mechanisms contributing to fault weakness in our model. Our assumed dynamic friction coefficient, $f\mathrm{w} = 0.1$, falls within the range of values typically observed in laboratory experiments and considered by the dynamic rupture community (e.g. Gabriel et al, 2012; Shi and Day, 2013; Noda et al, 2009). Nevertheless, we probed the necessity of such a low value by additional simulations, as detailed in Methods sec. Alternative model setups. By static considerations, we find that a sustained cascading rupture under a higher f_w would require conditions that disagree with stress inversion inferences, namely a too low stress shape ratio (Supplementary Fig. 5). In addition, prescribing higher f_w results in a prestress distribution of larger variability, less favourable for rupture cascading.

Frictional failure in our model initiates at the best-oriented fault segment, in contrast with the 'keystone fault' model (Fletcher et al, 2016) in which large multi-fault earthquakes nucleate on a misoriented fault. The dynamic rupture cascade does not require laterally heterogeneous initial stresses, as those arising on fault networks in which optimally oriented faults release stress not only during large earthquakes but also via smaller events or aseismic creep.

We find that a zigzagged propagation path, accompanied by rupture delays at the transitions between faults, can explain apparently slow rupture speeds. While the surprisingly slow apparent rupture velocity and long rupture duration were depicted widely in seismological observations, our dynamic model provides a mechanically viable explanation for this observation.

Physics-based dynamic modeling contributes crucial arguments to the debate of whether the rupture of multiple crustal faults during the Kaikōura earthquake was promoted by slip on the underlying Hikurangi subduction interface. Rupture of the subduction interface is not favored by the regional stresses we inferred. A planar, shallowly dipping subduction interface approximated similar to previous studies (Hamling et al, 2017) experiences very low shear stresses when included in our model. Dynamic triggering of such a subduction interface is further impeded by its large depth below the crustal fault network. However, slip may be promoted if the stresses rotate at depth or if the megathrust is frictionally weaker than the crustal faults (e.g. Hardebeck, 2015; Suppe, 2014). We show that incorporating the shallowly dipping (35°) Point Kean fault segment successfully links the Southern and Northern parts of the fault system without involvement of the Hikurangi subduction interface. Our model is equally compatible with long-period teleseismic data as models assuming slip on the subduction interface and may be further tested by tsunami observations.

Features of the Kaikōura earthquake that remain unexplained by our dynamic models suggest opportunities to better understand the role of fault heterogeneities. These features include the inferred localized slip at depth on the Upper Kowhai fault as well as incompletely modeled aspects of the observed waveforms. Our dynamic rupture scenario is able to explain the early rupture termination to the South, but does not give a definitive answer concerning the origin of rupture termination to the North. On the Humps fault zone, spontaneous rupture termination to the West is observed, associated with a slight change in the strike direction resulting in a less favorable fault orientation. In additional dynamic rupture simulations including the nearest identified faults to the South, the Leonard Mound and the Culverden reverse faults (e.g. Pettinga et al, 2001), we found that the rupture is not able to trigger those faults. To the North, we have to locally reduce the initial stresses on the Northernmost part of the Needles fault to prevent its rupture with large slip. The very straight surface rupture of the Needles fault (Litchfield et al, 2017) does not suggest a high segmentation that may have prevented the rupture to extend further North. Hamling et al and Wang et al suggest a steeper geometry for this segment (dip angle of 70°) which would result in an increased shear over normal stress ratio, favouring rupture instead of terminating it. These considerations indicate that the most likely reason for the rupture termination to the North is the presence of an asperity to which the many aftershocks in the region (Kaiser et al, 2017) might be associated.

Our model provides a solution to one of the fundamental riddles of the Kaikōura earthquake: why did the rupture by-pass the Hope fault? The lack of significant slip observed on the Hope fault is surprising given its orientation similar to the Kekerengu fault, its fast geologic slip-rate and short recurrence interval (180-310 years (Stirling et al, 2017) and references therein), and its linkage to most mapped faults involved in the rupture. In our model, the Hope and Conway-Charwell faults are less than 1 km apart at the surface, and diverge at depth because of their different dipping angles. Both faults are well oriented relative to the background stress. Yet, the Hope fault is not triggered by the rupture of the Conway-Charwell fault, nor later on by the rupture of the Hundalee and Point Kean faults. We interpret this non-rupture as a consequence of the restraining step-over configuration formed by the Conway-Charwell and Hope faults, leading to an unfavourable distribution of dynamic stresses on the Hope fault (e.g. Oglesby, 2005). Dynamic modeling allows assessing the possibility of rupture jumping across such unconventional stepover configurations, combining thrust and strike-slip faulting mechanisms and faults of different dip angles.

Dynamic rupture modeling is now approaching a state of maturity and computational efficiency that should soon allow it to be integrated synergistically with data inversion efforts within the first days following the occurrence of an earthquake, making physics-based interpretations an important part of the rapid earthquake response toolset.

2.5 Acknowledgments

The work presented in this paper was supported by the German Research Foundation (DFG) (projects no. KA 2281/4-1, GA 2465/2-1, GA 2465/3-1), by BaCaTec (project no. A4), by KONWIHR - the Bavarian Competence Network for Technical and Scientific High Performance Computing (project NewWave), by the Volkswagen Foundation (ASCETE, grant no. 88479), by KAUST-CRG (GAST, grant no. ORS-2016-CRG5-3027 and FRAGEN, grant no. ORS-2017-CRG6 3389.02), by the European Union's Horizon 2020 research and innovation program (ExaHyPE, grant no. 671698 and ChEESE, grant no. 823844), by NSF CAREER award EAR-1151926, by the French government through the UCAJEDI Investments in the Future project ANR-15-IDEX-01 managed by the National Research Agency (ANR), by the Hong Kong Polytechnic University startup grant (1-ZE6R) and by the Hong Kong Research Grants Council Early Career Scheme Fund (F-PP4B). Computing resources were provided by the Institute of Geophysics of LMU Munich (Oeser et al, 2006), the Leibniz Supercomputing Centre (LRZ, projects no. h019z, pr63qo, and pr45fi on SuperMUC). We thank J. Townend for sharing his stress inversion data, J. Zhang and M. Vallée for sharing moment rate functions, C. Holden and E. d'Anastasio who provided processed GPS time-series, GNS Science for providing active fault database, earthquake rupture maps and reports, continuous GPS data, and strong motion waveform data and Simone Cesca and an anonymous reviewer for their positive feedback and thoughtful reviews.

2.6 Author contributions

This project was initiated by J.-P. A. Modelling was conducted by T. U. under the supervision of A.-A. G. with input from J.-P. A. and W. X.. The manuscript was written jointly by T. U., A.-A. G. and J.-P. A..

2.7 Competing interests

The authors declare no competing interests and no conflict of interests.

Appendix

2.A Methods

2.A.1 Numerical method

We solve the coupled dynamic rupture and wave propagation problem using the freely available software SeisSol(SeisSol GitHub, 2019; Dumbser and Käser, 2006; Pelties et al, 2014) based on the Arbitrary high-order accurate DERivative Discontinuous Galerkin method (ADER-DG). SeisSol employs fully adaptive, unstructured tetrahedral meshes to combine geometrically complex 3D geological structures, nonlinear rheologies and high-order accurate propagation of seismic waves. Our model (Fig. 2.3) includes a geometrically complex fault network, high-resolution topography (Mitchell et al, 2012), 3D subsurface structure (Eberhart-Phillips et al, 2010) and plastic energy dissipation off the fault (Andrews, 2005; Wollherr et al, 2018). A high resolution model is crucial for accurately resolving rupture branching and (re-)nucleation processes. The degree of realism and accuracy achieved in this study is enabled by recent computational optimizations targeting strong scalability on many-core CPUs (Breuer et al, 2014; Heinecke et al, 2014; Rettenberger et al, 2016) and a ten-fold speedup owing to an efficient local time-stepping algorithm (Uphoff et al, 2017). Simulating 90 seconds on a computational mesh consisting of 29 million elements required typically 2 hours on 3000 Sandy Bridge cores of the supercomputer SuperMuc (Leibniz Supercomputing Centre, Germany), which is well within the scope of resources available to typical users of supercomputing centres. The few dynamic rupture simulations required to constrain the initial stress setup (Methods sec. Initial stresses) employed a coarser discretization of wave propagation in the volume while still finely resolving the faults, reducing computational cost by 80%.

2.A.2 Mesh

The domain is discretized into an unstructured computational mesh of 29 million high-order (spatio-temporal order 4) four-node linear tetrahedral elements (Fig. 2.3). The mesh resolution is refined to element edge lengths of 300 m close to faults. Topography and bathymetry are discretized by at most 1000 m and refined in regions of strong variations. The mesh allows resolving the seismic wavefield at frequencies up to 3 Hz in the vicinity of the faults.

2.A.3 Fault friction

We use a rate- and state-dependent friction law with fast velocity-weakening at high speed proposed in the community benchmark problem TPV104 of the Southern California Earthquake Center (Harris et al, 2018) and similar to the friction law introduced by Dunham et al (2011a). Here we provide the governing equations using the notations defined in Supplementary Table 2.A.1. The magnitude of the shear traction τ is assumed to always equal the fault strength, defined as the product of the friction coefficient f and the effective normal stress ${\sigma_\mathrm{n}}'$:

$$\tau = f(V, \Psi){\sigma_\mathrm{n}}', \tag{2.1}$$

The traction $\boldsymbol{\tau}$ and slip rate $\boldsymbol{V}$ vectors are parallel and satisfy:

$$\tau \boldsymbol{V} = V \boldsymbol{\tau}, \tag{2.2}$$

The friction coefficient f depends on the slip rate V and a state variable Ψ:

$$f(V, \Psi) = a \,\mathrm{arcsinh}\Big(\frac{V}{2V_0} \exp\Big(\frac{\Psi}{a}\Big)\Big), \tag{2.3}$$

The state variable Ψ evolves according to the following differential equation:

$$\frac{\mathrm{d}\Psi}{\mathrm{d}t} = -\frac{V}{L}(\Psi - \Psi_{\mathrm{ss}}(V)), \tag{2.4}$$

where Ψ_{ss} is the value of the state variable at steady-state given by:

$$\Psi_{\mathrm{ss}} = a \ln\Big(\frac{2V_0}{V} \sinh\Big(\frac{f_{\mathrm{ss}}(V)}{a}\Big)\Big), \tag{2.5}$$

where the steady-state friction coefficient is

$$f_{\mathrm{ss}}(V) = f_\mathrm{w} + \frac{f_{\mathrm{LV}}(V) - f_\mathrm{w}}{(1 + (V/V_\mathrm{w})^8)^{1/8}}, \tag{2.6}$$

and the low-velocity steady-state friction coefficient f_{LV} is given by:

$$f_{\mathrm{LV}}(V) = f_0 - (b - a) \ln \frac{V}{V_0}, \tag{2.7}$$

At slip rates higher than the characteristic slip rate V_w, f_{ss} asymptotically approaches the fully weakened friction coefficient f_w, with a decay roughly proportional to $1/V$. This feature of friction is observed in laboratory experiments and is present in thermal weakening theories. At low slip velocities, this friction law is consistent with classical rate-and-state friction.

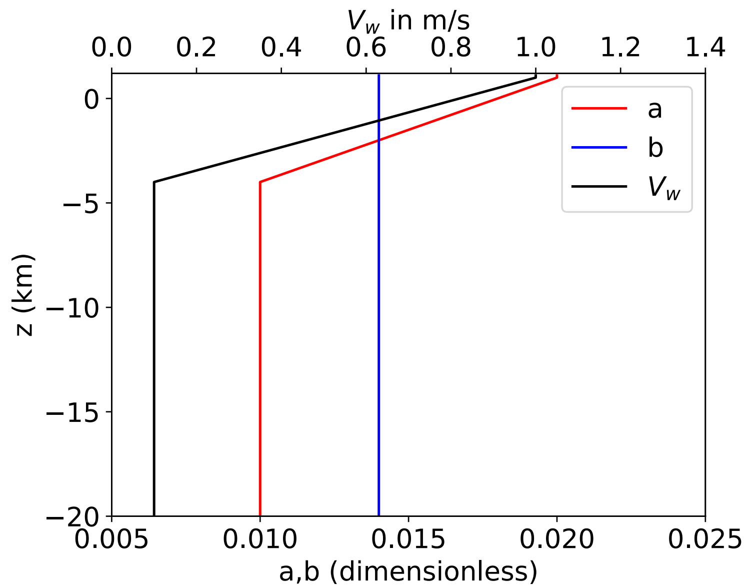

Figure 2.A.1: Depth dependence of friction parameters.

The initial distribution of the state variable Ψ_{ini} is obtained, from eqs. 2.1 and 2.3, assuming that the faults are initially at steady state, sliding at a slip rate of magnitude $V_{\text{ini}} = 10^{-16}$ m/s:

$$\Psi_{\text{ini}} = a \ln\left(\frac{2V_0}{V_{\text{ini}}} \sinh\left(\frac{\tau_{\text{ini}}}{a\sigma_{\text{ini}}}\right)\right), \tag{2.8}$$

where σ_{ini} and τ_{ini} are the (spatially varying) initial shear and normal tractions on the fault.

The values of the frictional properties adopted in this study are given in Supplementary Table 2.A.1. Some parameters are depth dependent, as indicated in Supplementary Fig. 2.A.1. To suppress shallow supershear transition, V_{w} is assumed to be larger at shallow depth (e.g. Shi and Day, 2013) on all faults (except for the Leader segment, to avoid suppressing its emerging shallow rupture quickly after branching from the Humps fault).

We infer the equivalent slip-weakening distance Dc_{eq} of our simulations from the resulting curves of shear stress as a function of slip at various points along the rupture. We define

$$Dc_{\text{eq}} = \frac{2G_{\text{c}}}{\tau_{\text{peak}} - \tau_{\text{final}}} \text{ where } G_{\text{c}} = \int_{D_{\text{peak}}}^{\infty} (\tau_D - \tau_{\text{final}}) dD \tag{2.9}$$

Supplementary Fig. 2.A.2 shows the typical stress change at 5 fault locations. The values of fall in the range from 0.2 to 0.5 m. In addition, following Kaneko et al (2017), we apply the method of Mikumo et al (2003) to our modeled seismograms at station KEKS (Supplementary Fig. 2.A.3) to estimate an apparent slip-weakening distance D_{c}'' defined as twice the fault-parallel displacement at the time the peak fault-parallel velocity is reached. The fault-parallel velocity waveform has two peaks of similar amplitude, separated by

Table 2.A.1: Fault frictional properties assumed in this study.

Direct-effect parameter	a	0.01
Evolution-effect parameter	b	0.014
Reference slip rate	V_0	10^{-6} m/s
Steady-state low-velocity friction coefficient at slip rate V_0	f_0	0.6
Characteristic slip distance of state evolution	L	0.2 m
Weakening slip rate	V_w	0.1 m/s
Fully weakened friction coefficient	f_w	0.1
Initial slip rate	V_{ini}	10^{-16} m/s

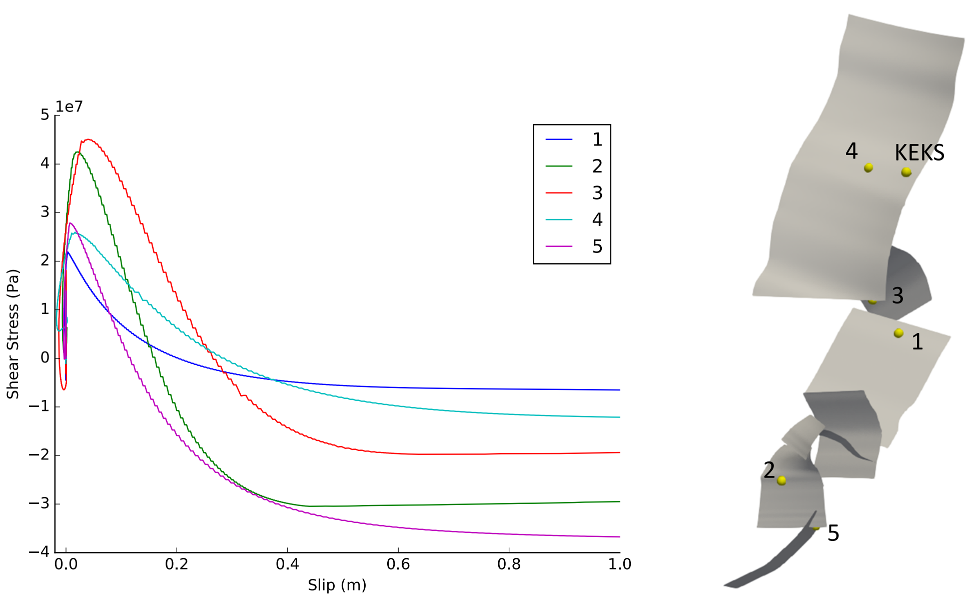

(a) (b)

Figure 2.A.2: Slip-weakening response and equivalent critical slip-weakening distance. (a) Changes of shear traction in the direction of initial shear traction as a function of slip at 5 fault locations shown in (b). The stress drops over slip distances in the range from 0.2 to 0.5 m.

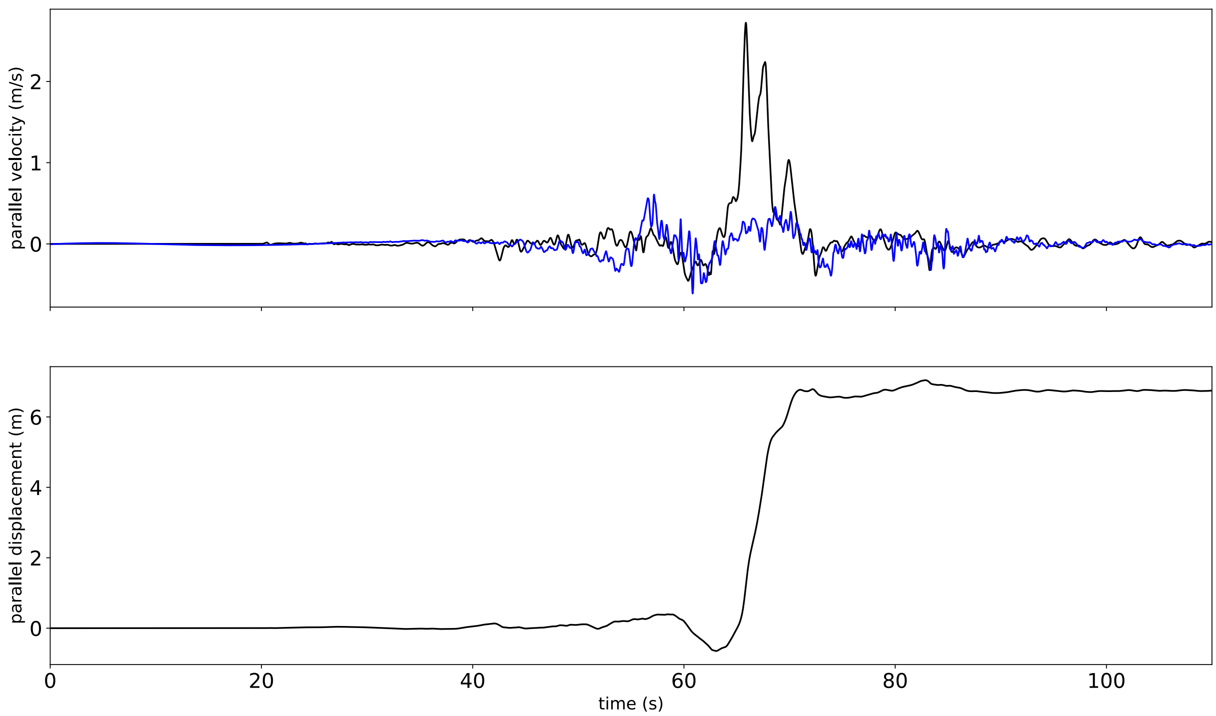

Figure 2.A.3: Synthetic (black) and observed (blue) fault-parallel velocity and displacement waveforms at station KEKS (location shown in Supplementary Fig. 2.A.2b). The apparent slip-weakening distance D_c'' is estimated following the method of Mikumo et al (2003) as twice the fault-parallel displacement observed when the peak fault-parallel velocity is reached. We estimate $D_c'' = 5.6$m averaging over the two largest parallel velocity peaks caused by segmented on-fault dynamic rupture fronts.

a few seconds, which may result from multiple slip fronts on the Kekerengu fault (see Supplementary movie 2). We estimate D_c''=2.4 m from the first peak. The second peak gives D_c''=8.9 m, larger than the value of 4.9 m estimated by Kaneko et al (2017). These D_c'' estimates are larger than the on-fault D_c'' for at least three reasons. First, the station is at a distance from the fault (≈2.7 km) much larger than the maximum distance for resolution of Mikumo et al (2003)'s method ($R_c = 0.8 V_s T_c$ =232 m, where V_s=2.9 km/s is the shear wave velocity and T_c=0.1 s is the breakdown time. Note that T_c in our simulations is much smaller than the apparent value of 5.5 s reported by Kaneko et al (2017)). Second, off-fault plasticity (included in our model) can contribute to increase the apparent D_c''. Third, our dynamic model features multiple slip fronts contributing to the cumulative fault-parallel displacement, thus increasing D_c''.

2.A.4 Off-fault plasticity

We model off-fault dissipation assuming a Drucker-Prager elasto-viscoplastic rheology (Wollherr et al, 2018). The failure criterion is parameterized by two material properties,

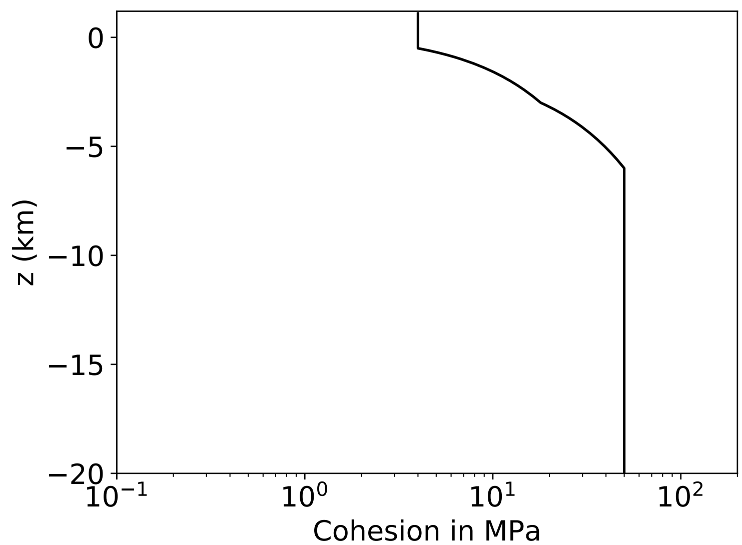

Figure 2.A.4: Depth dependence of cohesion in the off-fault plastic yielding criterion.

internal friction coefficient and cohesion. We set the internal friction coefficient equal to the reference fault friction coefficient (0.6). Following Roten et al (2018), we consider an empirically-motivated depth-dependent distribution of cohesion (Supplementary Fig. 2.A.4) to account for the tightening of the rock structure with depth. Lower cohesion in the upper 6 km allows suppressing the unrealistic occurence of shallow supershear transitions without preventing rupture cascading by dynamic triggering. A viscoplastic relaxation mechanism is adopted to ensure convergence of the simulation results upon mesh refinement. Its relaxation time T_v also controls the effectiveness of plasticity. We set T_v=0.05 s, independently of the mesh resolution. We consider depth-dependent off-fault initial stresses consistent with the initial stresses prescribed on the fault.

2.A.5 Initial stresses

Following Townend et al (2012), we first constrain the initial stress tensor using the parameters SH_max, ν and θ. Following Lund and Townend (2007), SH_max is defined as the azimuth of the maximum horizontal compressive stress. It coincides with the commonly used horizontal projection of the largest subhorizontal stress if the state of stress is Andersonian, i.e. if one principal stress component is vertical. The stress shape ratio is defined as:

$$\nu = \frac{s_2 - s_3}{s_1 - s_3} \tag{2.10}$$

where s_k are the amplitudes of the principal stresses. The angle θ is the orientation of the intermediate principal stress relative to the horizontal plane.

We set the initial stresses in the rupture area to be consistent with regional stress parameters inferred from earthquake focal mechanisms by Townend et al (2012) and their

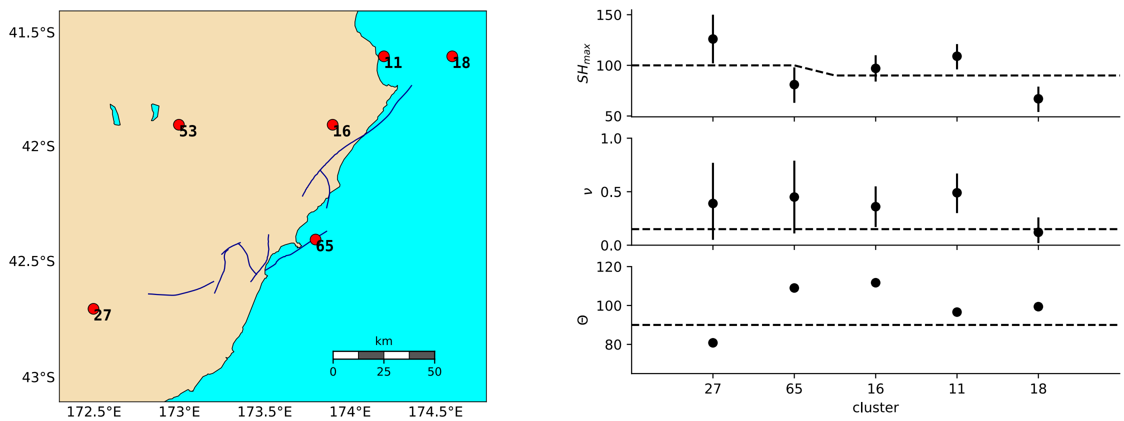

(a) (b)

Figure 2.A.5: Observationally constrained regional stress state. (a) Centroid locations of the earthquake clusters from Townend et al (2012) that are close to the Kaikōura earthquake source. We discard cluster 53 because it is too deep. (b) Stress parameters of the 5 remaining clusters. Uncertainties of $\mathrm{SH}_{\max}$ and ν are indicated by their 10% - 90% percentile ranges (vertical bars). The dashed lines show the stress parameter values we chose.

uncertainties. Among the earthquake clusters they considered, the ones within our region of interest are, from North to South, clusters 27, 65, 16, 11 and 18 (Supplementary Fig. 2.A.5a). We ignore cluster 53, located between 50 and 100 km depth, because it is much deeper than the Kaikōura earthquake source. The stress parameters at the considered clusters are shown in Supplementary Fig. 2.A.5b. The average $\mathrm{SH}_{\max}$ is 96°(the average over the whole South Island is 115°). The value of ν is inferred to be in the range of 0.4 to 0.5, but lower values cannot be ruled out. Note, that we use a different definition of ν than Townend et al. The value of θ falls in the range 80° to 110°.

An additional parameter, the relative prestress ratio R between fault stress drop and breakdown strength drop, allows constraining the magnitude of the deviatoric stresses:

$$R = \frac{\tau_0 - \mu_\mathrm{s}\sigma_\mathrm{n}}{(\mu_\mathrm{s} - \mu_\mathrm{d})\sigma_\mathrm{n}}, \tag{2.11}$$

To compute R we assume $\mu_\mathrm{d} = f_\mathrm{w}$ =0.1, as we observe that the fully weakened friction f_w is typically reached in our simulations. The maximum friction coefficient reached during rupture (μ_s) is not a prescribed model parameter. Its value varies along the fault and often exceeds f_0 but rarely falls below this value. For simplicity, we use $\mu_\mathrm{s} = f_0$ =0.6 as a conservative value: in our simulation results, the real R can be smaller than the one we prescribe but is rarely larger.

Following the notations of Aochi and Madariaga (2003), we define

$$P = (s_1 + s_3)/2 \text{ and } ds = (s_1 - s_3)/2 \tag{2.12}$$

$(P, 0)$ is the center of the Mohr-Coulomb circle and ds is its radius. The s_{i} are related to P, ds and ν by:

$$\begin{aligned} s_1 &= P + ds \\ s_2 &= P + 2\nu ds \\ s_3 &= P - ds \end{aligned} \tag{2.13}$$

The effective confining stress $\sigma_{\mathrm{c}}' = (s_1 + s_2 + s_3)/3$ is related to P by:

$$\sigma_{\mathrm{c}}' = P + (2\nu - 1)ds/3 \tag{2.14}$$

We assume a lithostatic confining stress given by $\sigma_{\mathrm{c}}(z) = \rho g z$ and a rock density of 2670 kg/m3. In a transpressional regime, this results in an average stress $\sigma_{\mathrm{c}}(z) = (s_1 + s_2 + s_3)/3 = \rho g z$, which is slightly lower than when adopting the conventional assumption of $\sigma_{\mathrm{zz}}(z) = \rho g z$. Switching the depth-dependance of stress while not altering stress drop and rupture dynamics in our model can readily be achieved by slightly adjusting fluid pressure.

We assume fluid pressure throughout the crust is proportional to the lithostatic stress: $P\mathrm{f} = \gamma\sigma_{\mathrm{c}}(z)$, where γ is the fluid-pressure ratio. The effective confining stress is thus $\sigma_{\mathrm{c}}(z)' = (1 - \gamma)\sigma_{\mathrm{c}}(z)$. The value $\gamma = \rho_{\mathrm{water}}/\rho$=0.37 corresponds to a hydrostatic state; higher γ values 0.37 correspond to overpressurized states.

The shearτ and normal stresses σ_{n} and on a fault plane oriented at an angle Φ relative to the maximum principal stress are:

$$\begin{aligned} \tau &= ds \sin(2\Phi) \\ \sigma_{\mathrm{n}} &= P - ds \cos(2\Phi) \end{aligned} \tag{2.15}$$

An optimally oriented fault plane is one that, under homogeneous initial stress and stressing rate, would reach failure before any other fault with different orientation. At failure, its shear to normal stress ratio is maximized (compared to other fault orientations) and equal to μ_{s}. Its angle is:

$$\Phi = \Pi/4 - 0.5 \arctan(\mu_{\mathrm{s}}) \tag{2.16}$$

We will prescribe $R_{\mathrm{opt}}(z) = R_0 g(z)$ on the (virtual) optimally oriented fault plane, where $g(z)$, described hereafter, is a stress modulation function accounting for stress concentrations expected right above the seismogenic depth of faults loaded by deep fault creep (Supplementary Fig. 3.7). Using eqs. 3.3, 2.14 and 2.15, we solve for ds and obtain:

$$ds = \frac{\sigma_{\mathrm{c}}(z)'}{\sin(2\Phi)/(\mu_{\mathrm{d}} + (\mu_{\mathrm{s}} - \mu_{\mathrm{d}})R_{\mathrm{opt}}) + (2\nu - 1)/3 + \cos(2\Phi)} \tag{2.17}$$

For given values of ν and $R0$, we can compute the depth-dependent s_{i} using eqs. 2.13, 2.14 and 2.17. The orientations of the three principal stress components (assumed depth-independent) are determined by the angles $\mathrm{SH_{max}}$ and θ and by the constraint that the

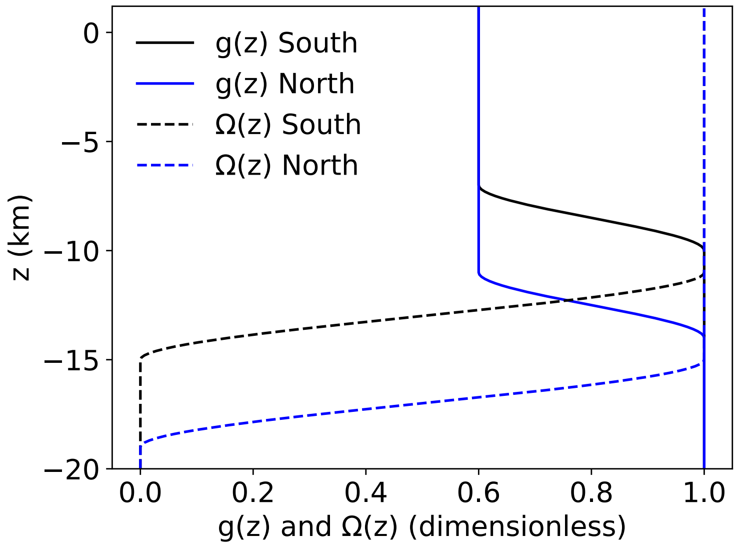

Figure 2.A.6: Depth-dependent stress modulation functions $g(z)$ and $\Omega(z)$. The former tapers off following a Smoothstep function at some distance above the seismogenic depth z_{seis}. The latter tapers off below z_{seis}. The seismogenic depth is prescribed as slightly shallower ($z_{\mathrm{seis}} = 10.5\,\mathrm{km}$) in the Northern part of the rupture than in its Southern part ($z_{\mathrm{seis}} = 14.5\,\mathrm{km}$).

faulting mechanism on the optimally oriented plane is strike-slip. This defines a depth-dependent stress tensor (b_{ij}). The final stress tensor (s_{ij}) is obtained by applying a second stress modulation function $\Omega(z)$, which smoothly cancels the deviatoric stresses below the seismogenic depth z_{seis} (Supplementary Fig. 3.7):

$$s_{ij} = \Omega(z)b_{ij}(z) + (1 - \Omega(z))\sigma_{\mathrm{c}}(z)'\delta_{ij} \tag{2.18}$$

The initial stress model depends on four parameters constrained by observations ($\mathrm{SH}_{\mathrm{max}}$, θ, ν and z_{seis}) and on three unknown parameters related to fluid pressure, background shear stress and deep stress concentration (γ, R_0 and $g(0)$). To determine the preferred values adopted in our final simulations, instead of running costly dynamic rupture simulations for each parameter set, we developed the following workflow, illustrated in Supplementary Fig. 2.A.7.

In a first step, we constrain $\mathrm{SH}_{\mathrm{max}}$, θ and ν to ensure compatibility of the stress with inferred fault geometry and slip rake. As a first assumption, we use a fluid-pressure ratio γ=0.75 (Uphoff et al, 2017). We set uniform stress modulation functions, $g(z)$=1 and $\Omega(z)$=1, and assume $R_{\mathrm{opt}}(z) = R_0$=0.7 on the optimal plane. We expect this R_0 value to be high enough to allow a sustained rupture on faults of highly varying orientations and low enough to result in a reasonable stress drop. An order-of-magnitude estimate of stress drop is $R_0(1-\gamma)\sigma_{\mathrm{c}}(\mu_{\mathrm{s}} - \mu_{\mathrm{d}})$, under the assumption $R_{\mathrm{opt}}(z) = R_0$. We test different stress configurations, by varying $\mathrm{SH}_{\mathrm{max}}$ in the range 50°-120°, ν in the range 0-0.5 and θ in the

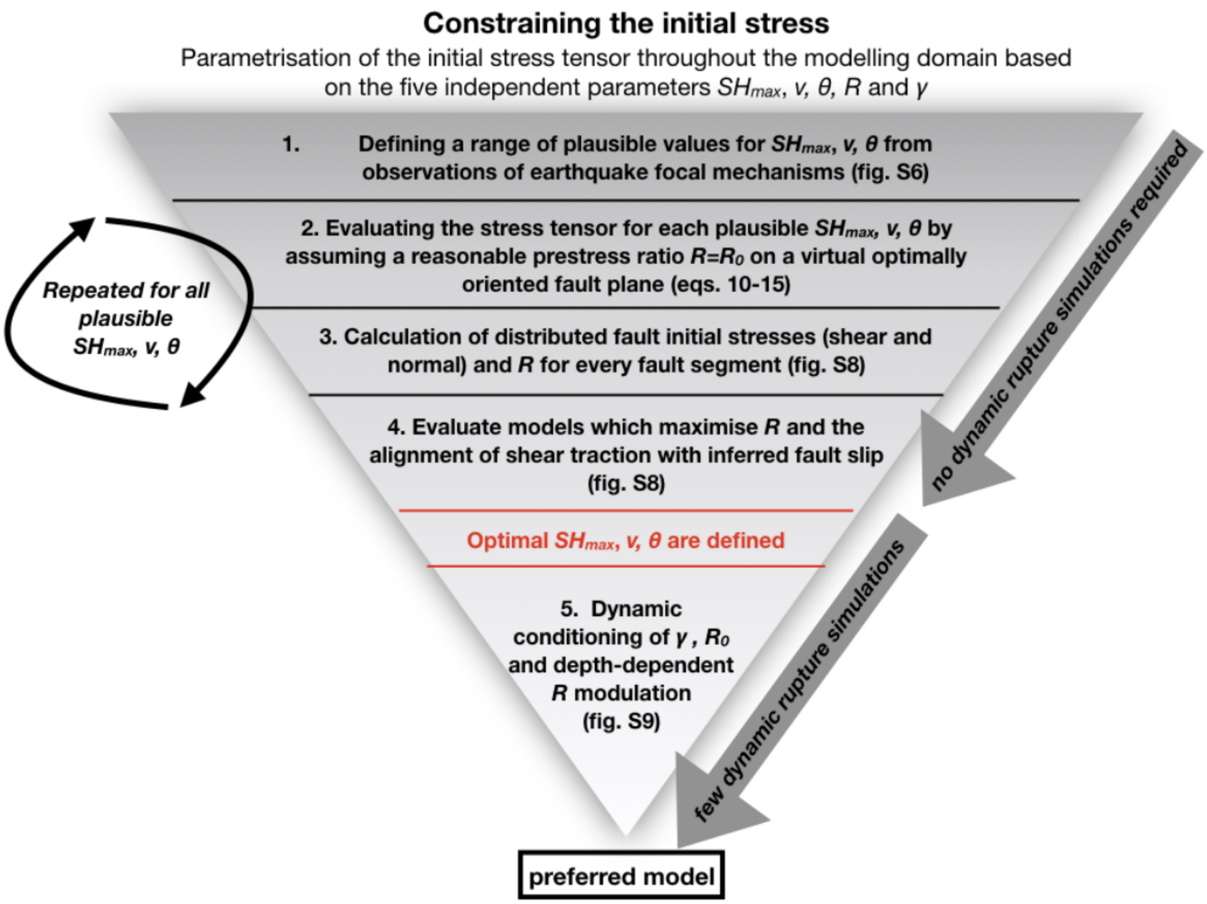

Figure 2.A.7: Workflow for constraining the initial stress from observations and simple theoretical analysis requiring only few trial dynamic rupture simulations. The independent parameters that fully describe the initial stress tensor are: $\mathrm{SH}_{\mathrm{max}}$ denotes the azimuth of maximum horizontal compressive stress, ν is the stress shape ratio, θ is the orientation of the intermediate principal stress relative to horizontal, R is the relative prestress ratio, γ is the ratio between fluid-pressure and lithostatic confining stress, and the stress modulation functions $g(z)$ and $\Omega(z)$, all described in the text.

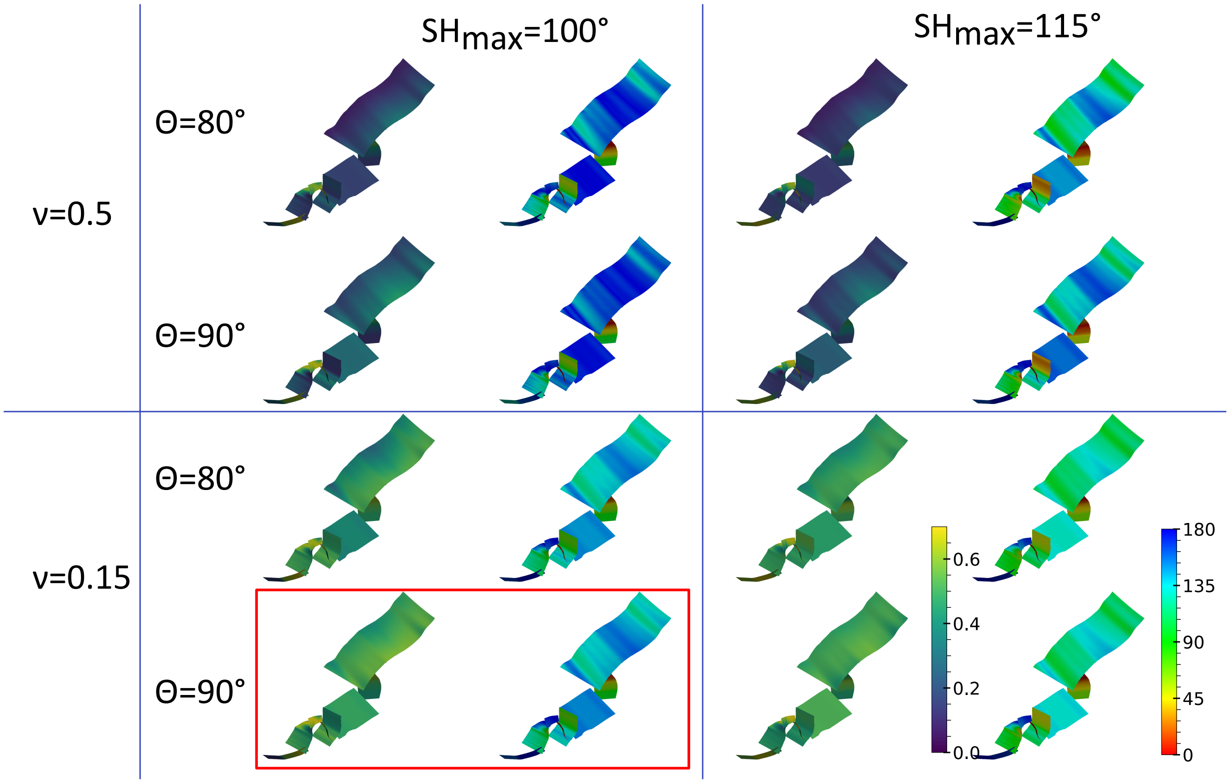

Figure 2.A.8: A representative sample of initial stress models tested. We show 8 examples that correspond to all permutations involving the two values indicated in the labels for each stress parameter, $\mathrm{SH}_{\mathrm{max}}$, ν and θ. For each example, two plots show the spatial distribution on the fault surfaces of (left) the pre-stress ratio and (right) the rake angle of the shear traction. Here we assume a uniform $R_{\mathrm{opt}}(z) = 0.7$ on the optimal plane.

range 70°-110°. For each value of the $(\mathrm{SH}_{\mathrm{max}}, \theta, \nu)$ triplet we do the following: compute the principal stress components using equations 11-16; obtain the principal stress orientations from $\mathrm{SH}_{\mathrm{max}}$, θ and the additional constraint that the faulting mechanism of the optimal plane is strike-slip; compute and visualize the distribution of R and of the shear traction orientation resolved on the fault system (Supplementary Fig. 2.A.8). We then select the stress configuration $(\mathrm{SH}_{\mathrm{max}}, \theta, \nu)$ that maximizes R all along the fault system, especially around rupture transition zones to enable triggering, and that optimizes the alignment between initial fault shear tractions and the slip directions inferred by Xu et al (2018). We rerun the procedure with a lower and a larger R_0 (0.5 and 0.9, respectively) to confirm that the conclusion obtained with R_0=0.7 still holds. In the next step of our stress setup we will determine the preferred value of R_0 based on dynamic considerations.

Supplementary Fig.2.A.8 presents a few of the many cases we tested. Eight examples are shown, which correspond to all permutations of the following values: $\mathrm{SH}_{\mathrm{max}}$= 100°and 115°, θ= 80°and 90°, ν=0.5 and 0.15. The value ν=0.5 results in a favorable stress orientation only for the eastern part of the Humps Fault Zone and on the Conway-Charwell fault.

Lower values of ν are required to obtain a favorable stress orientation on the other faults. Our preferred value is ν=0.15. The value $\mathrm{SH}_{\mathrm{max}}$=100° achieves the best overall alignment between initial shear tractions and target slip on all faults. We find that the angle θ has a limited influence within the range tested, and thus opt for the simplest assumption of an Andersonian stress regime: θ=90°.

In a second step, we constrain γ, R_0 and the shape of the initial stress modulation functions, $g(z)$ and $\Omega(z)$, to allow the rupture to cascade along the whole fault system with a realistic amount of fault slip. This is done by trial-and-error based on dynamic rupture simulations. To save computational resources, we do the trial simulations on a coarser mesh (except near the fault) and first only simulate the initial 25 s to test if rupture can be sustained on the highly segmented southern part of our fault structure. Our stress modulation function is described by a minimum number of parameters (the width of the stress concentration area, the seismogenic depth z_{seis} and the stress concentration shape, described hereafter). It is designed to capture the essential features of the stresses caused by deep creep: it is peaked at the base of the seismogenic zone ($g(z)$=1) and decays to $g(0) < 1$ at shallower depth to represent the background stress. Most probably, any function with these general features could be used to achieve similar dynamic rupture results. We define z_{seis} as the depth at which $\Omega(z)$ starts to decrease. We set it equal to the average maximum depth of the slip patches inferred by Xu et al (2018). We define the width of the stress concentration area as the depth range above z_{seis} in which $g(z)$=1. We prescribe its value just large enough to enable rupture transfer driven by stress concentration. We find that the values R_0=0.85, $g(0)$=0.6 and γ=0.66 ensure a subshear rupture and slip amounts consistent with results of previous source inversion studies. Supplementary Fig. 2.2 depicts the resulting shape of the initial stress modulation functions $g(z)$ and $\Omega(z)$. We also consider a small lateral variation in the regional stress, summarized in Fig. 2.2 and described in the main text.

The strength of the stress concentrations in our model (through parameters R_0 and $g(0)$) is partially constrained by observed rupture properties. The average stress drop in a dynamic model affects the average fault slip, rupture speed and rupture size, and is roughly

$$d\tau \approx R_0 g(0)(\mu_{\mathrm{s}} - \mu_{\mathrm{d}})(1-\gamma)\sigma_{\mathrm{c}} \tag{2.19}$$

A high average stress drop leads to supershear rupture and unrealistically large slip, whereas a low value results in rupture terminating too early. Eq. 4.1 allows identifying trade-offs between modeling parameters. For instance, a high $g(0)$ can be compensated by an increased pore pressure γ. Some trade-offs of modeling parameters can nevertheless be mitigated by physical constraints. For instance, a too small value of $g(0)$ would lead to a stress drop too peaked in the deeper portion of the rupture (too marked stress concentration), which would be inconsistent with slip models from source inversion. Nevertheless, resolving the detailed shape of such stress concentration might be challenging because finite source inversion and interseismic geodetic studies suffer from poorer resolution at depth and entail smoothing due to regularization. In future work, the depth-dependency of stress could be constrained by seismic cycle modeling capable of handling complex fault geometries.

Table 2.A.2: Parameter values of the additional dynamic rupture scenarios probing the robustness of the preferred model. Variations to our preferred model are marked in bold.

	fully-weakened friction coefficient f_w	stress shape ratio ν	fluid-pressure ratio γ	unmodulated pre-stress ratio R_0	stress concentration intensity $g(0)$
'preferred model'	0.1	0.15	0.66	0.85	0.6
model DR1 (no deep stress concentrations)	0.1	0.15	**0.7**	**0.7**	**1**
model DR2 (increased dynamic friction)	**0.3**	**0.05**	**0.44**	0.85	0.6
model DR3 (combination of DR1 and DR2)	**0.3**	**0.05**	**0.59**	0.85	**1**

To probe the importance of deep stress concentration, we performed a new model DR1 comparable to our preferred model but omitting deep stress concentrations. We decrease R_0 and simultaneously adjust the fluid pressure ratio γ to preserve the average stress drop, and find the smallest R_0 enabling the full rupture cascade. The model DR1 has $R_0 = R_{\text{opt}}(z)$=0.7 and γ=0.7 (Supplementary Table 2.A.2). Its final fault slip is roughly similar to the slip of our preferred model. However, this alternative model has drawbacks compared to observations. In particular, it is less realistic in terms of timing. Its overall rupture duration is about 10 s shorter than our best scenario. This difference is mainly due to quicker shallow rupture transitions, such as the Humps-Leader branching, which are made easier by the increased prestress at shallow depth. Although this alternative model does not compare as well with observations as our preferred model, we cannot exclude the existence of an equally well performing model featuring less pronounced stress concentrations.

2.A.6 Apparent fault weakness

Our preferred model is characterized by a low value of the initial shear to normal stress ratio over most of the seismogenic zone (Supplementary Fig. 2.A.9). Yet, most of the modeled faults are relatively well oriented with respect to the regional stress field. In the following we describe the relation between our model assumptions and fault weakness, first in the static, then in the dynamic sense. We explore additional models, to assess the robustness of our preferred model, and quantify the effects contributing to the apparent fault weakness in our model.

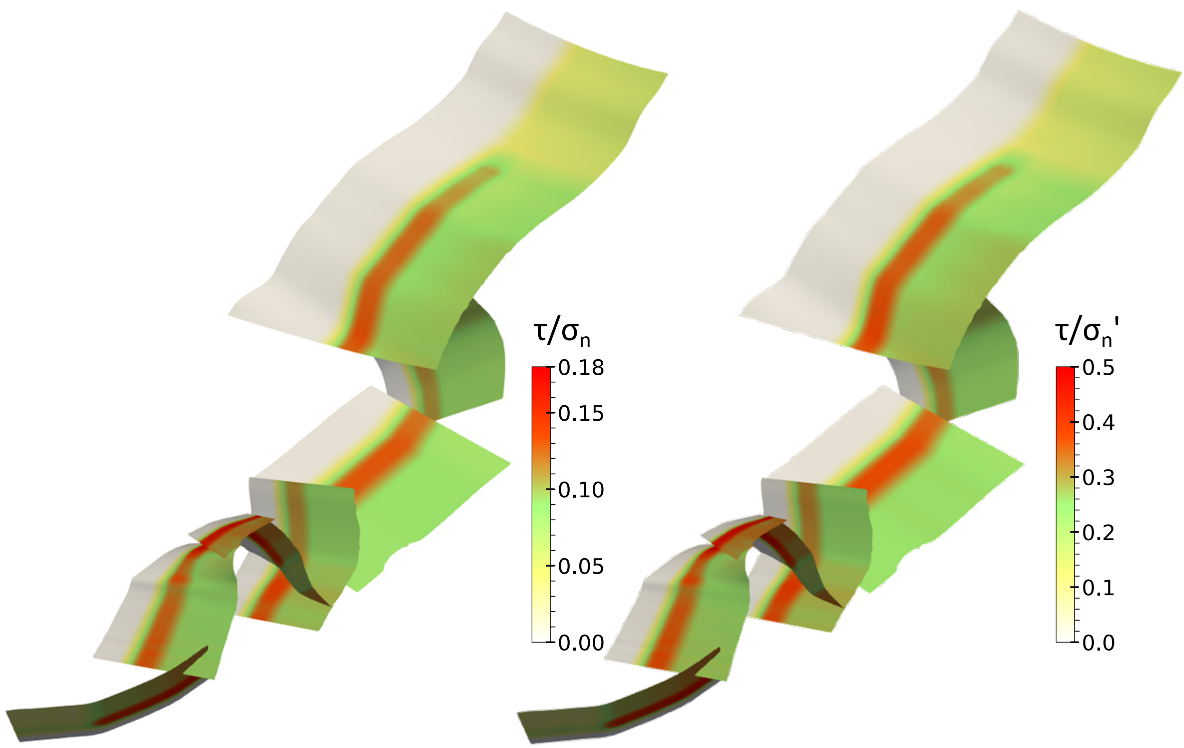

Figure 2.A.9: Ratio of initial shear stress τ over normal stress σ_{n} (a) and over effective normal stress σ_{n}' (b).

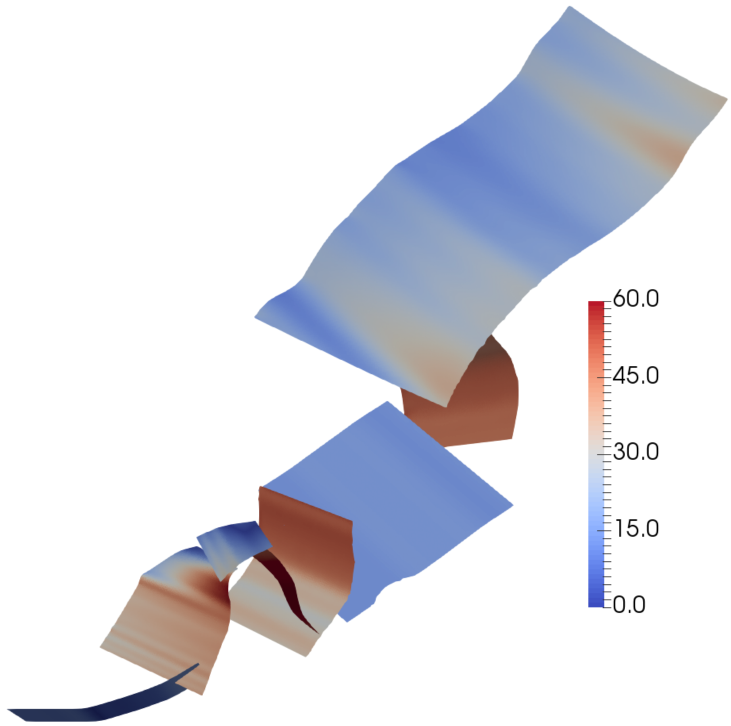

Figure 2.A.10: Fault angle ψ relative to the maximum principal stress. Faults featuring ψ close to $\Phi = 30°$ are well oriented. To compute ψ, we first select the fault normals whose scalar product with the vector pointing toward SH_{max} is positive. We then compute the angle ϕ between these normals and SH_{max}. Finally, we obtain ψ as $\psi = 90° - \phi$.

Apparent fault weakness in the classical sense

In the classical sense, the fault system is considered strong since it is well oriented relative to the regional stress.

In the classical Andersonian faulting theory, the strength of a fault is related to its orientation relative to the regional stress, in particular to the angle Ψ between the fault surface and the direction of maximum principal stress. This theory assumes that optimal faults are uniformly stressed at failure prior to an earthquake, with a ratio of shear to normal stress (τ/σ_n) equal to the static friction μ_s everywhere along the fault. Their angle Ψ is the optimal angle Φ defined in eq. 2.16. A typical value is Φ=30° for μ_s=0.6. Faults away from the optimal orientation have a lower τ/σ_n. Under these assumptions an active fault is weak (fails at low τ/σ_n) if its orientation Ψ differs significantly from the optimal angle Φ.

According to this theory, most of our fault system is relatively well oriented relative to the regional stress. In fact, about 60% of the area of the fault system is oriented at angles ranging from 10 to 50°relative to the maximum principal stress (Supplementary Fig. 2.A.10). We point out, that in a transpressional regime these considerations may be less meaningful than under tectonic stresses resulting in unique faulting mechanisms.

Static apparent fault weakness

Statically, the model features a low ratio of fault shear to normal stress despite being well oriented.

In the framework of dynamic rupture modeling, faults can be stressed well below failure (τ/σ_n much lower than μ_s) almost everywhere and yet break spontaneously. Only a small portion of the fault needs to reach failure to nucleate a rupture. In our model τ/σ_n is low over most of the rupture area (median value 0.09) and yet most faults are well oriented relative to the maximum compressive stress. Because the spatially-averaged stress ratio τ/σ_n at the time of failure is a natural measure of the macroscopic fault strength, the faults in our model can be considered apparently weak, in a macroscopic sense, despite their local strength μ_s being high and their orientation being close to optimal.

The apparent strength (τ/σ_n) of optimally oriented faults is related to our model parameters as follows. In dynamic rupture simulations, a relative fault strength is typically defined with respect to the frictional strength drop. This is quantified by the relative prestress ratio R in our study (eq. 3.3):

$$R = \frac{\tau - f_\mathrm{w}\sigma_\mathrm{n}(1-\gamma)}{(f_0 - f_\mathrm{w})\sigma_\mathrm{n}(1-\gamma)}, \tag{2.20}$$

One of our input model parameters is R_0, the maximum value of R within the deep stress concentrations on optimally oriented faults. The background value of R governing the shallower fault areas is given as $R_0 g(0)$. A smooth transition from this background value to the deep stress concentration is prescribed by the stress modulation shape function g(z) (Supplementary Fig. 3.7). The ratio of shear to normal stress on optimally oriented faults is then:

$$\frac{\tau}{\sigma} = (1-\gamma)(f_0 - f_\mathrm{w})R_0 g(z) + f_\mathrm{w} \tag{2.21}$$

By varying the value of $R_0 g(z)$ between 0 and 1, we can prescribe any value of τ/σ_n between $(1-\gamma)f_\mathrm{w}$ and $(1-\gamma)f_0$ independently of the fault orientation. Nevertheless, it is important to note that the portions of the fault experiencing deep stress concentration are characterized locally by a higher τ/σ_n ratio.

Dynamic apparent fault weakness

Dynamically, the modelled faults weaken dramatically at co-seismic slip rates while stress drops are limited by the interplay between elevated fluid pressure and deep stress concentration.

In our model, we assume strong dynamic weakening (f_w= 0.1). This is motivated by the dramatic friction decrease observed in laboratory experiments at co-seismic slip rates and by the theory of thermal weakening processes (as detailed in the main text sec. Friction and in Methods sec. Fault friction). Furthermore, previous dynamic rupture studies utilizing fast velocity weakening with low values of f_w successfully reproduced rupture complexities, such as rupture re-activation and pulse-like ruptures, without assuming small-scale (potentially

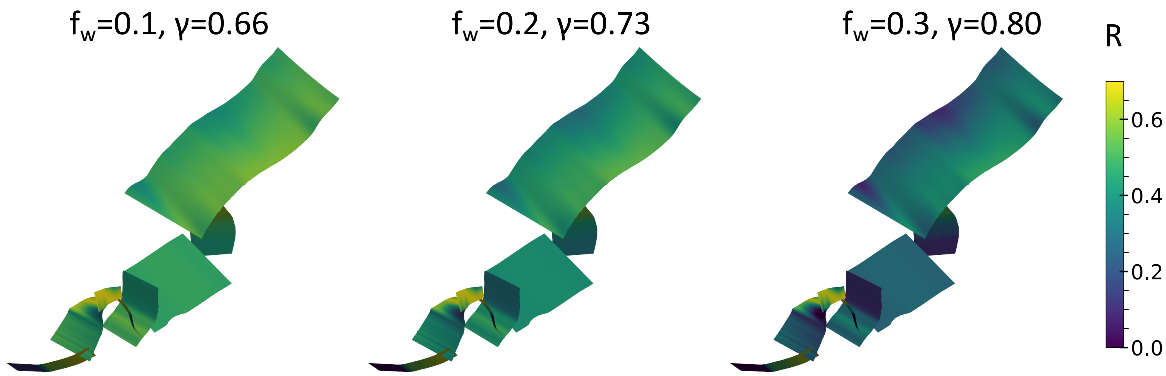

Figure 2.A.11: Spatial distribution of the relative prestress ratio R across fault surfaces for varying values of dynamic friction coefficient assuming an intermediate stress ratio ν of 0.15 and a uniform $R_{\mathrm{opt}}(z) = 0.7$ on the optimal plane.

tuned) heterogeneities. In our model, adopting such friction law enables full cascading rupture and realistic amounts of slip, in contrast with simplified friction laws, as discussed in section Initial stresses of the main text.

Under this assumption, a low level of prestress is required to achieve a reasonable stress drop. To this end, we consider here two effects rarely taken into account together in dynamic rupture scenarios: 1) increased fluid pressure and 2) deep stress concentrations. We discussed their trade offs in more detail in Methods sec. Initial stresses. For example, very high values of fluid pressure alone could enable a suitable level of stress drop. However, model DR1 of Methods sec. Initial stresses illustrates that the slow apparent rupture speed can only be reproduced by a model featuring stress concentrations at depth. We infer that the interplay of deep creep, elevated fluid pressure and frictional dynamic weakening govern the apparent strength of faults and that these factors cannot be treated in isolation for such complex fault systems.

Alternative model setups

In our preferred model we assumed a fully weakened friction coefficient f_{w} of 0.1. Here we present additional dynamic rupture experiments performed with higher values of f_{w} as summarized in Supplementary table 2.A.2 to probe the robustness of our preferred model.

Increasing f_{w} decreases the relative prestress ratio R on most of the faults (Supplementary Fig. 2.A.11). To restore the rupture potential of these faults, the stress shape ratio (eq. 2.10) must be decreased accordingly (Supplementary Fig. 2.A.12). The resulting values of ν are in stronger disagreement with stress inversion results than our preferred model with f_{w}=0.1 and ν=0.15 (Supplementary Fig. 2.A.5b). Also, the resulting spatial distribution of prestress (under decreased ν) has larger variability, which may hinder rupture cascading.

We performed two dynamic rupture simulations with increased f_{w}=0.3 to probe the robustness of our assumption of low dynamic frictional resistance. In both models, ν is decreased from 0.15 to 0.05 to restore the rupture potential and the fluid pressure ratio γ

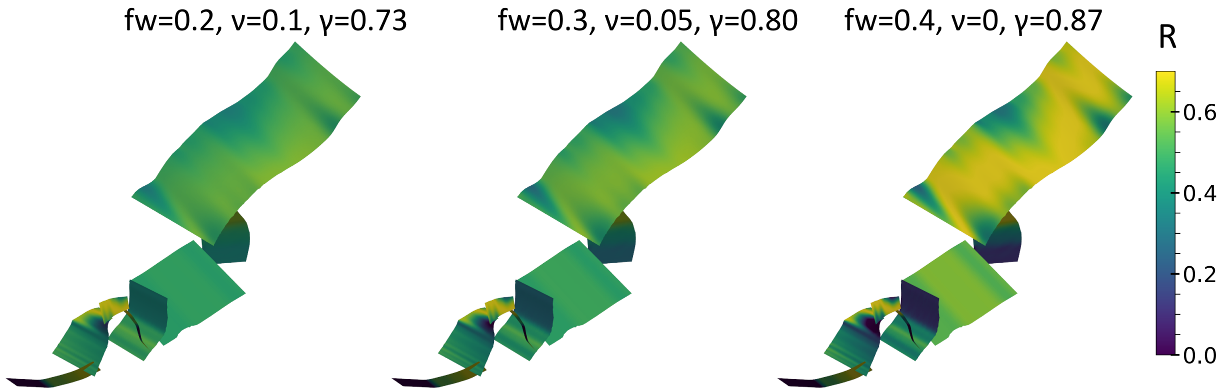

Figure 2.A.12: Spatial distribution of the relative prestress ratio R across fault surfaces for varying values of dynamic friction coefficient assuming decreased intermediate stress ratio ν to restore the rupture potential of the dip-slip segments. The Northern part of Hundalee and the Southern part of Papatea faults experience considerably lower levels of prestress compared with the preferred model featuring $f_{\mathrm{w}} = 0.1$.

is decreased to retrieve a stress drop comparable to the one of the preferred model. The nucleation area is increased to account for the change in critical nucleation size. Both models differ only in their deep stress concentration. The first model, DR2, has similar deep stress concentration patterns as our best model. In the second model, DR3, we remove the depth dependence of the prestress ratio; that is, we set $R(z)$=0.85 and $g(z)$=1 above the stress tapering area, and we adjusted the fluid pressure ratio γ.

In model DR2 the rupture did not propagate successfully beyond the first rupture branching point connecting the Humps and Leader faults. It nevertheless yields a realistic amount of slip on the Humps fault zone, which confirms that the stress drop is unchanged. The second model, DR3, results in rupture branching towards the Leader fault but dies out at the next step-over, probably because of the now too low prestress on the shallow parts of the Southern Leader fault.

Quantifying the relative contributions to apparent fault weakness

The effects of overpressurized fault fluids and deep stress concentrations and the additional effect of a low dynamic friction result in a low apparent friction coefficient which can be approximated as:

$$\mu \approx (\mu_{\mathrm{d}} + (\mu_{\mathrm{s}} - \mu_{\mathrm{d}})g(0)R_0)(1-\gamma) \tag{2.22}$$

Together with eq. 2.21 this allows us to quantify the relative contribution of each effect to the fault apparent weakness in our preferred model: fluid overpressure $1-\gamma$, deep stress concentration $g(0)R_0$ and dynamic weakening μ_{d}. In our preferred model μ_{d}=0.1, $1-\gamma$=0.33 and $(\mu_{\mathrm{s}} - \mu_{\mathrm{d}})g(0)R_0$=0.26.

Our unsuccessful attempt to reproduce all aspects of the rupture cascade in a model omitting stress concentrations (model DR1, Supplementary Table 2.A.2) illustrates that all three effects are important in allowing complex fault systems to operate at low apparent friction. Our findings warrant studies of the mechanical feedbacks between long-term geodynamic processes and the short-term processes of dynamic rupture and earthquake cycles.

2.A.7 Rupture nucleation

Rupture is nucleated by overstressing an area centered at the hypocenter, smoothly in space and time. This is achieved by increasing the initial relative prestress ratio R_0 as:

$$R_{0,\,\mathrm{nuc}} = R_0 + F(r)G(t) \tag{2.23}$$

$F(r)$ is a Gaussian shaped function:

$$\begin{aligned} F(r) &= 5 \exp \frac{r^2}{r^2 - r_\mathrm{c}^2} \text{ if } r < r_\mathrm{c} \\ &= 0 \text{ elsewhere} \end{aligned} \tag{2.24}$$

where r_c=2 km is the nucleation radius. The coefficient 5 is determined by trial on error numerical experiments to allow nucleation of sustained sub-shear rupture. $G(t)$ is a smoothed step function:

$$\begin{aligned} G(t) &= \exp \frac{(t-T)^2}{t(t-2T)} \text{ if } 0 < t < T \\ &= 1 \text{ if } t > T \end{aligned} \tag{2.25}$$

where T=0.5 s is the nucleation time.

2.A.8 Data availability

The authors declare that all data supporting the findings of this study are available within the paper and its Methods section. In particular, all data required to run a simulation of the Kaikōura earthquake can be downloaded from https://zenodo.org/record/2538024. We provide a detailed readme file summarizing the data and data formats provided. We use the following projection: WGS 84 / UTM Mercator 41 (EPSG:3994). We used the SeisSol (master branch, version tag 201807_Kaikoura) available on Github. The procedure to download, compile and run the code is described on the wiki (https://github.com/SeisSol/SeisSol/wiki).

3

Coupled, Physics-based Modeling Reveals Earthquake Displacements are Critical to the 2018 Palu, Sulawesi Tsunami

3.1 Abstract

The September 2018, M_w 7.5 Sulawesi earthquake occurring on the Palu-Koro strike-slip fault system was followed by an unexpected localized tsunami. We show that direct earthquake-induced uplift and subsidence could have sourced the observed tsunami within Palu Bay. To this end, we use a physics-based, coupled earthquake-tsunami modeling framework tightly constrained by observations. The model combines rupture dynamics, seismic wave propagation, tsunami propagation and inundation. The earthquake scenario, featuring sustained supershear rupture propagation, matches key observed earthquake characteristics, including the moment magnitude, rupture duration, fault plane solution, teleseismic waveforms and inferred horizontal ground displacements. The remote stress regime reflecting regional transtension applied in the model produces a combination of up to 6 m left-lateral slip and up to 2 m normal slip on the straight fault segment dipping 65° East beneath Palu Bay. The time-dependent, 3D seafloor displacements are translated

This chapter has been published in slightly altered form as Ulrich T, Vater S, Madden EH, Behrens J, van Dinther Y, van Zelst I, Fielding EJ, Liang C, Gabriel AA (2019) Coupled, Physics-Based Modeling Reveals Earthquake Displacements are Critical to the 2018 Palu, Sulawesi Tsunami. Pure and Applied Geophysics DOI 10.1007/s00024-019-02290-5

into bathymetry perturbations with a mean vertical offset of 1.5 m across the submarine fault segment. This sources a tsunami with wave amplitudes and periods that match those measured at the Pantoloan wave gauge and inundation that reproduces observations from field surveys. We conclude that a source related to earthquake displacements is probable and that landsliding may not have been the primary source of the tsunami. These results have important implications for submarine strike-slip fault systems worldwide. Physics-based modeling offers rapid response specifically in tectonic settings that are currently underrepresented in operational tsunami hazard assessment.

3.2 Introduction

Tsunamis occur due to abrupt perturbations to the water column, usually caused by the seafloor deforming during earthquakes or submarine landslides. Devastating tsunamis associated with submarine strike-slip earthquakes are rare. While such events may trigger landslides that in turn trigger tsunamis, the associated ground displacements are predominantly horizontal, not vertical, which does not favor tsunami genesis.

However, strike-slip fault systems in complex tectonic regions, such as the Palu-Koro fault zone cutting across the island of Sulawesi, may host vertical deformation. For example, a transtensional tectonic regime can favour strike-slip faulting overall, while also inducing normal faulting. Strike-slip systems may also include complicated fault geometries, such as non-vertical faults, bends or en echelon step-over structures. These can host complex rupture dynamics and produce a variety of displacement patterns when ruptured, which may promote tsunami generation (Legg and Borrero, 2001; Borrero et al, 2004).

To mitigate the commonly under-represented hazard of strike-slip induced tsunamis, it is crucial to fundamentally understand the direct effect of coseismic displacements on tsunami genesis. Globally, geological settings similar to that governing the Sulawesi earthquake-tsunami sequence are not unique. Large strike-slip faults crossing off-shore and running through narrow gulfs include the elongated Bodega and Tomales bays in northern California, USA, hosting major segments of the right-lateral strike-slip San Andreas fault system, and the left-lateral Anatolian fault system in Turkey, extending beneath the Marmara Sea just south of Istanbul. Indeed, historical data do record local tsunamis generated from earthquakes along these and other strike-slip fault systems, such as in the 1906 San Francisco (California), 1994 Mindoro (Philippines), and 1999 Izmit (Turkey) earthquakes (Legg et al, 2003) and, more recently, the 2016 Kaikōura, New Zealand earthquake (Ulrich et al, 2019a; Power et al, 2017). Large magnitude strike-slip earthquakes can also produce tsunamigenic aftershocks (e.g., Geist and Parsons, 2005).

In most tsunami modelling approaches, the tsunami source is computed according to the approach of Mansinha and Smylie (1971) and subsequently parameterized by the Okada model (Okada, 1985), which translates finite fault models into seafloor displacements. Okada's model allows for the analytical computation of static ground displacements generated by a uniform dislocation over a finite rectangular fault assuming a homogeneous elastic half space. Heterogeneous slip can be captured by linking several dislocations in space, and time-dependence is approximated by allowing these dislocations to move in sequence (e.g., Tanioka et al, 2006). While seafloor and coastal topography are ignored, the contribution of horizontal displacements may be additionally accounted for by a filtering approach suggested by Tanioka and Satake (1996), which includes the gradient of local bathymetry. Applying a traditional Okada source to study tsunami genesis is specifically limited for near-field tsunami observations and localized events due to its underlying, simplifying assumptions.

Realistic modeling of earthquakes and tsunamis benefits from physics-based approaches. Kinematic models of earthquake slip are the result of solving data-driven inverse problems. Such models aim to closely fit observations with a large number of free parameters. In contrast, dynamic rupture models aim at reproducing the physical processes that govern the way the fault yields and slides, and are therefore often referred to as 'physics-based'. Finite fault models are affected by inherent non-uniqueness, which may spread via the ground displacement fields to the modeled tsunami genesis. Constraining the kinematics of multi-fault rupture is especially challenging, since initial assumptions on fault geometry strongly affect the slip inversion results. Mechanically viable earthquake source descriptions are provided by dynamic rupture modeling combining spontaneous frictional failure and seismic wave propagation. Dynamic rupture simulations fully coupled to the time-dependent response of an overlying water layer have been performed by Lotto et al (2017a,b, 2018). These have been instrumental in determining the influence of different earthquake parameters and material properties on coupled systems, but are restricted to 2D. Maeda and Furumura (2013) showcase a fully-coupled 3D modeling framework capable of simultaneously modeling seismic and tsunami waves, but not earthquake rupture dynamics. Ryan et al (2015) couple a 3D dynamic earthquake rupture model to a tsunami model, but these are restricted to using a static snapshot of the seafloor displacement field as the tsunami source.

In order to capture the physics of the interaction between the Palu earthquake and the subsequent tsunami, we utilize a physics-based, coupled earthquake-tsunami model. While the feasibility of formal dynamic rupture inversion approaches has been demonstrated (e.g. Peyrat et al, 2001; Gallovič et al, 2019a,b), these are limited by the computational cost of each forward dynamic rupture model and therefore rely on model simplifications. In this study, we do not perform a formal dynamic rupture inversion, but constrain the earthquake model by static considerations and few trial dynamic simulations. The forward model of the dynamic earthquake rupture incorporates 3D spatial variation in subsurface material properties, spontaneously developing slip on a complex, non-planar system of 3D faults, off-fault plastic deformation, and the non-linear interaction of frictional failure with seismic waves. The coseismic deformation of the crust generates time-dependent seafloor displacements, which we translate into bathymetry perturbations to source the tsunami. The tsunami model solves for non-linear wave propagation and inundation at the coast.

Using this coupled approach, we evaluate the influence of coseismic deformation during the strike-slip Sulawesi earthquake on generating the observed tsunami waves. The physics-based model reveals that the rupture of a fault crossing Palu Bay with a moderate, but wide-spread, component of normal fault slip produces vertical deformation, which can explain the observed tsunami wave amplitudes and inundation elevations.

3.3 The 2018 Palu, Sulawesi earthquake and tsunami

3.3.1 Tectonic setting

The Indonesian island of Sulawesi is located at the triple junction between the Sunda plate, the Australian plate and the Philippine Sea plate (Bellier et al, 2006; Socquet et al, 2006, 2019) (Fig. 3.1a). Convergence of the Philippine and Australian plates toward the Sunda plate is accommodated by subduction and rotation of the Molucca Sea, Banda Sea and Timor plates, leading to complicated patterns of faulting.

In central Sulawesi, the NNW-striking Palu-Koro fault (PKF) and the WNW-striking Matano faults (MF) (Fig. 3.1a) comprise the Central Sulawesi Fault System. The Palu-Koro fault runs off-shore to the north of Sulawesi through the narrow Palu Bay and is the fault that hosted the earthquake that occurred on 28 September 2018. With a relatively high slip rate inferred from recent geodetic measurements (40 mm/yr, Socquet et al, 2006; Walpersdorf et al, 1998) and from geomorphology (upper limit 58 mm/yr, Daryono, 2018) and clear evidence for Quaternary activity (Watkinson and Hall, 2017), the Palu-Koro fault was presumed to pose a threat to the region (Watkinson and Hall, 2017). In addition, four tsunamis associated with earthquakes on the Palu-Koro fault have struck the northwest coast of Sulawesi in the past century (1927, 1938, 1968 and 1996) (Pelinovsky et al, 1997; Prasetya et al, 2001).

The complex regional tectonics subject northwestern Sulawesi to transtensional strain (Socquet et al, 2006). Transtension promotes some component of dip-slip faulting on the predominantly strike-slipping Palu-Koro fault (Bellier et al, 2006; Watkinson and Hall, 2017) and leads to more complicated surface deformation than is expected from slip along a fault hosting purely strike-slip motion.

3.3.2 The 2018 Palu, Sulawesi earthquake

The M_w 7.5 Sulawesi earthquake that occurred on September 28, 2018 ruptured a 180 km long section of the Palu-Koro fault (Socquet et al, 2019). It nucleated 70 km north of the city of Palu at shallow depths, with inferred hypocentral depths varying between 10 km and 22 km (Valkaniotis et al, 2018). The rupture propagated predominantly southward, passing under Palu Bay and the city of Palu. It arrested after a total rupture time of 30–40 seconds (Socquet et al, 2019; Okuwaki et al, 2018; Bao et al, 2019). The earthquake was well-captured by satellite data and inversions of these data by Socquet et al (2019) return several locations of dip-slip offset along the rupture, including within Palu Bay. Similarly, Song et al (2019) reveal predominantly left-lateral, strike-slip faulting on relatively straight, connected fault segments with a component of dip-slip offset. Song et al (2019) also suggest possible rupture on a secondary normal fault north of Palu Bay.

The earthquake appears to have propagated at a supershear rupture speed, i.e., faster than the shear waves produced by the earthquake are able to travel through the surrounding rock (e.g., Socquet et al, 2019; Bao et al, 2019; Mai, 2019). Socquet et al (2019) note that the characteristics of the relatively straight, clear rupture trace south of the Bay, with

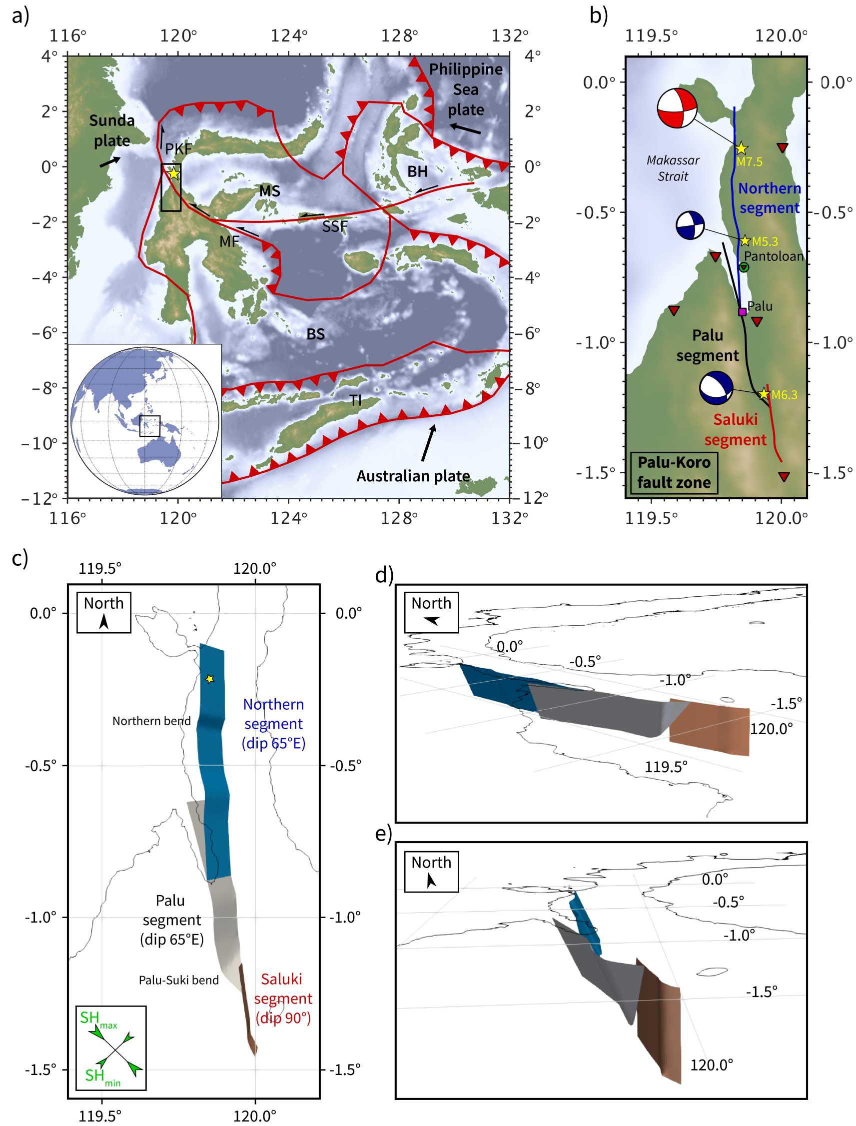

Figure 3.1: (a) Tectonic setting of the September 28, 2018 M_w 7.5 Sulawesi earthquake (epicenter indicated by yellow star). Black lines indicate plate boundaries based on Bird (2003); Socquet et al (2006); Argus et al (2011). Abbreviations: BH – Bird's Head plate; BS – Banda Sea plate; MF – Matano fault zone; PKF – Palu-Koro fault zone; MS – Molucca Sea plate, SSF – Sula-Sorong fault zone, and TI – Timor plate. Arrows indicate the far-field plate velocities with respect to Eurasia (Socquet et al, 2006). The black box corresponds to the region displayed in (b). (b) A zoom of the region of interest. The site of the harbor tide gauge of Pantoloan is indicated as well as the city of Palu. Locations of the GPS stations at which we provide synthetic ground displacement time series (see Appendix 3.A.2) are indicated by the red triangles. Focal mechanisms and epicenters of the September 28, 2018 Palu earthquake (USGS (2018a), top), October 1, 2018 Palu aftershock (middle), and January 23, 2005 Sulawesi earthquake (bottom) are shown. These later two events provide constraints on the dip angles of individual segments of the fault network. Individual fault segments of the Palu-Koro fault used in the dynamic rupture model are coloured. (c), (d) and (e) 3D model of the fault network viewed from top, SW and S.

few aftershocks, match those for which supershear rupture speeds have been inferred in other earthquakes. Using back-projection analysis, which maps the location and timing of earthquake energy from the waves recorded on distant seismic arrays, Bao et al (2019) do not resolve any portion of the rupture as traveling at sub-Rayleigh speeds. The authors conclude that this fast rupture velocity began at, or soon after, earthquake nucleation and was sustained for the length of the rupture. Surprisingly, Bao et al (2019) infer supershear rupture speeds at the lower end of speeds considered theoretically stable, possibly due to the influence of widespread, pre-existing damage around the fault. While the exact speed, point of onset, and underlying mechanics of this event's supershear rupture propagation remain to be studied further, it will initiate re-assessment of the hazard associated with supershear rupture on strike-slip faults worldwide, with respect to the potential intensification of shaking.

3.3.3 The induced tsunami

The Palu earthquake triggered a local but powerful tsunami that devastated the coastal area of Palu Bay quickly after the earthquake. Inundation depths of over 6 m and run-up heights of over 9 m were recorded at specific locations (e.g. Yalciner et al, 2018). At the only tide gauge with available data, located at Pantoloan harbor, a trough-to-peak wave amplitude of almost 4 m was recorded just 5 minutes after the rupture (Muhari et al, 2018). In Ngapa (Wani), on the northeastern shore of Palu Bay, CCTV coverage show the arrival of the tsunami wave after only 3 minutes.

Coseismic subsidence and uplift, as well as submarine and coastal landsliding, have been suggested as causes of the tsunami in Palu Bay (Heidarzadeh et al, 2019). Both displacements and landsliding are documented on land (Valkaniotis et al, 2018; Løvholt et al, 2018; Sassa and Takagawa, 2019), and also at coastal slopes (Yalciner et al, 2018).

Early tsunami models of the Sulawesi event performed using Okada's solution in combination with the USGS finite fault model (USGS, 2018b) do not generate tsunami amplitudes large enough to agree with observations (Heidarzadeh et al, 2019; Sepulveda et al, 2018; Liu et al, 2018; van Dongeren et al, 2018). Liu et al (2018) and Sepulveda et al (2018) perform Okada-based tsunami modeling with earthquake sources generated by inverting satellite data, but also produce wave amplitudes that are too small. Reasonable tsunami waves are produced by combining tectonic and hypothetical landslide sources (van Dongeren et al, 2018; Liu et al, 2018). However, the predominantly short wavelengths associated with the observed small scale, localized landsliding (Yalciner et al, 2018) appears to be incompatible with the observed long period tsunami waves (Løvholt et al, 2018).

3.4 Physical and Computational Models

3.4.1 Earthquake-tsunami coupled modeling

Since the earthquake and tsunami communities use different vocabulary, we specify the terminology used throughout this manuscript here. We refer to the complete physical setup, including, e.g., the bathymetry data set, fault structure and the governing equations for an earthquake or tsunami, as a 'physical model'. A computer program discretizing the equations and implementing the numerical workflow is termed a 'computational model'. The result of a computation for a specific event achieved with a computational model and according to a specific physical model is called a 'scenario'. We use 'model' where the use of the term as either physical or computational model is unambiguous.

SeisSol, the computational model used to produce the earthquake scenario (e.g., Dumbser and Käser, 2006; Pelties et al, 2014; Uphoff et al, 2017), solves the elastodynamic wave equation for spontaneous dynamic rupture and seismic wave propagation. It determines the temporal and spatial evolution of slip on predefined frictional interfaces and the stress and velocity fields throughout the modeling domain. With this approach, the earthquake source is not predetermined, but evolves spontaneously as a consequence of the model's initial conditions and of the time-dependent, non-linear processes occurring during the earthquake. Initial conditions include the geometry and frictional strength of the fault(s), the tectonic stress state, and the regional lithological structure. Fault slip evolves as frictional shear failure according to an assigned friction law that controls how the fault yields and slides. Model outputs include spatial and temporal evolution of the earthquake rupture front(s), off-fault plastic strain, surface displacements, and the ground shaking caused by the radiated seismic waves.

SeisSol uses the Arbitrary high-order accurate DERivative Discontinuous Galerkin method (ADER-DG). It employs fully non-uniform, unstructured tetrahedral meshes to combine geometrically complex 3D geological structures, nonlinear rheologies, and high-order accurate propagation of seismic waves. Fast time to solution is achieved thanks to end-to-end computational optimization (Breuer et al, 2014; Heinecke et al, 2014; Rettenberger et al, 2016) and an efficient local time-stepping algorithm (Breuer et al, 2016; Uphoff et al, 2017). To this end, dynamic rupture simulations can reach high spatial and temporal resolution of increasingly complex geometrical and physical modelling components (e.g. Bauer et al, 2017; Wollherr et al, 2019). SeisSol is verified with a wide range of community benchmarks, including dipping and branching fault geometries, laboratory derived friction laws, as well as heterogeneous on-fault initial stresses and material properties (Puente et al, 2009; Pelties et al, 2012, 2013, 2014; Wollherr et al, 2018) in line with the SCEC/USGS Dynamic Rupture Code Verification exercises (Harris et al, 2011, 2018). SeisSol is freely available (SeisSol website, 2019; SeisSol GitHub, 2019).

The computational model to generate the tsunami scenario is StormFlash2D, which solves the nonlinear shallow water equations using an explicit Runge-Kutta discontinuous Galerkin discretization combined with a sophisticated wetting and drying treatment for the inundation at the coast (Vater and Behrens, 2014; Vater et al, 2015, 2017). A tsunami is triggered by a (possibly time-dependent) perturbation of the discrete bathymetry. The shallow water approximation does not account for complex 3D effects such as dispersion and non-hydrostatic effects (e.g., compressive waves). Nevertheless, StormFlash2D allows for stable and accurate simulation of large-scale wave propagation in deep sea, as well as small-scale wave shoaling and inundation at the shore, thanks to a multi-resolution adaptive mesh refinement approach based on a triangular refinement strategy (Behrens et al, 2005; Behrens and Bader, 2009). Bottom friction is parameterized through Manning friction by a split-implicit discretization (Liang and Marche, 2009). The model's applicability for tsunami events has been validated by a number of test cases (Vater et al, 2019), which are standard for the evaluation of operational tsunami codes (Synolakis et al, 2007).

Coupling between the earthquake and tsunami models is realized through the time-dependent coseismic 3D seafloor displacement field computed in the dynamic earthquake rupture scenario, which is translated into 2D bathymetry perturbations of the tsunami model using the ASCETE framework (Advanced Simulation of Coupled Earthquake and Tsunami Events, Gabriel et al, 2018).

3.4.2 Earthquake model

The 3D dynamic rupture model of the Sulawesi earthquake requires initial assumptions related to the structure of the Earth, the structure of the fault system, the stress state, and the frictional strength of the faults. These input parameters are constrained by a variety of independent near-source and far-field data sets. Most importantly, we aim to ensure mechanical viability by a systematic approach integrating the observed regional stress state and frictional parameters and including state-of-the-art earthquake physics and fracture mechanics concepts in the model (Ulrich et al, 2019a).

Earth structure

The earthquake model incorporates topography and bathymetry data and state-of-the-art information about the subsurface structure in the Palu region. Local topography and bathymetry are honored at a resolution of approximately 900 m (GEBCO, 2015; Weatherall et al, 2015). 3D heterogeneous media are included by combining two subsurface velocity data sets at depth (see also Sec. 3.A.7). A local model by Awaliah et al (2018), which is built from ambient noise tomography, covers the model domain down to 40 km depth. In this region, we assume a Poisson medium. The Collaborative Seismic Earth Model (Fichtner et al, 2018) is used for the rest of the model domain down to 150 km.

Fault structure

For this model, we construct a network of non-planar, intersecting crustal faults involved in this earthquake. This includes three major fault segments: the Northern segment, a previously unmapped fault on which the earthquake nucleated, and the Palu and the Saluki segments of the Palu-Koro fault (cf. Fig. 3.1b-e). We map the fault traces from the horizontal ground displacement field inferred from correlation of Sentinel-2 optical images (De Michele, 2019) and from synthetic aperture radar (SAR) data (Bao et al, 2019), which is discussed more below. Differential north-south offsets clearly delineate the on-land traces of the Palu and Saluki fault segments. The trace of the Northern segment is less well-constrained in both data sets. Nevertheless, we produce a robust map by honoring the clearest features in both data sets and smoothing regions of large variance using QGIS v2.14 (Quantum GIS, 2013).

Beneath the Bay, we adopt a relatively simple fault geometry motivated by the on land fault strikes, the homogeneous pattern of horizontal ground deformation east of the Bay (De Michele, 2019), which suggests slip on a straight, continuous fault under the Bay, and the absence of direct information available to constrain the rupture's path. We extend the Northern segment southward as a straight line from the point where it enters the Bay to the point where the Palu segment enters the Bay. We extend the Palu segment northward, adopting the same strike that it displays on land to the south of the Bay. This trace deviates a few km from the mapping reported in Bellier et al (2006, their Fig. 2), both on and off land. South of the Bay, the modeled segment mostly aligns with the fault as mapped by Watkinson and Hall (2017, their Fig. 5).

We constrain the 3D structure of these faults using focal mechanisms and geodetic data. We assume that the Northern and Palu segments both dip 65° East, as suggested by the mainshock focal mechanisms (67°, USGS (2018a) and 69°, IPGP (2018), Fig. 3.1b) and the focal mechanism of the 2018, October 1st M_w 5.3 aftershock (67°, BMKG solution, Fig. 3.1b). This also is consistent with pronounced asymmetric patterns of ground displacement suggesting slip on dipping faults around the city of Palu and the Northern fault segment in both the optical and SAR data. In addition, the eastward dip of the Palu segment on land is consistent with the analysis of Bellier et al (2006). The southern end of the Palu segment bends towards the Saluki segment and features a dip of 60° to the northeast, as constrained by the source mechanism of the 2005 M_w 6.3 event (see Fig. 3.1b). In contrast, we assume that the Saluki segment is vertical. The assigned dip of 90° is consistent with the inferred ground displacement of comparable amplitude and extent on both sides of this fault segment (De Michele, 2019). All faults extend from the surface to a depth of 20 km.

Stress state

The fault system is subject to a laterally homogeneous regional stress field with systematic constraints following Ulrich et al (2019a) from seismo-tectonic observations, knowledge of fault fluid pressurization, and the Mohr-Coulomb theory of frictional failure. This is motivated by the fact that the tractions on and strength of natural faults are difficult to quantify. With this approach, only four parameters must be specified to fully describe the state of stress and strength governing the fault system, as further detailed in Appendix 3.A.3. This systematic approach facilitates rapid dynamic rupture modeling of an earthquake.

Using static considerations and few trial dynamic simulations, we identify an optimal stress configuration for this scenario that simultaneously (i) maximizes the ratio of shear over normal stress across the fault system; (ii) determines shear traction orientations that predict surface deformation compatible with the measured ground deformation and focal mechanisms; and (iii) allows dynamic rupture across the fault system's geometric complexities.

The resulting physical model is characterized by a stress regime acknowledging transtensional strain, high fluid pressure, and relatively well oriented, apparently weak faults. The effective confining stress increases with depth by a gradient of 5.5 MPa/km. From 11–15 km depth, we taper the deviatoric stresses to zero, to represent the transition from a brittle to a ductile deformation regime. This depth range is consistent with the 12 km interseismic locking depth estimated by Vigny et al (2002).

Earthquake nucleation and fault friction

Fault failure is initiated within a highly overstressed circular patch with a radius of 1.5 km situated at the hypocenter location as inferred by the GFZ (119.86°E, 0.22°S, at 10km depth). This depth is at the shallow end of the range of inferred hypocentral depths (Valkaniotis et al, 2018) and shallower than the modeled brittle-ductile transition, marking the lower limit of the seismogenic zone.

Slip evolves on the fault according to a rapid velocity-weakening friction formulation, which is motivated by laboratory experiments that show strong dynamic weakening at coseismic slip rates (e.g., Di Toro et al, 2011). This formulation reproduces realistic rupture characteristics, such as reactivation and pulse-like behavior, without imposing small-scale heterogeneities (e.g., Dunham et al, 2011a; Gabriel et al, 2012). We here use a form of fast-velocity weakening friction proposed in the community benchmark problem TPV104 of the Southern California Earthquake Center (Harris et al, 2018) and as parameterized by Ulrich et al (2019a). Friction drops rapidly from a steady-state, low-velocity friction coefficient, here 0.6, to a fully weakened friction coefficient, here 0.1 (see Appendix 3.A.4).

Model resolution

A high resolution computational model is crucial in order to accurately resolve the full dynamic complexity of the earthquake scenario. The required high numerical accuracy is achieved by combining a numerical scheme that is accurate to high-orders and a mesh that is locally refined around the fault network.

The earthquake model domain is discretized into an unstructured computational mesh of 8 million tetrahedral elements. The shortest element edge lengths are 200 m close to faults. The static mesh resolution is coarsened away from the fault system. Simulating 50 s of this event using 4th order accuracy in space and time requires about 2.5 hours on 560 Haswell cores of phase 2 of the SuperMUC supercomputer of the Leibniz Supercomputing Centre in Garching, Germany. We point out that running hundreds of such simulations is well within the scope of resources available to typical users of supercomputing centres. All data required to reproduce the earthquake scenario are detailed in Appendix 3.A.11.

3.4.3 Tsunami model

The bathymetry and topography for the tsunami model is composed of the high-resolution data set BATNAS (v1.0), provided by the Indonesian Geospatial Data Agency (DEMNAS, 2018). This data set has a horizontal resolution of 6 arc seconds (or approximately 190 m), and it allows for sufficiently accurate representation of bathymetric features, but is certainly relatively inaccurate with respect to inundation treatment. However, we note that the data set is more accurate than data sets for which the vertical 'roof-top' approach is used, such as typical SRTM data (see, e.g., the accuracy analysis in McAdoo et al, 2007; Kolecka and Kozak, 2014).

The coupling between the earthquake and tsunami models is enforced by adding a perturbation derived from the 3D coseismic seafloor displacement in the dynamic rupture scenario to the initial 2D bathymetry and topography of the tsunami model. These time-dependent displacement fields are given by the three-dimensional vector $(\Delta x, \Delta y, \Delta z)$. In addition to the vertical displacement Δz, we incorporate the east-west and north-south horizontal components, Δx and Δy into the tsunami source by applying the method proposed by Tanioka and Satake (1996). This is motivated by the potential influence of Palu Bay's steep seafloor slopes (more than 50%). The ground displacement of the earthquake model is translated into the tsunami generating bathymetry perturbation by

$$\Delta b = \Delta z - \Delta x \frac{\partial b}{\partial x} - \Delta y \frac{\partial b}{\partial y}, \tag{3.1}$$

where $b = b(x, y)$ is the bathymetry (increasing in the upward direction). Δb is time-dependent, since Δx, Δy and Δz are time-dependent. The tsunami is sourced by adding Δb to the initial bathymetry and topography of the tsunami model. It should be noted that a comparative scenario using only Δz as the bathymetry perturbation (see Appendix 3.A.5) does not result in large deviations with regards to the preferred model.

The domain of the computational tsunami model (latitudes ranging from $-1°$ to $0°$, longitudes ranging from $119°$ to $120°$, see Fig. 3.2) encompasses Palu Bay and the nearby surroundings in the Makassar Strait, since we here focus on the wave behavior within the Palu Bay. The tsunami model is initialized as an ocean at rest, for which (at $t = 0$) the initial fluid depth is set in such manner that the sea surface height (ssh, deviation from mean sea level) is equal to zero everywhere in the model domain. Additionally, the fluid velocity is set to zero. This defined initial steady state is then altered by the time-dependent bathymetry perturbation throughout the simulation, which triggers the tsunami. The simulation is run for 40 min (simulation time), which needs 13 487 time steps.

The triangle-based computational grid is initially refined near the coast, where the highest resolution within Palu Bay is about 3 arc seconds (or 80 m). This results in an initial mesh of 153 346 cells, which expands to more than 300 000 cells during the dynamically adaptive computation. The refinement strategy is based on the gradient in sea surface height.

The parametrization of bottom friction includes the Manning's roughness coefficient n. We assume $n = 0.03$, which is a typical value for tsunami simulations (Harig et al, 2008).

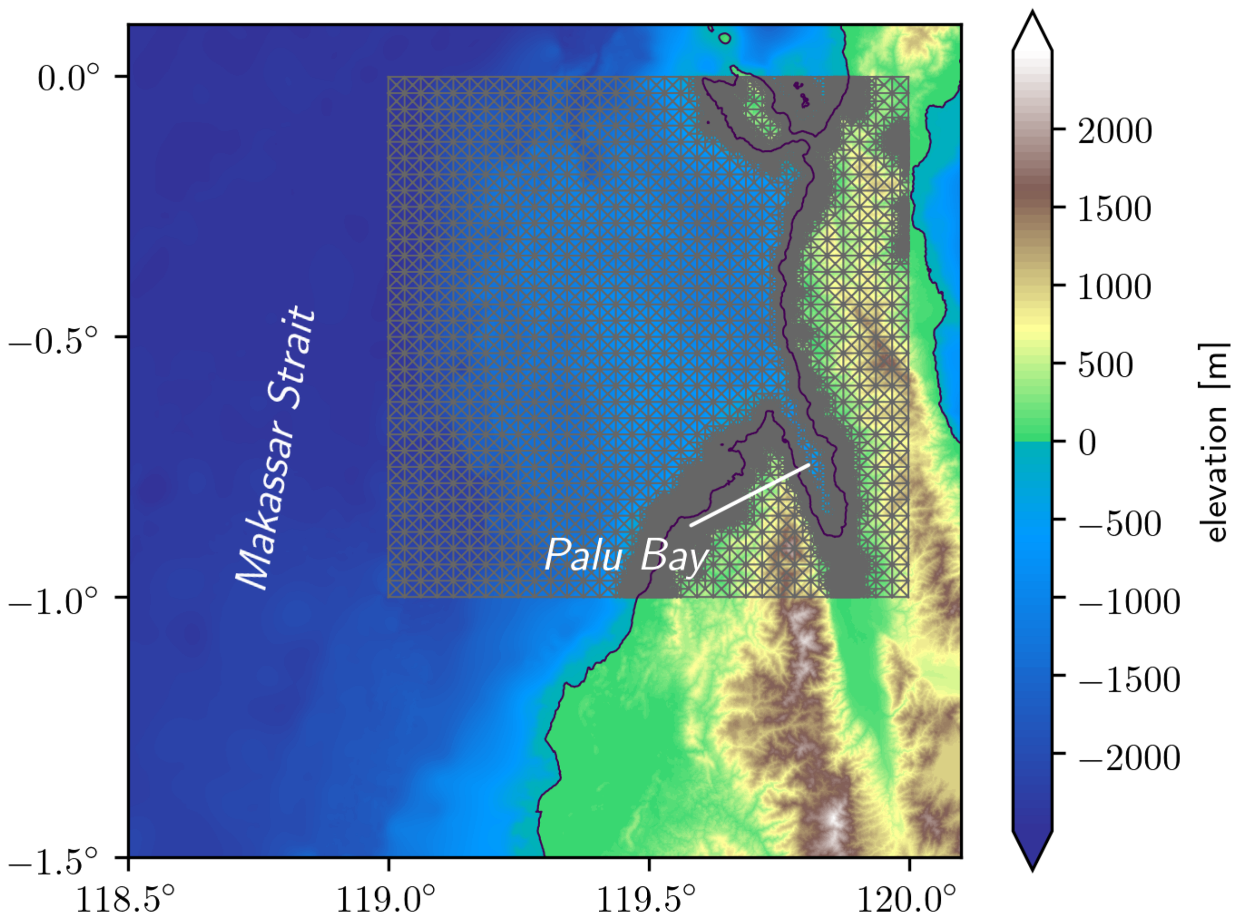

Figure 3.2: Setup of the tsunami model including high-resolution bathymetry and topography data overlain by the initial adaptive triangular mesh refined near the coast.

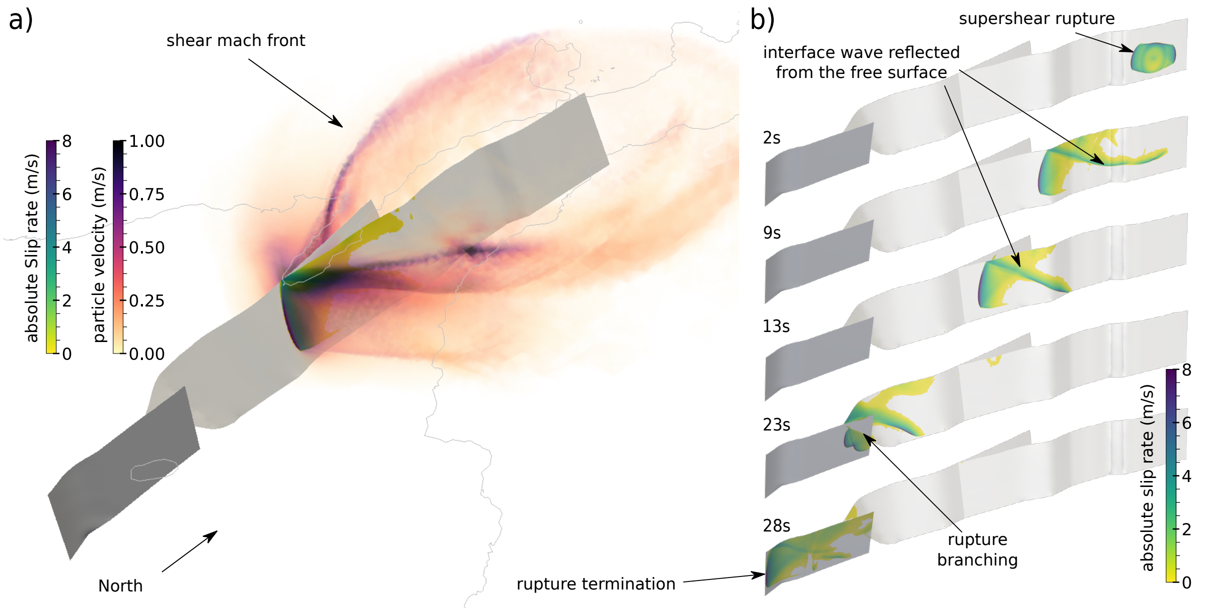

Figure 3.3: (a) Snapshot of the wavefield (absolute particle velocity in m/s) and the slip rate (in m/s) across the fault network at a rupture time of 15 s. (b) Overview of the simulated rupture propagation. Snapshots of the absolute slip rate are shown at a rupture time of 2, 9, 13, 23 and 28 s. Labels indicate noteworthy features of the rupture.

3.5 Results

In the following, we present the physics-based coupled earthquake and tsunami scenario. We highlight key features and evaluate the model results against seismic and tsunami observations.

3.5.1 The dynamic earthquake rupture scenario: sustained super-shear rupture and normal slip component within Palu Bay

This earthquake rupture scenario is based on the systematic derivation of initial conditions presented in Sec. 3.4.2. We evaluate it by comparison of model synthetics with seismological data, geodetic data, and field observations in the near- and far-field.

Earthquake rupture

The dynamic earthquake scenario is characterized by an unilaterally propagating southward rupture (see Fig. 3.3 and animations in Appendix 3.A.10). The rupture nucleates at the northern tip of the Northern segment, then transfers to the Palu segment at the southern end of Palu Bay. Additionally, a shallow portion of the Palu-Koro fault beneath the Bay ruptures from North to South (see inset of Fig. 3.9a). This segment is dynamically unclamped due to a transient reduction of normal tractions while the rupture passes on the Northern segment. The rupture passes from the Palu segment onto the Saluki segment through a restraining bend at a latitude of -1.2°. In total, 195 km of faults are ruptured leading to a M_w 7.6 earthquake scenario.

Teleseismic waves, focal mechanism, and moment release rate

The dynamic rupture scenario satisfactorily reproduces the teleseismic surface waves (Figs. 3.4a and 3.A.12) and body waves (Figs. 3.4b, 3.A.13). Synthetics are generated at 15 teleseismic stations around the event (Fig. 3.5). Note that the data from these teleseismic stations is not used to build our model, as it is done in classical kinematic models, but to validate the dynamic rupture scenario a posteriori, by comparing the model results to these measurements. Following Ulrich et al (2019a), we translate the dynamic fault slip time histories of the dynamic rupture scenario into a subset of 40 double couple point sources (20 along strike by 2 along depth). From these sources, broadband seismograms are calculated from a Green's function database using Instaseis (Krischer et al, 2017) and the PREM model (Preliminary Reference Earth Model) for a maximum period of 2 s and including anisotropic effects. The synthetics agree well with the observed teleseismic signals in terms of both the dominant, long-period surface waves and the body wave signatures.

The focal mechanism of the modeled source is compatible with the one inferred by the USGS (compare in Fig. 3.1b and Fig. 3.5). The nodal plane characterizing this model earthquake features strike/dip/rake angles of $354°/69°/-14°$, which are very close to the values of $350°/67°/-17°$ for the focal plane determined by the USGS.

The dynamically released moment rate is in agreement with source time functions inferred from teleseismic data (Fig 3.6). The scenario yields a relatively smooth, roughly box-car shaped moment release rate spanning the full rupture duration. This is consistent with the source time function from Okuwaki et al (2018) and also with the smooth fault slip reported by Socquet et al (2019). The rupture slows down at the Northern segment restraining bend at -0.35° latitude. This resembles the moment rate solutions by the USGS and SCARDEC at $\approx$ 5 s rupture time. The transfer of the rupture from the Palu segment to the Saluki segment at 23 s also produces a transient decrease in the modeled moment release rate in the model, which is discernible in those inferred from observations as well.

Earthquake surface displacements

We use observations from optical and radar satellites, both sensitive to the horizontal coseismic surface displacements, to validate the outcomes of the earthquake scenario (Fig.s 3.7 and 3.8). Along most of the rupture, fault displacements are sharp and linear, highlighting smooth and straight fault orientations with a few bends.

The patterns and magnitudes of the final horizontal surface displacements (black arrows in Fig. 3.7) are determined from subpixel correlation of coseismic optical images acquired by the Copernicus Sentinel-2 satellites operated by the European Space Agency (ESA) (De Michele, 2019). We use both the east-west and north-south components from optical image correlation.

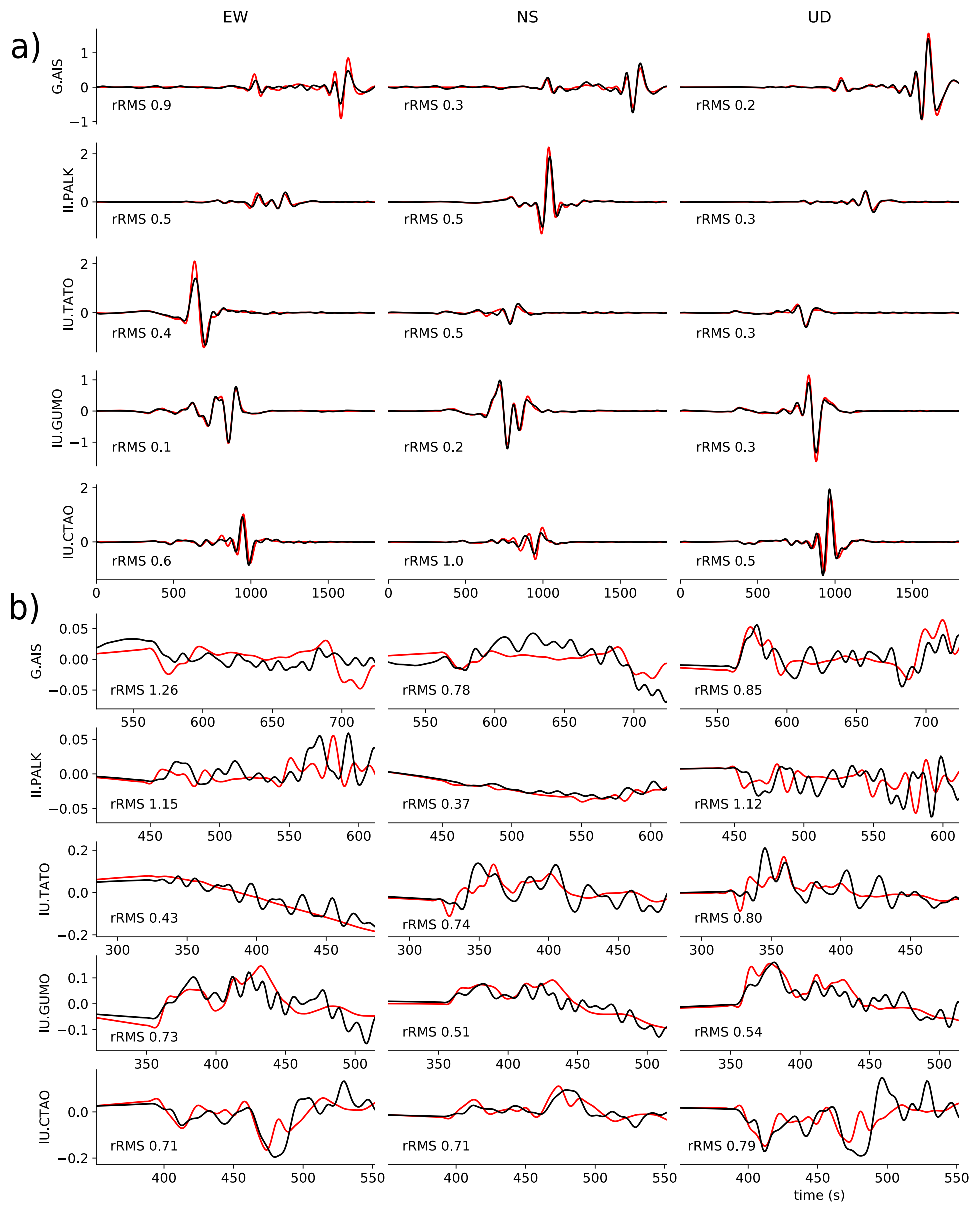

Figure 3.4: Comparison of modeled (red) and observed (black) teleseismic displacement waveforms. (a) Full seismograms dominated by surface waves. A 66-450 s band-pass filter is applied to all traces. (b) Zoom in to body wave arrivals. A 10-450 s band-pass filter is applied to all traces. Synthetics are generated using Instaseis (Krischer et al, 2017) and the PREM model including anisotropic effects and a maximum period of 2 s. For each panel, a misfit value (rRMS) quantifies the agreement between synthetics and observations. rRMS equal to 0 corresponds to a perfect fit. For more details see Appendix 3.A.8. Waveforms at 10 additional stations are compared in Figs. 3.A.12, 3.A.13.

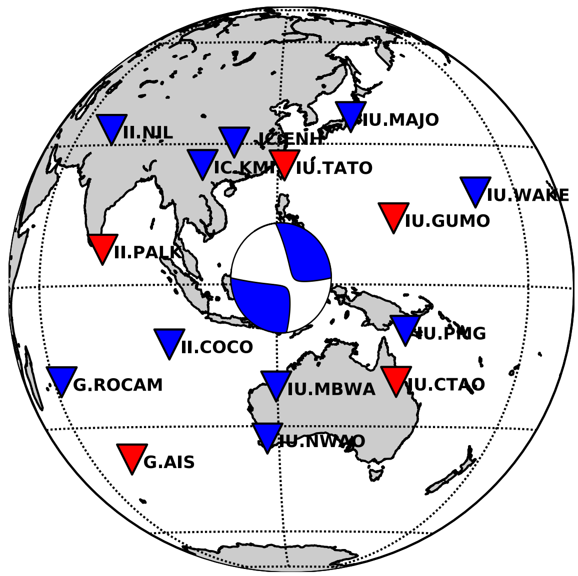

Figure 3.5: Moment-tensor representation of the dynamic rupture scenario and locations at which synthetic data are compared with observed records (red: stations compared in Fig. 3.4 blue: stations compared in Figs. 3.A.12 and 3.A.13).

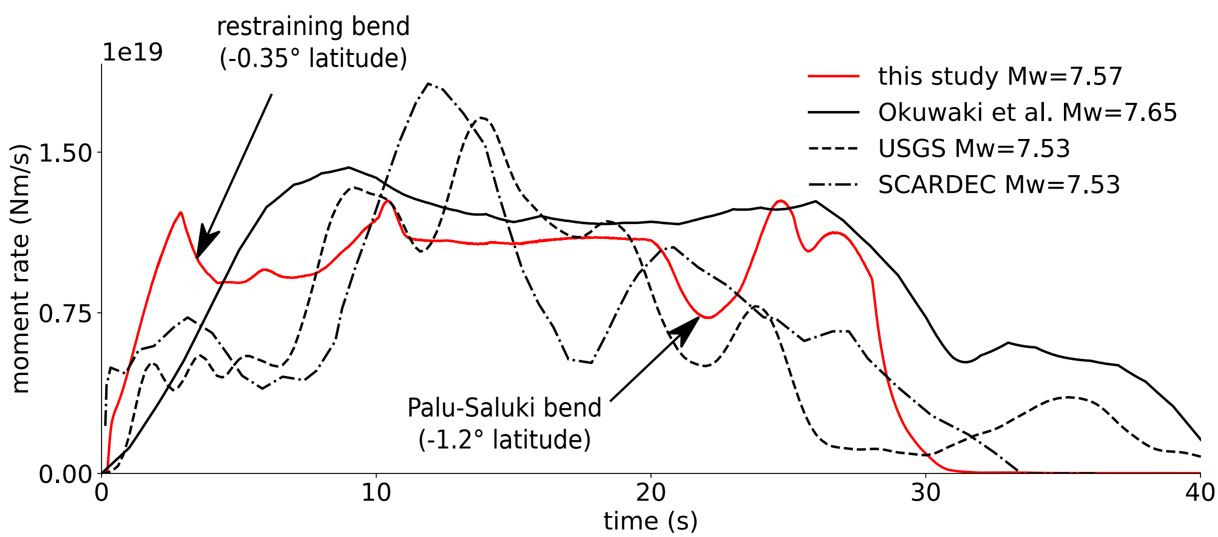

Figure 3.6: Synthetic moment rate release function compared with those inferred from teleseismic data by Okuwaki et al (2018), the USGS and the SCARDEC method (optimal solution, Vallée et al, 2011)

.

We also infer coseismic surface displacements by incoherent cross correlation of synthetic aperture radar (SAR) images acquired by the Japan Aerospace Exploration Agency (JAXA) Advanced Land Observation Satellite-2 (ALOS-2). SAR can capture horizontal surface displacement in the along-track direction and a combination of vertical and horizontal displacement in the slant range direction between the satellite and the ground. Here, we use the along-track horizontal displacements (Fig. 3.8b) which are nearly parallel to the strike of the ruptured faults. Further details about the SAR data can be found in Appendix 3.A.6.

The use of two independent but partially coinciding data sets provides insight into data quality. We identify robust features in the imaged surface displacements by projecting the optical data into the along-track direction of the SAR data. The data sets appear to be consistent to first order (± 1 m) in a 30 km wide area centered on the fault and south of $-0.6°$ latitude (region identified in Fig. 3.7). North of the Bay, we find that the optical displacements are large in magnitude relative to the SAR measurements. Such large displacements continue north of the inferred rupture trace, suggesting a bias in the optical data in this region. These large apparent displacements may be due to partial cloud cover in the optical images or to image misalignment. The east-west component seems unaffected by this problem. Significant differences are also observed near the Palu-Saluki bend. Thus, deviations between model synthetics and observational data in these areas are analyzed with caution.

Overall, the earthquake dynamic rupture scenario matches observed ground displacements well. East of the Palu segment, a good agreement between synthetic displacements and observations is achieved. Horizontal surface displacement vectors predicted by the model are well aligned with and of comparable amplitude to optical observations (Fig. 3.7). West of the Palu segment, the modeled amplitudes are in good agreement with the SAR (Fig. 3.8a) and optical data, however the synthetic orientations point to the southwest, whereas the optical data are oriented to the southeast (Fig. 3.7). While surface displacement orientations around the Saluki segment are reproduced well, amplitudes may be overestimated by about 1 m on the eastern side of the fault (Fig. 3.8c). North of the Bay, the modeled amplitudes exceed SAR measurements by about 2 m (Fig. 3.8c). Nevertheless, the subtle eastward rotation of the horizontal displacement vectors near the Northern segment bend (at $-0.35°$ latitude) is captured well by the scenario (Fig. 3.7).

Fault slip

The modeled slip distributions and orientations (Fig. 3.9) are modulated by the geometric complexities of the fault system. On the northern part of the Northern segment, slip is lower than elsewhere along the fault due to a restraining fault bend near -0.35° latitude (Fig. 3.9a). South of this small bend, the slip magnitude increases and remains mostly homogeneous, ranging between 6 and 8 m. Peak slip occurs on the Palu segment.

Over most of the fault network, the faulting mechanism is predominantly strike-slip, but does include a small to moderate normal slip component (Fig. 3.9b). This dip-slip component varies as a function of fault orientation with respect to the regional stress field. It increases at the junction between the Northern and Palu segment just south of Palu Bay,

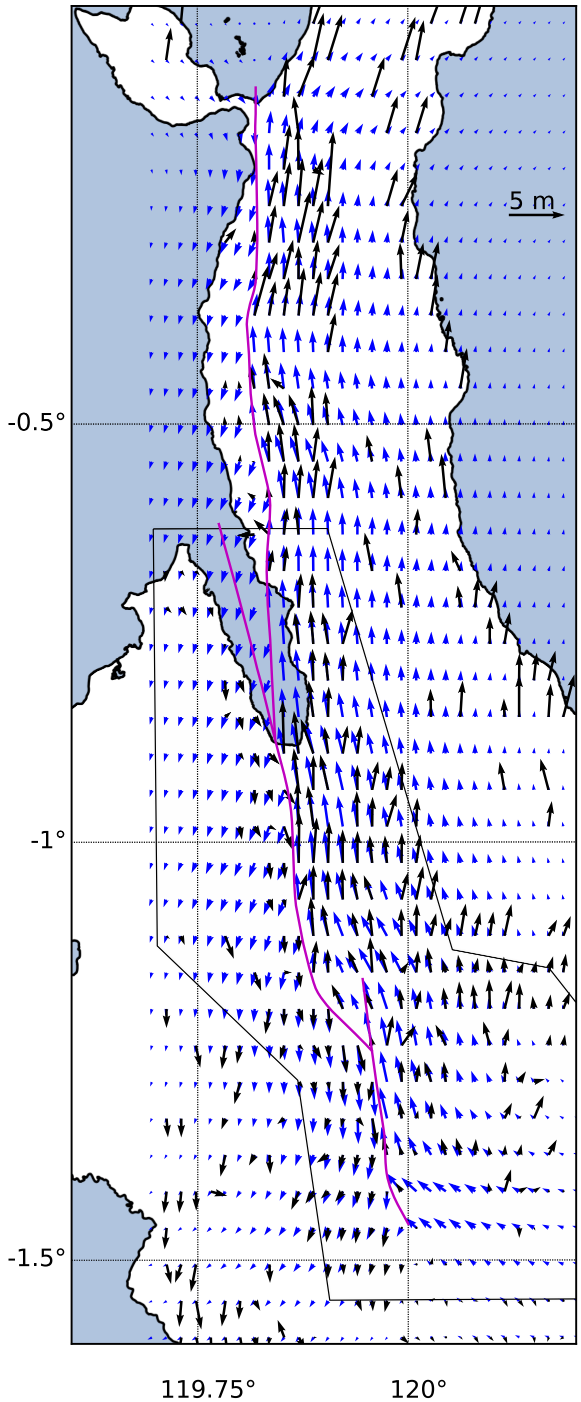

Figure 3.7: Comparison of the modeled and inferred horizontal surface displacements from subpixel correlation of Sentinel-2 optical images by De Michele (2019). Some parts of large inferred displacements, e.g., north of $-0.5°$ latitude, are probably artifacts, because they are not visible in the SAR data (see Fig. 3.8). The black polygon highlights where an at least first order agreement between SAR and optical data is achieved.

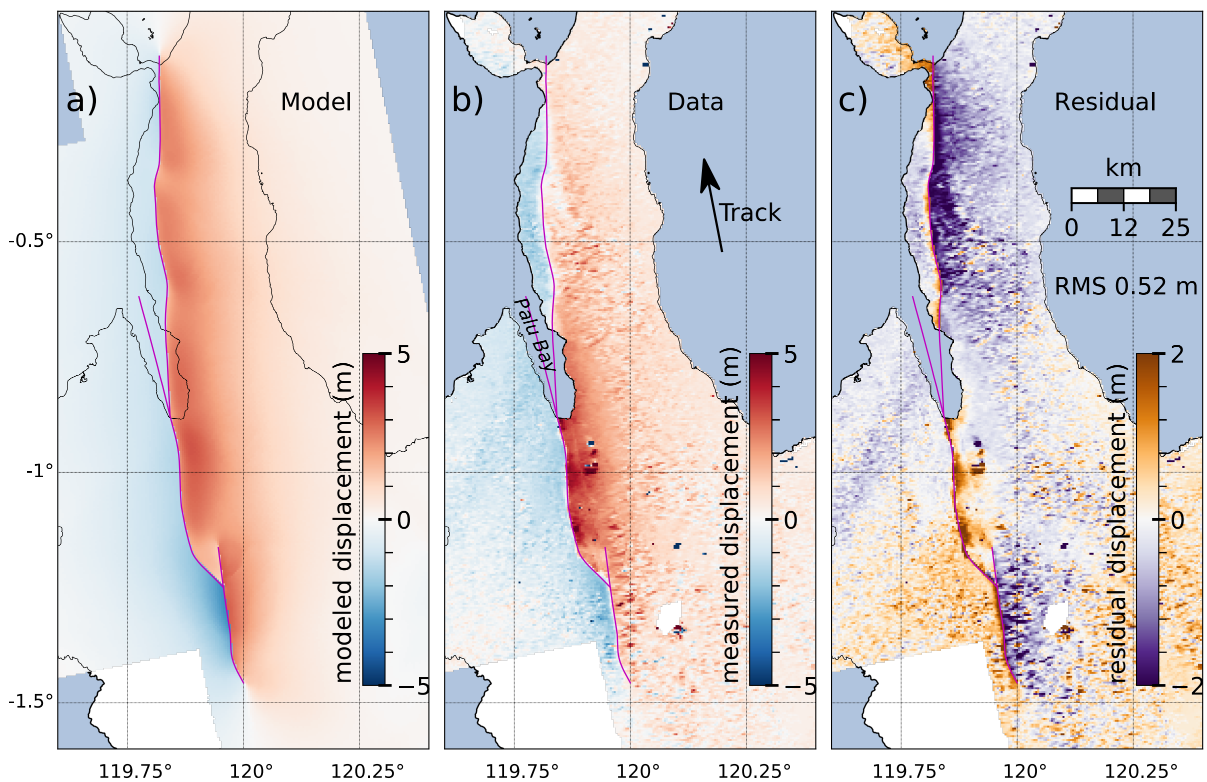

Figure 3.8: Our (a) modeled and (b) measured ground displacements in the SAR satellite along-track direction (see text). (c) residual = (b) − (a).

and at the big bend between the Palu and Saluki fault segments, where dip-slip reaches a maximum of approx. 4 m. Pure strike-slip faulting is modeled on the southern part of the vertical Saluki segment (Fig. 3.9b). The dip-slip component along the rupture shown in Fig. 3.9b produces subsidence above the hanging wall (east of the fault traces) and uplift above the foot wall (west of the fault traces). The resulting seafloor displacements are further discussed in Sec. 3.5.2.

Earthquake rupture speed

The earthquake scenario features an early and persistent supershear rupture velocity (Fig. 3.9d). This means that the rupture speed exceeds the seismic shear wave velocity (V_s) of 2.5–3.1 km/s in the vicinity of the fault network from the onset of the event. This agrees with the inferences for supershear rupture by Bao et al (2019) from back-projection analyses and by Socquet et al (2019) from satellite data analyses. However, we here infer supershear propagation faster than Eshelby speed ($\sqrt{2}V_s$), thus faster than Bao et al (2019) and well within the stable supershear rupture regime (Burridge, 1973).

3.5.2 Tsunami propagation and inundation: an earthquake-induced tsunami

The surface displacements induced by the earthquake result in a bathymetry perturbation Δb (as defined in Eq. (3.1)), which is visualized after 50 s simulation time (20 s after rupture arrest, which is when seismic waves have left Palu Bay) in Fig. 3.10a. In general, the bathymetry perturbation shows subsidence east of the faults and uplift west of the faults. The additional bathymetry effect incorporated through the approach of Tanioka and Satake (1996) locally modulates the smooth displacement fields from the earthquake rupture scenario (see Appendix 3.A.5, Fig. 3.A.6–3.A.7). Four cross-sections of the final perturbation in the west-east direction are shown in Fig. 3.10b. These capture the area of Palu Bay and clearly show the step induced by the normal component of fault slip. The step varies between 0.8 m and 2.8 m, with an average of 1.5 m. Note that this step is defined as fault throw in structural geology. However, here we explicitly incorporate effects of bathymetry and thus 'step' here refers to the total seafloor perturbation. Variation in the step magnitude along the fault is displayed in Fig. 3.10c.

The tsunami generated in this scenario is mostly localized in Palu Bay, which is illustrated in snapshots of the dynamically adaptive tsunami simulation after 20 s and 600 s simulation time in Fig. 3.11. This is expected as the modeled fault system is offshore only within the Bay. At 20 s, the seafloor displacement due to the earthquake is clearly visible in the sea surface height (ssh) within Palu Bay. Additionally, the effect of a small uplift is visible along the coast north of the Bay. The local behavior within Palu Bay is displayed in Fig. 3.12 at 20 s, 180 s and 300 s (see also the tsunami animation in Appendix 3.A.10). The local extrema along the coast reveal the complex wave reflections and refractions within the Bay caused by complex, shallow bathymetry as well as funnel effects.

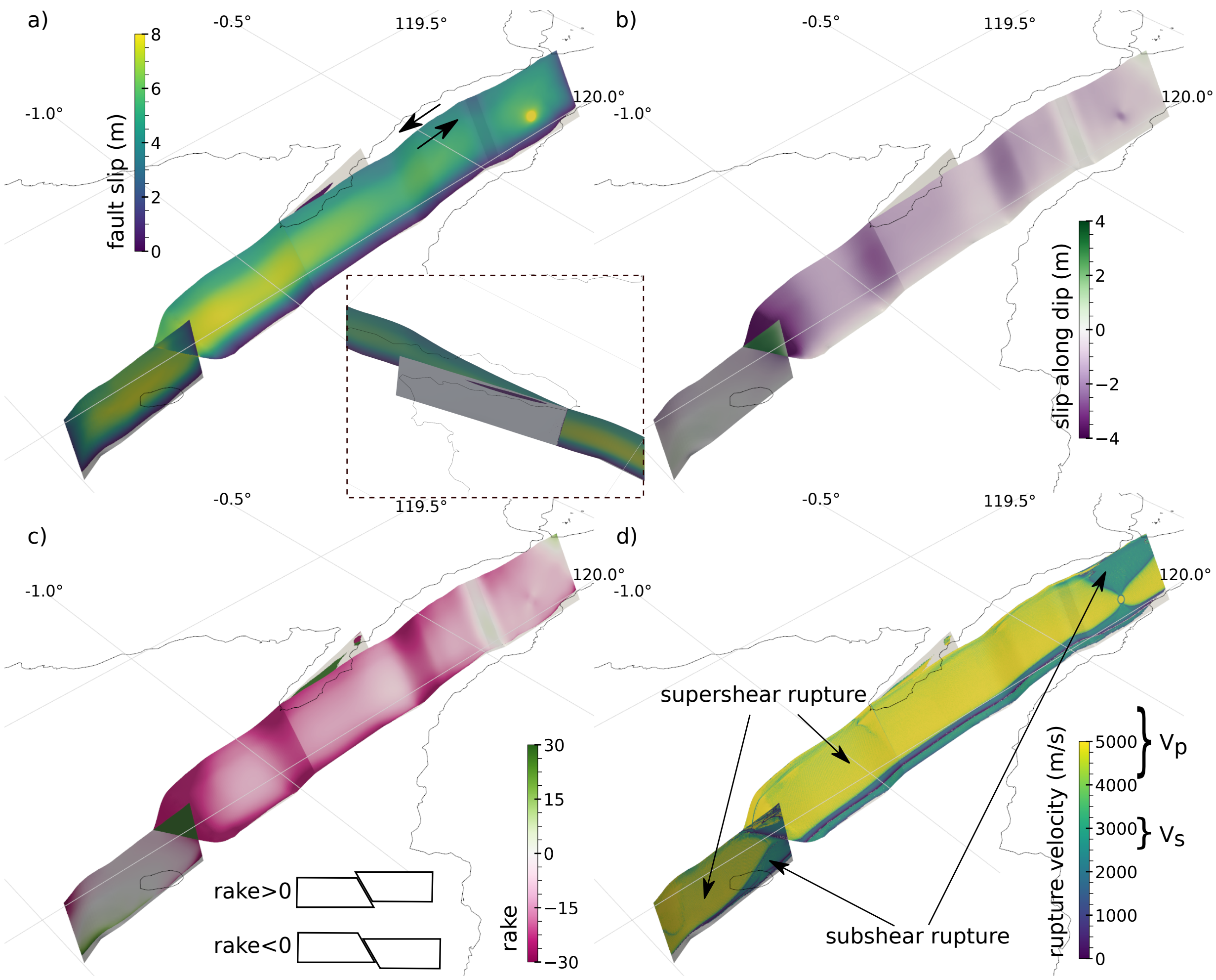

Figure 3.9: Source properties of the dynamic rupture scenario. (a) Final slip magnitude. The inset shows the slip magnitude on the main Palu-Koro fault within the Bay. (b) Dip-slip component. (c) Final rake angle. (b) and (c) both illustrate a moderate normal slip component. (d) Maximum rupture velocity indicating pervasive supershear rupture.

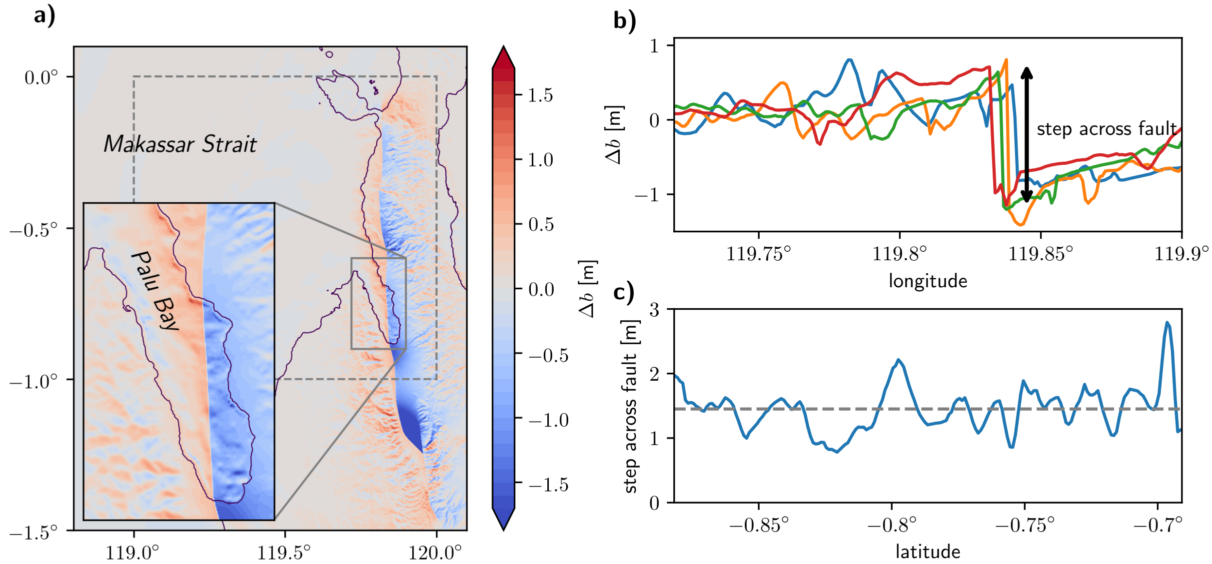

Figure 3.10: (a) Snapshot of the computed bathymetry perturbation Δb used as input for the tsunami model. The snapshot corresponds to a 50 s simulation time at the end of the earthquake scenario. (b) west-east cross-sections of the bathymetry perturbation at $-0.85°$ (blue), $-0.8°$ (orange), $-0.75°$ (green), $-0.7°$ (red) latitude showing the induced step in bathymetry perturbation across the fault. (c) step in bathymetry perturbation (as indicated in panel (b)) as function of latitude. Grey dashed line shows the average.

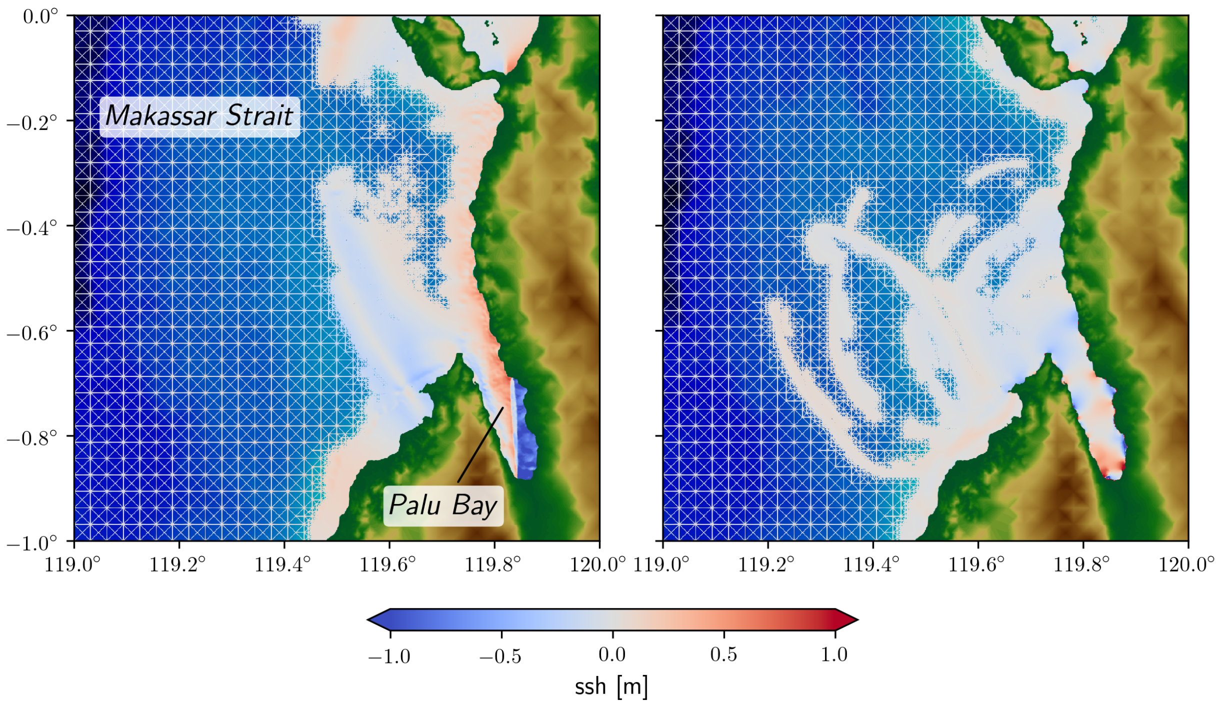

Figure 3.11: Snapshots of the tsunami scenario at 20 s (left) and 600 s (right), showing the dynamic mesh adaptivity of the model.

We compare the synthetic time series of the Pantoloan harbor tide gauge at (119.856155°E, 0.71114°S) to the observational gauge data. Additionally, a wealth of post-event field surveys characterize the inundation of the Palu tsunami (e.g. Widiyanto et al, 2019; Muhari et al, 2018; Omira et al, 2019; Yalciner et al, 2018; Pribadi et al, 2018). We compare the tsunami modeling results with observational data from a comprehensive overview of run-up data, inundation data, and arrival times of tsunami waves around the shores of the Palu Bay compiled by Yalciner et al (2018) and Pribadi et al (2018).

The Pantoloan tide gauge is the only tide gauge with available data in Palu Bay. The instrument is installed on a pier in Pantoloan harbor and thus records the change of water height with respect to a pier moving synchronously with the land. It has a 1-minute sampling rate and the observational time series was detided by a low-pass filter eliminating wave periods above 2 hours. The tsunami arrived five minutes after the earthquake onset time with a leading trough (Fig. 3.13). The first and highest wave arrived approximately eight minutes after the earthquake rupture time. The difference between trough and cusp amounts to almost 4 m. A second wave arrived after approximately 13 minutes with a preceding trough at 12 minutes.

The corresponding synthetic time series derived from the tsunami scenario is also shown in Fig. 3.13. Although a leading wave trough is not present in the scenario results, the magnitude of the wave is well captured. Note that coseismic subsidence produces a negative shift of approx. 80 cm within the first minute of the scenario. This effect is not captured by

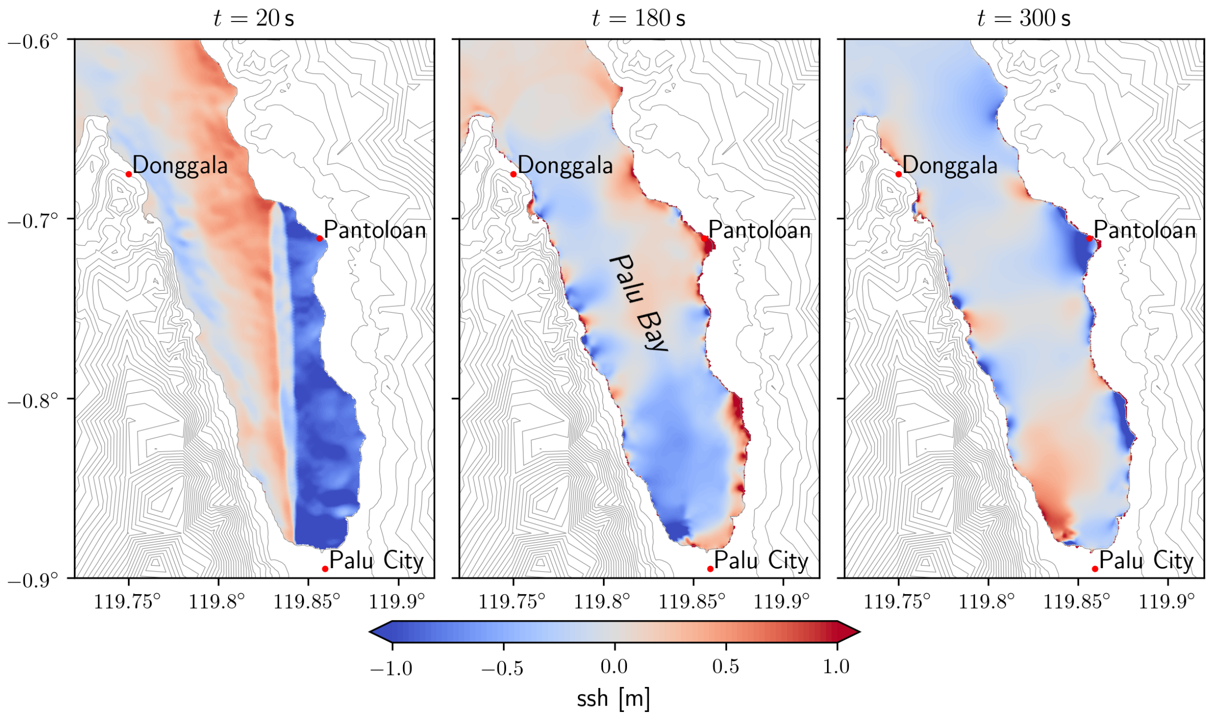

Figure 3.12: Snapshots of the tsunami scenario at 20 s, 180 s and 300 s (left to right), showing only the area of Palu Bay. Colors depict the sea surface height (ssh), which is the deviation from mean sea level.

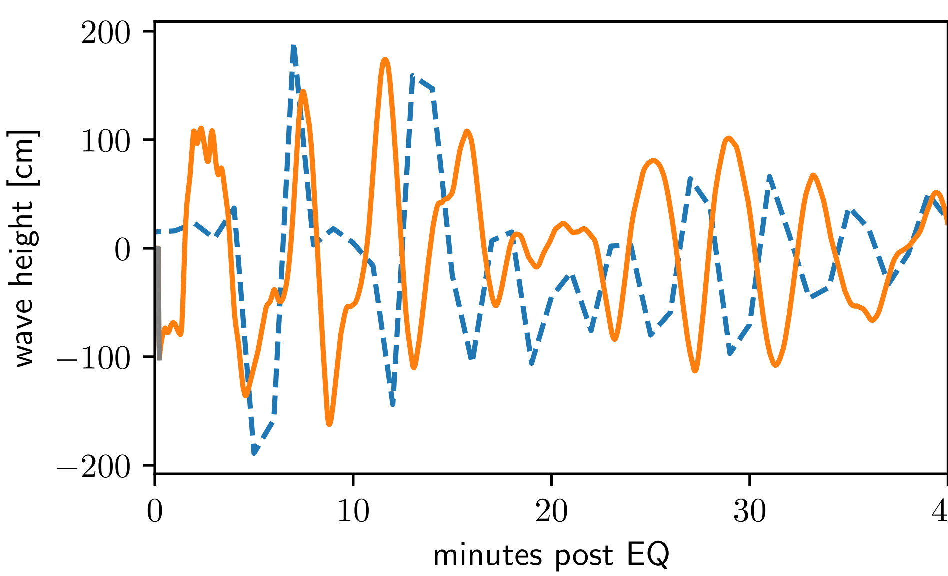

Figure 3.13: Time series from the wave gauge at Pantoloan port. Blue dashed: measurements, orange: output from the model scenario.

the tide gauge due to the way the instrument is designed. We detail this issue in Sec. 3.6.3. It cannot be easily filtered out, due to re-adjustments throughout the computation to the background mean sea level. After 5 min of simulated time, the model mareogram resembles the measured wave behavior, characterized by a dominant wave period of about 4 min. The scenario exposes a clear resonating wave behavior due to the narrow geometry of the Bay. We note that these wave amplitudes are produced due to displacements resulting from the earthquake, without any contribution from landsliding.

We conduct a macro-scale comparison between the scenario and the inundation data, rather than point-wise comparison, in view of the relatively low resolution topography data available. We adopt the following terminology, which is commonly used in the tsunami community and in the field surveys we reference (Yalciner et al, 2018; Pribadi et al, 2018): inundation elevation at a given point above ground is measured by adding the inundation depth to the ground elevation. In distinction, run-up elevation is the inundation elevation measured at the inundation point that is the farthest inland. We consistently report synthetic inundation elevations from the model.

In Fig.s 3.14 and 3.15, we compare model results to run-up elevations that are reported in the field surveys. For practical reasons, we compare the observed run-up elevations to synthetic inundation elevations at the exact measurement locations. In doing so, we consider only those points on land that are reached by water in the tsunami scenario. While inundation and run-up elevations are different observations, observed run-up and simulated inundation elevations can be compared if the run-up site is precisely georeferenced, which is here the case. Fig. 3.14 illustrates the distribution of the modeled maximum inundation elevations around the Bay. A quantitative view comparing these same results with observations is shown in Fig. 3.15. Because of the limited model resolution, the validity of the scenario cannot be analysed site by site, and we only discuss the overall agreement of the simulated inundation elevations with observations. It is remarkable that the model yields similar inundation elevations as observed, with some overestimation at the northern margins of the bay and some slight underestimation in the southern part near Grandmall Palu City. What we can conclude is that large misfit in the inundation elevations are more or less randomly distributed, suggesting it comes from local amplification effects that cannot be captured in the scenario due to insufficient bathymetry/topography resolution. Fig. 3.16 shows maximum inundation depths computed from the tsunami scenario near Palu City. Qualitatively, the results from the scenario agree quite well with observations, as the largest inundation depths are close to the Grandmall area, where vast damage due to the tsunami is reported.

In summary, the tsunami scenario sourced by coseismic displacements from the dynamic earthquake rupture scenario yields results that are qualitatively comparable to available observations. Wave amplitudes match well, as do the inundation elevations given the limited quality of the available topography data.

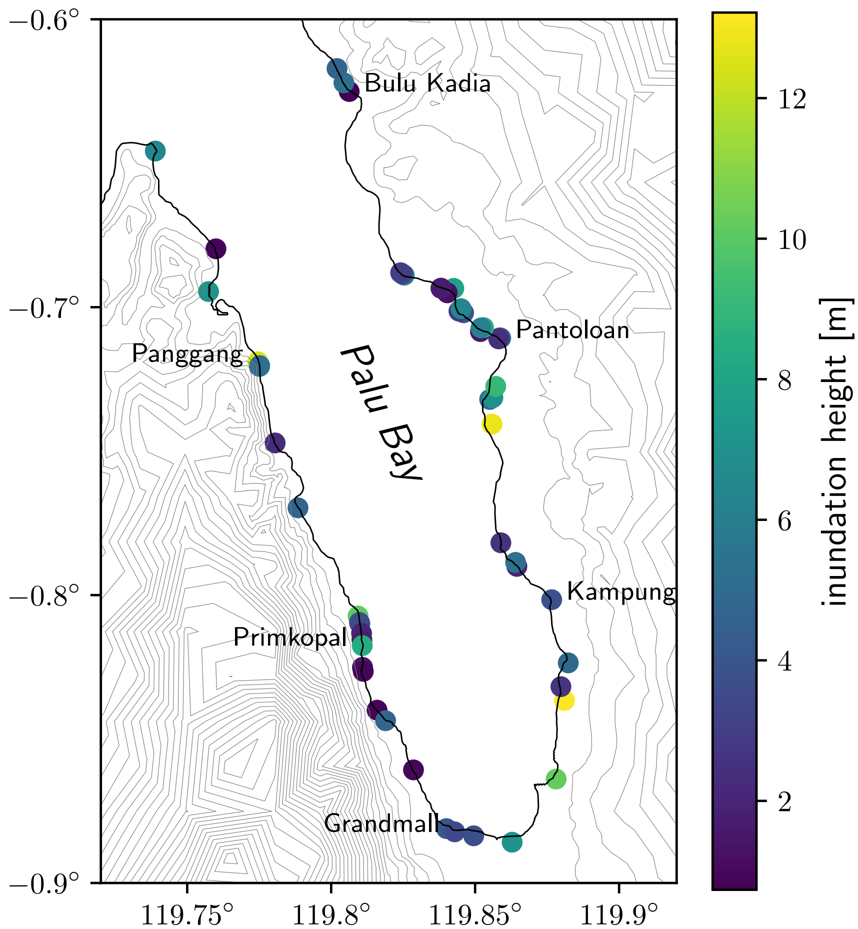

Figure 3.14: Simulated inundation elevations at different locations around Palu Bay, where observations have been recorded.

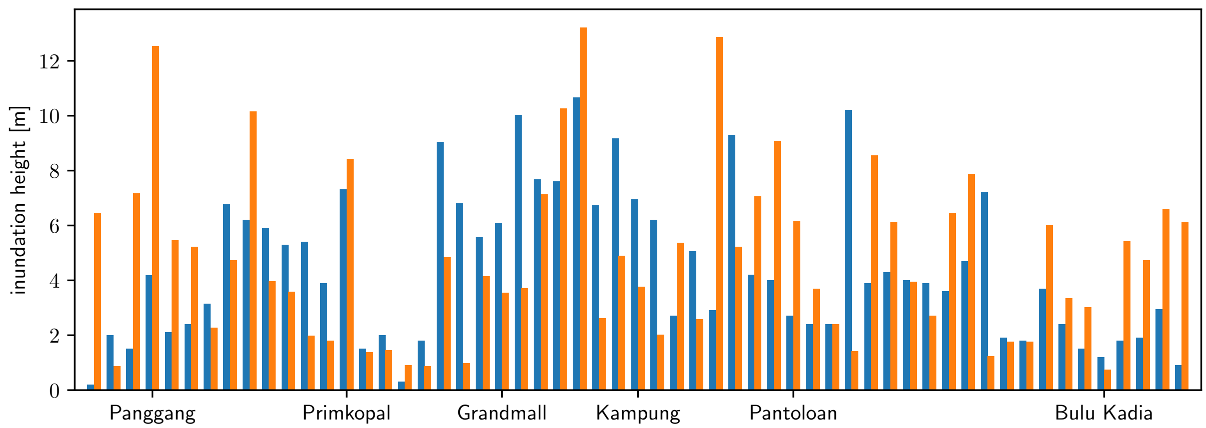

Figure 3.15: Inundation elevations from observation (blue) and simulation (orange) at different locations around Palu Bay (left to right: around the Bay from the northwest to the south to the northeast, see Fig. 3.14 for locations).

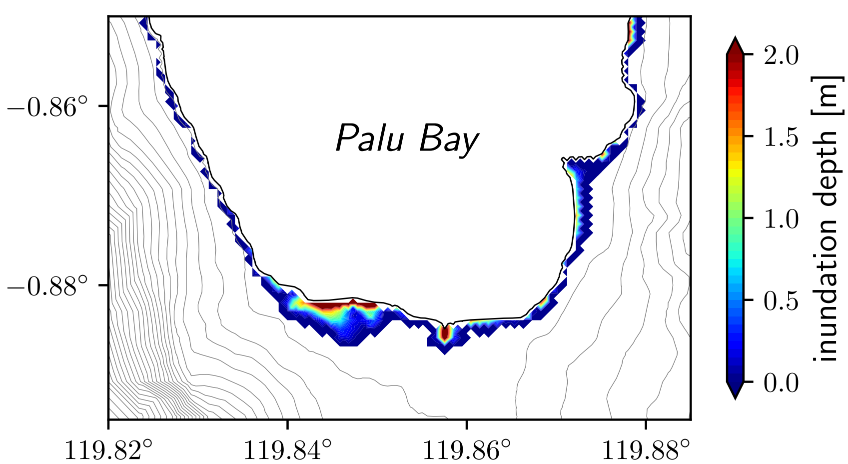

Figure 3.16: Maximum inundation depth near Palu City computed from the tsunami scenario.

3.6 Discussion

The Palu, Sulawesi tsunami was as unexpected as it was devastating. While the Palu-Koro fault system was known as a very active strike-slip plate boundary, tsunamis from strike-slip events are generally not anticipated. Fears arise that other regions, currently not expected to sustain tsunami-triggering ruptures, are at risk. This physics-based, coupled earthquake-tsunami model shows that a submarine strike-slip fault can produce a tsunami, if a component of dip-slip faulting occurs.

In the following, we discuss advantages and limitations of physics-based models of tsunamigenesis as well as of the individual earthquake and tsunami models. We then focus on the broader implications of rapid coupled scenarios for seismic hazard mitigation and response. Finally, we look ahead to improving the here-presented coupled model in light of newly available information and data.

3.6.1 Success and limitation of the physics-based tsunami source

We constrain the initial conditions for the coupled model according to the available earthquake data and physical constraints provided by previous studies, including those reporting regional transtensional strain (Walpersdorf et al, 1998; Socquet et al, 2006; Bellier et al, 2006). A stress field characterized by transtension induces a normal component of slip on the dipping faults in the earthquake scenario. The degree of transtension assumed here translates into a fault slip rake of about 15° on the 65° dipping modeled faults (Fig. 3.9c), which is consistent with the earthquake focal mechanism (USGS, 2018a).

This normal slip component results in widespread uplift and subsidence. The surface rupture generates a throw across the fault of 1.5 m on average in Palu Bay, which translates into a step of a similar magnitude in the bathymetry perturbation used to source the tsunami (Fig. 3.10c). This is sufficient for triggering a realistic tsunami that reproduces the observational data quite well. In particular it is enough to obtain the observed wave amplitude at the Pantoloan harbor wave gauge and the recorded inundation elevations.

However, we point out that transtension is not an necessary condition to generate oblique faulting on such a fault network. From static considerations, we show that specific alternative stress orientations can induce a considerable dip-slip component, particularly near fault bends, in biaxial stress regimes reflecting pure-shear (Appendix 3.A.3, Fig. 3.A.4).

The coupled earthquake-tsunami model performs well at reproducing observations from a macroscopic perspective and suggests that additional tsunami sources are not needed to explain the main tsunami. However, it does not constrain the small-scale features of the tsunami source and thus does not completely rule out other, potentially additional, sources, such as those suggested by Carvajal et al (2019) based on local tsunami waves captured on video.

For example, despite the overall consistency of the earthquake scenario results with data, the fault slip scenario has viable alternatives. The fault within Palu Bay may have hosted a different or more complicated slip profile than this scenario produces. Also, the fault geometry underneath the Bay is not known. We choose a simple geometry that honors the information at hand (see Sec. 3.4.2). However, complex faulting may also exist within Palu Bay, as is observed south of the Bay where slip was partitioned between minor dip-slip fault strands and the primary strike-slip rupture (Socquet et al, 2019). Such complexity would change the seafloor displacements and therefore the tsunami results. Furthermore, a less smooth fault geometry in the Northern region, closely fitting inferred fault traces, could reduce fault slip locally, and therefore produce better fitting ground displacement observations in the North. However, the influence on seafloor displacements within Palu Bay is likely to be small. In contrast, a different slip scenario along the Palu-Koro fault within Palu Bay could have a large influence on the seafloor displacements and modeled tsunami. The earthquake model shows a decrease in normal stress (unclamping) here as the model rupture front passes. Though slip is limited in the current scenario, alternative fault geometry or a lower assigned static coefficient of friction on the Palu-Koro fault could lead to more triggered slip and alternative earthquake and tsunami scenarios.

Finally, incorporating the effect of landslides is likely necessary to capture local features of the tsunami wave and inundation patterns. Constraining these sources is very difficult without pre- and post-event high-resolution bathymetric charts. This study suggests that these sources play a secondary role in explaining the overall tsunami magnitude and wave patterns, since these can be generated by strike-slip faulting with a normal slip component.

3.6.2 The Sulawesi earthquake scenario

We review and discuss the dynamic earthquake scenario here and note avenues for additional modeling. For example, the speed of this earthquake is of utmost interest, although it does not provide an important contribution to the tsunami generation in this scenario. The initial stress state and lithology included in the physical earthquake model are areas that could be improved with more in-depth study and better available data.

The dynamic earthquake model requires supershear rupture velocities to produce results that agree with the teleseismic data and moment rate function. This scenario also provides new perspectives on the possible timing and mechanism of this supershear rupture. Bao et al (2019) infer an average rupture velocity of about 4 km/s from back-projection. This speed corresponds to a barely stable mechanical regime, which is interpreted as being promoted by a damage zone around the mature Palu-Koro fault that formed during previous earthquakes.

In contrast, the earthquake scenario features an early and persistent rupture velocity of 5 km/s on average, close to P-wave speed. Supershear rupture speed is enabled in the model by a relatively low fault strength and triggered immediately at rupture onset by a highly overstressed nucleation patch. Supershear transition is enabled and enhanced by high background stresses (or more generally, low ratios of strength excess over stress drop) (Andrews, 1976). The transition distance, the rupture propagation distance at which supershear rupture starts to occur, also depends on nucleation energy (Dunham, 2007; Gabriel et al, 2012, 2013). Observational support for the existence of a highly stressed nucleation region arises from the series of foreshocks that occurred nearby in the days before the mainshock, including a M_w 6.1 on the same day of the mainshock.

We conducted numerical experiments reducing the level of overstress within the nucleation patch, reaching a critical overstress level at which supershear is no longer triggered immediately at rupture onset. These alternative models initiate at subshear rupture speeds and never transition to supershear. Importantly, these slower earthquake scenarios do not match the observational constraints, specifically the teleseismic waveforms and moment release rate.

Stress and/or strength variations due to, for example, variations in tectonic loading, stress changes from previous earthquakes, or local material heterogeneities are expected, but poorly constrained, and therefore not included in this dynamic rupture model. Accounting for such features in relation to long term deformation can distinctly influence the stress field and lithological contrasts (e.g., van Dinther et al, 2013; Dal Zilio et al, 2018, 2019; Preuss et al, 2019; D'Acquisto et al, 2018; van Zelst et al, 2019). Realistic initial conditions in terms of stress and lithology are shown to significantly influence the dynamics of individual ruptures (Lotto et al, 2017a; van Zelst et al, 2019). Specifically, different fault stress states for the Palu and the Northern fault segments are possible, since the Palu-Koro fault acts as the regional plate-bounding fault that likely experiences increased tectonic loading (Fig. 3.1a). The introduction of self-consistent, physics-based stress and strength states could be obtained by coupling this earthquake-tsunami framework to geodynamic seismic cycle models (e.g., van Dinther et al, 2013, 2014; van Zelst et al, 2019), as done in Gabriel et al (2018). However, in light of an absence of data or models justifying the introduction of complexity, we here use the simplest option with a laterally homogeneous stress field that honors the regional scale transtension.

We also note that the earthquake scenario is dependent on the subsurface structural model (e.g., Lotto et al, 2017a; van Zelst et al, 2019). The local velocity model of Awaliah et al (2018) is of limited resolution within the Palu area, since only one of the stations used illuminates this region. Despite the strong effects of data regularization, this is, to our knowledge, the most detailed data set characterizing the subsurface in the area of study.

3.6.3 The Sulawesi tsunami scenario

Overall, the tsunami model shows good agreement with available key observations. Wave amplitudes and periods at the only available tide gauge station in Palu Bay match well. Inundation data from the model show satisfactory agreement with the observations by international survey teams (Yalciner et al, 2018).

Apart from the earthquake model limitations discussed in Sec. 3.6.1 that may influence the tsunami characteristics, the following items may cause deviations between the tsunami model results and observations: (a) insufficiently accurate bathymetry/topography data; (b) approximation by hydrostatic shallow water wave theory; (c) simplified coupling between earthquake rupture and tsunami scenarios. In the following we will briefly discuss these topics.

The limited resolution of the bathymetry and topography data sets may prevent us from properly capturing local effects, which in turn may affect site-specific tsunami and inundation observations. This is discussed further and quantified in Appendix 3.A.9. While the adaptively refined computational mesh, which refines down to 80 m near the shore, allows inundation to be resolved numerically, interpolating the bathymetry data does not increase its resolution. Therefore, in Sec. 3.5.2, we focus on the overall agreement between model and observation in the distribution of simulated inundation elevations around Palu Bay. This is a relevant result, since it confirms that the modeled tsunami wave behavior is reasonable overall.

The accuracy of the tsunami model may also be affected by the simplifications underlying the shallow water equations. In particular, a near-field tsunami within a narrow bay may be affected by large bathymetry gradients. In the shallow-water framework, all three spatial components of the ground displacements generated by the earthquake model cannot be properly accounted for. In fact, a direct application of a horizontal displacement to the hydrostatic (single layer) shallow water model would lead to unrealistic momentum in the whole water column. Additionally, all bottom movements are immediately and directly transferred to the entire water column, since we model the water wave by (essentially 2D) shallow water theory. In reality, an adjustment process takes place. The large bathymetry gradients may also lead to non-hydrostatic effects in the water column, which cannot be neglected. Whilst fully 3D simulations of tsunami genesis and propagation have been undertaken (e.g. Saito and Furumura, 2009), less compute-intensive alternatives are underway (e.g., Jeschke et al, 2017), and should be tested to quantify the influence of such effects in realistic situations such as the Sulawesi event.

We account for the effect of the horizontal seafloor displacements by applying the method proposed by Tanioka and Satake (1996). We observe only minor differences in the modeled water waves when including the effect of the horizontal ground displacements (see Fig. 3.12, 3.16, 3.A.9 and 3.A.10). We thus conclude that vertical ground displacements are the primary cause of the tsunami.

Directly after the earthquake, about 80 cm of ground subsidence is imprinted on the synthetic mareogram at Pantaloan wave gauge, but is not visible in the observed signal (cf. Fig. 3.10, Fig. 3.13, and Fig. 3.A.2). The tide gauge at Pantaloan is indeed not sensitive to ground vertical displacements, since the instrument and the water surface are displaced jointly during ground subsidence, and therefore their distance remains fixed. Note that we also cannot remove this shift from the synthetic time series, since the tsunami model includes a background mean sea level, to which it re-adjusts throughout the computation.

The tsunami model produces inundation elevations of more than 10 m at several locations in Palu Bay. Similarly large values are also reported in field surveys (e.g. Yalciner et al, 2018). We note that offshore tsunami heights ranging between 0-2 m are not inconsistent with large run-up elevations. A moderate tsunami wave can generate significant run-up elevation if it reaches the shoreline with significant inertia (velocity). Amplification factors of 5-10 from wave height to local run-up height are not uncommon (see e.g. Okal et al, 2010), and result from shoaling due to local bathymetry features.

3.6.4 Advantages and outcome of a physics-based coupled model

A physics-based earthquake and coupled tsunami model is well-posed to shed light on the mechanisms and competing hypotheses governing earthquake-tsunami sequences as puzzling as the Sulawesi event. By capturing dynamic slip evolution that is consistent with the fault geometry and the regional stress field, the dynamic rupture model produces mechanically consistent ground deformation, even in submarine areas where space borne imaging techniques are blind. These seafloor displacement time-histories, which include the influence of seismic waves, in nature contribute to source the tsunami and are utilized as such in this coupled framework. However, the earthquake-tsunami coupling is not physically seamless. For example, as noted above, seismic waves cannot be captured using the shallow water approach, but rather require a non-hydrostatic water body (e.g. Lotto et al, 2018). The coupled system nevertheless remains mechanically consistent to the order of the typical spatio-temporal scales governing tsunami modeling.

The use of a dynamic rupture earthquake source has distinct contributions relative to the standard finite-fault inversion source approach, which is typically used in tsunami models. The latter enables close fitting of observations through the use of a large number of free parameters. Despite recent advances (e.g., Shimizu et al, 2019), kinematic models typically need to pre-define fault geometries. Naive first-order finite-fault sources are automatically determined after an earthquake and this can be done quickly (e.g. by the USGS or GFZ German Research Centre for Geoscience), which is a great advantage. Models can be improved later on by including new data and more complexity. However, kinematic models are characterized by inherent non-uniqueness and do not ensure mechanical consistency of the source (e.g., Mai et al, 2016). The physics-based model also suffers from non-uniqueness, but this is reduced, since it excludes scenarios that are not mechanically viable.

These advantages and the demonstrated progress potentially make physics-based, coupled earthquake-tsunami modeling an important tool for seismic hazard mitigation and rapid earthquake response. We facilitate rapid modeling of the earthquake scenario by systematically defining a suitable parameterization for the regional and fault-specific characteristics. We use a pre-established, efficient algorithm, based on physical relationships between parameters, to assign the ill-constrained stress state and strength on the fault using a few trial simulations (Ulrich et al, 2019a). This limits the required input parameters to subsurface structure, fault structure, and four parameters governing the stress state and fault conditions. This enables rapid response in delivering physics-driven interpretations that can be integrated synergistically with established data-driven efforts within the first days and weeks after an earthquake.

3.6.5 Looking forward

The coupled model presented here produces a realistic scenario that agrees with key characteristics of available earthquake and tsunami data. However, future efforts will be directed toward improving the model as new information on fault structure or displacements within the Bay or additional tide gauge measurements become available.

In addition, different earthquake models varying in their fault geometry or in the physical laws governing on- and off-fault behavior can be utilized in further studies of the influence of earthquake characteristics on tsunami generation and impact.

This model provides high resolution synthetics of, e.g., ground deformation in space and time. These results can be readily compared to observational data that are yet to be made available to the scientific community. We provide time series of modeled ground displacements in Appendix 3.A.2.

Spatial variations of regional stress and fault strength could be constrained in the future by tectonic seismic cycle modeling capable of handling complex fault geometries. Future dynamic earthquake rupture modeling may additionally explore how varying levels of preexisting and coseismic off-fault damage affect the rupture speed specifically and rupture dynamics in general.

Future research should also be directed towards an even more realistic coupling strategy together with an extended sensitivity analysis on the effects of such coupling. This, e.g., requires the integration of non-hydrostatic extensions for the tsunami modeling part (Jeschke et al, 2017) into the coupling framework.

3.7 Conclusions

We present a coupled, physics-based scenario of the 2018 Palu, Sulawesi earthquake and tsunami, which is constrained by rapidly available observations. We demonstrate that coseismic oblique-slip on a dipping strike-slip fault produces a vertical step across the submarine fault segment of 1.5 m on average in the tsunami source. This is sufficient to produce reasonable tsunami amplitude and inundation elevations. The critical normal-faulting component results from transtension, prevailing in this region, and the fault system geometry.

The fully dynamic earthquake model captures important features, including the timing and speed of the rupture, 3D geometric complexities of the faults, and the influence of seismic waves on the rupture propagation. We find that an early-onset of supershear rupture speed, sustained for the duration of the rupture across geometric complexities, is required to match a range of far-field and near-fault observations.

The modelled tsunami amplitudes and inundation elevations agree with observations within the range of modeling uncertainties dominated by the available bathymetry and topography data.We conclude that the primary tsunami source may have been coseismically generated vertical displacements. However, in a holistic approach aiming to match high-frequency tsunami features, local effects such as landsliding, non-hydrostatic wave effects, and high resolution topographical features should be included.

A physics-based earthquake and coupled tsunami model is specifically useful to assess tsunami hazard in tectonic settings currently underrepresented in operational hazard assessment. We demonstrate that high-performance computing empowered dynamic rupture modeling produces well-constrained studies integrating source observations and earthquake physics very quickly after an event occurs. In the future, such physics-based earthquake-tsunami response can complement both on-going hazard mitigation and the established urgent response tool set.

3.8 Acknowledgements

We thank Taufiqurrahman for helping us accessing data on Indonesian websites, and for putting us in contact with Indonesian researchers. We thank Dr. T. Yudistira for providing their crustal velocity model of Sulawesi and Dr. Andreas Fichtner for providing us part of their 'Collaborative Seismic Earth Model'. We thank Dr. Marcello de Michele for providing his inferred ground-deformations data and for fruitful discussions. The ALOS-2 original data are copyright JAXA and provided under JAXA RA6 PI projects P3278 and P3360. Dr. Widodo S. Pranowo provided access to very early field survey observations. Furthermore, Dr. Abdul Muhari supported this work by providing 1-minute tide gauge data for the Pantoloan tide gauge. We thank two anonymous reviewers and the editor-in-chief Alexander Rabinovich for their constructive comments. Finally we thank the #geotweeps twitter community and the participants of the AGU special session about the Palu earthquake and tsunami for stimulating discussions.

The work presented in this paper was enabled by the Volkswagen Foundation (project "ASCETE", grant no. 88479).

Computing resources were provided by the Institute of Geophysics of LMU Munich (Oeser et al, 2006), the Leibniz Supercomputing Centre (LRZ, projects no. h019z, pr63qo and pr45fi on SuperMUC), and the Center for Earth System Research and Sustainability (CEN) at University of Hamburg.

T.U., E.H.M. and A.-A.G. acknowledge support by the German Research Foundation (DFG) (projects no. KA 2281/4-1, GA 2465/2-1, GA 2465/3-1), by BaCaTec (project no. A4) and BayLat, by KONWIHR – the Bavarian Competence Network for Technical and Scientific High Performance Computing (project NewWave), by KAUST-CRG (GAST, grant no. ORS-2016-CRG5-3027 and FRAGEN, grant no. ORS-2017-CRG6 3389.02), by the European Union's Horizon 2020 research and innovation program (ExaHyPE, grant no. 671698 and ChEESE, grant no. 823844).

S.V. acknowledges support by Einstein Stiftung Berlin through grant EVF-2017-358(FU).

Part of this research was performed at the Jet Propulsion Laboratory, California Institute of Technology under contract with the National Aeronautics and Space Administration (NASA) by Earth Surface and Interior focus area and NISAR Science Team.

Appendix

3.A Appendix

3.A.1 Off-fault plasticity

We account for the possibility of off-fault energy dissipation, by assuming a Drucker-Prager elasto-viscoplastic rheology (Wollherr et al, 2018). The model is parameterized following Ulrich et al (2019a). The internal friction coefficient is set equal to the reference fault friction coefficient (0.6). Similarly, off-fault initial stresses are set equal to the depth-dependent initial stresses prescribed on the fault. The relaxation time T_v is set to 0.05 s. Finally, we assume depth-dependent bulk cohesion (see Fig. 4.A.6) to account for the hardening of the rock structure with depth.

3.A.2 Displacement time histories

Many high-rate GNSS stations have recorded the Palu event in the near field (Simons et al, 2018). Nevertheless, these data are not yet available. In Figure 3.A.2, we provide the displacements time histories at a few of these sites (see fig. 3.A.3). We hope future access to this data will provide further constraint on the model.

3.A.3 Initial stress

In this section, we detail the initial stress parametrization, presented in general terms in Sect. 3.4.2.

The fault system is loaded by a laterally homogeneous regional stress regime. Assuming an Andersonian stress regime, where $s_1 > s_2 > s_3$ are the principal stresses and s_2 is vertically oriented, the stress state is fully characterized by four parameters: $SH_{\max}$, ν, R_0 and γ. $SH_{\max}$ is the azimuth of the maximum horizontal compressive stress; ν is a stress shape ratio balancing the principal stress amplitudes; R_0 is a ratio describing the relative strength of the faults; and γ the fluid pressure ratio.

The World Stress Map (Heidbach et al, 2018) constrains $SH_{\max}$ to the range of $120 \pm 15°$. The stress shape ratio $\nu = (s_2 - s_3)/(s_1 - s_2)$ allows characterizes the stress regime: $\nu \approx 0.5$ indicates pure shear, $\nu > 0.5$ indicates transtension and $\nu < 0.5$ indicates transpression. A transtensional regime is suggested by geodetic studies (Walpersdorf et al, 1998; Socquet et al, 2006), fault kinematic analyses from field data (Bellier et al, 2006), and by the USGS

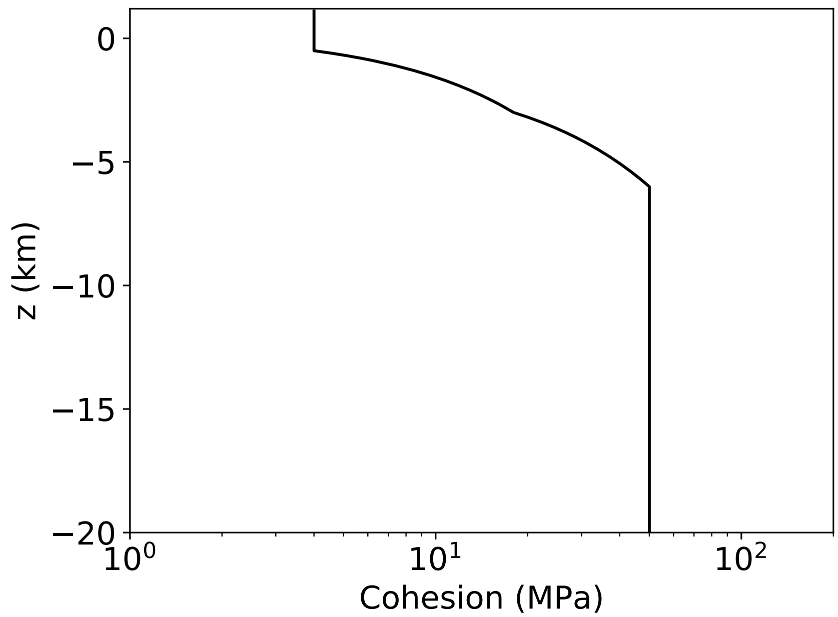

Figure 3.A.1: Depth dependence of bulk cohesion in the off-fault plastic yielding criterion

focal mechanism of the mainshock, which clearly features a normal faulting component. However, the exact value of ν is not constrained.

The fault prestress ratio R_0 describes the closeness to failure of a virtual, optimally oriented plane according to Mohr-Coulomb theory (Aochi and Madariaga, 2003). On this virtual plane, the Coulomb stress is maximized. Optimally oriented planes are critically loaded when $R_0 = 1$. Faults are typically not optimally oriented in reality. In a dynamic rupture scenario, only a small part of the modeled faults need to reach failure in order to nucleate sustained rupture. Other parts of the fault network can fail and slip progressively, even if well below failure before rupture initiation. The propagating rupture front or traveling seismic waves can raise the local shear tractions to match fault strength locally.

We assume fluid pressure P_f throughout the crust is proportional to the lithostatic stress: $P_f = \gamma\sigma_c$, where γ is the fluid-pressure ratio and $\sigma_c = \rho g z$ is the lithostatic pressure. A fluid pressure of $\gamma = \rho_{\text{water}}/\rho = 0.37$ indicates purely hydrostatic pressure. Higher values correspond to overpressurized stress states. Together, R_0 and γ control the average stress drop $d\tau$ in the dynamic rupture model as:

$$d\tau \sim (\mu_s - \mu_d) R_0 (1 - \gamma) \sigma_c. \tag{3.2}$$

where μ_s and μ_d are the static and dynamic fault friction assigned in the model, $d\tau$ is a critical characteristic of the earthquake dynamic rupture model, controlling the average fault slip, rupture speed and earthquake size.

Following Ulrich et al (2019a), we can evaluate different initial stress and strength settings using purely static considerations. By varying the stress parameters within their observational constraints we compute the distribution of the relative prestress ratio R and

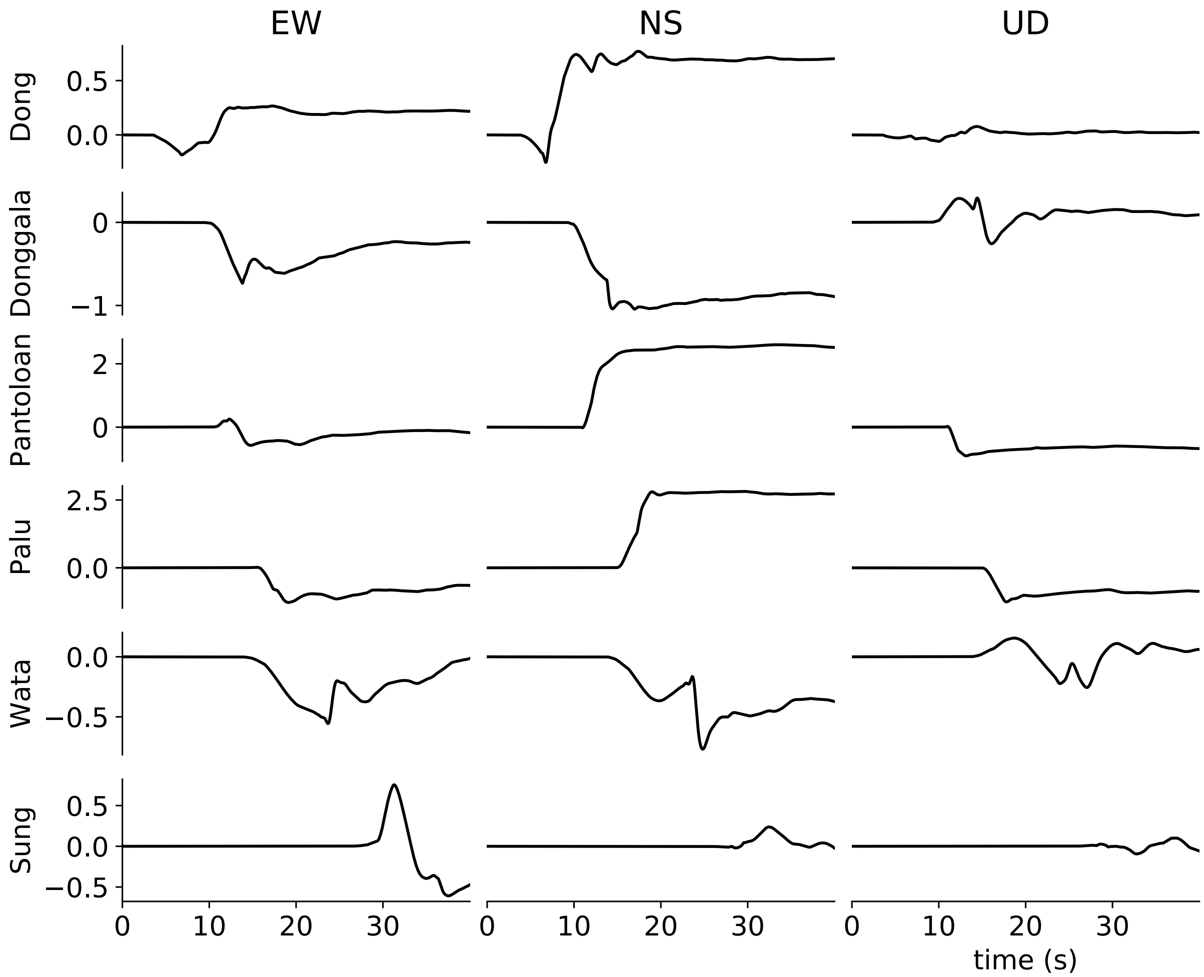

Figure 3.A.2: Synthetic unfiltered time-dependent ground displacement in meters at selected locations (see fig. 3.A.3)

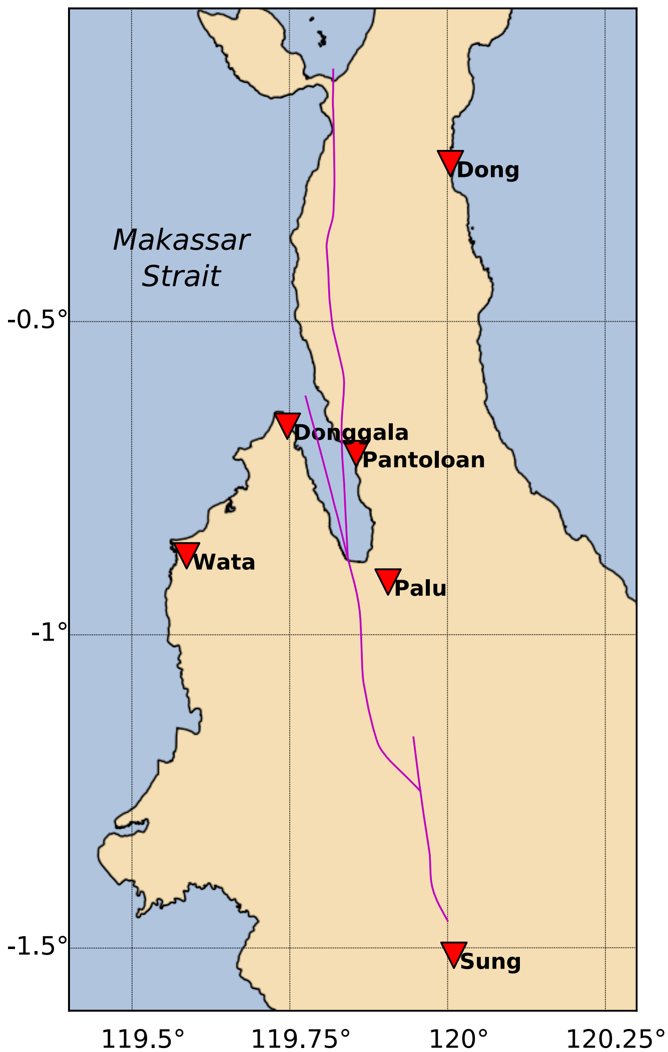

Figure 3.A.3: Locations of known geodetic observation sites for which we provide synthetic ground displacement time series (see fig. 3.A.2)

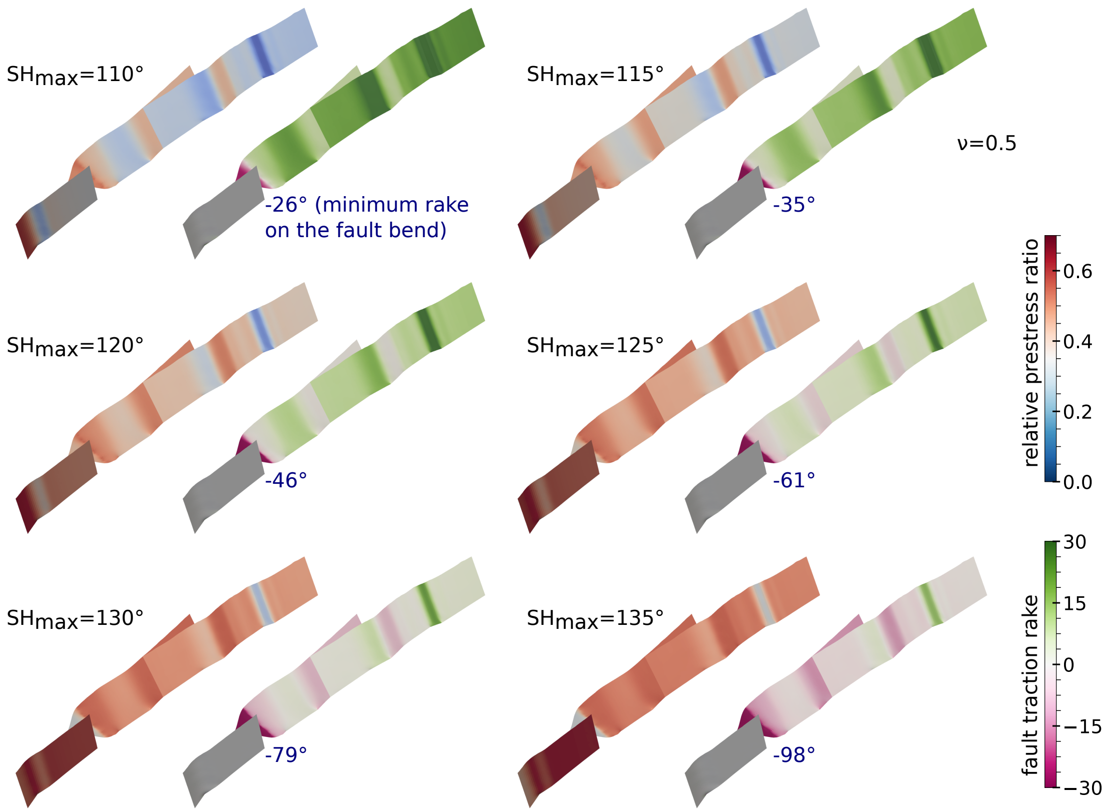

Figure 3.A.4: Magnitude and rake of prestress resolved on the fault system for a range of plausible $SH_{\max}$ values, assuming a stress shape ratio $\nu = 0.5$ (pure-shear). For each stress state we show the spatial distribution of the pre-stress ratio (left) and the rake angle of the shear traction (right). Here we assume $R_0 = 0.7$ on the optimal plane, which results in $R < R_0$ for all faults since these are not optimally oriented. In blue, we label the (out-of-scale) minimum rake angle on the Palu-Saluki bend.

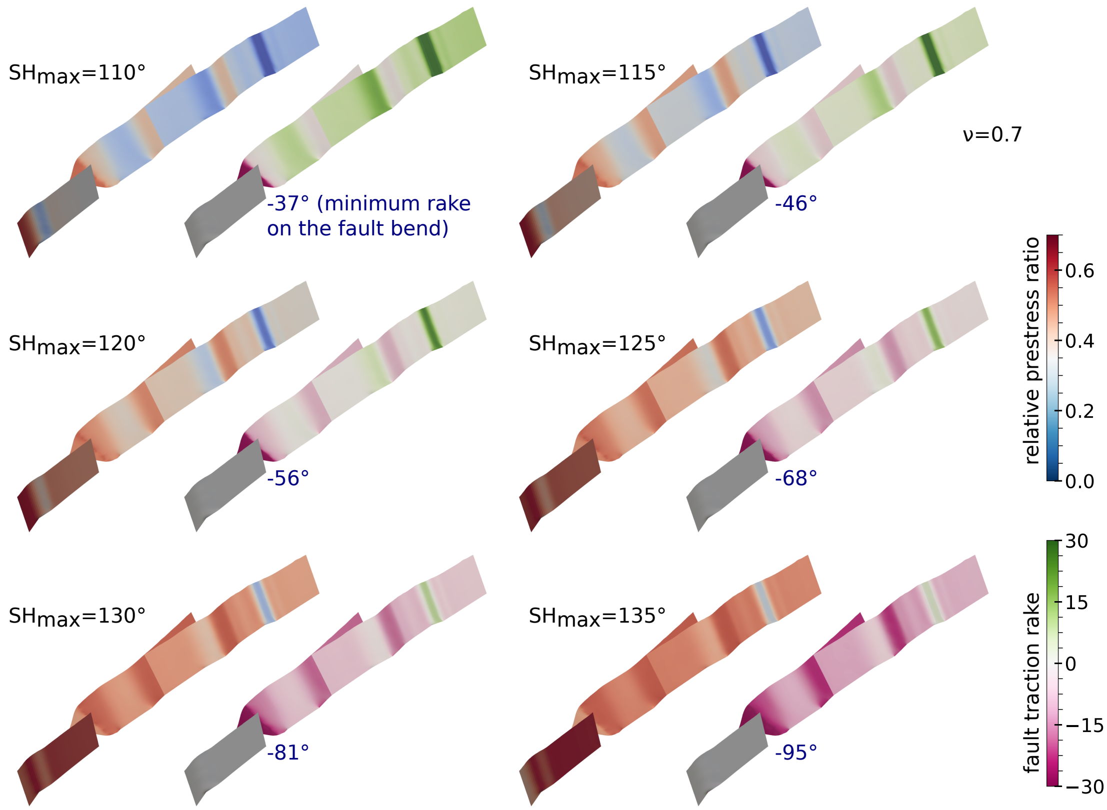

Figure 3.A.5: Same as Fig. 3.A.4, but assuming a stress shape ratio $\nu = 0.7$ (transtension).

of the shear traction orientation resolved on the fault system for each configuration. R is defined as:

$$R = (\tau_0 - \mu_s \sigma_n)/((\mu_s - \mu_d)\sigma_n) \ , \tag{3.3}$$

where τ_0 and σ_n are the initial shear and normal tractions resolved on the fault plane.

We can characterize the spatially variable fault strength in the model by calculating R (Eq. (3.3)) at every point on each fault (Fig. 3.A.4 and 3.A.5). By definition, R is always lower or equal to R_0, since the faults are not necessary optimally oriented.

We then select the stress configuration that maximizes R across the fault system, especially around rupture transition zones to enable triggering, and that represents a shear stress orientation compatible with the inferred ground deformations and the inferred focal mechanisms.

These purely static considerations suggest that a transtensional regime is required to achieve a favourable stress orientation on the fault system. In fact, we see that a biaxial stress regime ($\nu = 0.5$) does not resolve sufficient shear stress simultaneously on the main north-south striking faults and on the Palu-Saluki bend (see Fig. 3.A.4). Dynamic rupture experiments confirm that the Saluki fault could not be triggered under such a stress regime.

Table 3.A.1: Fault frictional properties assumed in this study.

Direct-effect parameter	a	0.01
Evolution-effect parameter	b	0.014
Reference slip rate	V_0	10^{-6} m/s
Steady-state low-velocity friction coefficient at slip rate V_0	f_0	0.6
Characteristic slip distance of state evolution	L	0.2 m
Weakening slip rate	V_w	0.1 m/s
Fully weakened friction coefficient	f_w	0.1
Initial slip rate	V_ini	10^{-16} m/s

On the other hand, such optimal configuration can be achieved by a transtensional stress state, for instance by choosing $\nu = 0.7$ and SH_max in the range 125 to 135° (see fig. 3.A.5). We choose $SH_\mathrm{max} = 135°$, which allows for nucleation with less overstress than lower values and generates ruptures with the expected slip orientations and magnitudes.

The here assumed fault system does not feature pronounced geometrical barriers apart from the Palu-Saluki bend. As a consequence, R_0 is actually poorly constrained, and trade-offs between R_0 and γ are expected. The preferred, realistic model is characterized by $R_0 = 0.7$ and $\gamma = 0.79$. This results in an effective confining stress $(1-\gamma)\sigma_c$ that increases with depth by a gradient of 5.5 MPa/km.

3.A.4 Friction law

We here use a form of fast-velocity weakening friction proposed in the community benchmark problem TPV104 of the Southern California Earthquake Center (Harris et al, 2018) and as parameterized by Ulrich et al (2019a). Friction drops rapidly from a steady-state, low-velocity friction coefficient, here $f_0 = 0.6$, to a fully weakened friction coefficient, here $f_w = 0.1$ (see Table 3.A.1).

3.A.5 Horizontal displacements as additional tsunami source

For computing the bathymetry perturbation used as the source for the tsunami model, we apply the method of Tanioka and Satake (1996) to additionally account for horizontal displacements, computed in the earthquake model. The final states of the three displacement components Δx,Δy and Δz are given in Fig. 3.A.6 and 3.A.7. Applying the approach

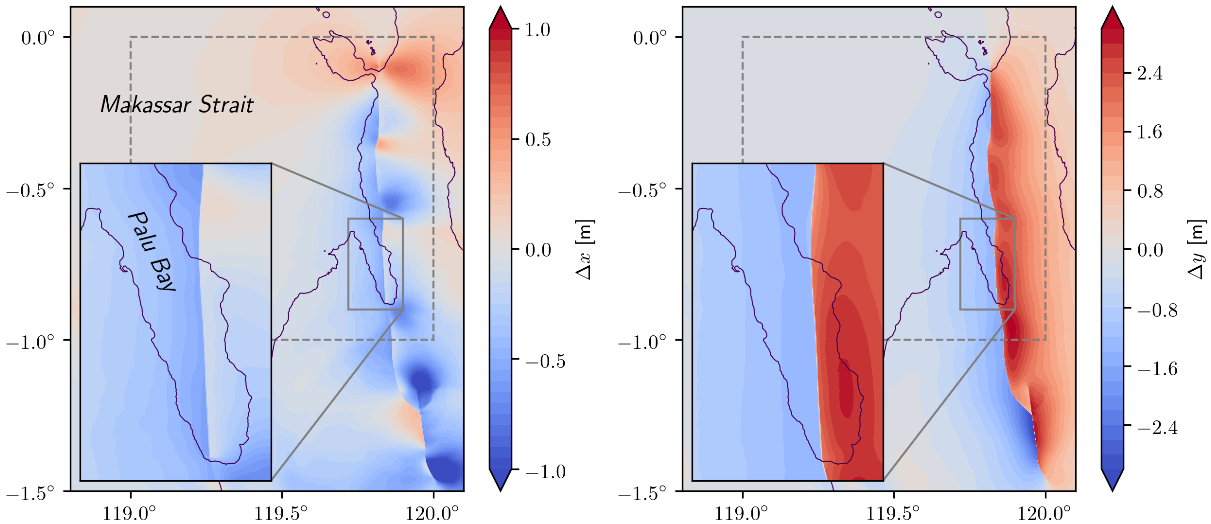

Figure 3.A.6: Final horizontal surface displacements (Δx and Δy) as computed by the earthquake model.

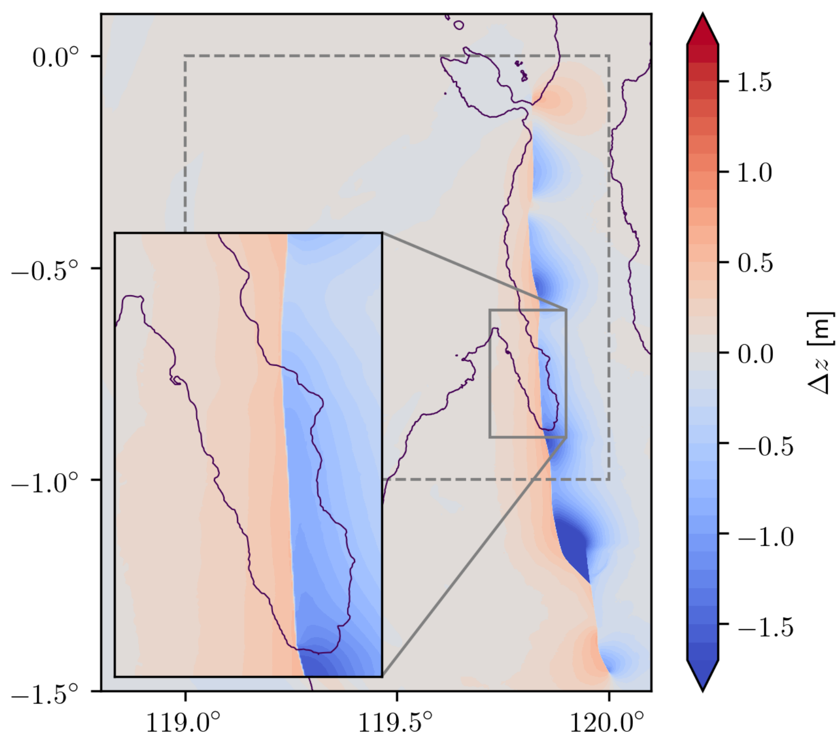

Figure 3.A.7: Final vertical surface displacements (Δz) as computed by the earthquake model.

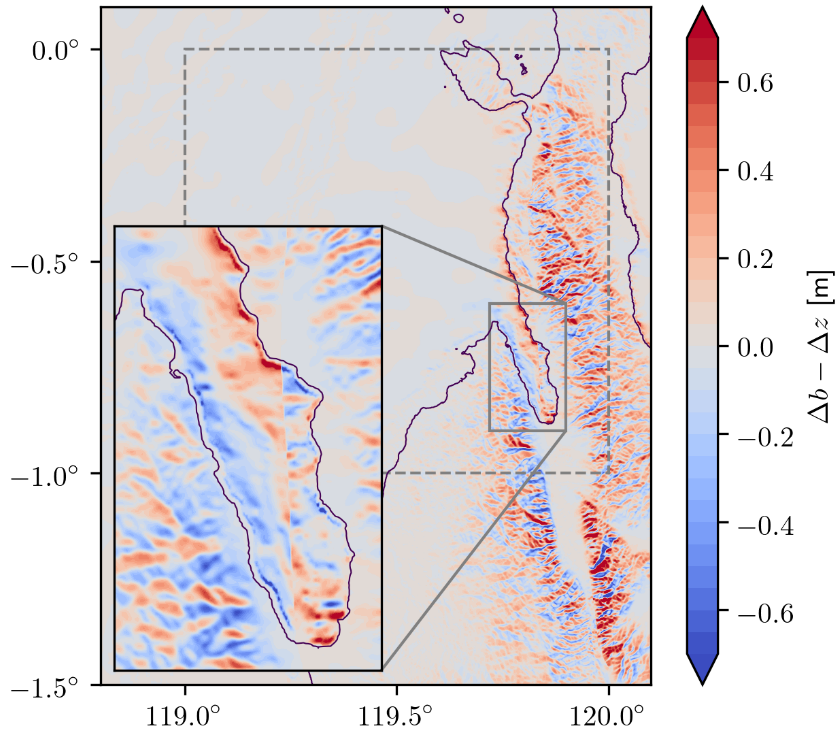

Figure 3.A.8: The contribution $\Delta b - \Delta z$ of horizontal displacements to the final bathymetry perturbation, following Tanioka and Satake (1996).

of Tanioka and Satake by using Eq. (3.1) the displacements are transformed into the bathymetry perturbation Δb (Fig. 3.10). The difference between Δz and Δb locally is up to 0.6 m, as shown in Fig. 3.A.8. Although this difference is quite large, and compared to the overall magnitude more than 30%, it is only very local.

We have run the same tsunami scenario but with the computed seafloor displacement Δz as tsunami source. Snapshots of this scenario in Palu Bay can be seen in Fig. 3.A.9. Such new scenario differs from the original scenario only by local effects (Fig. 3.12), especially at points along the coast. The maximum inundation depths at Palu city are mapped for this alternative scenario in Fig. 3.A.10. Again, only minor differences appear (compare with Fig. 3.16). This illustrates that the method by Tanioka and Satake (1996) might be important to capture some local effects of the tsunami, but is not crucial for the general result, which is also confirmed by other studies (Heidarzadeh et al, 2019).

3.A.6 Along-track SAR measurements

We here describe measurements of the final coseismic surface displacements in along-track direction from SAR images acquired by the Japan Aerospace Exploration Agency (JAXA)

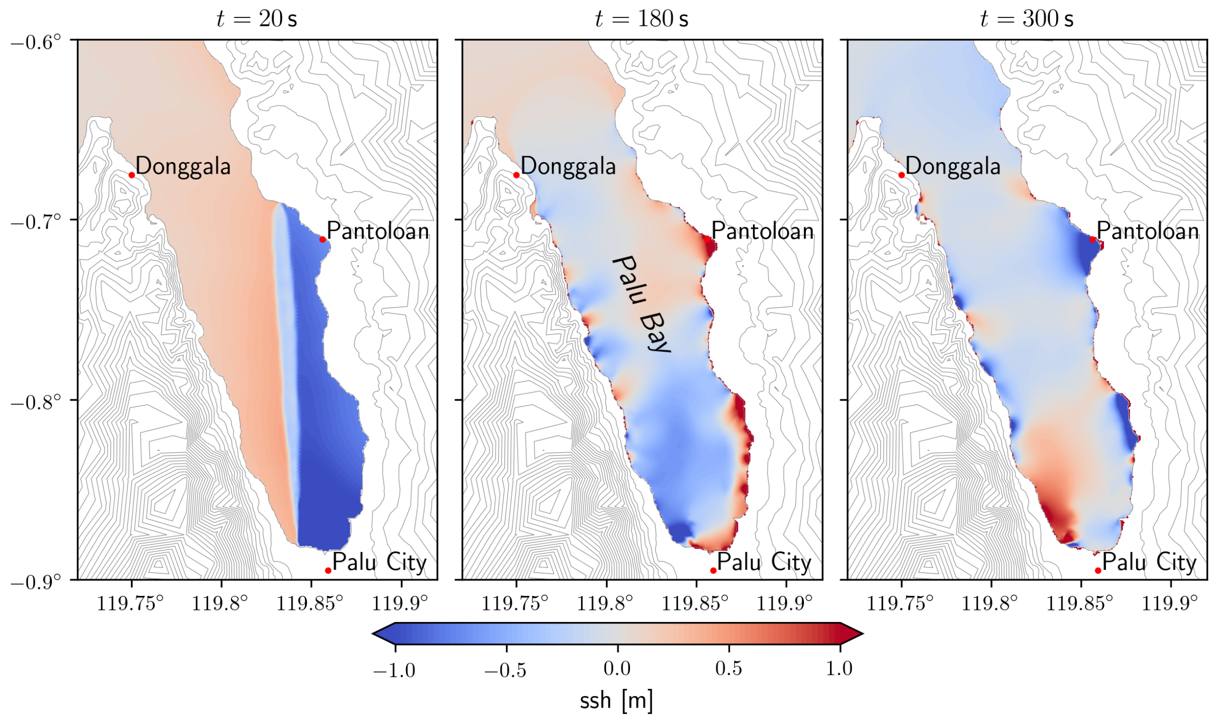

Figure 3.A.9: Snapshots at 20 s, 180 s, and 300 s of the tsunami scenario using only the vertical displacement Δz from the rupture simulation as the source for the tsunami model.

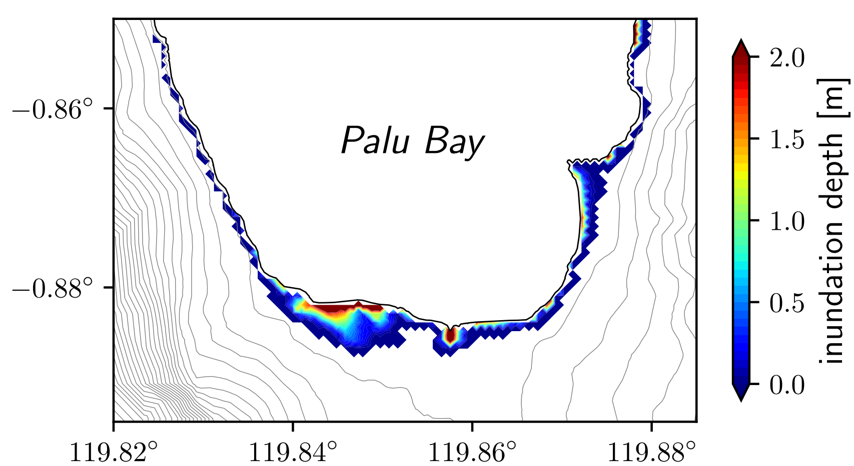

Figure 3.A.10: Computed maximum inundation at Palu City using only the vertical displacement Δz from the rupture simulation as the source for the tsunami model.

Advanced Land Observation Satellite-2 (ALOS-2) SAR. We measure along-track pixel offsets incoherent cross correlation of ALOS-2 stripmap SAR images acquired along ascending path 126 on 2018/08/17 and 2018/10/12 and ascending path 127 on 2018/08/08 and 2018/10/03. We used modules of the InSAR Scientific Computing Environment (ISCE) (Liang and Fielding, 2017; Rosen et al, 2012) for ALOS-2 SAR data processing.

3.A.7 3D subsurface structure

3D heterogeneous media are included in the earthquake model by combining the local model of Awaliah et al (2018), which is built from ambient noise tomography and covers the model domain down to 40 km depth and the Collaborative Seismic Earth Model (Fichtner et al, 2018), which covers the model domain down to 150 km. 3.A.11 shows a few cross-sections of the 3D subsurface structure of Awaliah et al (2018). As this model only defines V_s, we compute the P-wave speed V_p assuming a Poisson's ratio of 0.25.

$$V_p = V_s \sqrt(3) \tag{3.4}$$

The density ρ is calculated using an empirical relationship (Aochi et al, 2017, and references therein).

$$\rho = -0.0000045 V_s^2 + 0.432 V_s + 1711 \tag{3.5}$$

3.A.8 Model validation with teleseismic data

The teleseismic data used in the manuscript for validation of the earthquake model were downloaded from IRIS using Obspy (Beyreuther et al, 2010). The instrument response is removed using the remove_response function of Obspy. Waveform fits are estimated by computing a relative root-mean-square misfit given by:

$$rRMS = (1/RMS_{obs}) \sqrt{\int_{t_0}^{t_1} (d_{syn}(t) - d_{obs}(t))^2 dt} \tag{3.6}$$

where d_{syn} and d_{obs} are respectively the synthetic and observed displacement waveforms, t_0 and t_1 define the interval over which the misfit is calculated (here we use the same range as the range that we plot in Fig. 3.4a and b) and RMS_{obs} is given by:

$$RMS_{obs} = \sqrt{\int_{t_0}^{t_1} d_{obs}(t)^2 dt} \tag{3.7}$$

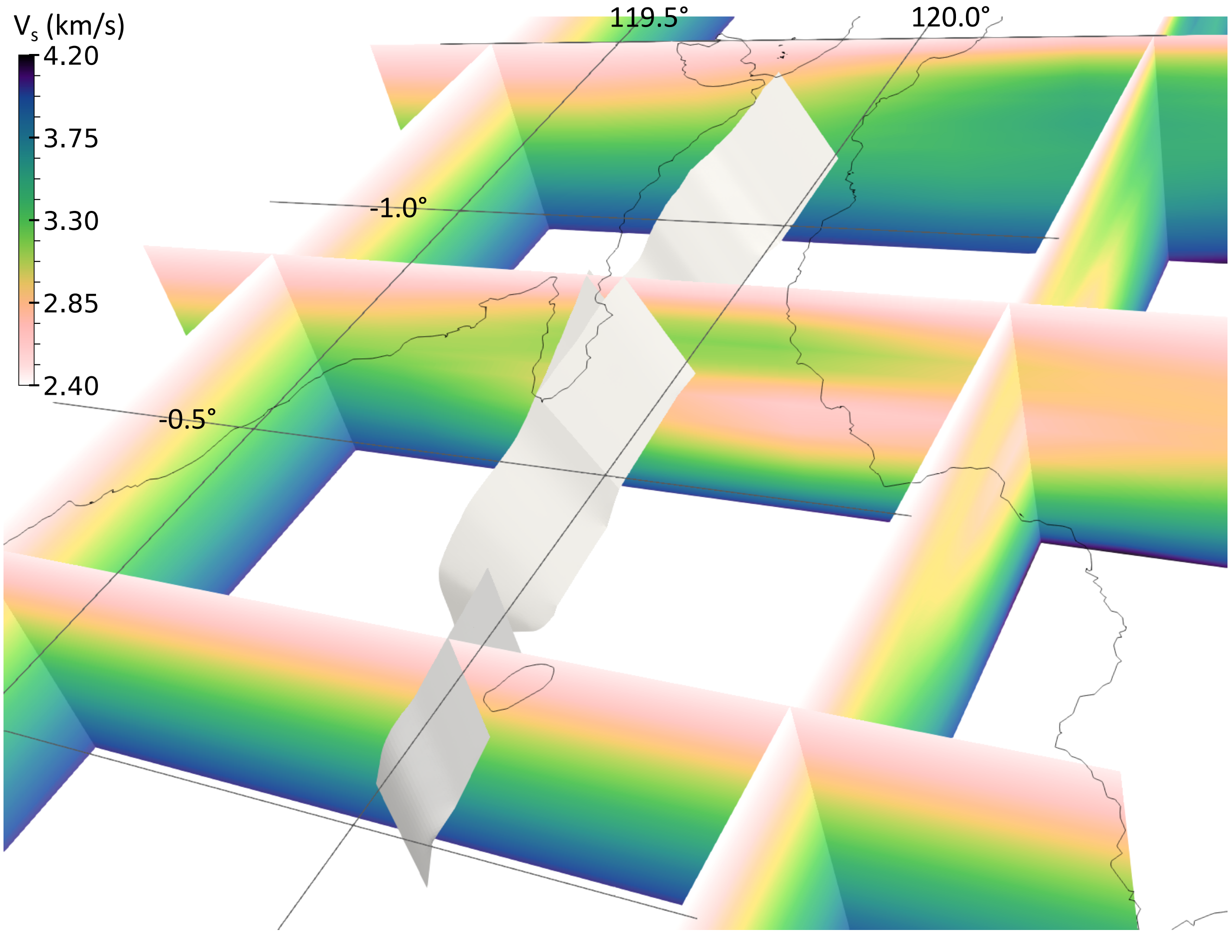

Figure 3.A.11: S-wave speeds (V_s) on five cross-sections of the 3D subsurface structure of Awaliah et al (2018), incorporated into the model.

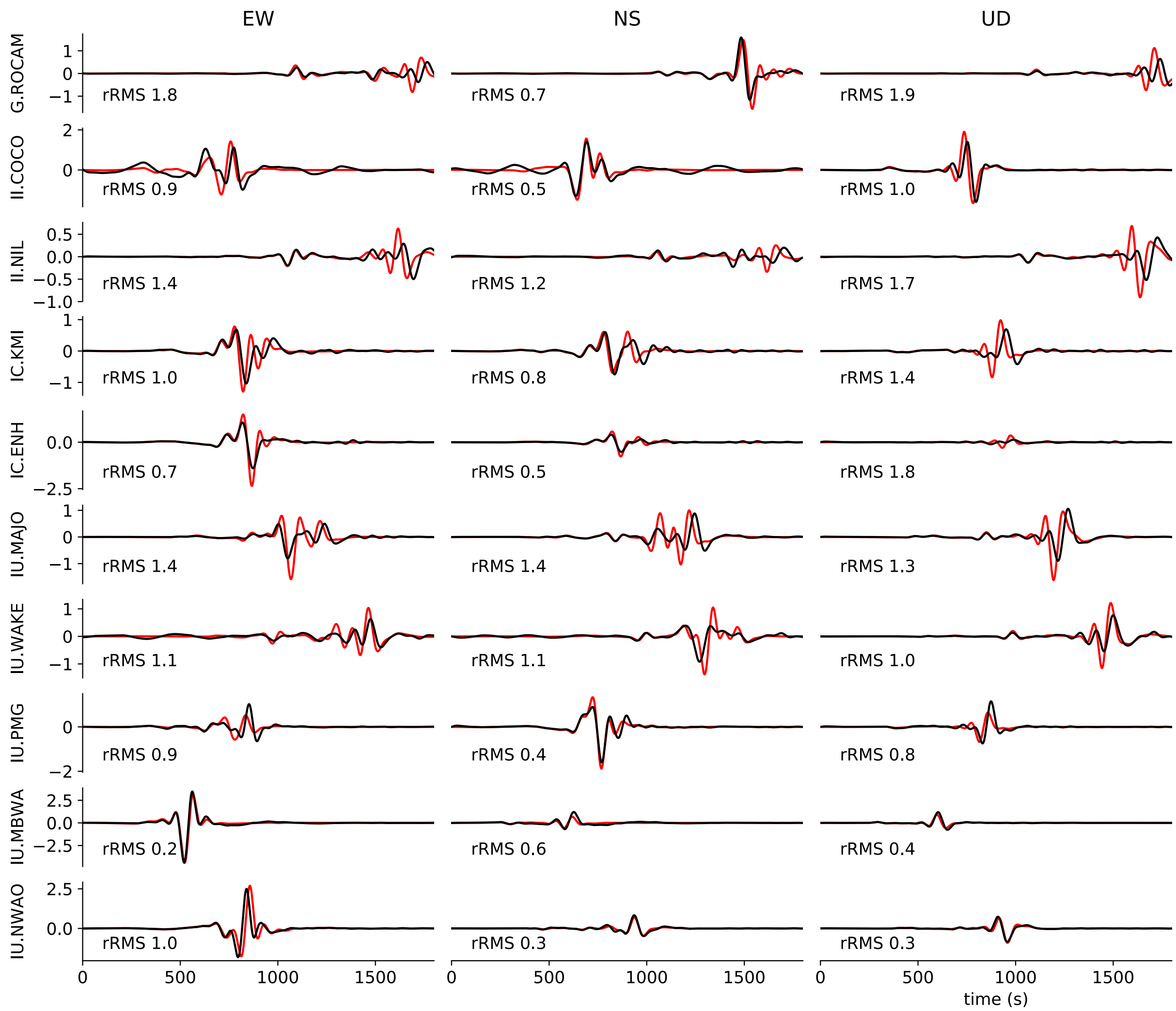

Figure 3.A.12: Comparison of modeled (red) and observed (black) teleseismic displacement waveforms at the 10 stations identified by blue triangles in Fig. 3.5. Full seismograms are dominated by surface waves. For more information, please refer to the caption of Fig. 3.4.

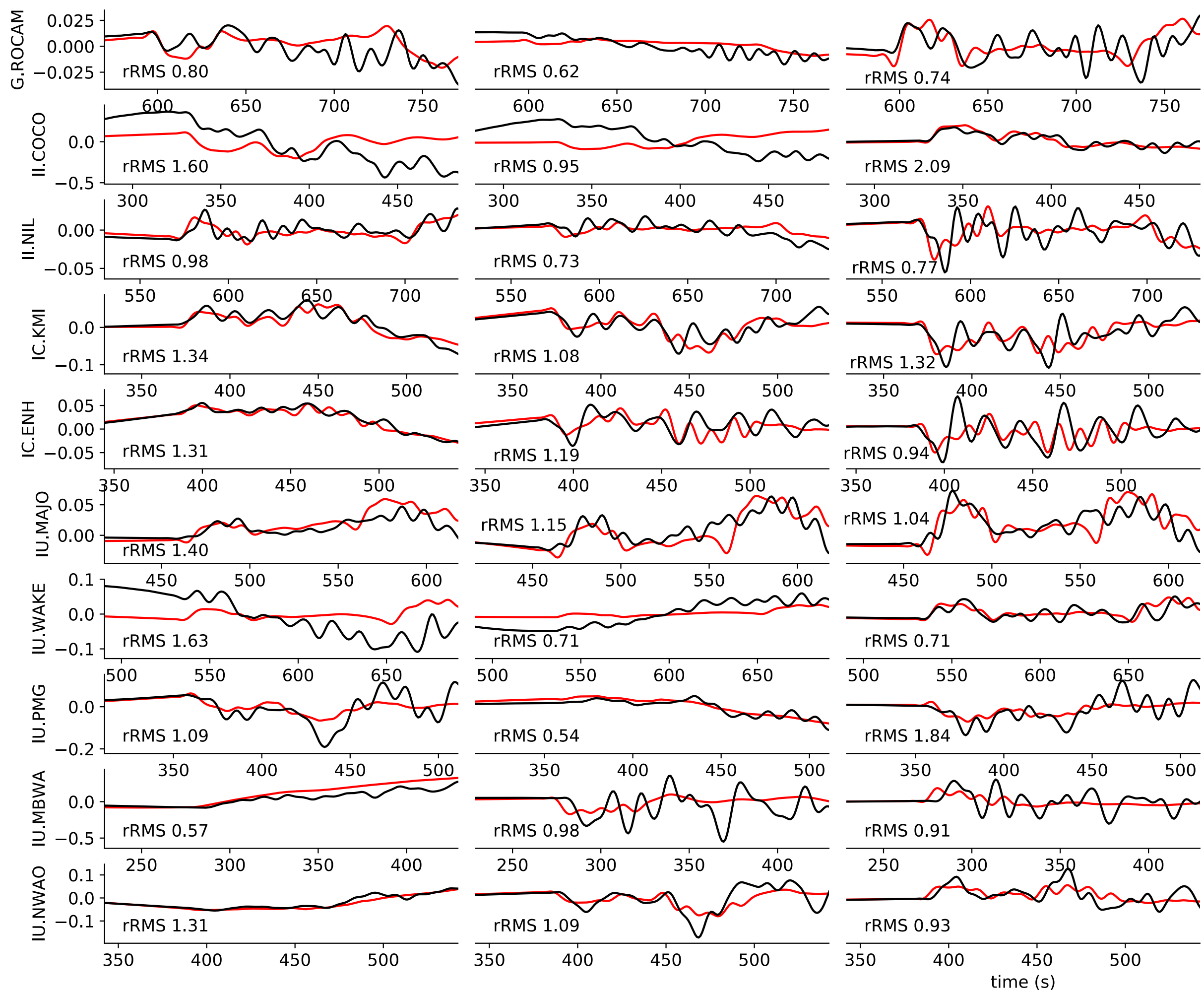

Figure 3.A.13: Comparison of modeled (red) and observed (black) teleseismic displacement waveforms at the 10 stations identified by blue triangles in Fig. 3.5. Zoom in to body wave arrivals. For more information, please refer to the caption of Fig. 3.4.

3.A.9 Reliability of the BATNAS data set in Palu Bay nearshore areas

BATNAS (v1.0) (DEMNAS, 2018) is to our knowledge the highest resolution data set describing the pre-event bathymetry in the area of interest, with a horizontal resolution of approximately 190 m. This allows for sufficiently accurate representation of bathymetric features. However, the resolution is relatively inaccurate with respect to inundation treatment. High resolution (8 m) topography (but not bathymetry) is available from DEMNAS ((DEMNAS, 2018)). Thus, DEMNAS topography and BATNAS bathymetry could be used conjointly in an effort to improve the local resolution of the modeled inundation. Nevertheless, merging the two data sets is a non-trivial task. To analyze whether this is necessary to support the conclusions of this paper, we here provide a quantitative analysis.

We randomly pick 8 profiles crossing the Bay (Figs. 3.A.14, 3.A.15) along which we compare BATNAS and DEMNAS data. Within the range of the observed inundation elevation (0-10 m), we observe that BATNAS captures slopes rather realistically (e.g., profiles 2, 4, 8), especially if topography is smooth. At specific locations, however, the topography is clearly smoothed by the BATNAS data set (e.g. profiles 1, 6, 7) and local biases can be expected.

We conclude that the amplitude variation of inundation synthetics around the bay based on BATNAS data, and the qualitative comparison to observations, is relevant as discussed in the main text (Sec. 3.5.2). Despite limited resolution, the qualitative analysis of inundation behavior across the Bay yields valuable insights on the interplay of tsunami waves and (smoothed) nearshore topography.

3.A.10 Animations

Three animations illustrating the earthquake and tsunami scenario are provided. The animations can be downloaded at https://doi.org/10.5281/zenodo.3233885. The earthquake animations show the absolute slip rate (m/s) across the fault network during the modelled earthquake, with (movie_Sulawesi_wavefield-cp.mov) and without (movie_Sulawesi_SR-cp.mov) the seismic wavefield (absolute particle velocity in m/s). The tsunami animation (SulawesiTanioka.mp4) shows the evolution with time of the sea surface height (m) as predicted by the tsunami scenario.

3.A.11 Code and data availability

For the earthquake modeling we use the open-source software SeisSol (master branch, version tag 201905_Palu), which is available on GitHub (www.github.com/seissol/seissol). The procedure to download, compile, and run the code is described in the documentation (https://seissol.readthedocs.io). All data required to reproduce the earthquake scenario can be downloaded from https://zenodo.org/record/3234664. We use the following projection: DGN95 / Indonesia TM-3 zone 51.1 (EPSG:23839).

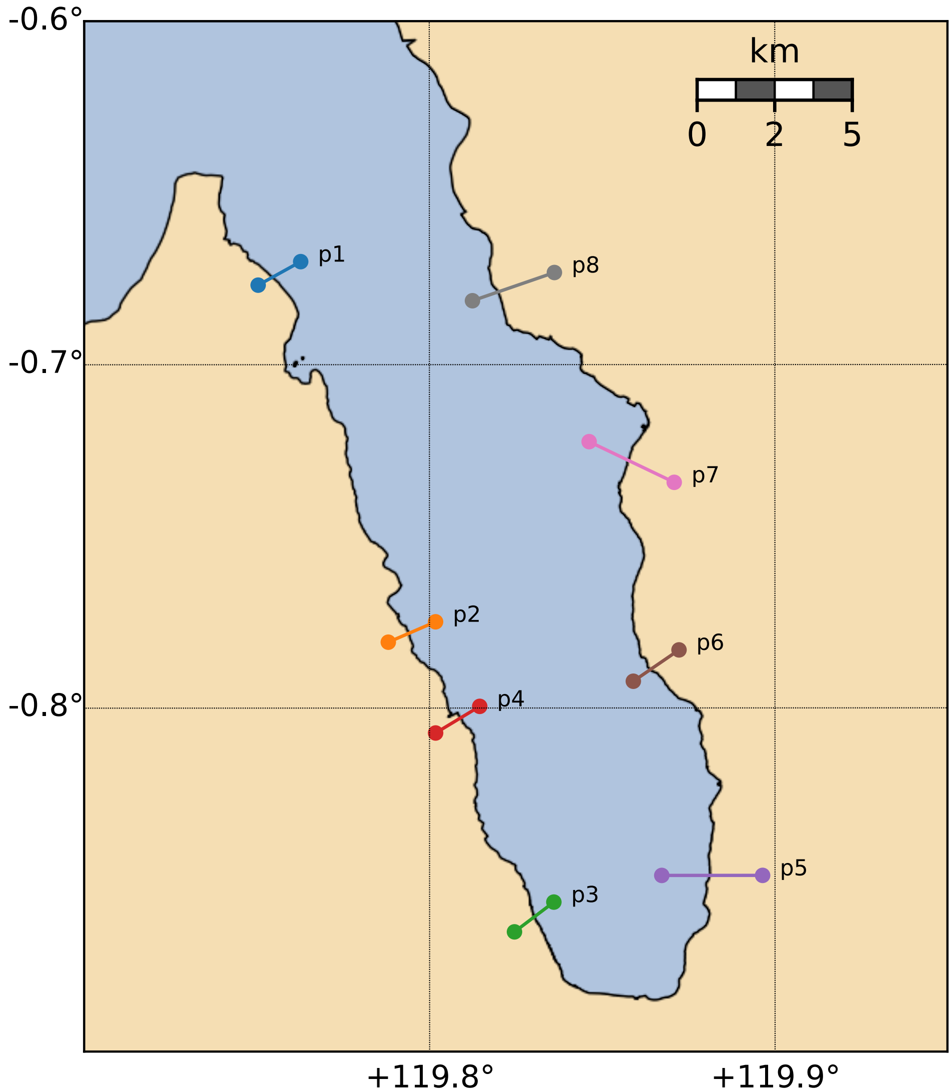

Figure 3.A.14: Locations of 8 sections across the shoreline across which the topography of the 8 m resolution DEMNAS data set and the 190 m sampled BATNAS bathymetry and topography data set are compared in Fig. 3.A.15.

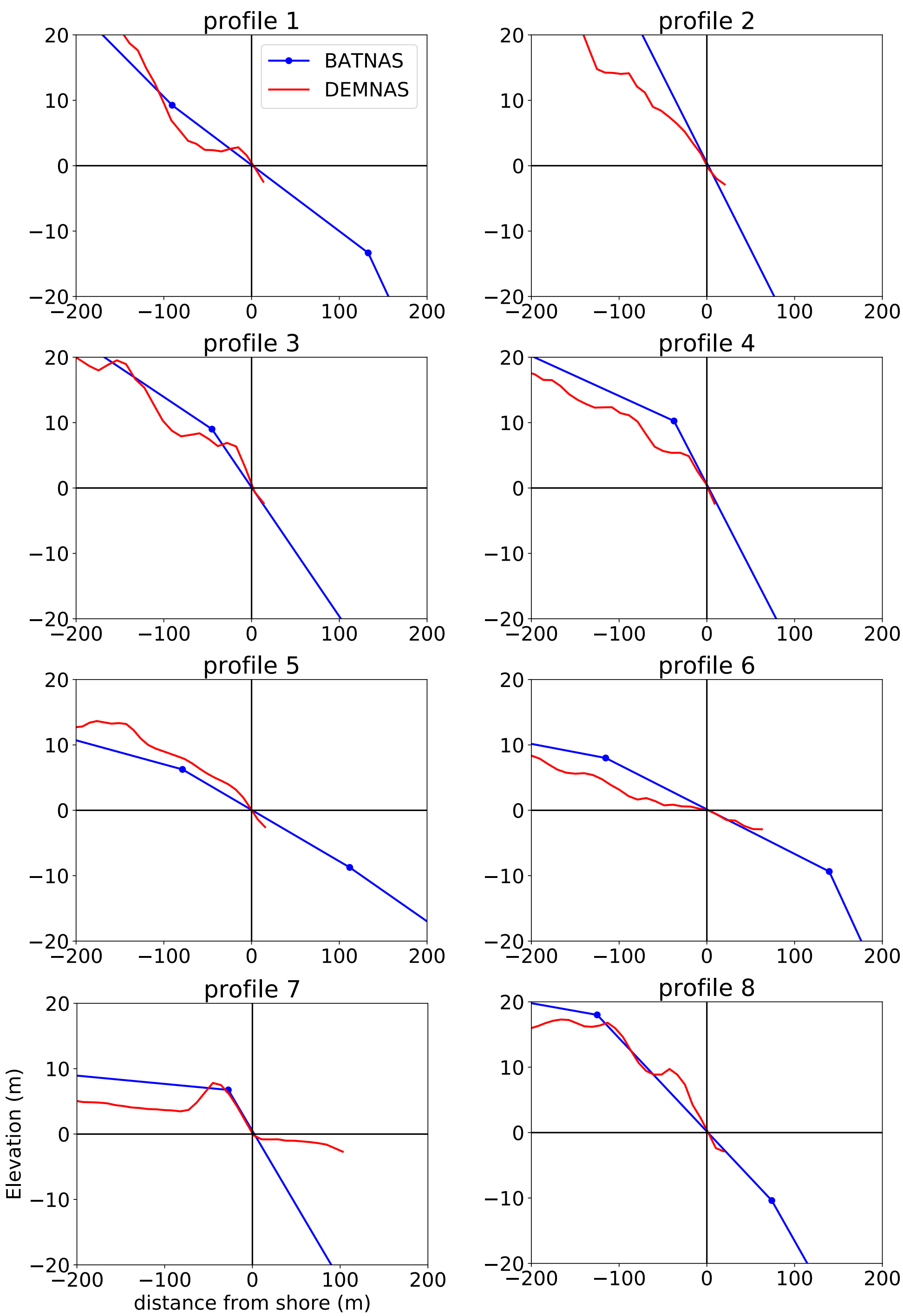

Figure 3.A.15: Topography and bathymetry profiles of BATNAS and DEMNAS data sets across the 8 sections of Fig. 3.A.14. Profiles are aligned with respect to the shoreline to facilitate comparison.

4

Trench sediments, regional stresses and tectonic convergence rates control rupture dynamics, kinematics and tsunamigenesis of the 2004 Sumatra-Andaman megathrust earthquake

4.1 Abstract

The 2004 M_w 9.1 - 9.3 Sumatra-Andaman earthquake and subsequent Indian Ocean tsunami began a new era of geophysical studies into the complex source characteristics and tsunami potential of large megathrust earthquakes. The sheer dimensions of the earthquake and sparse and asymmetric instrumental coverage challenge data-driven analyses of this event. Here we demonstrate that 3D dynamic rupture modeling of megathrust earthquakes and tsunami genesis is now feasible and is critical to understanding the interplay of subduction mechanics, megathrust earthquakes and tsunami genesis, particularly when observations are sparse. We i) develop a stringent framework to constrain initial stress and strength based on observations ii) identify controlling mechanisms of the event's unexpected kinematics and dynamics iii) study the effect of dynamic 3D on- and off-fault deformation on tsunami genesis. The dynamic rupture scenario we develop incorporates a 3D structural model of the subduction region, bathymetry and topography combined with observational inferred regional tectonic stresses, rigidity, frictional strength, fluid pressure and convergence rates. It captures key observed characteristics, including the moment magnitude release, mechanism,

rupture duration, teleseismic waveforms and ground displacements. Our scenario suggests that along-depth variation of trench sediments, including off-fault plastic yielding, as well as along-arc variations of regional stresses and tectonic convergence rates are the dominant factors controlling the event's dynamics and kinematics. Depending on the intensity of the plastic wedge failure, the earthquake may have produced a narrow band of shallow and large slip. This would have translated into localized high ground displacement, invisible to teleseismic and near-field geodetic measurements, but able to modulate locally the tsunami.

4.2 Introduction

The 2004 M_w 9.1-9.3 Sumatra-Andaman earthquake, which ruptured 1300-1500 km of the Sunda trench for 8-10 minutes is one of the largest and most devastating earthquakes recorded. It triggered a large tsunami which in conjunction with the vulnerability and unpreparedness of the affected population lead to a dramatic death toll of more than 227 000 fatalities in 14 countries.

The unexpectedly large moment magnitude of the 2004 Sumatra-Andaman earthquake challenged the established concepts of convergence rate and age of the oceanic lithosphere controlling the largest earthquake size observed on subduction interfaces (e.g. Ruff and Kanamori, 1980). Before the 2004 event, large megathrust earthquakes were assumed to occur preferably on young oceanic lithosphere, while the Indian plate is middle-aged (50 to 70 million years, Müller et al, 1997). Old oceanic crust, being colder and therefore denser, is expected to sink abruptly into the mantle, because of large slab pull effects.This could potentially lead to weak coupling. Younger, more buoyant oceanic crust subducts at a lower angle and is therefore expected to build-up stresses across larger seismogenic areas (Rikitake, 1976; Uyeda and Kanamori, 1979). Fast plunging oceanic lithosphere promotes large megathrust earthquakes, the along-depth width of the locked area being controlled by the rate at which cold material is subducted in concurrence with the rate at which subduction heats up. The Indian plate, however, is characterized by relatively slow convergence rates, estimated to be less than 20 mm/year in the Northern Andaman section (Curray, 2005) in comparison to the 50 mm/year estimated offshore Sumatra (Curray, 2005) and the 85 mm/year inferred at the Japan trench (e.g. DeMets et al, 2010). In line with such empirical expectations, historical records across the Andaman trench report only thrust earthquakes of magnitude less than 7.9 (in 1847, 1881 and 1941, Bilham et al, 2005, and Fig. 4.1) until the 2004 earthquake occurred.

The oblique convergence of the Indian-Australian and Eurasian plates gives rise to highly complex regional tectonics, especially in the overriding continental crust due to fault-partitioning (e.g. Platt, 1993) between the Sunda trench, which accommodates most of trench-parallel motions and multiple faults within the overriding plate accommodating most of the trench-parallel motions (e.g. Curray, 2005; McCaffrey, 2009). The subducting Indian-Australian plate is composed of two separate plates bounded by a deforming region around the Ninety East Ridge (DeMets et al, 1994). The pronounced along-strike variation of megathrust geometry combined with a significant component of northward motion of the oceanic plate lead to increasingly oblique convergence (Curray, 2005) to the North.

Data-driven earthquake analysis for this event is challenged by sparse and asymmetric seismic and geodetic instrumental coverage (e.g., Jade et al, 2005). Static or kinematic inversion of seismic and/or geodetic data (e.g. Ammon et al, 2005; Chlieh et al, 2007; Rhie et al, 2007) were complemented by less conventional data inferences, including normal modes (Stein and Okal, 2005), multiple centroid moment tensors (CMT, Tsai et al, 2005), gravity (e.g. de Linage et al, 2009), tsunami (e.g. Fujii and Satake, 2007) or hydroacoustic waves (e.g. de Groot-Hedlin, 2005) and seismic arrays (Ishii et al, 2005). The such inferred earthquake source models of the event (Shearer and Bürgmann, 2010, and references herein) exhibit a large kinematic and macrosocopic variability, including variations of the seismic moment by a factor 2 (M_{w} 9.1-9.3, Shearer and Bürgmann, 2010).

The co-seismically generated tsunami was up to 30 m high along the northern coast of Sumatra. The shallow subduction interface and the height of the tsunami may suggest that slip did occur on additional faults above the megathrust, dipping at much higher angles (e.g., Sibuet et al, 2007; DeDontney and Rice, 2012; Waldhauser et al, 2012).

Physics-based dynamic-rupture modeling have proven to be insightful for studying complex and/or poorly instrumented crustal earthquakes (e.g., Olsen et al, 1997; Douilly et al, 2015; Kyriakopoulos et al, 2017; Wollherr et al, 2019; Ulrich et al, 2019a,b).

However, computational models able to account for the curved thrust interface, splay-fault networks and intersecting bathymetry, the narrow accretionary wegde and complex lithological structures of subduction are rare. Additionally challenging are off-fault yielding processes which can significantly modulate fault slip near the trench (e.g. Ma, 2012; Ma and Nie, 2019). These challenges are overcome by the SeisSol software package, that couples highly accurate seismic wave propagation with geometrically complex frictional fault failure and off-fault inelasticity and is optimized for high-performance computing (e.g. Breuer et al, 2014; Heinecke et al, 2014; Uphoff et al, 2017).

In contrast to a kinematic (non-unique, e.g., Mai et al, 2016) fitting of observations with a large number of free parameters, here, mechanical viability is ensured by modeling the physical processes that govern the way faults yield and slide. In the following, we present a dynamic rupture scenario tightly constrained by observations. It allows inferences on tectonic, mechanical and geometric controlling factors of megathrust earthquake dynamics and kinematics as well as tsunamigenesis.

4.3 Modeling Ingredients

4.3.1 Regional lithological structure

We build a 3D velocity model of the Sumatra-Andaman region (see also Sect. 4.A.2) incorporating explicitly the subduction interface, the large-scale thickness variations of the crust (Laske et al, 2013) and topography and bathymetry data (Weatherall et al, 2015). Such a model is motivated by the lack of large-scale crustal tomographic data of the region, and because 1D layered velocity models cannot capture the strong spatial variations of

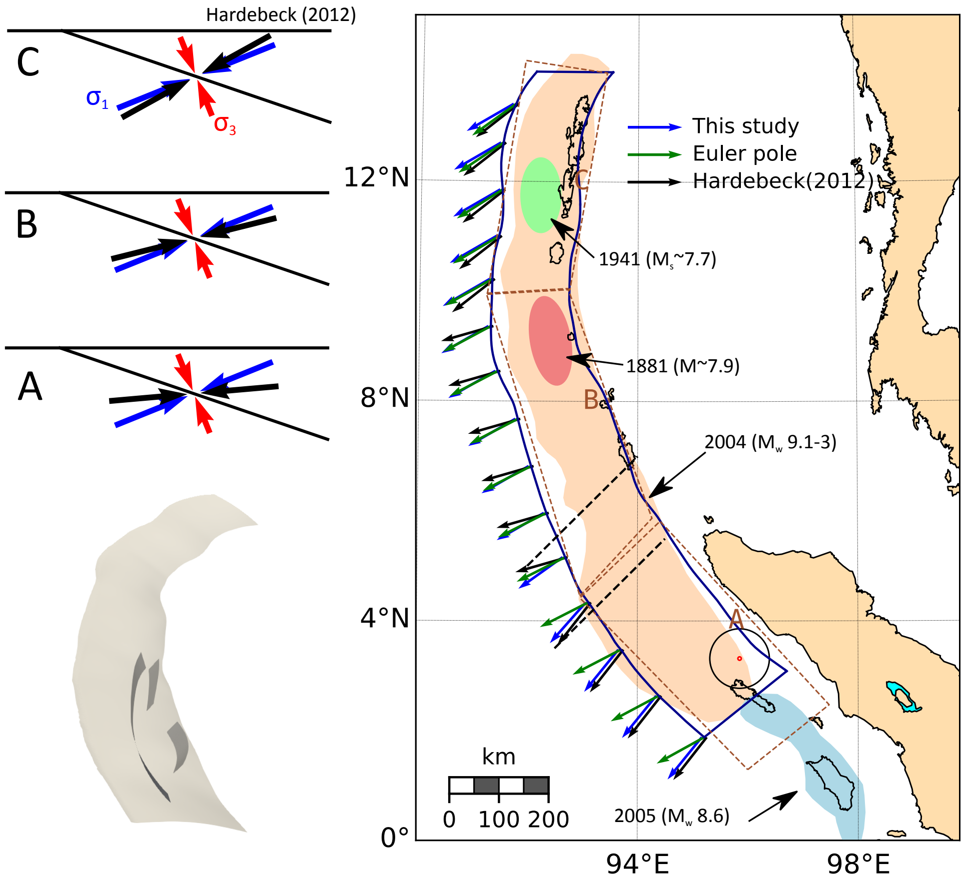

Figure 4.1: Tectonic setting and stress state of the Sumatra subduction zone. The filled shapes indicate past earthquakes and their magnitudes adapted from McCaffrey (2009) (Their Fig. 10). The dashed brown polygons indicate the locations of the 3 regions (A, B and C) over which stress parameters are inverted in Hardebeck (2012). The arrows compare the trend of σ_1, the largest principal stress, used in the scenario of this study (blue), to the trend inferred from tectonic considerations, using the Euler pole inferred by Gahalaut and Gahalaut (2007) (green) and to the stress inversion of Hardebeck (2012) (black). The cross-sections on the right hand-side illustrate the plunge of the maximum (blue, σ_1) and minimum (red, σ_3) principal stresses used in the scenario of this study, compared to the plunge of σ_1 inferred by Hardebeck (2012) (black). The dashes black lines delimit the area where the trend of σ_1 increases from 309 to 330 in our models. The red and black circles are circles centered at the hypocenter of radius 3.5 and 60 km. The slip weakening distance D_c increases linearly from 0.2 to 2.5 m in between these 2 circles. A 3D view of the fault network modeled is displayed on the bottom-left corner of the figure.

material properties expected around a subduction interface.

Our model incorporates strong along-depth rigidity variations in the vicinity of the megathrust interface, as inferred by Bilek and Lay (1999) and Lay et al (2012) from earthquake source duration. In our model, the rigidity along the megathrust increases by a factor 4 along depth, from 10 to 43 MPa. Such a model, therefore, accounts for soft rocks at shallow depth, which consist of both materials scraped off the oceanic crust and younger deposits.

4.3.2 Fault geometry

We construct a non-planar model (see Fig.4.1) of the subduction interface and of some of the splay faults that may have ruptured during the 2004 earthquake (e.g., Sibuet et al, 2007; DeDontney and Rice, 2012; Waldhauser et al, 2012, see also Sect. 4.A.3).

We build the slab interface from Slab 1.0 (Hayes et al, 2012), that we extend to the north and to the trench, to cover the full span of the 2004 rupture.

The model also includes 3 potentially activated splay faults dipping 45°, 1 long forethrust (dipping landwards) and 2 backthrust faults (dipping trenchwards), which extend from their inferred trace to the megathrust interface. The forethrust unifies the Upper Splay Fault mapped by Sibuet et al (2007) and the splay fault suggested by DeDontney and Rice (2012). The northern backthrust is mapped by Sibuet et al (2007) and Chauhan et al (2009) along the WG2 seismic line. The southern backthrust is identified by Singh et al (2008) along the WG1 seismic line. The true extents of these faults are not known; mapped lengths are restricted to the area of data coverage. A double peak in the tsunami waves recorded by Jason-1 satellite (DeDontney and Rice, 2012), large tsunami run-ups observed in Aceh province in the near-source region (e.g. Banerjee et al, 2007), high reflectivity in shallow seismic reflection data (Singh et al, 2008), aftershock distribution (Lin et al, 2009; Waldhauser et al, 2012) alongside other observations (e.g., Sibuet et al, 2007) suggest these faults may have rupture coseismically during the 2004 event.

4.3.3 Stress state and fault friction

The stresses acting on faults and their strength, which are key initial conditions of dynamic rupture models, are poorly known. Laboratory friction experiments offer insight about strength parameters, but extrapolating these results to a natural scale is complicated. We here introduce new procedures to constrain these parameters from stress inversion results (Hardebeck, 2012), including the inference of coseismic rotation of the principal stress axes (Hardebeck, 2012, 2015).

Principal stress orientation

We here constrain the principal stress orientations using the stress inversion results of Hardebeck (2012) and geodetic observations. Our pre-stress is non-Andersonian, that is none of the principal stresses are nearly vertical. It features a maximum compressive stress axis σ_1 shallowly plunging, an intermediate stress axis σ_2 near-horizontal and a minimum principal σ_3 stress steeply dipping, in line with Hardebeck (2012)'s results. We use a constant σ_1 plunge of 22 °, allowing optimal stressing of fault dipping 8°.

We try and align stress inversion and geodetic observations in choosing the intermediate principal stress σ_2 orientation. Our model accounts for the inferred rotation of σ_2 (Hardebeck, 2012), which rotates clockwise from 309° in the South to 330° in the North, with a linear transition of the trend over 2° around 5° latitude (see Fig. 4.1). The trend of σ_2 we choose is consistent with rigid plate tectonics models. It is overall normal to the India-Burma plate convergence calculated using the Euler pole inferred by Gahalaut and Gahalaut (2007) (see Fig. 4.1).

Principal stress magnitudes

The principal stress magnitudes are systematically constrained based on seismo-tectonic observations, fault fluid pressurization and the Mohr-Coulomb theory of frictional failure.

Rupture dynamics are above all governed by the stress drop and the fault strength. These are constrained by the effective confining stress, fault friction drop $\mu_s - \mu_d$ (where μ_s and μ_d are the static and dynamic friction coefficients) and relative prestress ratio R_0, defined by prestress over strength drop on optimally-oriented fault planes (e.g. Aochi and Madariaga, 2003), which are therefore all subject to mutual trade-offs. In the model, we assume lithostatic confining pressure ($\sigma_c = \rho g z$) and a near-lithostatic fluid pressure ($P_f = 0.974\sigma_c$), which ensures a realistic stress drop. The resulting effective confining stress increases with depth by a gradient of about 1 MPa/km. From 25 km depth and over 20 km, we slowly taper the deviatoric stresses to zero, to represent the transition from a brittle to a creeping regime.

Our model accounts for along-arc variations of the initial prestress, related to the along-arc variations in convergence rate. This is in line with Hardebeck (2012)'s observations that the accumulated slip since the last great earthquake inferred using convergence rate along-arc variations is consistent with the observed 2004 mainshock along-arc slip distribution, with more slip in the South than in the North. We modulate the relative prestress ratio R_0 on optimally oriented faults with the convergence rate inferred from rigid plate tectonics considerations, using the Euler pole inferred by Gahalaut and Gahalaut (2007) (see Fig. 4.A.1). Our modulation applies only above 6° North. Our choice of a constant $R_0 = 0.65$ below this latitude, is a proxy for accounting for the effect of internal deformations of the sliver plate to the South and is constrained by the magnitude of the geodetic measurement.

Coseismic stress rotation

The inference of coseismic rotation of the principal stress axes during the 2004 event (Hardebeck, 2012, 2015), allows constraining the ratio of the stress drop over the prestress. A significant principal stress rotation indicates that the stress drop is large enough to change the deviatoric background stress (e.g. Hardebeck and Hauksson, 2001), that is the pre-stress and the stress drop are of the same order.

If we estimate the average stress drop $d\tau$ in the dynamic rupture model by:

$$d\tau \sim (\mu_s - \mu_d) R_0 (\sigma_c - P_f). \tag{4.1}$$

and if we name ξ the ratio of residual stress over pre-stress, we then have:

$$\xi \sim \frac{\mu_d}{(\mu_s - \mu_d) R_0 + \mu_d} \tag{4.2}$$

Which can also be written as:

$$\mu_d \sim \frac{\mu_s}{(1-\xi)/(R_0 \xi) + 1} \tag{4.3}$$

Eq. 4.3 allows relating μ_d to μ_s and R_0. For example assuming $\mu_s = 0.6$ (Byerlee, 1978) $\xi = 0.2$ (value inferred in the northern part of the rupture) and $R_0 = 0.65$, yields $\mu_d = 0.08$, which is a typical value measured at coseismic slip rates (e.g. Di Toro et al, 2011). $\xi = 0.4$ (value inferred in the southern part of the rupture), $R_0 = 0.65$ and $\mu_s = 0.6$ yields $\mu_d = 0.18$.

Fault friction parametrization

Building upon these considerations, we consider a linear slip weakening law, parameterized by $\mu_s = 0.6$ and $\mu_d = 0.2$. We choose a classical linear slip weakening law rather than a strong velocity weakening rate-and-state friction law because this latter yields small rupture process width, because of the strong velocity weakening term, and therefore cannot account for wide rupture process zone, characteristic of large megathrust earthquakes.

Our model features overall a large slip weakening distance ($D_c = 2.5$ m), which reflects the scale dependence of slip pulse width (e.g. Melgar and Hayes, 2017). Nevertheless, we decrease this value around the hypocenter (to 0.2 m), which allows for a smaller and therefore more realistic nucleation area. The transition from a small D_c to a larger D_c is done linearly over 60 km. Such a transition from a small characteristic spatial scale to a larger spatial scale may reflect hierarchical rupture growth (e.g. Okuda and Ide, 2018).

A smooth nucleation process is achieved by artificially reducing the friction coefficient from its static to its dynamic value over 0.5 s within a spherical zone surrounding the hypocenter expending over time, following the procedure suggested by the SCEC dynamic rupture community (Harris et al, 2018). Such a spherical zone yields a final radius of 3.5 km. The model hypocenter is chosen at 30 km depth on the subduction interface, at the shortest distance to the location inferred by USGS (3.316°N, 95.854°E).

4.3.4 Model resolution

The large process zone width characteristic of a megathrust earthquake enable by large slip weakening distance value, combined with the smooth geometry of the subduction interface, only modulated by long-wavelengths features, allows the dynamics of the earthquake scenario to be satisfactorily resolved using a computational model of relatively coarse resolution compared with dynamic rupture models on segmented crustal fault networks (e.g. Ulrich et al, 2019a; Wollherr et al, 2019).

Practically, a 4 million tetrahedral element mesh featuring 2.5 km mesh size on faults and strong mesh coarsening away from the faults, combined with a 4th order accurate numerical scheme yields converged on-fault results and static ground-deformations overall. We ensure that the dynamics are well captured by running higher resolution computational models (1 km mesh size on faults, slower mesh coarsening away from the fault system, yielding 14 million tetrahedral elements, combined with a 5th order accurate numerical scheme). Simulating 900 s on such a 14 million elements mesh typically requires 4 h on 5000 Sandy Bridge cores of the supercomputer SuperMucNG (Leibniz Supercomputing Center, Germany), well within the scope of resources available to typical users of supercomputing centers.

4.4 Model Validation

4.4.1 Earthquake rupture

The dynamic earthquake scenario is characterized by a unilateral northwards rupture (Fig. 4.2). The rupture evolution is overall simple. A steady rupture front over a large depth span gets formed after about 50 s and steadily propagates northwards over 1300 km of the trench. Along-depth rigidity variations of off-fault materials tend to bend the rupture front, which travels faster in the down-dip region than in the shallow sediments (Fig. 4.4c).

The rupture nucleates at depth, at the southern tip of the modeled subduction interface, and propagate upwards and northwards. In the hypocentral region, the subduction interface has a nearly optimal orientation with regards to regional stresses and, therefore, cannot promote the arrest of the southwards propagating rupture. We here assume lower accumulated tectonic stress south from the hypocenter to explain the southwards rupture arrest. To the North, rupture spontaneously arrests as a consequence of the lower accumulated stress there, caused by lower convergence rate.

Our preferred scenario has a moment magnitude $M_w = 9.08$, in the lower range of the inferred magnitude for this event (9.1 to 9.3).

4.4.2 Focal mechanism and moment release rate

The focal mechanism of the modeled source (Fig. 4.3) is compatible with the one inferred by USGS. The nodal plane characterizing this model features strike/dip/rake angles of 340°/14°/109°, which is very close to the 336°/7°/114° focal plane inferred by USGS.

The dynamically released moment rate function of the preferred scenario (Fig 4.4a) resembles the moment rate release of Ammon et al (2005)'s models, inferred from teleseismic data. The rupture gains momentum in the first 100 s until a peak of moment rate release is reached around this time. The moment rate release then steadily decreases from 100 s

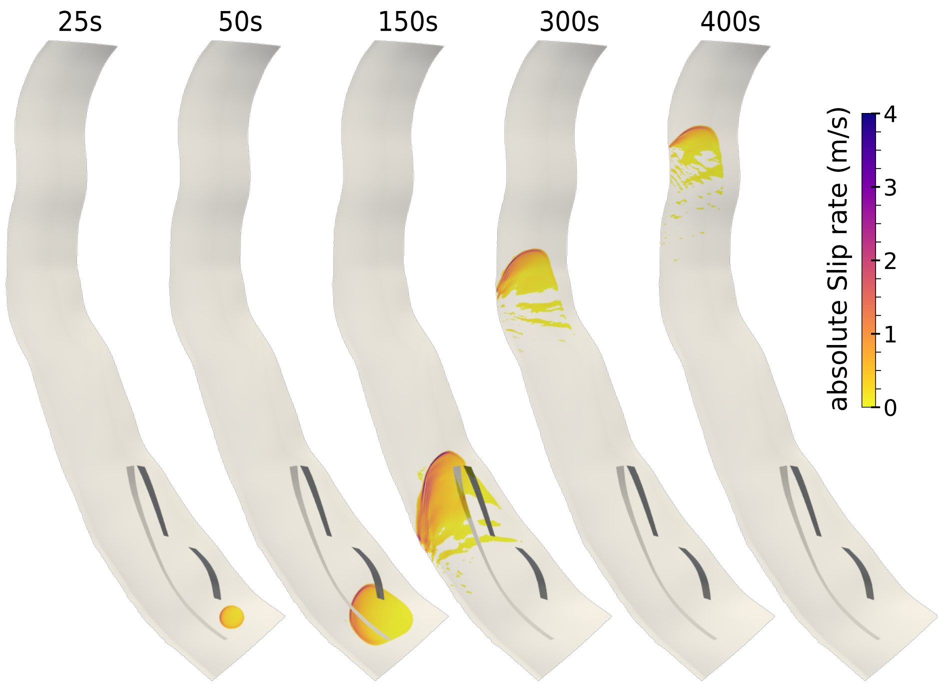

Figure 4.2: Overview of the simulated rupture propagation of the preferred model (m_1). Snapshots of the absolute slip rate are shown at a rupture time of 25, 50, 150, 300 and 400 s.

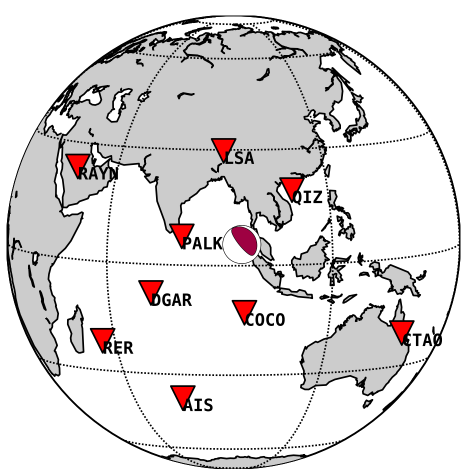

Figure 4.3: Moment-tensor representation of the preferred dynamic rupture scenario and locations at which synthetic data are compared with observed records in Fig. 4.6.

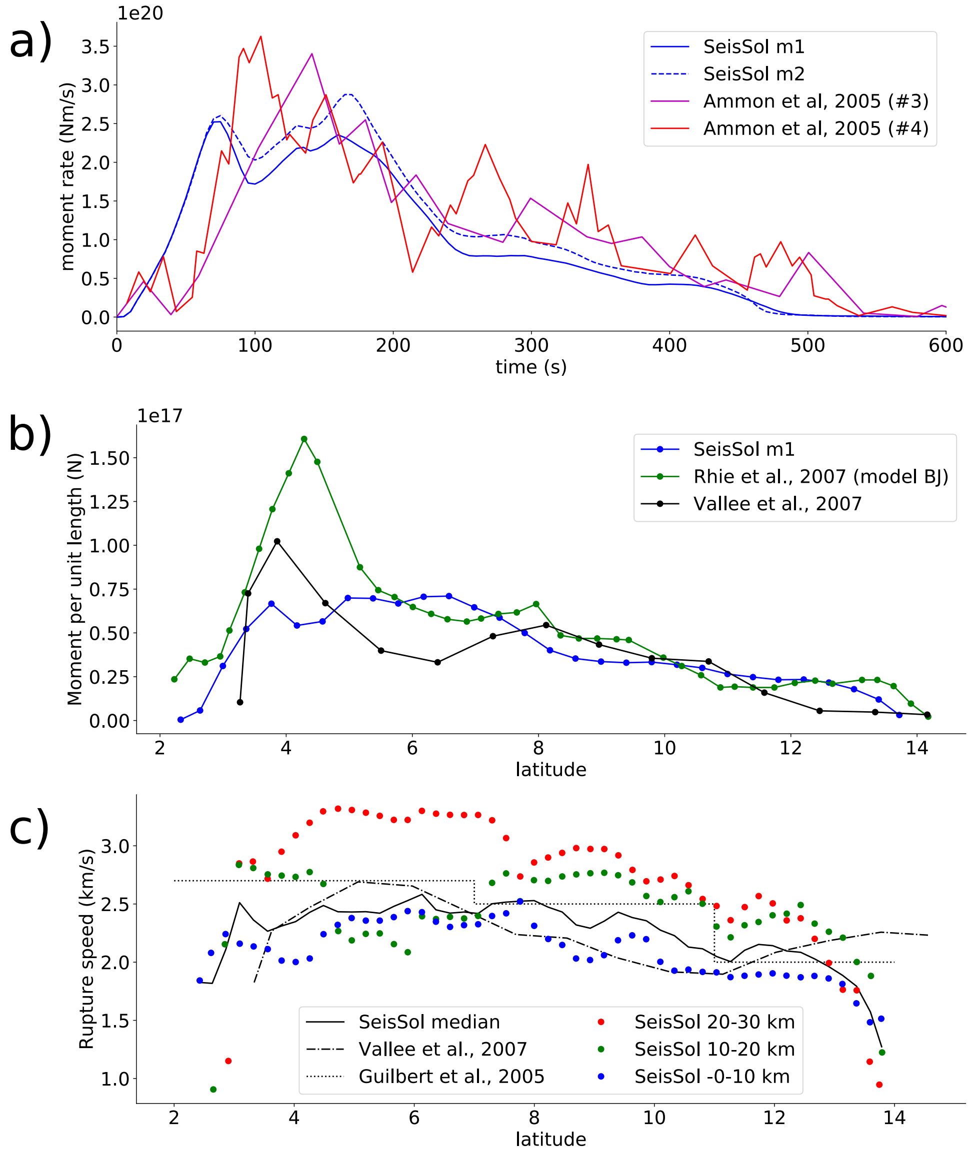

Figure 4.4: a) Synthetic moment rate release functions of the preferred model (m_1) and of an alternative model (m_2) featuring more slip at the trench compared with moment rate release functions observationally inferred from teleseismic data by Ammon et al (2005) b) Synthetic moment rate per unit length compared to Rhie et al (2007)'s inference from a joint inversion of GPS and teleseismic data and to Vallee (2007)'s inference from Rayleigh waves (empirical Green's function method). c) Along arc-variations of the rupture velocity, compared with Vallee (2007)'s inference from Rayleigh waves and Guilbert (2005)'s inference from acoustic data.

to 500 s, until rupture arrest. The triangular shape of Ammon et al (2005)'s inference, including its timing and amplitudes, are captured by the model.

The duration of the simulated rupture (8 min) is in the lower range of the inferred rupture duration for this event (8 to 10 min). This translates to an average rupture velocity of 2.7 km/s. The modeled rupture velocity (Fig. 4.7a) is subshear everywhere. The rupture speed presents strong along-depth variations. The overall average rupture velocity (2.7 km/s) is close to the modeled rupture velocity at depth, suggesting that the rupture at depth is driving the rupture overall (see Fig. 4.4c). Along-arc variations of the rupture speed are less pronounced than in Vallee (2007) and Guilbert (2005)'s inferences.

Fig. 4.4b compares the along-arc variations of the scenario's moment density against inferences of Vallee (2007) from a Rayleigh waves analysis and of Rhie et al (2007) from a joint inversion of GPS and teleseismic data. The decrease of the moment density from 7° latitude Northwards is well captured by the model. A peak of the moment density at about 7° latitude is less obvious in the scenario that in the inferences.

The modeled source appears compatible with the 5 point-sources model of Tsai et al (2005) inverted from teleseismic data. We compare both models by translating the dynamic fault slip time histories of the dynamic rupture scenario into 5 double couple point sources. In that purpose, we partition the rupture area in 5 sections along a North-South axis and compute the equivalent moment tensor of each sections. While the mechanism of each moment tensors are in excellent agreement, the moment released by each source is significantly larger in Tsai et al (2005)'s model, which features an overall moment magnitude of 9.3. The fact that shallow dipping faults radiate less efficiently seismic waves than steeper faults have been suggested to explain the large magnitude inferred by Tsai et al (2005). The dynamic rupture model appears faster than Tsai et al (2005)'s inference, which is in the upper range of the inferred rupture durations.

4.4.3 Teleseismic surface waves

The dynamic rupture scenario is able to reproduce key features of the teleseismic surface waves (Figs. 4.6a). Following Ulrich et al (2019a), we translate the dynamic fault slip time histories of the preferred dynamic rupture scenario into a subset of 50 double couple point sources (25 along strike times 2 along depth) and we generate broadband synthetics from a Green's function database using Instaseis (Krischer et al, 2017) and the PREM model for a maximum period of 10 s and including anisotropic effects. Synthetics are generated at 9 teleseismic stations around the event (Fig. 4.3), ensuring good azimuthal coverage of the event. Globally, the dynamic rupture scenario is able to reproduce the amplitude and to some extent the shape of the observed long-period waveforms. The timing of the largest peak of the observed waves at the frequency considered is well recovered by the synthetics at many stations (e.g. RAYN, DGAR, LSA, PALK), while it is slightly in advance at others (e.g. COCO, AIS). Amplitudes are overall too low compared to observations. This might suggest that the model does not release sufficient energy. In fact, models (e.g. Rhie et al, 2007; Chlieh et al, 2007) published later than the earliest models agree on a slightly larger moment magnitude (about 9.15) than our model. Teleseismic surface waves are best

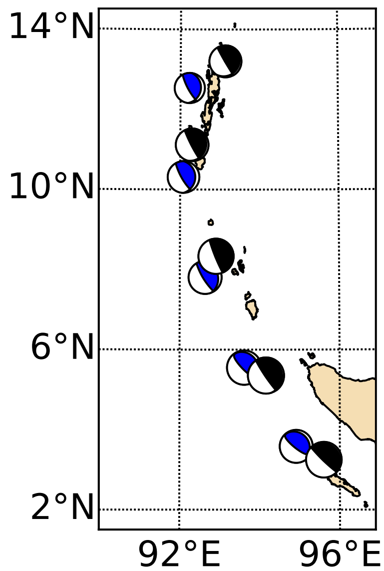

(a)

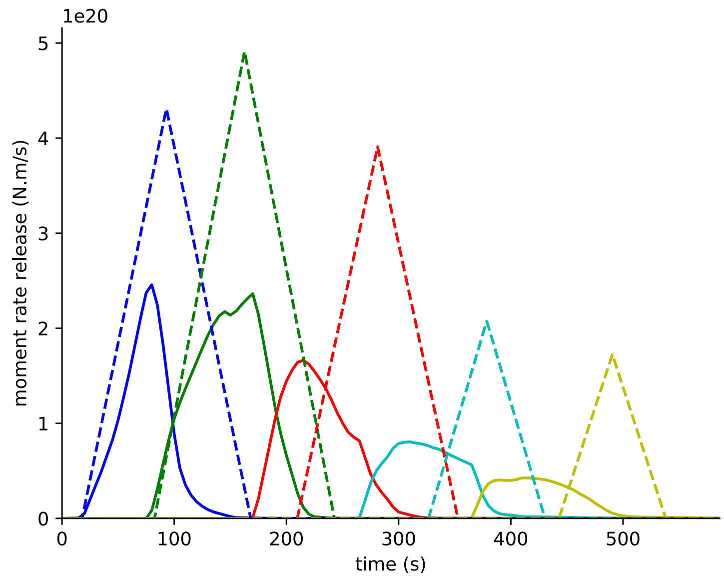

(b)

Figure 4.5: (a) Comparison of a 5 point-sources model derived from the dynamic rupture scenario (blue) with Tsai et al (2005, black) teleseismic inversion. (b) Moment rate release of each point source. Dashed line: Tsai et al (2005), solid line: dynamic rupture scenario.

reproduced at stations PALK, RAYN, and DGAR, which are all west from the rupture area.

4.4.4 Fault slip

The scenario yields a smooth and uniform fault slip distribution (Fig. 4.7c), less patchy than most kinematics models of the event. Slip is modulated along the trench by the non-rupture of some of the flatter portion of the interface at shallow depth, by the along-depth variation in rock shear modulus, and by the along-arc variation of the prestress, reflecting the along-arc variations in convergence rate. Accounting for softer rocks at shallow depth in the models yields larger slip magnitude to the trench. Slip in the southern region is mostly thrusting, while further north increasing oblique faulting is modeled (Fig. 4.7b). This is consistent with the fault geometry and the regional stresses considered. The fault slip distribution of the preferred scenario are in first order agreement with the slip distribution and magnitudes obtained by Rhie et al (2007) from a joint inversion of teleseismic and geodetic data (Fig. 4.7d) and by Chlieh et al (2007) from geodetic data (Fig. 4.7e).

4.4.5 Co-seismic displacements

The preferred scenario is able to explain ground displacements observations to first order (Fig. 4.8 and 4.9). Overall, displacements observed on the forearc sliver plate are accurately

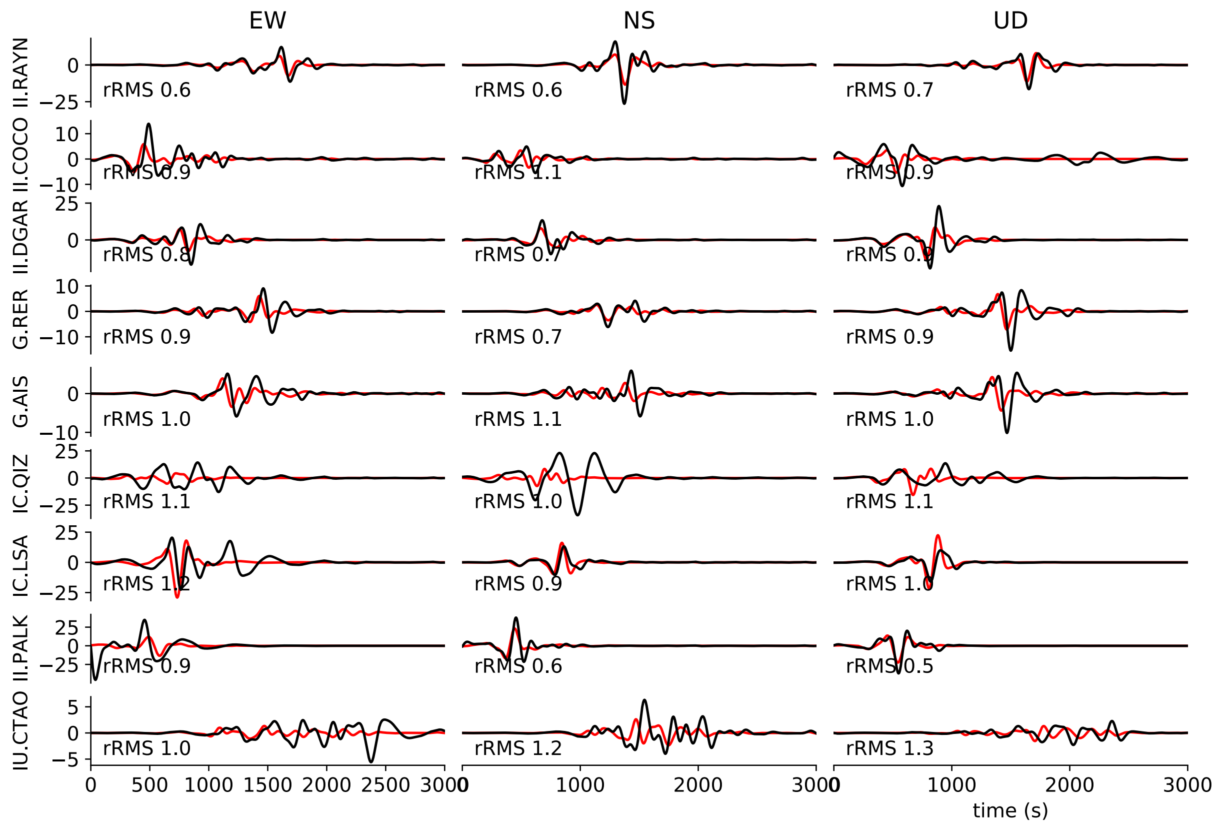

Figure 4.6: Comparison of modeled (red) and observed (black) teleseismic waveforms. A 66-500 s band-pass filter is applied to all traces. Synthetics are generated using Instaseis (Krischer et al, 2017) and the PREM model including anisotropic effects and a maximum period of 10 s.

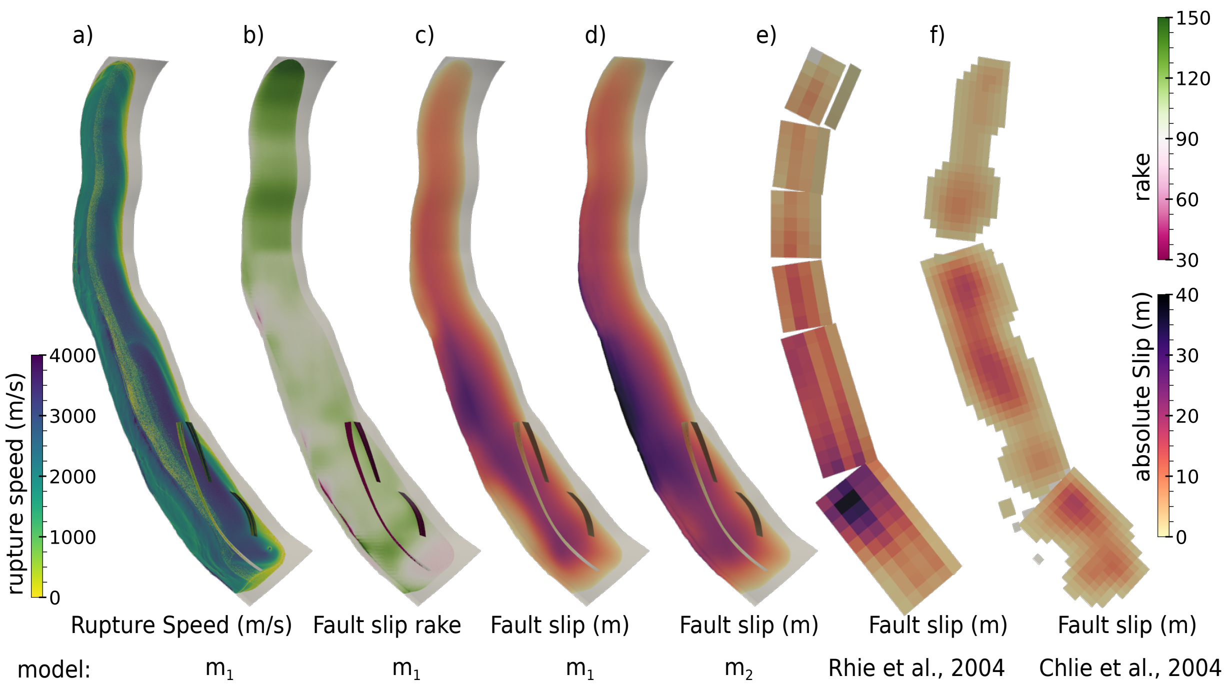

Figure 4.7: Source properties of the dynamic rupture scenario. Comparison with previously published models and with the alternative scenario m_2. (a) Rupture speed. (b) Final rake angle (c) Final slip magnitude (d) Final slip magnitude of the alternative model m_2, featuring more slip at the trench (e) Final slip magnitude of Rhie et al (2007)'s model (f) Final slip magnitude of Chlieh et al (2007)'s model.

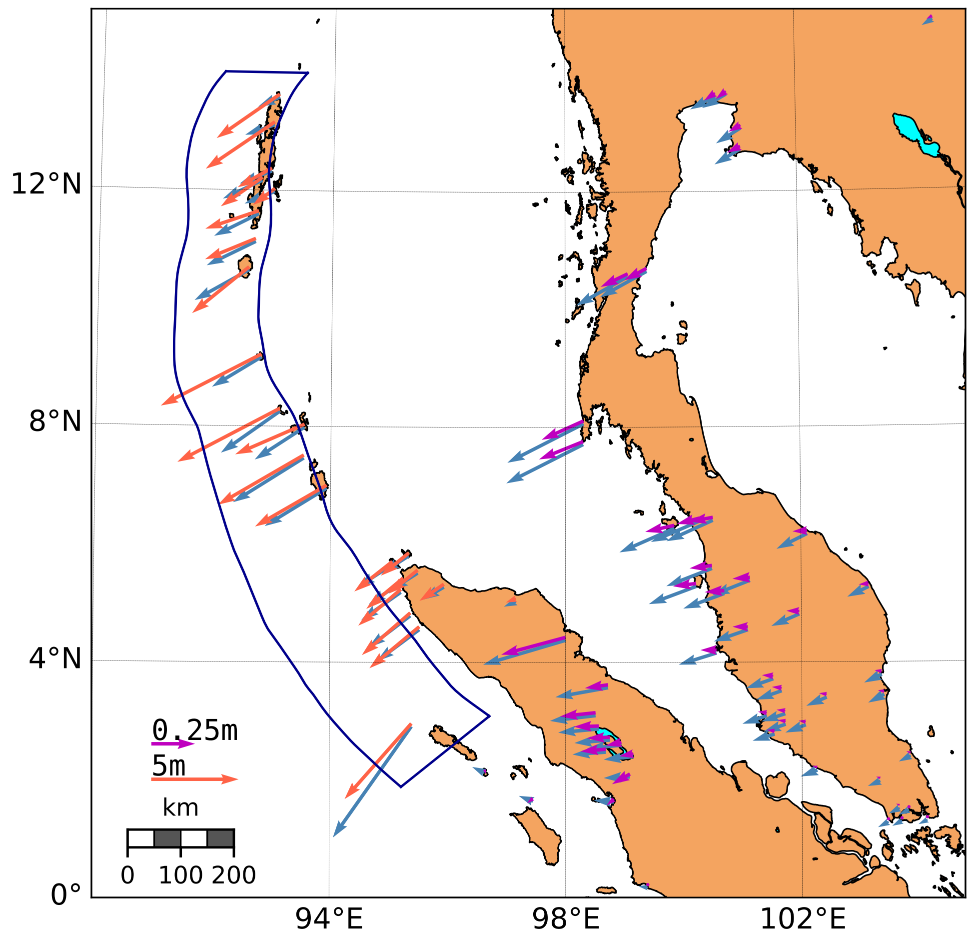

Figure 4.8: Comparison between synthetic horizontal ground displacements (blue) and geodetic observations (orange and magenta). A different scaling is applied to highlight smaller-scale distant ground displacements.

reproduced, while the (small) displacements observed in the far-field are overshot. The orientation and magnitude of the horizontal displacements are well recovered on most of the back-arc but are too small above 12° latitude, in the North of Andaman islands. This resembles Rhie et al (2007)'s model, suggesting that teleseismics and geodetic displacements cannot be reconciled there. The magnitude of the horizontal displacements is also under-predicted at two locations around 8° latitude. The vertical displacements are in overall agreement on the forearc but show fewer variations than observed to the North. The uplift over Andaman islands is especially not captured. Over Sumatra and Northern Thailand, the horizontal displacements are well oriented but of too large magnitude, while over Southern Thailand, both magnitude and orientations are off. It is worth noticing that most observed data contain significant afterslip. This will be further discussed in Sec. 4.6.

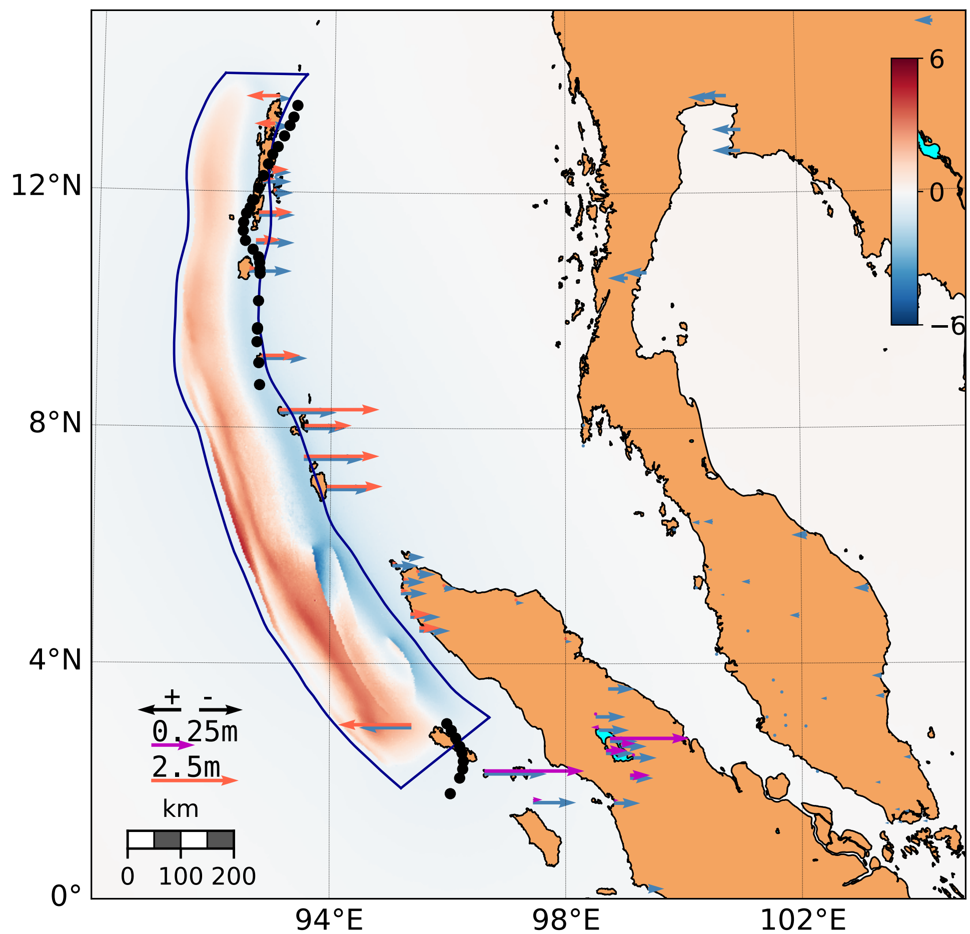

Figure 4.9: Comparison between synthetic vertical ground displacements (blue) and geodetic observations (orange and magenta). A different scaling is applied to highlight smaller-scale distant ground displacements. Synthetics vertical surface displacements are also shown in the figure. The black dots delimit the pivot line inferred by Meltzner et al (2006) from satellite imagery and a tidal model (North) and from field measurements of emerged coral microatolls (South), which divides regions of subsidence and uplift.

4.4.6 Off-fault plasticity and alternative model

The occurrence of large slip near the trench during a megathrust earthquake is possible, and can lead to large tsunami. The 2011 Tohoku earthquake did rupture to the trench (Fujiwara et al, 2011), and tsunami deposits along the Kuril trench suggest that such unusual events occured in the past (Nanayama et al, 2003). In our model, slip to the trench is limited by asymmetric, wide-spread plastic yielding in the shallow part of the accretionary wedge (Fig. 4.A.7).

To highlight the effect of off-fault yielding on the rupture, we build an alternative model (m_2) to the preferred model (m_1) in which off-fault material is made stronger, that is less easy to yield. Practically the bulk cohesion in our models is set such as it combines a depth-dependent term, which localizes plastic strain at shallow depth, and a constant term, which controls the magnitude of off-fault yielding at shallow depth. In m_1, such constant term is set at 1 MPa, whereas in m_2 we increase it to 10 MPa.

The alternative model m_2 is overall equivalent with m_1 in terms of rupture kinematics, but presents significantly more slip at the trench (Fig. 4.7f).

The overall rupture duration is not affected by off-fault yielding because it mostly happens at shallow depth (up to 15 km) while the rupture is driven by deeper portions of the subduction interface (see Sec. 4.4.2).

m_2 yields similar teleseismic (Fig. 4.A.4) and geodetic synthetics (Fig. 4.A.2 and 4.A.3) as the preferred model m_1, suggesting that geodetic and teleseismic observations do not efficiently constrain the slip at the trench. In fact, fault slip at shallow depth produces intense but localized surface displacements compared to slip at a deeper depth. The contribution of the shallower portion of the subduction interface (up to about 10 km depth) is therefore negligible at the closest geodetic measurements, on the fore-arc islands. Because of the presence of sediments at these depths, the contribution to the seismic moment of the shallow slip is also small. This effect, combined with the fact that shallow dipping faults do not radiate efficiently teleseismic waves yields a negligible contribution of the shallow subduction interface to the teleseismic waveforms.

4.4.7 Splay fault activation

The three splay faults incorporated in the model are activated (Fig. 4.A.5) and leave a noticeable signature in the synthetic vertical displacements (Fig. 4.9), although they host significantly less slip than the subduction interface. In fact, slip on these faults more directly transfers into vertical uplift due to their steeper geometry compared to the subduction interface. While it is unlikely that the far-field tsunami could have been significantly impacted by these splay faults, as their contribution to the vertical uplift is limited in space and magnitude, such splay faults may have modulated the tsunami in the near-source region (e.g. DeDontney and Rice, 2012). By simulating the tsunami and inundation resulting from an earthquake scenario with and without splay faults, the signature of the activation of such splay faults could be identified in the synthetics, fueling the debate of their possible activation.

4.5 Coupling to dynamic tsunami genesis

We test the preferred dynamic earthquake rupture scenario (model m_1) and its alternative (model m_2) for tsunami genesis by sourcing their synthetic coseismic 3D seafloor displacement fields into a tsunami model.

Accurate and efficient tsunami modeling is achieved by the used of sam(oa)^2 (Samoa Gitlab, 2019), a highly scalable software (Meister et al, 2016) solving the shallow water equations efficiently using adaptive mesh refinement (see Appendix Sec. 4.A.4 for more details about the modeling).

Both dynamic rupture scenarios are able to source a large-scale tsunami which impacts the whole simulated domain with waves of realistic amplitudes.

Because of the limited resolution of the bathymetry dataset and of our models, we restrict our comparison to selected tide-gauge observations and altimetry data from satellites. In particular, we do not try to match the many runup observations available for this event, which would require higher resolution bathymetry data and finer sampling of the tsunami-inundation model.

The tsunami scenarios match the main features of the water heights anomalies profile captured by the satellite Jason-1 about 2 hours after the mainshock (see Fig. 4.11). Timing and amplitude are recovered. The high frequency signals, which modulate the long wavelength signal of the observed profile is not captured by the synthetics.

The tsunami scenario is also able to explain the main features of the signals recorded at 5 selected stations in the Northern Indian ocean (Figs. 4.10 and 4.12). In particular, the maximum sea surface height of the first tsunami wave and its timing are well captured at all stations. This suggests that the sea-floor displacements time-history generated by the dynamic rupture scenarios is realistic and, therefore, that the earthquake scenarios are realistic. The use of a finer bathymetry around the buoys should allow better-capturing tsunami dynamics in shallow depth areas and inundation effects, which may allow resolving some of the unexplained features of the observed tsunami.

The tsunami synthetics generated from the alternative model are almost identical to the synthetics from the preferred model (Figs. 4.11 and 4.12). Significant differences are nevertheless noticeable along the Jason profile: model m_2 captures the two-peaks shape of the first tsunami wave, a feature which is not recovered by many of the models analyzed by Poisson et al (2011). Splay fault ruptures have been suggested to explain the double peak in the tsunami waves recorded by Jason-1 satellite (DeDontney and Rice, 2012). Our model m_2 offers an alternative explanation for this puzzling observation.

Altogether, these results suggest that tsunami observations, contrary to teleseismic and geodetic observations, are sensitive to the magnitude of fault slip to the trench, and ,therefore, offer insights into the shallow rupture of the Sumatra-Andaman earthquake.

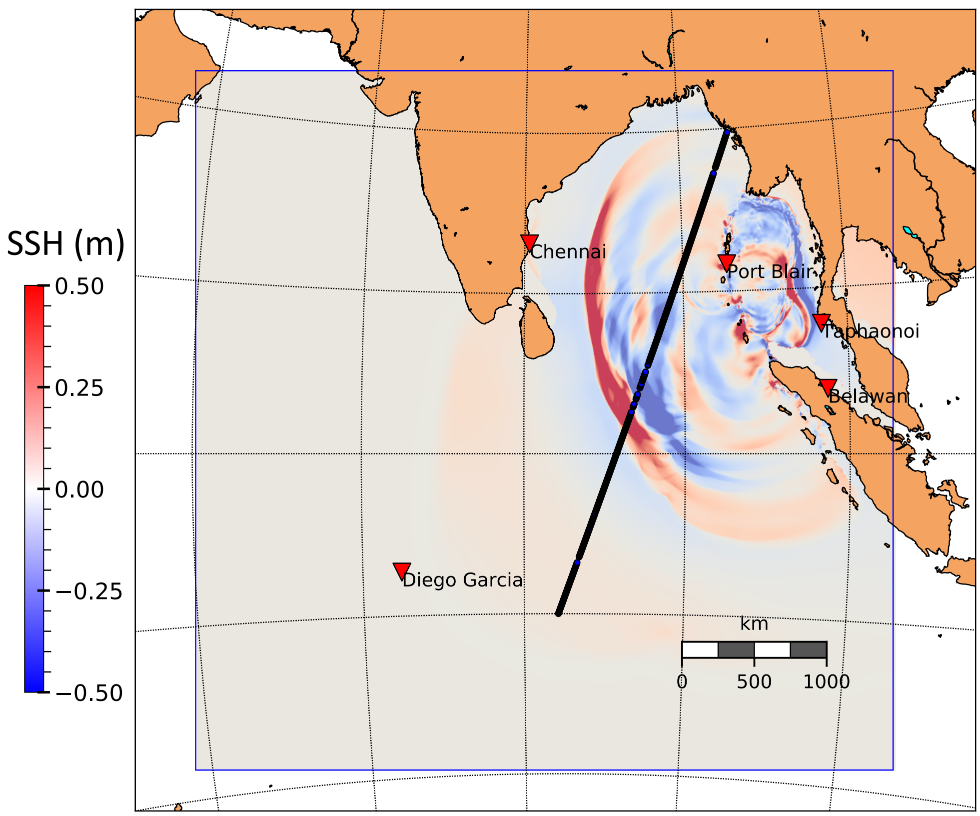

Figure 4.10: Snapshots of the tsunami scenario at 1 h 23 min simulation time (sea surface height in m), and location at which synthetic tsunami data are compared to observed data (see Fig. 4.12). The black line displays the location of the profile over which water height anomalies (m) were recorded by Jason-1 satellite (see Fig. 4.11). The blue box shows the domain of the tsunami simulation.

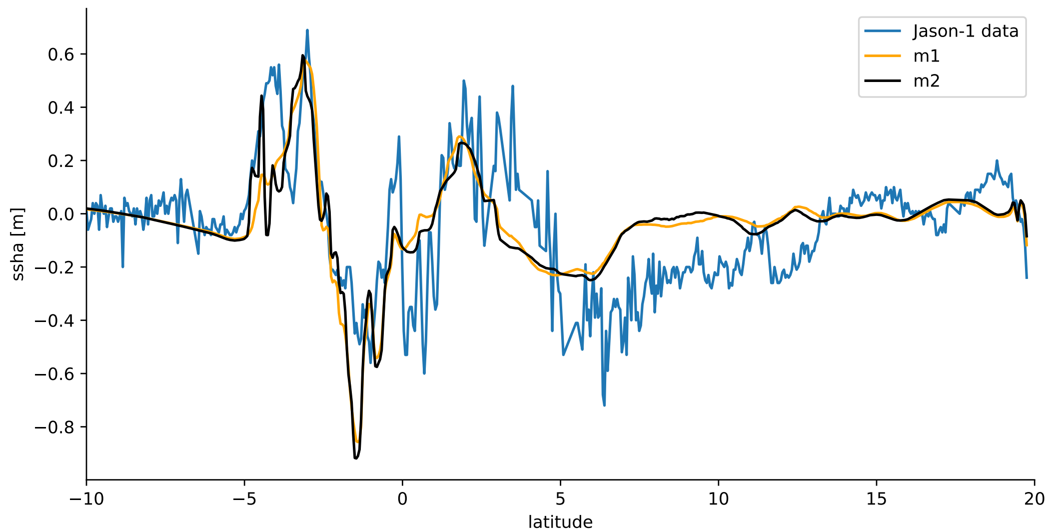

Figure 4.11: Water height anomalies (m) recorded by Jason-1 satellite about 2 hours after the mainshock over a SE-NW 1D profile of the Indian ocean compared with synthetic sea surface heights (m) achieved with the preferred scenario m_1 (orange) and the alternative scenario m_2 (black).
.

4.6 Discussion

We present two simple scenarios able to capture many aspects of the rupture process, and to recover many features of many kinds of observations including near-field geodetic observations, long-period teleseismic data and tsunami observations. Features of the earthquake that remain unexplained by the scenario suggest opportunities to better understand the role of fault heterogeneities.

4.6.1 Role of heterogeneities

Higher complexity in the subduction interface geometry could impact the modeled rupture process and allow recovering some of the heterogeneities in the slip distribution suggested by the kinematic models. The considered subduction interface geometry only incorporates the larger-scale geometric features captured by Slab1.0. The real geometry of the subduction interface is probably less smooth, and might also be segmented. Accounting for such additional complexity could potentially affect the rupture process, and lead to a longer rupture duration.

Unaccounted heterogeneity in the seismic coupling is suspected to play an important role in modulating megathrust ruptures and controlling their extends (e.g., Hardebeck and Loveless, 2018; Yang et al, 2019) and could also have significantly modulated the earthquake

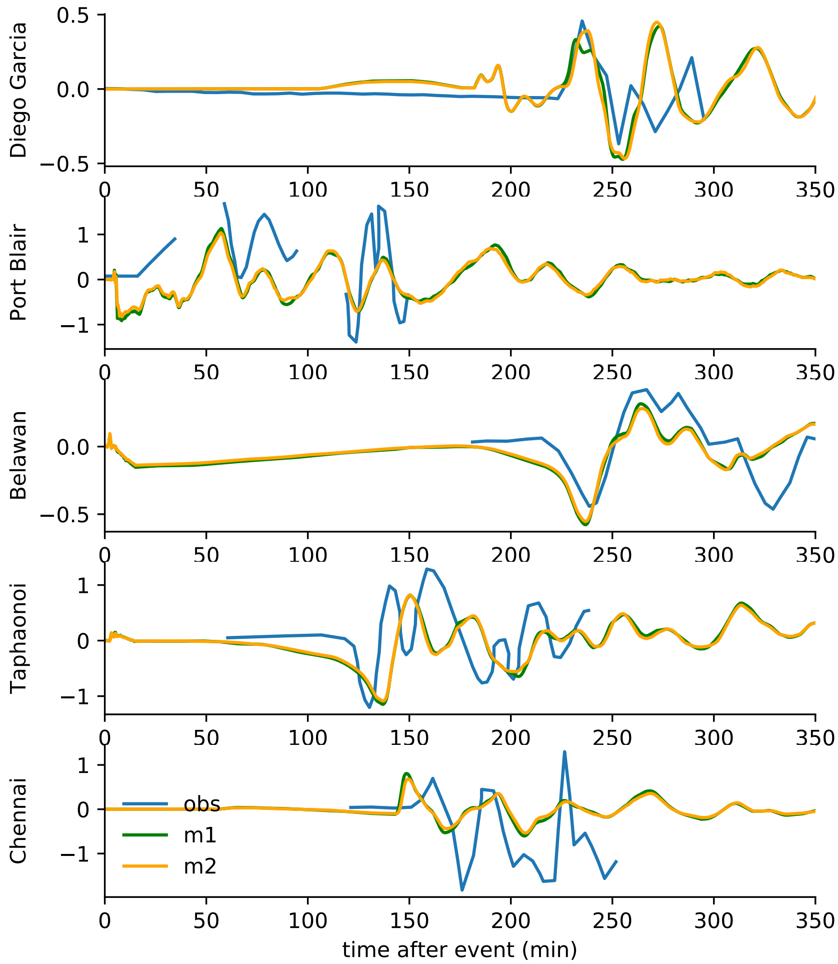

Figure 4.12: Time series from the tide gauge at 6 locations indicated in Fig. 4.10. Blue: measurement, green: output from the scenario m_1, orange: output from the scenario m_2.

.

pre-stresses of this event. Such heterogeneities, mapped along Sumatra (Chlieh et al, 2008), in general, correlate with the segmentation of previous events. A locally lower seismic coupling could especially be responsible for the spontaneous rupture termination to the South, which cannot be explained by the fault geometry itself. Subducted bathymetric features, such as seamounts are thought to be responsible for some of the heterogeneities in seismic coupling (Singh et al, 2011).

Unaccounted stress perturbations from previous motion including earthquakes certainly modulated the event prestress. Our pre-stress parametrization is equivalent to assuming that the previous large megathrust earthquake did wipe out any prestress heterogeneities, and that stress changes from other events following this mega-earthquake, including slow-slip and earthquake are negligible. This is obviously not true and might explain why we are unable to fit some observable. The occurrence of such previous events could have been accounted for by incorporating different rupture parameters (e.g. smaller D_c) or different prestress level in the area of such known previous earthquakes (e.g. Aochi and Ide, 2011; Ide and Aochi, 2013). Nevertheless, this is probably not applicable in this section of the subduction arc, as the historical seismicity is poorly known.

Uncaptured spatial variations in the rheology of the crust could have modulated the rupture process. In particular, the rupture has been inferred to be faster in its southern region compared to its northern region. This is probably related to softer material being in contact with the subduction to the North, associated with the thicker sediments in that region (Subarya et al, 2006), which could result in more sediments being subducted there.

Depth-variations in seismic wave radiation have been inferred for the 2004 event, as well as for the M_w 8.8 2010 Chile and the M_w 9.0 Tohoku earthquakes (e.g., Lay et al, 2012). During these events, coherent short-period radiations were inferred to emanate mostly from the deeper megathrust region, while large slip was inferred at shallower depths, associated with little short-period radiations. Hierarchical models featuring asperities of different sizes in which frictional properties are given by their size allow qualitatively reproducing the depth-dependent frequency content of the source (Ide and Aochi, 2013; Aochi and Ide, 2011; Galvez et al, 2014), and may be incorporated to our models in the future.

4.6.2 Static and dynamic triggering

Static and dynamic stress changes from the Sumatra-Andaman have been suggested to play a major role in the post-2004 regional seismicity. In particular, the M_w 8.7 Nias earthquake, occurring 3 months after the Sumatra-Andaman event, was probably indirectly triggered by the Sumatra-Andaman earthquake (e.g. Hughes et al, 2010). Our model generates significant stress changes south from the rupture, that could have indeed advanced rupture of the Nias earthquake. Also, the Sumatra-Andaman earthquake significantly altered seismicity in the Andaman backarc rift-transform system. On a specific section of the backarc, the rate of transform events dropped by two-thirds, while the rate of rift events increased eightfold (Sevilgen et al, 2012). Moderate size earthquakes could have been dynamically triggered on the backarc and would have remained unnoticed because of the widespread wavefield generated by the Sumatra-Andaman earthquake. Nevertheless, Sevilgen et al

(2012) suggests that static stress changes, although small, are more likely to explain the change in seismicity on the backarc. Our model, which captures the localized rupture front and the 3D fast subducting lithosphere might allow generating large dynamic stresses compatible with remote triggering of parts of these faults during the event. This may be investigated in a future study.

4.6.3 Afterslip

Most observed geodetic data contain significant afterslip, as summarized in Fig. 1 of Bletery et al (2016). Chlieh et al (2007) estimate that 30% of the inverted moment from the 40 days survey-model GPS data is afterslip. This is in line with Rhie et al (2007)'s inferences, whose model inverted from gedetic data yields 35% more seismic moment than their model from teleseismic data only.

Coseismic displacements along the arc are especially polluted by afterslip and may, therefore, be smaller than observed. The scenario does not agree with the pivot line inferred by Meltzner et al (2006) (see Fig. 4.9) which divides region of subsidence and uplift (Fig. 4.9). As this inference was made 90 days after the event, it is likely that deep afterslip (e.g. Subarya et al, 2006) has significantly shifted this line away from the trench, and that our model may better agree with the actual coseismic pivot line.

Smaller along-arc coseismic displacements than observed, in conjunction with the overshot far-field slip, suggest less slip overall. But less slip implies less moment release, while the scenario moment magnitude is already in the lower end of the inferred moment magnitude. Using stiffer material on the fault could allow decreasing the fault slip magnitude without affecting the moment magnitude, but would yield a faster rupture. A rupture process less linear than modeled, associated with a more heterogeneous slip distribution could nevertheless lead to a longer rupture duration and therefore reconcile model and observation.

4.6.4 Tectonic stress rotation

Our model allows evaluating the distribution of coseismic stress rotation generated by the earthquake (see Fig. 4.13). The stress rotation is highly heterogeneous. Large rotations, of up to 50° are inferred in the subduction wedge, while the subducting continental lithosphere present very little stress rotations.

4.7 Conclusion

We present physics-based scenarios of the 2004 Sumatra-Andaman megathrust earthquake. We demonstrate that a geometrically complex 3D model, in which we prescribe regional, smoothly varying along-arc fault pre-stresses constrained by earthquake focal mechanisms and by along-arc convergence rate variations, is sufficient to capture important features of the event, such as the Northern rupture arrest and the along-arc variations of the moment

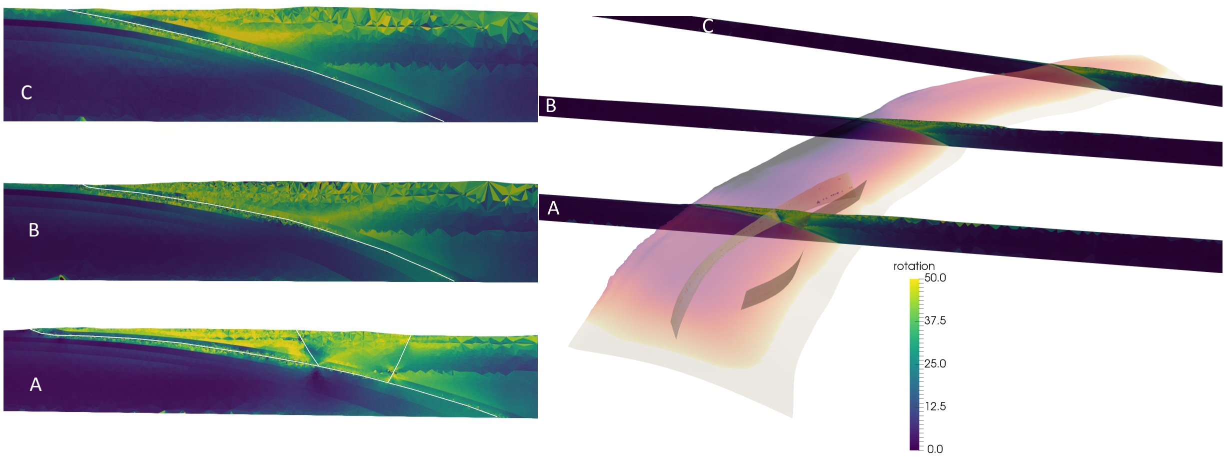

Figure 4.13: Inferred rotation of the maximum principal stress in model m_1. Left: coseismic stress rotation along 3 slices, in the southern (a), central (b) and northern (c) part of the earthquake rupture. Right: 3D view showing the fault slip on the megathrust interface and splay faults and a the 3 slices a b and c
.

rate release. The scenario appears in good agreement with near-field geodetic observations, long-period teleseismic data and tsunami observations.

The models suggest the importance of along-depth rigidity variations in the off-fault material around the subduction interface. Stiffer material at depth are responsible for the release of most of the moment magnitude and are driving the rupture evolution. The presence of soft sediments at shallow depth might have given rise to large slip at the trench, which almost does not leave any signature on teleseismic and geodetic data but does modulate some features of the tsunami.

We demonstrate the feasibility of achieving a realistic dynamic rupture scenario of a subduction megathrust earthquake. The methods we develop for constraining regional stress state and frictional parameters based on observations could enhance the modeling of previous and future megathrust events. A physics-based earthquake model is specifically useful to understand the processes ruling poorly instrumented events, such as the Sumatra-Andaman event.

4.8 Acknowledgements

We thank Dr. Mohamed Chlieh for providing his model of the Sumatra-Andaman event. Computing resources were provided by the Institute of Geophysics of LMU Munich (Oeser et al, 2006) and the Leibniz Supercomputing Centre (LRZ, projects no. h019z, pr63qo and pr45fi on SuperMUC).

Appendix

4.A Appendix

4.A.1 Computational framework

We produce scenarios of the 2004 Sumatra-Andaman earthquake using SeisSol (Dumbser and Käser, 2006; Pelties et al, 2012; Uphoff et al, 2017), which solves simultaneously for spontaneous dynamic rupture, seismic wave propagation and off-fault damage (e.g. Wollherr et al, 2018). SeisSol implements the Arbitrary high-order accurate DERivative Discontinuous Galerkin method (ADER-DG), which allows modeling seismic waves propagation with high-order accuracy. It uses fully non-uniform, unstructured tetrahedral meshes allowing geometrically complex models incorporating complex 3D structures, including curved and mutually intersecting faults, geologic layers and finely sampled topography. End-to-end computational optimizations (Breuer et al, 2014; Heinecke et al, 2014; Rettenberger et al, 2016), including an efficient local time-stepping algorithm (Uphoff et al, 2017), allow fast time to solution on high-performance computing clusters. SeisSol is verified with a wide range of community benchmarks (Pelties et al, 2014) in line with the SCEC/USGS Dynamic Rupture Code Verification exercises (Harris et al, 2011, 2018). SeisSol is freely available (SeisSol website, 2019; SeisSol GitHub, 2019).

4.A.2 3D velocity model

We here give some details about the 3D velocity model of the Sumatra-Andaman region we designed for this work.

The model is based on a global model of the crust compiled from geologic and geophysical data (Crust 1.0, Laske et al, 2013) and is refined in the subduction region to be geometrically compatible with the subduction interface. Practically, we first partition the computational domain into 2 regions using the subduction interface geometry, described in Sec. 4.3.2. For the oceanic crust region, west to the trench, we then incorporate in the structural model the (smoothed) geometry of the 3 deepest layers of the crustal model (Laske et al, 2013). These layers are bent downwards at the trench so that they do not intersect the subduction interface and they resemble a subducted crust. This is done by constraining the minimum vertical distance between each layer and the megathrust to be 6, 12 and 24 km respectively. Within each layer, we use crust 1.0 averaged elasticity parameters values, as detailed in Table 4.A.1. In the continental crust region, we use for practical reason a simple 1D velocity

Table 4.A.1: Elastic parameters assumed in the conceptual lithological model. ρ, μ, λ, V_p and V_s are respectively the density, the lame parameters and the P and S wave velocities. In the continental crust and the zone enclosing the subduction interface (fault zone, FZ), ρ, μ and λ vary linearly between the values indicated.

	lower depth (km)	ρ (kg/m^3)	μ (MPa)	λ (MPa)	V_p (m/s)	V_s (m/s)
Continental 1	6	2550	15.94	15.27	4300	2500
Continental 2	20	2720	33.32	31.28	6000	3500
Continental 3	∞	2850	39.02	42.38	6500	3700
FZ 1	10	2500	10.00	20.00	4000	2000
FZ 2	15	2500	22.50	27.90	5400	3000
FZ 3	30	2700	36.96	40.15	6500	3700
FZ 4	50	2850	43.35	56.97	7100	3900
FZ 5	∞	3050	46.39	60.97	7100	3900
Oceanic 2	meshed	2850	39.02	42.38	6500	3700
Oceanic 3	meshed	3050	50.03	53.70	7100	4050
Oceanic 4	meshed	3330	65.94	81.24	8000	4450

structure, not explicitly meshed, detailed in Table 4.A.1. In this region, we constrain layers thickness and elasticity parameters by the inversion results of Gupta et al (2016) of the continental crust beneath the Andaman Island. In addition to this 1D velocity structure, a thin layer (6 km width) above the subduction interface, allows in conjunction with the first layer of oceanic crust, to incorporate strong along-depth rigidity variations in the vicinity of the megathrust interface, as inferred by Bilek and Lay (1999) and Lay et al (2012).

4.A.3 building a realistic fault geometry

Incorporating a realistic fault geometry is fundamental for realistic dynamic rupture modeling as the fault geometry modulates the on-fault normal and shear tractions and therefore the rupture process. In particular, the along-depth steepness of the slab interface play a major role at modulating the simulated ground displacements (Subarya et al, 2006) and should be properly captured by the model. We build the slab interface from Slab 1.0 (Hayes et al, 2012), which offers 3D maps of most megathrust interfaces, constrained by seismological and geophysical data sets (e.g. CMT solutions, active seismic profiles). Slab 1.0 suggests that the Sunda subduction is increasingly steep from north to south and from the trench to deeper depth. In this data set, the Sunda subduction geometry is only defined below 10° latitude. Slab 1.0 has been recently updated to Slab 2.0 (Hayes, 2018), which defines the Sunda interface along the full span of the 2004 rupture. Nevertheless, as we initiated the study before the publication of this updated dataset, we here only rely on Slab 1.0 dataset, that we extend to the North following the northernmost profile of Slab 1.0. Our extension agrees well with the geometry of Slab 2.0.

Surface rupture during the 2004 event may have been enabled by a shallow thrust fault splaying from the slab interface within the accretionary wedge, as may suggest inferred shallow patches of large fault slip (e.g. Bletery et al, 2016). In this study, we acknowledge such a possibility by extending the subduction interface geometry toward the ground surface. The shallowest part of the Slab 1.0 geometry, located a few km below the ground surface, is mostly horizontal. Surface rupture is made possible by incorporating a short splay fault at the tip of the subduction interface, smoothly connected with the subduction interface by a depth-dependent dip (varying between 5 and 15°, steeper at shallow depth).

4.A.4 Details about the tsunami modeling

To model the tsunami, we use sam(oa)^2 (Samoa Gitlab, 2019), a highly scalable software (Meister et al, 2016) solving the shallow water equations efficiently using adaptive mesh refinement. sam(oa)^2 implements a second-order Runge-Kutta discontinuous Galerkin scheme (Cockburn and Shu, 1998; Giraldo and Warburton, 2008) on triangular grids and features an accurate and robust wetting and drying scheme for the simulation of flooding and drying events at the coast (Vater and Behrens, 2014; Vater et al, 2015, 2019). Such an adaptive mesh refinement approach allows for stable and accurate simulation of large-scale wave propagation in deep sea and small-scale wave shoaling and inundation at the shore. Bottom friction is parameterized through Manning friction by a split-implicit discretization (Liang and Marche, 2009).

We use the GEBCO 2019 topography and bathymetry dataset (Weatherall et al, 2015), which has a horizontal resolution of 15 arc seconds (or approximately 450 m). This allows for a sufficiently accurate representation of bathymetric features in deeper sea regions, where tsunamis have large wavelengths, but is certainly relatively inaccurate at shallow depth.

The tsunami is sourced by time-dependent bathymetry perturbations parametrized by the synthetic coseismic seafloor displacement. In addition to the vertical displacement, we incorporate the east-west and north-south horizontal components, into the tsunami source by applying the method proposed by Tanioka and Satake (1996).

The domain of the computational tsunami model (Fig. 4.10) encompasses the source region and a large part of the Indian ocean. The triangle-based computational grid is initially refined near the coast, where the highest resolution is about 1.7km. This results in an initial mesh of 1 million cells, which expands to more than 5 million cells during the dynamically adaptive computation. The refinement strategy is based on the gradient in sea surface height (ssh). The simulation is run for 4 h 45 min (simulation time).

4.A.5 Off-fault plasticity

We account for the possibility of off-fault energy dissipation, by assuming a Drucker-Prager elasto-viscoplastic rheology (Wollherr et al, 2018). The internal friction coefficient ν is set equal to the reference fault friction coefficient (0.6). Similarly, off-fault initial stresses are set equal to the depth-dependent initial stresses prescribed on the fault. The relaxation time T_v is set to 0.03 s. Finally, we assume depth-dependent bulk cohesion $C(z)$ (see Fig. 4.A.6)

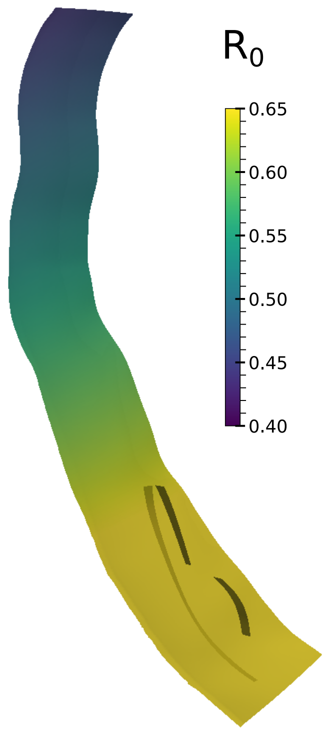

Figure 4.A.1: On-fault distribution of the relative prestress ratio R_0 on optimally oriented faults, modulated using the magnitude of the convergence rate inferred from rigid plate tectonics considerations, using the Euler pole inferred by Gahalaut and Gahalaut (2007).

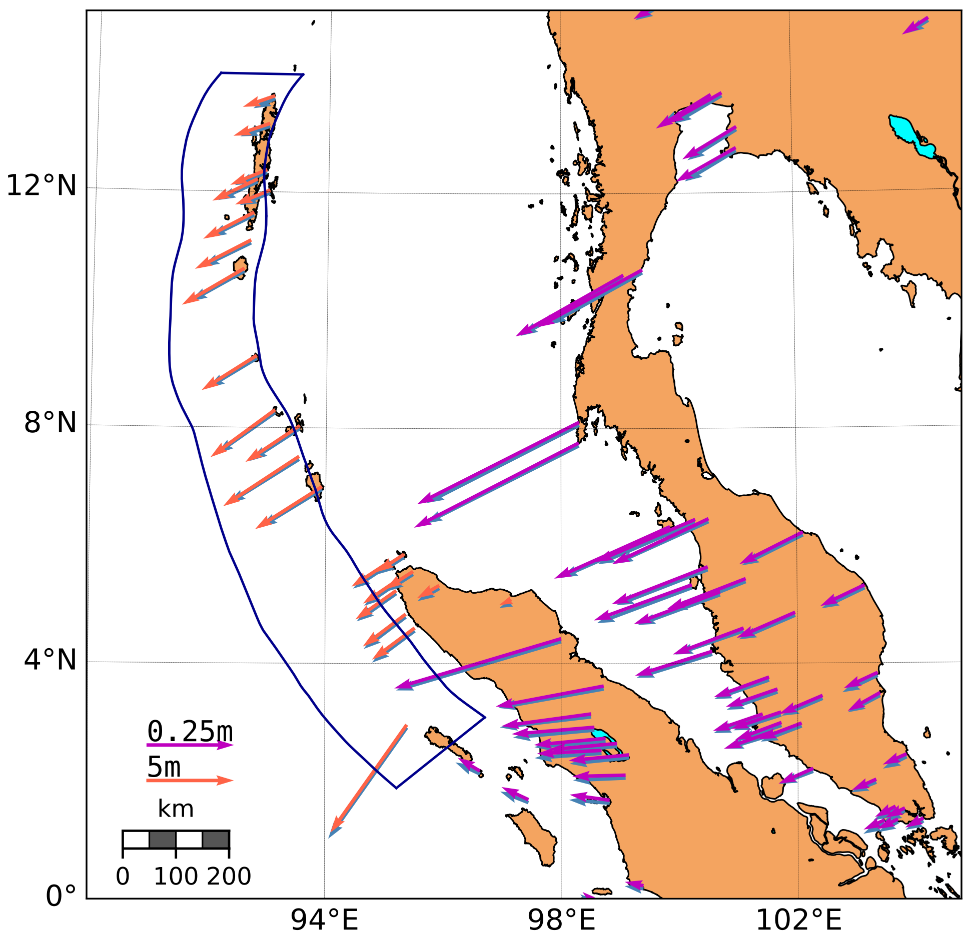

Figure 4.A.2: Comparison between horizontal ground displacements produced by the preferred model (blue, m_1) and by an alternative model featuring more fault slip to the trench (orange and magenta, m_2, see Fig. 4.7). A different scaling is applied to highlight smaller scale distant ground displacements.

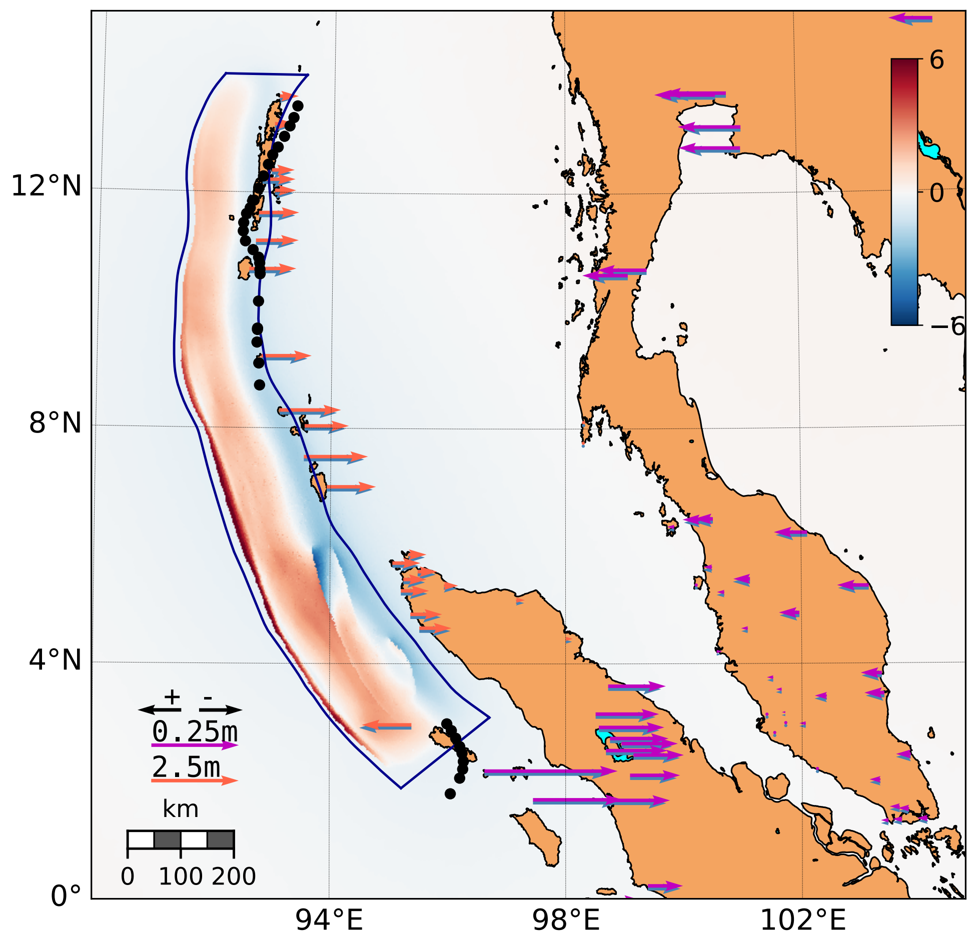

Figure 4.A.3: Comparison between vertical ground displacements produced by the preferred model (blue, m_1) and by an alternative model featuring more fault slip to the trench (orange and magenta, m_2, see Fig. 4.7). A different scaling is applied to highlight smaller scale distant ground displacements.

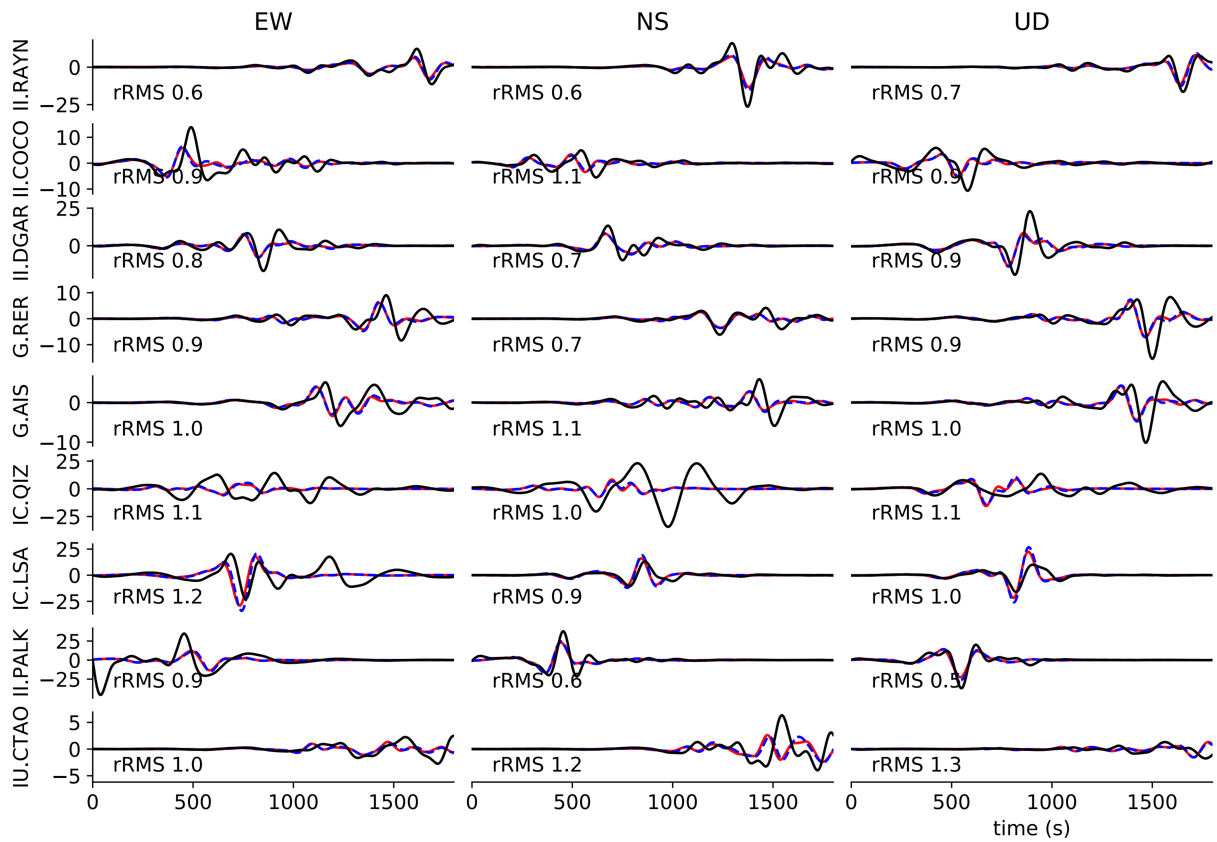

Figure 4.A.4: Comparison between modeled (red: m_1, blue: m_2, where m_1 is the preferred model and m_2 an alternative model featuring more fault slip to the trench, see Fig. 4.7d) and observed (black) teleseismic waveforms. A 66-500 s band-pass filter is applied to all traces. station location are show in Fig. 4.3.

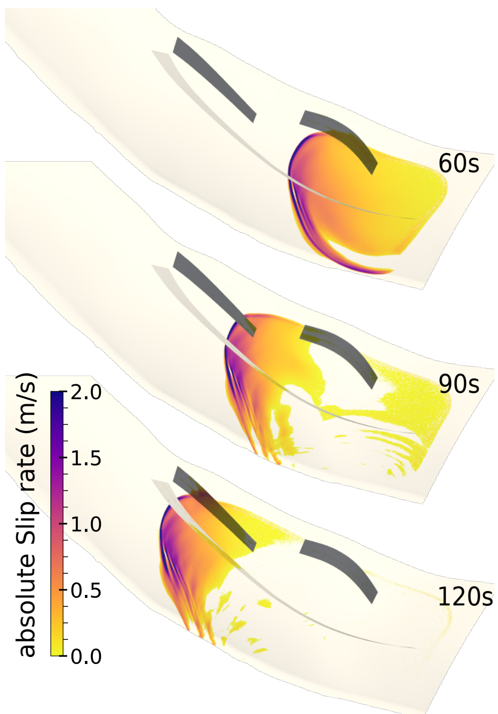

Figure 4.A.5: Activation of the splay faults in the preferred scenario (m_1). Snapshots of the absolute slip rate are shown at a rupture time of 60, 90 and 120 s.

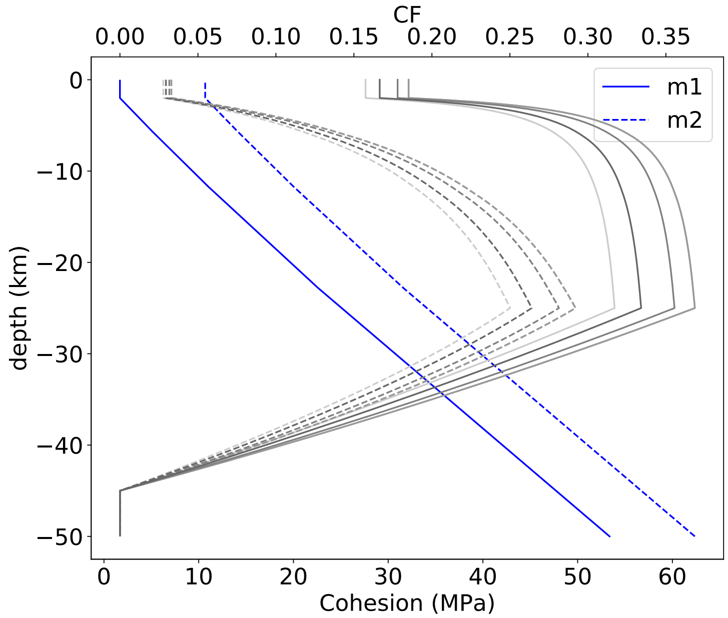

Figure 4.A.6: Depth dependence of the bulk cohesion and of the failure criterion CF (eq. 4.5) at four locations along the trench (darker grey represent locations more to the South).

to account for the hardening of the rock structure with depth:

$$C(z) = C_0 + \sigma_{zz} \tag{4.4}$$

where C_0 is 1 MPa for m_1 and 10 MPa for m_2 and σ_{zz} is the effective vertical stress. Closeness to failure (see Fig. 4.A.6) is quantified by the CF ratio (e.g., Ma, 2012):

$$CF = \frac{\sqrt{I_2}}{\tau_c} \tag{4.5}$$

where I_2 is the second invariant of the deviatoric stresses and τ_c the Drucker-Prager yield criterion, given by:

$$\tau_c = C(z)\cos(\Phi) - \sigma_m \sin(\Phi) \tag{4.6}$$

with $\Phi = \arctan(\nu)$ the internal angle of friction and $\sigma_m = \sum_{n=1}^{3} \sigma_{ii}/3$ the mean stress.

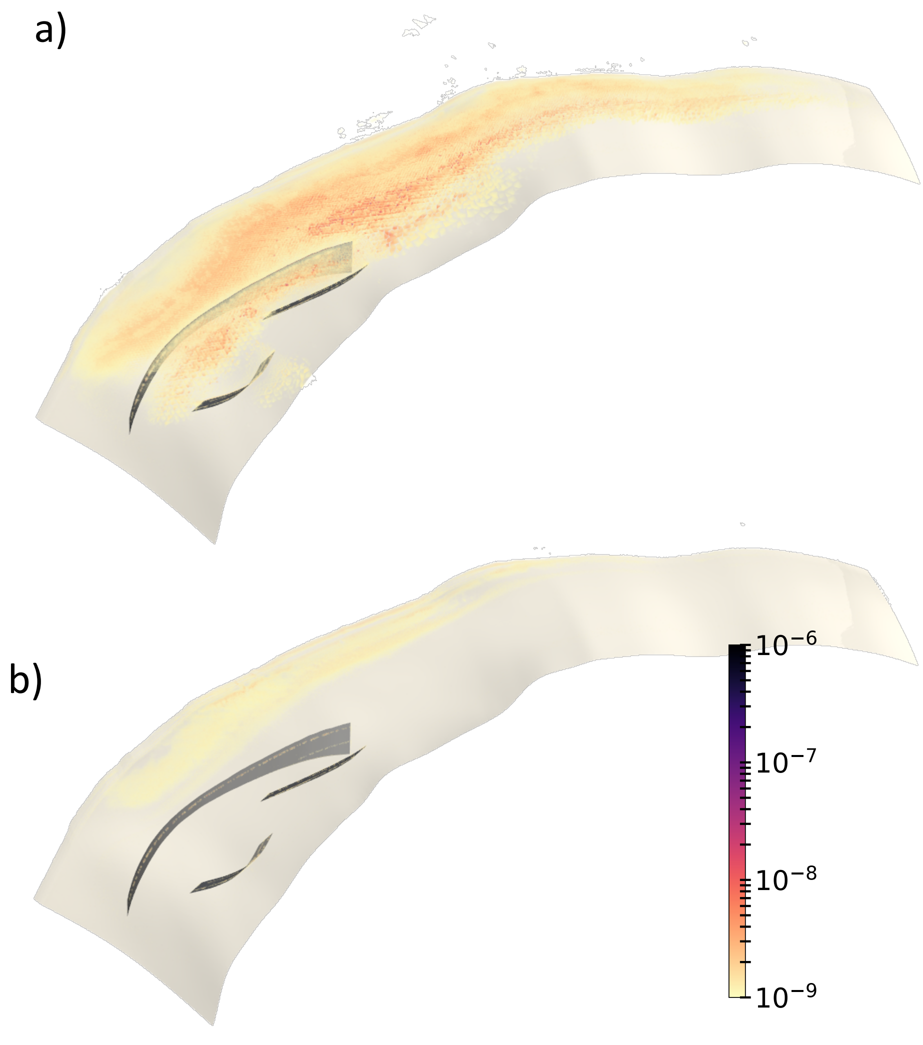

Figure 4.A.7: Off-fault plastic strain accumulated over the simulation for scenarios m_1 (a) and m_2 (b).

5

Scale-dependent effects of fault roughness on earthquake kinematics, dynamics and ground-motion

5.1 Abstract

The effect of fault roughness on earthquake rupture evolution and radiated seismic wavefield have been extensively studied using numerical models. Previous studies suggest that fault roughness promotes complex rupture processes, off-fault material yielding, supershear transitions, rupture segmentation, and high-frequency seismic radiations. Nevertheless, the scale-dependency of the physical mechanisms relating fault geometry to rupture behavior remains mostly unexplored. In particular, it is not clear whether or not specific wavelengths of fault roughness impact more earthquake dynamics than others. We here investigate such possible scale dependency using high-resolution 3D dynamic rupture models of earthquake rupture across faults incorporating band-limited roughness to varying length scales and based on varying fault friction parameters, yielding distinct process zone width. Our results suggest that the rupture process zone width is a key factor modulating the strength of the roughness effects. A larger rupture process zone leads to less coherent rupture fronts and higher variability of rupture speed. A systematic change in the spectral fall-off rate of the peak slip rate distribution at the length scale posed by the process zone width suggests that such length scale may play a critical role in modulating fault roughness dynamic effects. On the other hand, the spectral content of other rupture characteristics is consistently fractal over all scales, suggesting that such critical behavior is not an intrinsic characteristic of fault roughness effects.

The numerical cost of dynamic rupture models across rough faults may greatly depend on the smallest resolved wavelength of the fault geometry. We, therefore, test strategies to emulate the dynamic behavior on low-pass filtered faults. Building upon our results, we filter the reference fault for wavelengths smaller than the process zone width estimate. We show that dynamic rupture models on such smoother faults may capture the larger-scale kinematic features of the reference model if fault strength is scaled accordingly. By additionally accounting for the filtered small-scale geometric features through traction heterogeneities, small-scale variations of fault slip and rupture velocity can be also recovered. Both strategies produce earthquakes radiating high-frequency (up to 10 Hz) ground motion, with peak spectral acceleration presenting a high degree of similarity with the reference model. While spectral acceleration may not be strongly sensitive to smaller-scale variations in the rupture velocity, other ground motion intensity parameters may allow identifying the limits of the proposed strategies. Altogether, these results advance the understanding of fault roughness effects and should offer avenues towards more efficient physics-based seismic hazard characterization, integrating the synthetics of thousands of dynamic rupture simulation across rough faults.

5.2 Introduction

The majority of earthquake displacement is accommodated by thin principal slip zones of highly sheared fault gouge that can be viewed as fractal surfaces of complex geometry, deviating from planarity at all scales (e.g., Power and Tullis, 1991; Candela et al, 2012). Such a fractal nature has been observed consistently over nine decades of length scales from the µm scale to the regional scale by studying the topography of exhumed faults and the surface roughness of 2D surface ruptures of major continental earthquakes (Candela et al, 2012).

Fault roughness has extensive effects on earthquake dynamics. The variation in fault normal orientation along a rough fault results in heterogeneous initial fault tractions, even when considering a homogeneous tectonic stress field. Also, the complex geometry perturbs the stress locally during rupture propagation. This induces a shear resistance to slip (roughness drag), which adds up to the frictional resistance, and may explain why most faults operate at high stress levels (Fang and Dunham, 2013). Altogether, these effects lead to complex rupture processes. Simulated rupture across rough faults present heterogeneities in their kinematic and dynamic source properties, such as rupture speed and fault slip (e.g., Dieterich and Smith, 2009; Dunham et al, 2011b; Shi and Day, 2013). Additionnally, fault roughness promotes off-fault material yielding (e.g., Dunham et al, 2011b), supershear transitions (Bruhat et al, 2016) and rupture segmentation. Fault roughness could be one of the factors controlling a rupture extent (Zielke et al, 2017).

3D simulations of earthquake rupture, wave-propagation, and ground motions can complement data-based seismic hazard assessment, by predicting ground motion for scenario earthquakes (e.g., Olsen et al, 2009; Aochi and Ulrich, 2015). Because rupture on rough fault emits high-frequency ground motions and subsequent ground motion (e.g., Dunham et al, 2011b), they can produce valuable inputs for characterizing the hazard associated with small-structures, that typically have a fundamental eigenfrequency higher than 1 Hz. Also, deterministic simulations can supplement data-based ground-motion prediction equations, which are highly uncertain in the near-source region, due to the lack of near-source strong-motion records (e.g., Boore et al, 2014). Synthetics from 3D dynamic rupture simulations on rough faults can match most of the observed ground-motions characteristics if complex ingredients are included in the model, including a realistic 3D velocity structure, small-scale scattering, and frequency-dependent attenuation (Withers et al, 2019a,b). 3D dynamic rupture models across rough faults can also inform pseudo-dynamic models, which are kinematic-models, based on correlations between dynamic source quantities and resulting source parameters. Pseudo-dynamic models aim at emulating dynamic rupture behavior on complex faults, and more generally at producing realistic ground motion synthetics in a less computationally demanding framework than through the direct use of 3D dynamic rupture models (Guatteri, 2004; Mena et al, 2010; Schmedes et al, 2013; Mai et al, 2017).

While the effect of fault roughness on earthquake rupture evolution and radiated seismic wavefield have been already extensively studied, the scale-dependency of the physical mechanisms relating fault geometry to rupture behavior remains mostly unexplored. In particular, it is not clear whether or not specific wavelengths of fault roughness impact more earthquake dynamics than others. The average root-mean-square slope s_{rms} of a self-similar fault profile, equally sensitive to the lowest and highest wavelengths of the roughness range (see Appendix Sec 5.A.3) may suggest that some fault roughness effects are scale-invariant. The slope of the roughness is indeed a primary factor controlling the rupture process (e.g., Dunham et al, 2011b), as it modulates the heterogeneities in initial fault tractions caused by the geometry. Bruhat et al (2019), who study the spectral characteristics of the accumulated fault slip of an ensemble of 2D self-similar rough fault models and of high-resolution coseismic slip distributions from real earthquakes, suggest that the accumulated slip may follow a bi-modal fractal distribution, whose slope changes around a critical wavelength, that may be related to the rupture process and dynamic effects. In this study, we try to investigate the existence of such a critical length scale, below which fault roughness would have a distinct effect on earthquake dynamics. We especially identify a systematic change in the spectral fall-off rate of the peak slip rate distribution at the length scale posed by the process zone width, which suggests that such length scale plays a critical role in modulating fault roughness dynamic effects.

The viability of physics-based hazard characterization, integrating the synthetics of thousands of dynamic rupture simulation on rough faults, depends on the computational cost of each simulation. Deterministic simulations capturing the high frequencies ground motion require scalable codes optimized for high-performance computing. The source and its surrounding medium have to be defined in sufficient detail to produce ground motions of comparable energy content as observations. The cost of such simulation may be greatly affected by the choice of the smallest wavelength of the fault roughness. Building upon the results of our investigation on the scale-dependence of fault roughness effects, we try to emulate the dynamic behavior of a rupture on a reference fault using a derived fault low-pass filtered at the length scale posed by the process zone width. We test two strategies to approximate the kinematic features and radiated seismic wavefield of the reference model. In a first naive approach, we simply scale fault strength to account for the roughness drag contribution of the filtered out wavelengths. We also test a hybrid approach, in which the filtered small-scale geometric features are accounted for through traction heterogeneities. These strategies may allow modeling more efficiently realistic complex rupture process and associated ground motion on numerical schemes relying on low-order meshes.

5.3 Methods

5.3.1 Geometry

We construct a band-limited self-similar (H=1) fault geometry over the bandwidth 200 m to 50 km in the wavenumber domain following the method described by Shi and Day (2013). The fault is vertical, 50 km long, and 15 km deep and is parallel to the x-axis. While self-affine models (H <1) best fit independently the outcrop measurements and surface fault traces (Candela et al, 2012), they do not fit perfectly both datasets collectively, contrary to self-similar models, as discussed by Dunham et al (2011b) and Shi and Day (2013). Self-similar models are therefore widely used in numerical studies (e.g., Fang and Dunham, 2013; Shi and Day, 2013; Withers et al, 2019a,b), in which geometric complexity is modeled over several orders of magnitude of length scales. We consider a realistic but pronounced roughness, parametrized by an amplitude to wavelength ratio $\alpha = 10^{-2}$. α controls the amplitude of the roughness (see Appendix Sect.5.A.2). Power and Tullis (1991) estimate α for natural fault to be in the range $10^{-3} - 10^{-2}$.

The fault is embedded into a homogeneous half-space domain of 250 × 200 × 100 km. Such a large domain prevents the rupture and the near field wavefield to be perturbed by reflection from the domain absorbing boundaries. While our solver would allow incorporating more complexities (e.g. heterogeneous medium, free-surface topography, attenuation), we here consider a simple setup to isolate the effects of fault roughness on the rupture and ground motions from other complexities.

5.3.2 Computational model

Modeling rupture on rough faults spanning several orders of magnitude of length scales in 3D requires scalable codes optimized for high-performance computing. We here use SeisSol (Dumbser and Käser, 2006; Pelties et al, 2012; Uphoff et al, 2017), which solves simultaneously for spontaneous dynamic rupture, seismic wave propagation, and off-fault damage (e.g., Wollherr et al, 2018). SeisSol implements the Arbitrary high-order accurate DERivative Discontinuous Galerkin method (ADER-DG), which allows modeling seismic waves propagation with high-order accuracy. It uses fully non-uniform, unstructured tetrahedral meshes that allow geometrically complex models including fault networks, topography, and geologic layers. This geometric flexibility also allows straightforward modeling of earthquake ruptures on rough faults. Static mesh adaptivity allows focusing the computational effort in areas where high resolution is required (e.g. near the fault). SeisSol has been through end-to-end computational optimizations (Breuer et al, 2014; Heinecke et al, 2014; Rettenberger et al, 2016), including an efficient local time-stepping algorithm (Uphoff et al, 2017), that lead to fast time to solution and high scalability on high-performance computing clusters. SeisSol is verified with a wide range of community benchmarks (Pelties et al, 2014) including the SCEC/USGS Dynamic Rupture Code Verification exercises (Harris et al, 2011, 2018). In particular, the accuracy of Seissol is verified on the rough fault benchmarks TPV29 and TPV30, which feature a complex fault geometry spanning wavelength in the range 1 to 40 km.

5.3.3 Model resolution

Capturing the full complexity of a rough fault with a low-order mesh, based on 4 nodes tetrahedra, requires a fine sampling of the geometry shortest wavelength (e.g. 5 to 10 cells per wavelength). In this study, we only refine the smallest wavelength of the geometry by 2 elements (100 m on fault resolution for a minimum wavelength of the roughness of 200 m), but we initialize the fault tractions using precomputed values based on a finer (50 m sampled) fault geometry. This allows limiting the computational burden without significant loss of accuracy. The earthquake model domain is discretized into an unstructured computational mesh of 78 million tetrahedral elements. The cell size gradually varies within the mesh. An on-fault cell size of 100 m allows us to properly resolve the fault geometry and the rupture dynamics. A 250 m mesh size in a $70 \times 20 \times 15$ km box centered on the fault allows resolving the high-frequency ground motion over this area to about 9 Hz. This area concentrates most of the cells of the mesh. If no refinement area is considered, the mesh drops to 2.3 million elements. The maximum mesh size is 5 km. Simulating 20 s of earthquake rupture and seismic wave propagation using 5th order accuracy in space and time requires about 1 hour and 20 min on 7200 Skylake cores of the SuperMUC NG supercomputer of the Leibniz Supercomputing Centre in Garching, Germany.

5.3.4 Fault friction

In our models, slip across the fault is governed by a classical slip weakening law (Ida, 1972). While the use of rapid velocity-weakening friction has been adopted in several recent rough faults studies (e.g., Fang and Dunham, 2013; Shi and Day, 2013; Duru and Dunham, 2016), we opt for a more simple friction law, allowing better control of the process zone width. Withers et al (2019b) demonstrate that dynamic models of earthquake ruptures on rough faults modeled with linear slip weakening friction laws can yield broadband ground motions of similar characteristics as observed ground motion. The choice of the friction parameters is critical as it governs the intensity of the fault roughness effects on the rupture. In our models, friction drops from the static friction μ_s=0.6 to the dynamic friction μ_d=0.2 over the slip weakening distance D_c.

5.3.5 Initial stress state

The fault system is loaded by a laterally homogeneous regional stress regime. We assume an Andersonian stress field favoring strike-slip faulting (σ_2 vertical, where $\sigma_1 > \sigma_2 > \sigma_3$ are the principal stresses). We fully parametrize the stress state using four parameters: $SH_{\max}$, ν, R_0, and $\Delta\tau$. $SH_{\max}$ is the azimuth of the maximum horizontal compressive stress; ν is a stress shape ratio balancing the principal stress amplitudes; R_0 is a ratio describing the relative strength of faults; and $\Delta\tau$ is the potential stress drop, available to drive slip. We assume $SH_{\max} = 50°$. With this value, the median fault plane is not optimally oriented, as it deviates of 20° from the optimal orientation. The stress shape ratio $\nu = (s_2 - s_3)/(s_1 - s_2)$, which characterizes the stress regime is set to 0.5, indicating pure shear. The fault prestress ratio R_0 describes the closeness to failure of a virtual, optimally oriented plane according to Mohr-Coulomb theory (Aochi and Madariaga, 2003). R_0 relate to the relative fault strength S by $S = 1/R_0 - 1$. The rupture evolution is controlled by the energy balance between strain energy release and fracture energy (Madariaga and Olsen, 2000), which leads to trade-offs between R_0 and the linear slip weakening distance D_c. We here aim for conditions allowing a nearly full fault rupture propagating on average at subshear rupture speed. These conditions are achieved using R_0=0.75 and D_c=0.5 m.

Our models incorporate over-pressurized fault zone fluids (e.g., Suppe, 2014). In our reference model (D_c=0.5 m), fluid pressure increases along a hydrostatic gradient ($P_f = \rho_{water} g z$) up to a depth of about 2.5 km and along a lithostatic gradient below this depth. This yields a constant effective confining stress of 40 MPa at depth, and an average stress drop of 20 MPa (given R_0=0.75, μ_s=0.6 and μ_d=0.2). A depth-invariant effective confining stress translates into a depth-invariant estimate for the process zone width (see eq.5.1), which greatly facilitates analyzing the dependence of roughness effects with this characteristic length. The deviatoric stresses are tapered down below 11 km depth over 4 km. We do not apply any tapering near the lateral edges of the fault. Altogether, these conditions lead to M_w 7 earthquakes, consistent with a fault length of 50 km (Wells and Coppersmith, 1994).

5.3.6 Off-fault yielding

We account for the possibility of off-fault energy dissipation through a Drucker-Prager viscoplasticity rheology(e.g., Andrews, 2005; Wollherr et al, 2018). Ruptures hosted by rough faults are expected to generate high stress concentrations near the kinks of the geometry, which can result in off-fault material yielding. Accounting for off-fault yielding prevents unrealistic stresses near the fault. The viscoplastic rheology is parametrized by three parameters: angle of friction and cohesion, controlling rock strength, and the relaxation parameter T_v, the time-scale over which overstressed rocks readjust to the rock strength. The values we use are detailed in Table 5.1. Such a parameter set yields a closeness-to-failure ratio (CF, e.g. Ma, 2012) of 77% at depth.

Table 5.1: parameters of the Drucker-Prager viscoplasticity law

Cohesion (MPa/m^2)	friction angle	T_v (s)	CF
3	0.6	0.03	77%

5.3.7 Rupture nucleation

In all models, rupture is nucleated at (x, z) = (20, -8) km, by using a zone of forced rupture surrounding the hypocenter, in a similar way as in the SCEC/USGS Dynamic Rupture Code Verification exercises TPV29 and TPV30 (Harris et al, 2018). The friction coefficient is gradually reduced over an interval of time, to smooth the nucleation process and reduce unwanted oscillations. The forced rupture expands at a variable speed, from a speed of 0.7 V_s to a speed of zero at a distance of $1000 D_c$ m from the hypocenter. To facilitate rupture nucleation we prevent off-fault plastic yielding in a sphere of 1 km radius centered at the hypocenter.

5.3.8 Data and materials availability

All data required to reproduce the earthquake scenario can be downloaded from https://doi.org/10.5281/zenodo.4022525. We provide a detailed readme file summarizing the data and data formats provided. We use SeisSol, commit b553760, available on Github. The procedure to download, compile, and run SeisSol is described in its documentation (https://seissol.readthedocs.io).

5.4 Results

The rupture process zone width poses a critical wavelength in the dynamic rupture process. The role of such a critical wavelength in the roughness fault effects remains mostly unexplored. Geometric features significantly smaller than the rupture process zone width may not perturb the overall coherency of the rupture front. In fact, a rupture front may heal from the induced small-scale perturbations, over a distance comparable to the size of the geometric features, similarly as waves healing back into a coherent front after diffracting around a low-velocity anomaly of small size relative to their wavelengths.

To test the dependence of rupture dynamics on the rupture process zone width, we can either fix the rupture process zone width and change the shortest wavelength of the modeled fault roughness, or vary the rupture process zone width on a given rough fault. We first investigate this latter option.

5.4.1 Dependence of rupture dynamics on the rupture process zone width

The rupture process zone width is expected to scale linearly with D_c. For instance, Day et al (2005) derived estimates of a breakdown-zone width, which apply when rupture speed is very low, e.g. shortly after nucleation. Their estimate yields:

$$\Lambda_0^{III} = \frac{9\pi}{32}\mu\frac{D_c}{\tau_s - \tau_d} \tag{5.1}$$

In our reference model, featuring D_c=0.5 m and a strength drop of 26.6 MPa, this formula yields a breakdown-zone width estimate of about 700 m. The effective breakdown-zone width can also be estimated from the rupture time, the dynamic weakening time, and the rupture velocity (see Sect. 5.A.4), which are on-fault outputs of our simulations. Using this idea, we show that the breakdown-zone width features significant spatial variations over the fault in our models (see Fig. 5.A.1). We estimate its 5, 50, and 95 percentiles as 270, 950, and 3030 m. The estimate of Day et al (2005) here corresponds to the peak of the distribution of the measured breakdown-zone width.

We generate four ruptures on the same reference fault by varying the linear slip weakening distance D_c. We use D_c=0.1, 0.2, 0.3 and 0.5 m. As previously mentioned, the rupture evolution is controlled by the energy balance between strain energy release and the fracture energy (Madariaga and Olsen, 2000). We ensure that all four rupture have comparable overall kinematics (rupture duration, moment magnitude) by decreasing the prestress ratio R_0 when using lower values of D_c, and by simultaneously scaling the effective confining stress (by a factor $R_0/0.75$, where 0.75 is the value of R_0 in the reference simulation with D_c=0.5 m) to keep the stress drop unchanged. Our four Earthquake ruptures, which feature respectively (D_c, R_0) = (0.1, 0.45), (0.2, 0.55), (0.3, 0.65), (0.5, 0.75), yield all comparable kinematics and average moment release (Fig. 5.3a).

It is worth noticing that the process zone widths achieved by all four simulations do not linearly scale with D_c as R_0 and the effective confining stress and therefore the strength drop $\tau_s - \tau_d$ are also changed. In the framework of this study and following Day et al (2005)'s estimate, the ratio between the breakdown-zone width estimates of 2 simulations featuring (D_c, R_0) and (D'_c, R'_0) is $(D'_c R'_0)/(D_c R_0)$. Therefore, the breakdown-zone width estimates for the simulation featuring D_c=0.3, 0.2 and 0.1 m are respectively 368, 207 and 85 m.

Our results allow identifying a clear dependence of roughness effects on the rupture process zone width. Figs. 5.1a) to d) give an overview of the four simulated ruptures with varying D_c. A larger rupture process zone leads to less coherent rupture fronts (e.g. compare the snapshots 12 s after rupture initiation, which are increasingly coherent for decreasing D_c). Fig. 5.2a) to d) presents the on-fault distribution of some of the key kinematic and dynamic rupture properties: fault slip magnitude, rupture speed, and peak slip rate. Fault roughness induces small-scale variations in the distribution of all these dynamic rupture properties. All four ruptures lead to similarly looking fault slip magnitude distribution. 2D slip profiles are boxcar shaped and not elliptical shaped, in line with Dieterich and Smith

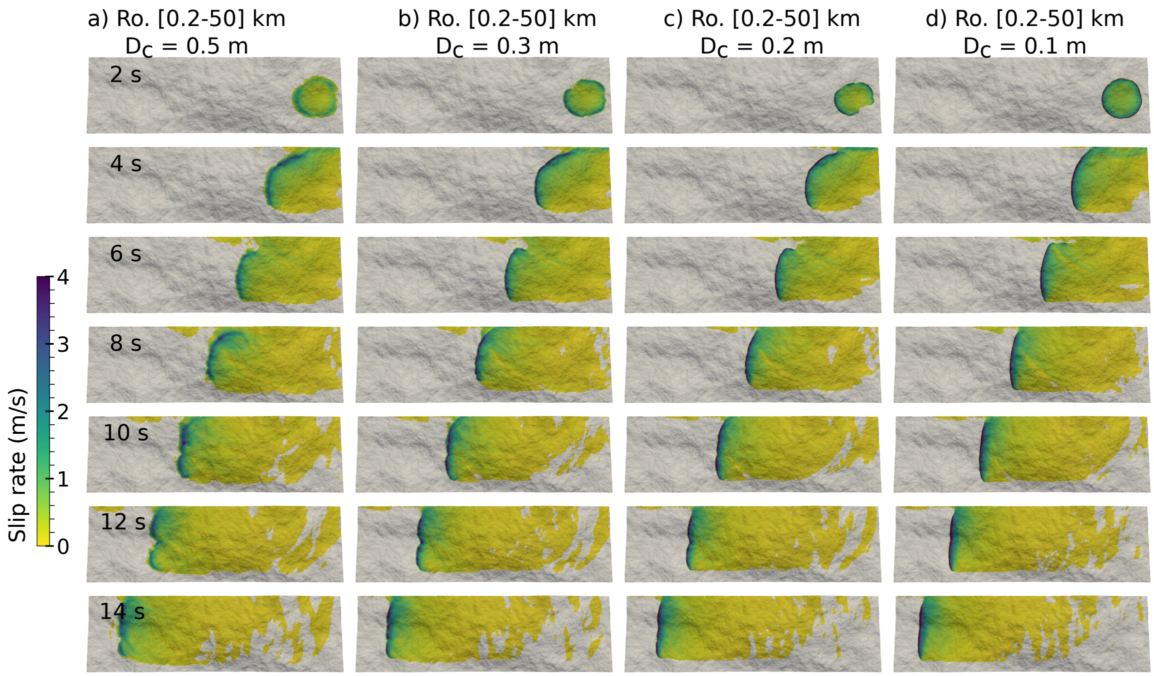

Figure 5.1: Overview of simulated earthquake ruptures on the reference fault (roughness wavelength range 200 m-50 km) for varying rupture process zone width estimates, controlled by the linear slip weakening distance D_c. Snapshots of the absolute slip rate at a rupture time of 2, 4, 6, 8, 10, 12 and 14 s. (a) D_c=0.5 m, (b) D_c=0.3 m, (c) D_c=0.2 m, (d) D_c=0.1 m.

(2009)'s inference from 2D numerical models of earthquake rupture across pronounced rough faults. The rupture speed distributions are smoother for decreasing D_c. Peak slip rate increases with decreasing D_c, which is expected, because the same amount of slip is generated in a shorter duration for shorter rupture process zone width.

We quantify the observations we made on the rupture dynamic properties by studying the average spectral properties of these quantities. In particular, we compute the radially-averaged amplitude spectral densities of each dynamic source quantity and we comment on their variations. The amplitude spectral density is obtained from the 2D Fourier transform of the spatial distribution of the dynamic source quantities (e.g. absolute slip). The amplitude spectral density equals the square root of the power spectral density, which is usually used to characterize fractal properties of surfaces. We find that the amplitude spectral density is more sensitive and therefore more suitable for identifying subtle changes in the fractal properties of the rupture dynamic properties distribution (compare Figs. 5.4, 5.5 and 5.7 with Figs. 5.A.2, 5.A.3 and 5.A.4).

We restrict our analysis to depths between 2.5 km and 12.5 km. In doing so, we remove the shallow part of the fault in which fault strength scales linearly with depth, that is where the breakdown-zone width estimate Λ_0^{III} is not constant, and the deeper part of the fault, which does not accumulate slip. We also exclude the nucleation area, by restricting the analysis to $x < 15$ km.

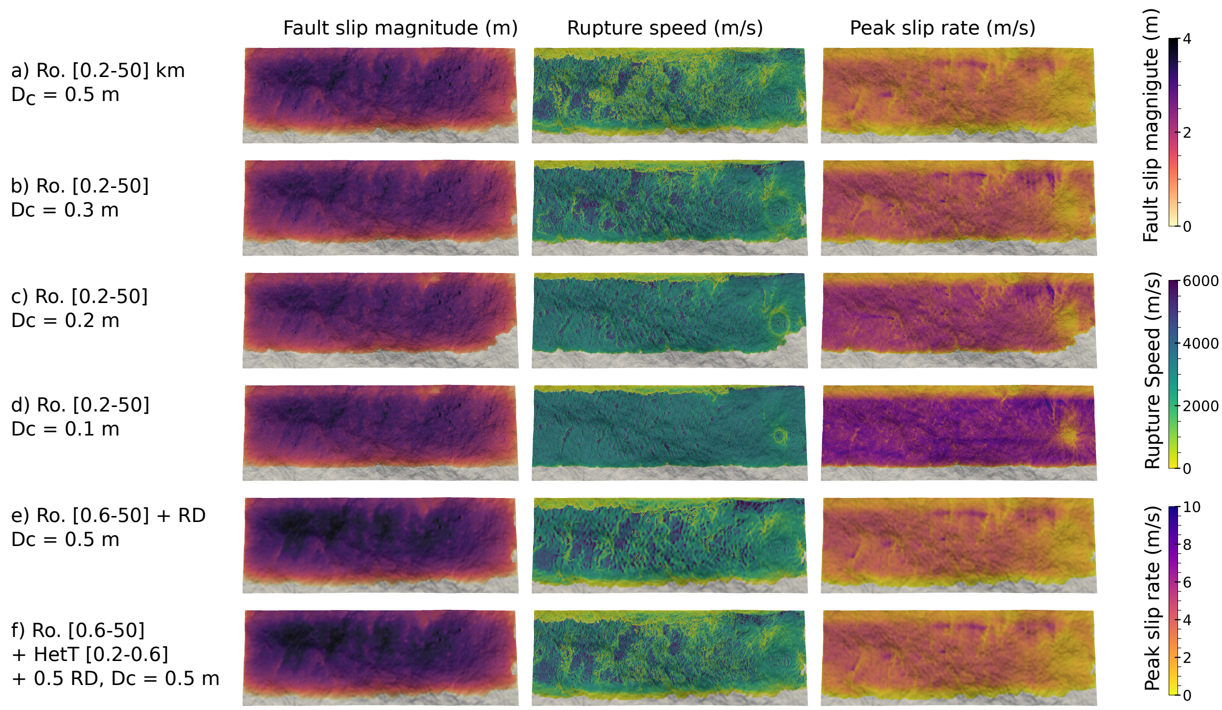

Figure 5.2: Source properties of simulated earthquake ruptures: final slip magnitude (first column, m), rupture speed (second column, m/s) and peak slip rate (third column, m/s). The simulations (a) to (d) correspond to the simulations presented in Sec. 5.4.1, in which the rupture process zone width in varied. (e) and (f) are the simulations presented in Sec. 5.4.2 in which ruptures are simulated on a fault derived (low-pass filtered) from the reference fault. HetT: heterogeneous tractions. RD: roughness drag.

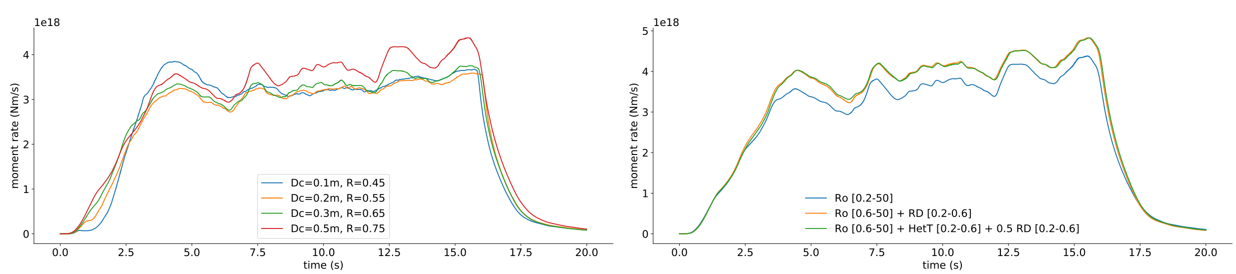

Figure 5.3: Moment rate functions of simulated earthquake ruptures. a) simulated earthquake ruptures on the reference fault for varying rupture process zone width estimates, controlled by the linear slip weakening distance D_c. b) simulated earthquake ruptures on the reference fault and on a derived fault including only part of the spectral content of the reference fault.

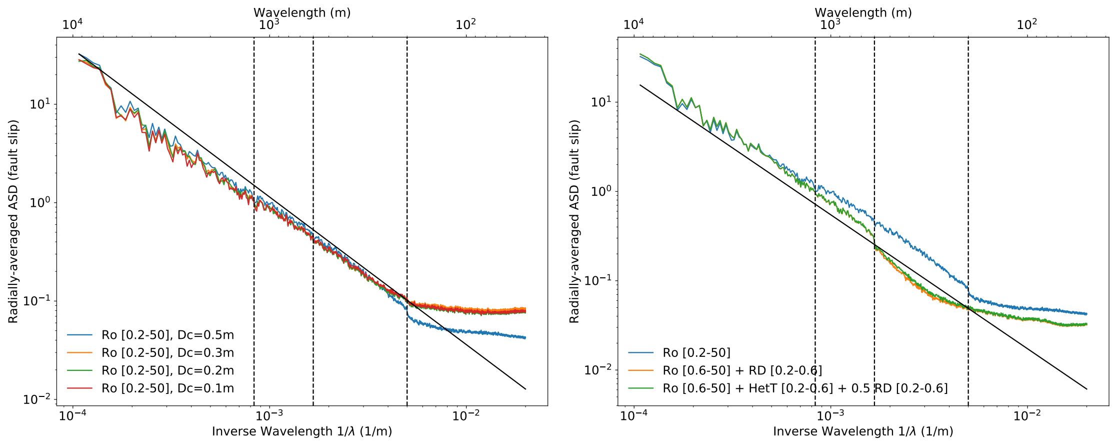

Figure 5.4: Radially-averaged amplitude spectral density of the final fault slip. The solid black line shows the fall-off rate of a self-similar model (H=1). See caption of Fig. 5.3 for more details about a) and b).

The amplitude spectral density of the accumulated slip is similar for all four simulations (see Fig. 5.4). The accumulated slip is self-affine (Hurst index H=0.8) over the whole roughness wavelength range.

The amplitude spectral density of the rupture speed (see Fig. 5.5) features also a self-affine distribution (H=0.35), with is shifted overall downwards for decreasing rupture process zone width. By normalizing the x-axis by the rupture breakdown zone width estimate Λ_0^{III} and by normalizing the functions by their values at 0.2, we see (Fig. 5.6a) that all normalized amplitude spectral density align (up to the smallest wavelength of the rough fault geometry), that is the rupture velocity is scale-invariant.

Most interestingly, the peak slip rate follows a fractal distribution (Fig. 5.7) only for wavelengths greater than the rupture breakdown zone width estimate Λ_0^{III}. The normalized distribution (Fig. 5.6b), allows highlighting this characteristic length in the amplitude spectral densities. The amplitudes spectral densities of simulations featuring D_c=0.2, 0.3, and 0.5 m drop below the fractal model (black line) at a wavelength around Λ_0^{III} and align for smaller wavelengths with a self-affine model (H=1.6). The simulation featuring $D_\mathrm{c} = 0.1$ m does not show such behavior as its Λ_0^{III} is smaller than the smallest wavelength of the fault roughness.

5.4.2 Dependence of rupture dynamics on the roughness bandwidth

The cost of rough faults models can be greatly affected by the choice of the shortest wavelength of the fault roughness. In fact, increasing the fault mesh resolution by a factor 2 leads to halved time steps, and to 8 times more elements in the volume for a regular mesh, altogether leading to computations 16 times more expensive (Note that doubling the fault mesh resolution can be significantly less expensive with SeisSol, thanks to static

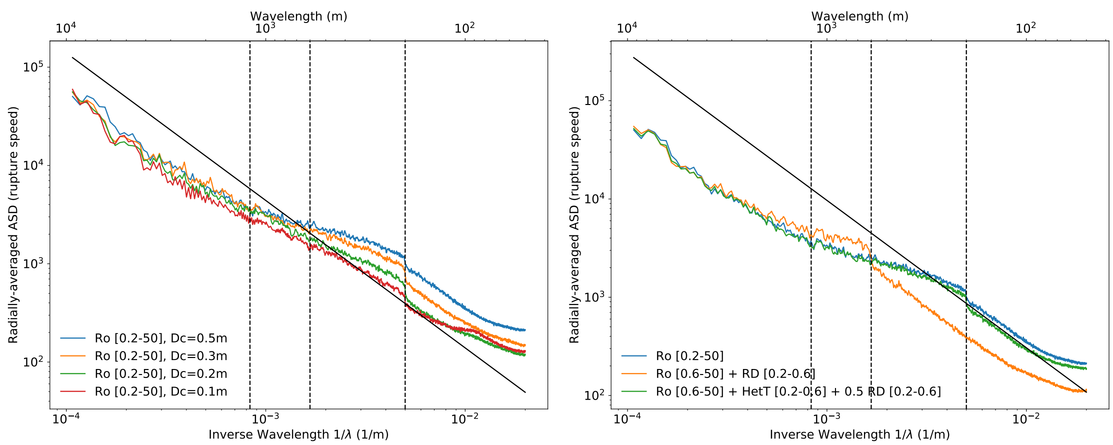

Figure 5.5: Radially-averaged amplitude spectral density of the rupture velocity. See caption of Fig. 5.3 for more details about a) and b)

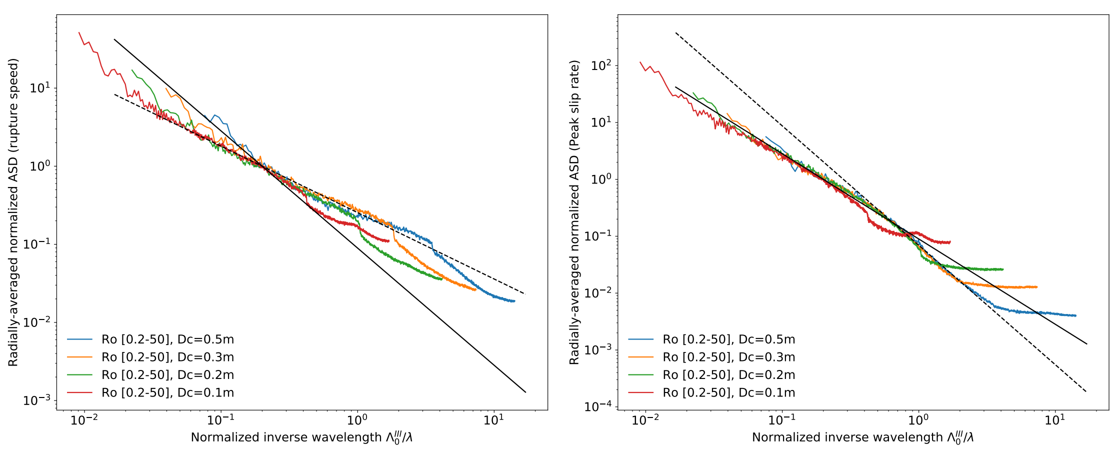

Figure 5.6: Normalized radially-averaged amplitude spectral density of the rupture speed (a) and the peak slip rate (b). The x axis is normalized by Day et al (2005)'s estimate of the breakdown-zone with. All curves are normalized by their value at 0.2. The solid black lines show the fall-off rate of a self-similar model (H=1). The dashed black lines show the fall-off rate of a self-affine model featuring H=0.35 (a) (resp. H=1.6, (b)).

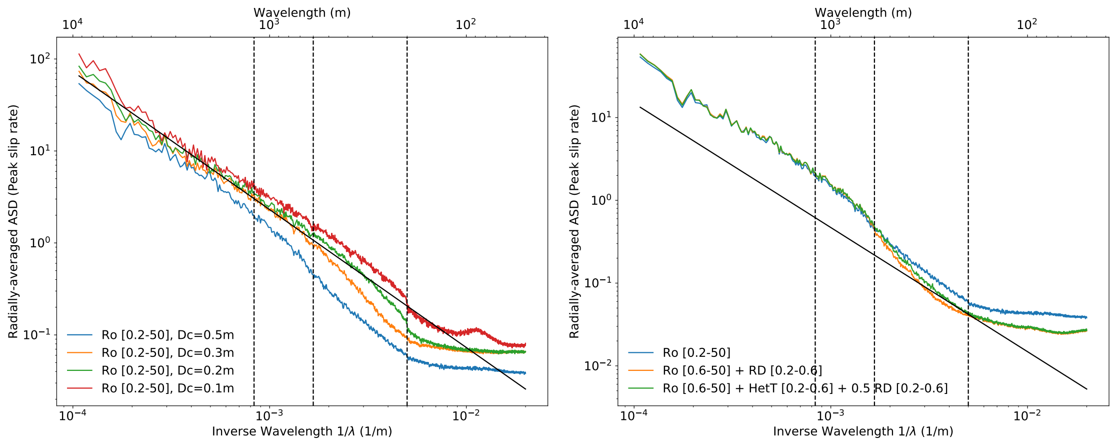

Figure 5.7: Radially-averaged amplitude spectral density of the peak slip rate. See caption of Fig. 5.3 for more details about a) and b)

mesh adaptivity and local-time-stepping (see Sect. 5.3.2)). We, therefore, try to investigate how the choice of the minimum wavelength of the modeled fault roughness affects rupture kinematics and dynamics. In that purpose, we low-pass filter the reference fault (that is, when generating the fault geometry in the wavenumber domain following the method described by Shi and Day (2013), we do not sum up the contribution of the shortest wavelengths up to the cut-off wavelength) and try to see if we can recover an earthquake rupture resembling the rupture on the reference fault. Based on our finding from Sect. 5.4.1, suggesting that the length scale posed by the process zone width may play a critical role in modulating fault roughness dynamic effects, we low-pass filter the reference fault at 400 and 600 m, that is below the process zone width estimate (700 m) of the reference model (D_c=0.5 m).

While smaller-scale wavelengths may not affect the rupture front coherence, they induce an additional shear resistance to slip (roughness drag), that have to be accounted for when simulating rupture on a low-passed filtered fault. Fang and Dunham (2013) demonstrate and quantify such effect, as:

$$\tau_{\text{drag}} = 8\pi\alpha^2 G^* \Delta/\lambda_{\text{min}} \tag{5.2}$$

Where α is the amplitude to wavelength ratio, G^* is given by $G^* = \mu/(1-\nu)$ with μ the shear modulus and ν the Poisson ratio, Δ is the fault slip and λ_{min} is the shortest modeled wavelength of the rough fault.

To recover equivalent rupture dynamics on the derived faults, we, therefore, decrease the initial shear traction on the derived faults by:

$$\tau_{\text{drag}} = 8\pi\alpha^2 G^* \Delta(1/\lambda_{\text{min}} - 1/\lambda_{\text{max}}) \tag{5.3}$$

Where λ_{min} and λ_{max} are the limits of the filtered-out wavelengths. The median slip in the reference scenario (roughness band 200 m–50 km) is of about 2.5 m. We find by trial

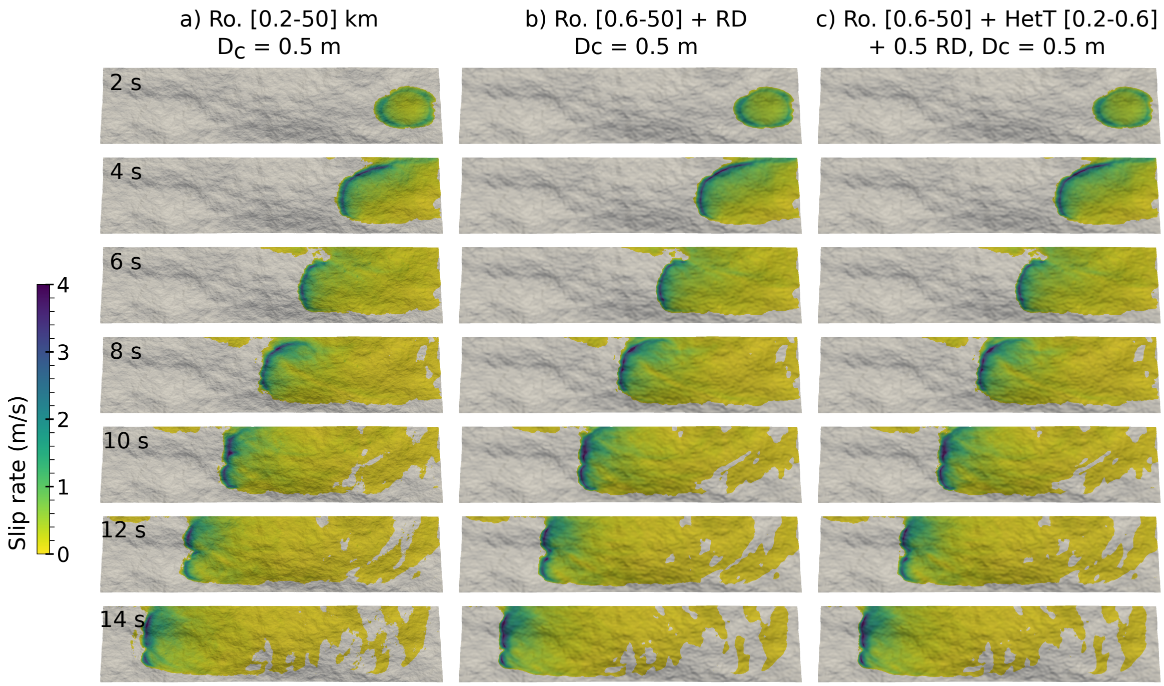

Figure 5.8: Overview of the simulated earthquake ruptures on the reference fault and on derived faults including only part of the spectral content of the reference fault. Snapshots of the absolute slip rate at a rupture time of 2, 4, 6, 8, 10, 12, and 14 s. (a) Earthquake rupture evolution on the reference fault (roughness wavelength range 200 m-50 km). (b) and (c) Earthquake rupture evolution on a derived fault, obtained by low-pass filtering the reference fault at wavelength 600 m. In (b) the unaccounted spectral range is substituted by its equivalent roughness drag (Fang and Dunham, 2013). (c) also accounts for the heterogeneous tractions caused by roughness in the range 200 m-600 m, in combination with a reduced roughness drag term. A linear slip weakening distance D_c of 0.5 m is used in all simulations.

and error that using Δ=1 m allows recovering a rupture of similar characteristics on a low-passed filtered to a minimum wavelength of 400 m. Such observation also holds for a fault low-passed filtered to wavelengths of 600 m.

Fig. 5.8 presents snapshots of the rupture evolving on the reference fault (a) and the 600 m low-passed filtered fault (b). Both ruptures have very similar kinematics. They have similar duration, slip rate amplitude and their rupture fronts are affected by the same geometric features. Fig. 5.3b, which compares the moment rate functions of the synthetics ruptures, confirms that these ruptures have very similar duration, magnitude, and kinematics.

Fig. 5.2 suggests that the derived scenario on the 600 m low-passed filtered fault (e) offers a satisfactory approximation of some of the source characteristics of the reference scenario, but a blurred image of at least the rupture velocity distribution, that is an image deprived of its smallest wavelengths (see also Fig. 5.A.5, which offer a zoomed-in view of

Fig. 5.2).

We can quantify these observations by studying the average spectral properties of these quantities, as we did before when varying the rupture process zone width. As expected, the fall-off rates of absolute slip magnitude (Fig. 5.4b), rupture speed (Fig. 5.5b) and peak slip rate (Fig. 5.7b) increase for wavelengths lower than the cut-off of the low-pass filter (600 m), that is all three rupture parameters are depleted of small-scale variations compared to the reference model. It is worth noticing that this is not obvious when looking at the power spectral density of the absolute slip magnitude and peak slip rate (see Fig. 5.A.2b and 5.A.4b). The rupture speed presents the most striking change in its fall-off rate below 600 m. Such change appears also clearly on the power spectral density (see Fig. 5.A.3b). The model based on the low-pass filtered fault over-predicted the variations of the rupture velocity for wavelengths greater than 600 m.

5.4.3 Heterogeneous tractions as a proxy for small-scale roughness

Our dynamic rupture model with the low-passed filtered fault suggests that rupture kinematics on such fault can resemble those of the reference fault if fault strength is scaled to account for the equivalent roughness drag of the filtered wavelength band. Nevertheless, our model based on a low-passed filtered fault does not properly capture the small-scale variations of some key on-fault kinematic and dynamic source quantities. These small-scale variations might yet be necessary for reproducing specific characteristics of observed high-frequency ground motion.

Fault roughness combined with a laterally-homogeneous stress state leads to highly heterogeneous tractions resolved on the fault. Such traction heterogeneities can be efficiently implemented in numerical schemes relying on high-order basis functions elements (even with low-order meshes) because they can be mapped at subcell resolution. We, therefore, propose and test a hybrid approach to model the effect of fault roughness in which the roughness is effectively meshed only to a given wavelength, while the smallest wavelengths are accounted for by traction heterogeneities, used as a proxy for fault roughness effects.

Traction heterogeneities are not the only effect induced by fault roughness on the earthquake rupture. In particular, a smooth geometry cannot capture transient stress concentrations developing near the kinks of the unaccounted small-scale geometric features. Therefore, traction heterogeneities cannot substitute the full roughness drag effect. We find that traction heterogeneities account for about half of the roughness drag effect in our simulations with the 600 m low-passed filtered fault. In fact, using traction heterogeneities combined with a decrease in the initial stress by half the roughness drag allow recovering an earthquake rupture of overall similar kinematics as the reference model (see Figs. 5.3b, 5.8c, 5.2f, and 5.A.5c).

Quite interestingly, the rupture modeled with such a hybrid approach better matches the amplitude spectral density functions of the rupture speed distribution (Fig. 5.5b). However, the (already satisfying) fits of the amplitude spectral density functions of the fault slip (Fig. 5.4b) and peak slip rate (Fig. 5.7b) are not improved.

Overall, this leads to the power spectral density functions of all kinematics and dynamic properties analyzed satisfactorily matching the power spectral density of the reference model. While further tests might be required to better characterize the limits of such a hybrid approach, it seems to offer a viable alternative to more demanding models in which fault roughness is explicitly meshed over a broader wavelength range, and may allow exploring the effect of smaller-scale geometric complexities.

5.4.4 Ground motion

We here investigate if the ground motion generated by the earthquake ruptures across the low pass-filtered fault (scaled fault strength and hybrid models) resemble those generated by the reference model. In other words, we investigate if the missing smaller-scale fluctuations in the source properties are reflected or not in the ground motion.

In spite of the limited complexity of the models, restricted to the only fault geometry and not accounting for a realistic 3D velocity structure, small-scale scattering or attenuation, the synthetic near-field ground motion compare well, in terms of spectral accelerations at various periods, with selected ground motion prediction equations (GMPE). Fig. 5.9, which shows the variation of the average and intra-event standard deviation of the synthetic spectral acceleration at periods 0.5, 1 and 2.5 s with distance, compared with 3 recents GMPE (Zhao, 2006; Chiou and Youngs, 2008; Akkar and Bommer, 2010), indeed suggests that the generated ground motion are realistic.

We observe that ruptures on both low-pass filtered and reference fault radiate highly similar ground motion (Fig. 5.10). The distribution of spectral acceleration at 9 Hz (highest frequency resolved within the refined mesh box) around the fault of the reference scenario, and of both scenarios based on the 600 m low-pass filtered fault are very similar, even in term of small-scale variations (Fig. 5.11a, b, and c).

We further characterize the synthetics ground accelerations by analyzing their amplitude Fourier spectrum (Fig. 5.12). We compute the median acceleration spectrum over a line of 100 receivers along the fault, all at coordinate y=0 km, that is roughly above the fault. We analyze the average properties of the Fourier spectra by fitting ω^{-2} models. The amplitude Fourier spectrum of near-field ground accelerations from the reference scenario (Fig. 5.12a) and the hybrid approach scenario (Fig. 5.12b) present similar overall properties.

This results may suggest that the smaller-scale fluctuations of the peak slip rate, relatively well captured by the scaled fault strength and hybrid models, are one of the main factor controlling the distribution of near-field ground motion. The smaller-scale fluctuations of the rupture velocity, not captured by the scaled fault strength model, and the smaller-scale fluctuations of the fault slip, not captured by both scaled fault strength and hybrid models, may not reflect significantly in the ground motion.

Fig. 5.12a, c, and d show that the simulated ground acceleration spectra are flat up to a corner frequency which increases with decreasing process zone width (Fig. 5.12). This is expected, as a narrower rupture front, that we can associate with a smaller rise time, will produce higher frequency seismic waves. This is can also be noticed by comparing the amplitude of the 9 Hz spectral accelerations of the scenarios with D_c =0.5 and 0.2 m (Fig. 5.11a, d).

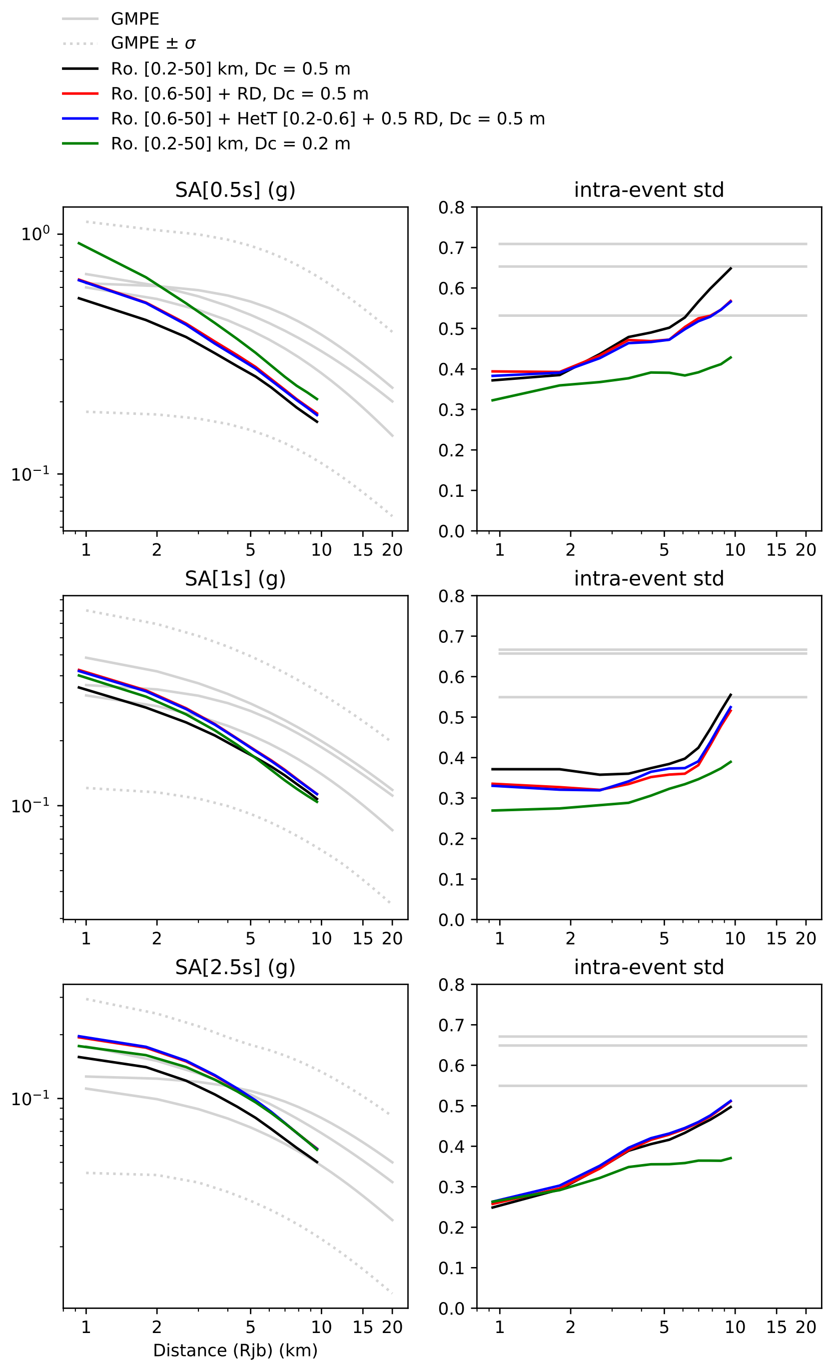

Figure 5.9: Comparison of synthetic near-field ground motion data with 3 recent ground motion prediction equations (GMPE) (Zhao, 2006; Chiou and Youngs, 2008; Akkar and Bommer, 2010). Left: variation of average spectral acceleration at 0.5, 1 and 2.5 s with fault distance. Right: variation of intra-event standard deviation with fault distance.

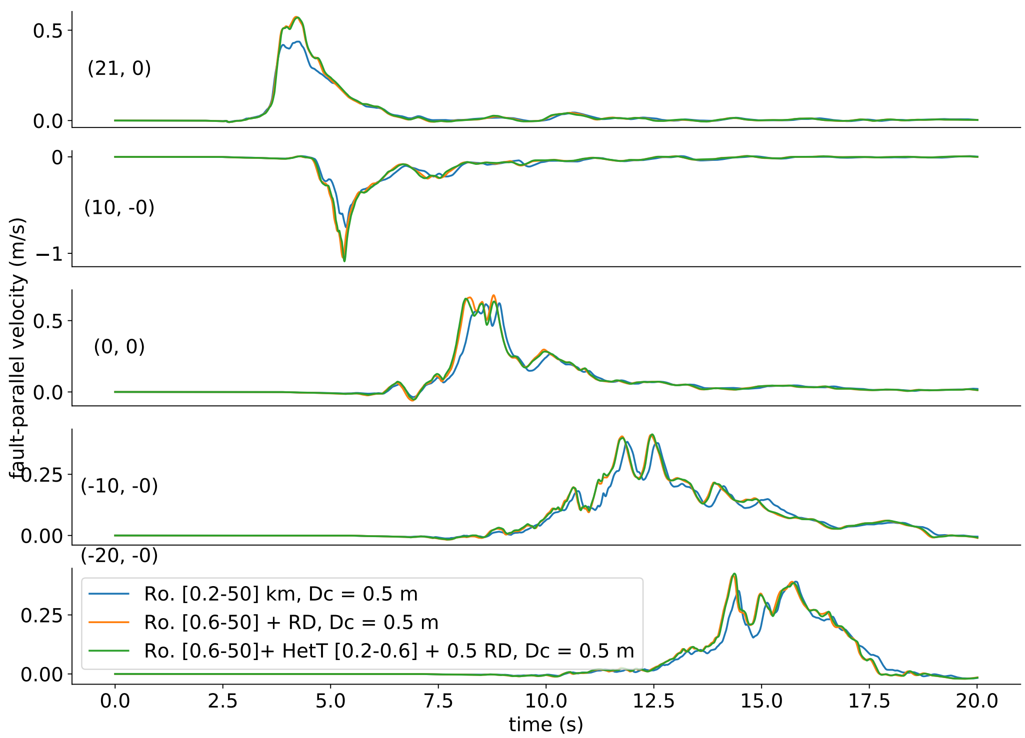

Figure 5.10: fault-parallel velocity time-histories at a 5 receivers above the fault. The receiver coordinates are indicated to the right of each y-axis.

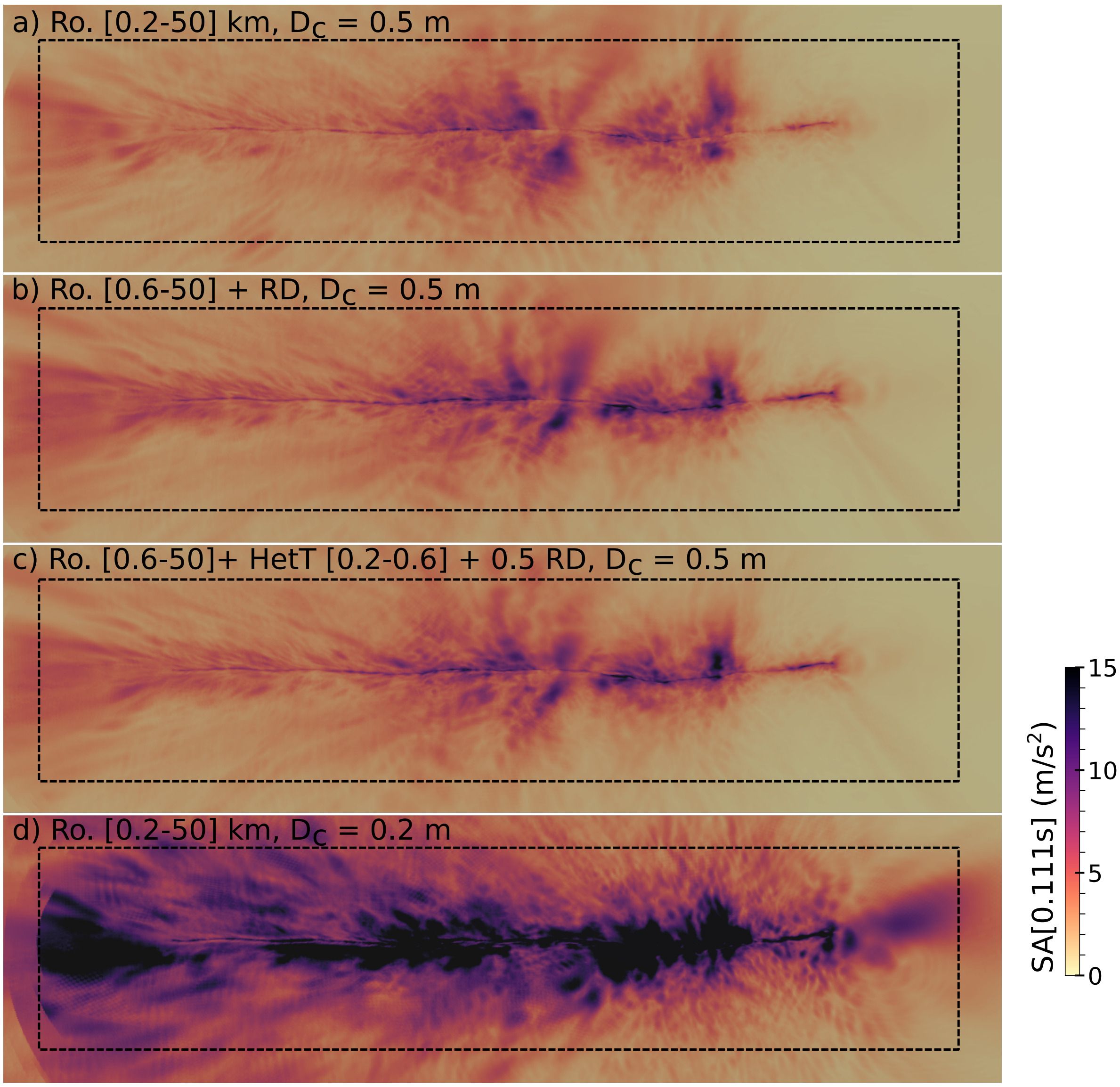

Figure 5.11: Near-field synthetic ground motion distribution: spectral acceleration computed at 9 Hz. The dashed rectangles shows the refined mesh area, over which high-frequency ground motion are properly resolved.

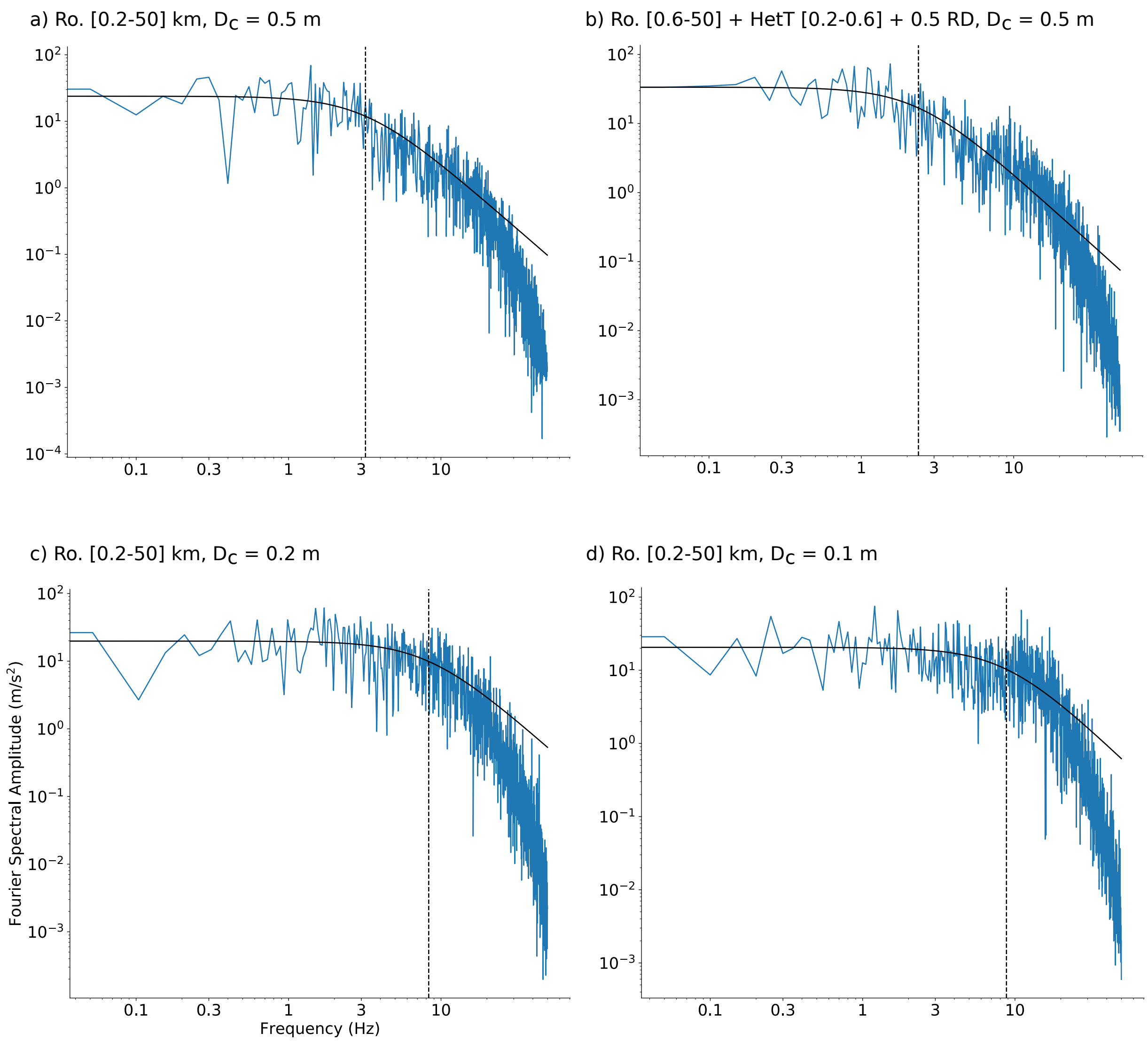

Figure 5.12: Median acceleration spectrum along a line of 100 receivers spaced every 0.5 km between x=−25 km and x=25 km at y=0 km (roughly above the fault). The black line correspond to the ω^{-2} model that best fits the data, and the dashed vertical line to the characteristic frequency of such a model.

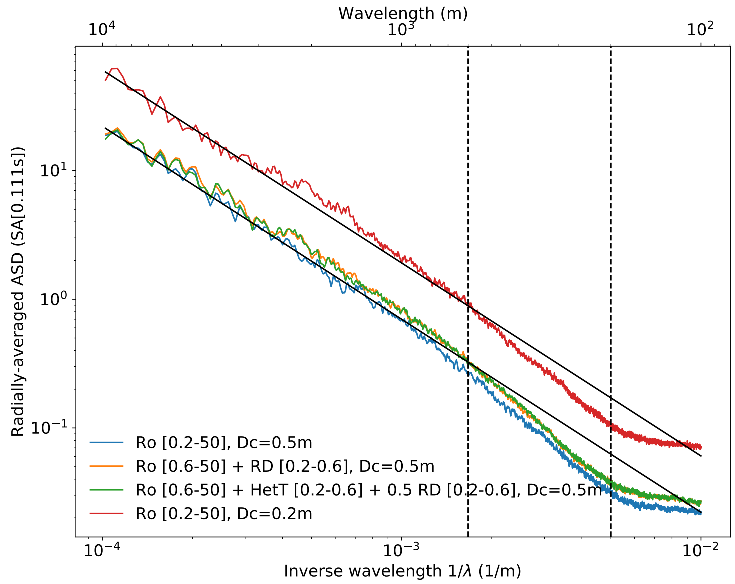

Figure 5.13: Radially-averaged amplitude spectral density of the spectral acceleration at 9 Hz (SA[0.111s]). The black lines illustrate the fall-off of a self-similar model.

On the other hand, the spectral properties of the high frequencies ground-motion distribution (spectral acceleration at 9 Hz, see Fig. 5.13) appear independent of the process zone width in our simulations. Overall, the amplitude spectral distributions of the synthetic ground motion follow the same pattern in all simulations, a fractal distribution, depleted of small-scale variations below 600 m wavelength.

5.5 Discussion

In all our models, fault slip is self-affine but does not deviate as much from self-similarity as inferred by Bruhat et al (2019) from a statistical analysis of 2D dynamic rupture simulations on rough faults. In Bruhat et al (2019), the slip distributions of models featuring a roughness as pronounced as the reference fault of this study (amplitude to wavelength ratio α=0.01) are characterized by Hurst index ranging between 0.55 and 0.7, to be compared with the value of 0.8 we report. The fact that 2D models are more sensitive to fault roughness effects than 3D models might explain such difference. In fact, a rupture front on a 2D rough fault can dodge around geometric asperities which is not the case with a 1D rough fault profile. The use in Bruhat et al (2019) of a different friction law (strong velocity weakening rate and state friction) could also be the cause of the different Hurst index. New simulations using the same friction law could allow determining if the friction law is the source of the observed differences. We note that the rupture scenario we designed may also have singular rupture characteristics. Additional simulations are required to test the sensitivity of our results to fault geometry.

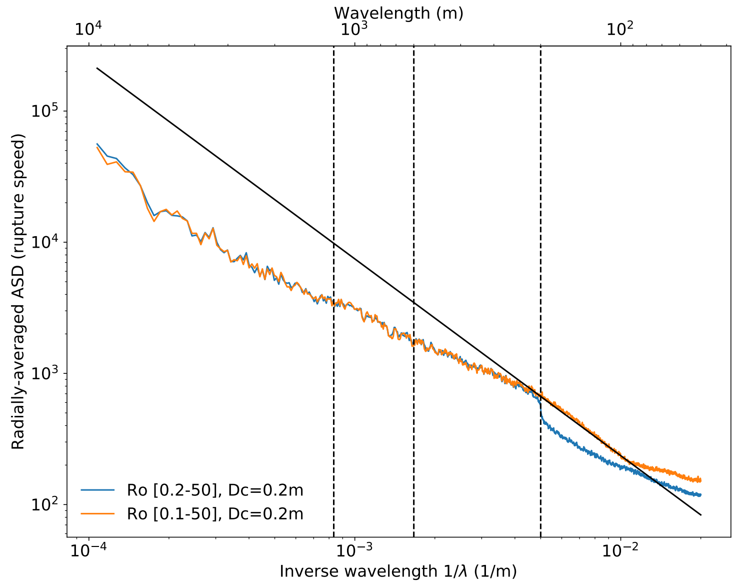

Figure 5.14: Radially-averaged amplitude spectral density of the fault rupture velocity assuming D_c=0.2m and a minimum wavelength for the fault geometry of 100 and 200 m. The black line illustrates the fall-off rate of a self-similar model.

Bruhat et al (2019) report fault slip to become increasingly self-affine at shorter wavelengths, while fault slip in our models decays consistently over the whole wavelength band of the fault roughness. The fact that such an effect is mostly discernible for α lower than 0.006 in Bruhat et al (2019) may explain why we do not see it in our models.

In our study, the rupture speed distribution appears smoother overall when the rupture process zone width is decreased (see e.g. Fig5.5a). It is worth noticing that in our simulations, the rupture process zone width may fall below the smallest wavelength of the roughness when decreasing D_c. For instance, the model featuring D_c=0.1 m is characterized by a breakdown-zone width estimate Λ_0^{III}=85 m, well below the minimum wavelength of our reference fault (200 m). We could then assume that the smaller rupture speed fluctuations at lower D_c are related to the bandlimited roughness, that is some roughness effects are not captured in the simulations with the smallest D_c values. We test this idea by generating a new model in which the roughness is modeled up to 100 m. We use D_c=0.2 m, as this model is associated with Λ_0^{III}=170 m, within the range of the additional wavelengths considered. We recover similar overall kinematics as on the reference fault by increasing the initial shear traction by the roughness drag estimate for the 100 to 200 m wavelengths (This time Δ=1.5 m works better than Δ=1.0 m). The Radially-average amplitude spectral density of the rupture velocity of the new model perfectly aligns with the model based on the coarser fault (Fig. 5.14), suggesting that a smooth rupture speed distribution is not an artifact of the bandlimited roughness, but a real characteristic of a smaller process zone width.

We did not notice any significant difference in the temporal and spatial distribution of ground motion emitted by the rupture hosted on the low-pass filtered fault compared with the reference scenario. Dunham et al (2011b) show that a rupture propagating at constant rupture speed v_r on a fault presenting sinusoidal-shaped fault of wavelength λ results in oscillating ground-motion acceleration records of frequency v_r/λ. We could, therefore, expect that wavelengths in the range 200 to 600 m emit mostly in the range 5 to 15 Hz, assuming an average rupture speed of 3 km. While our simulation does not capture the upper part of this frequency range, we observe that the ground-motion acceleration spectrum of both reference rupture and of the rupture on the low-pass filtered fault compare well in the lower part of the frequency range (see Figs. 5.12a,b). Further simulations are required for better constraining the minimum length scale of fault roughness to be resolve to properly capture ground motion up to a given frequency.

While low-passed filtered and reference simulation do not differ significantly in terms of high-frequency spectral acceleration and Fourier spectrum, other ground motion estimates may allow identifying features of the ground motion not captured properly by the derived scenario. For instance, Withers et al (2019b) suggest that small-scale velocity and density perturbation are not required to match ground motion prediction equations in terms of spectral acceleration, but are necessary for matching more complex proxy metrics characterizing ground motion.

Our simple models offer a new understanding of fault roughness effects but do not allow an exhaustive statistical characterization of these effects. We decided to restrict the complexity of the models to the only fault geometry to allow isolating the effects of fault roughness on the rupture and ground motion from other complexities. The main inferences we made should now be confirmed and complemented by a more systematic follow-up study. This may include alternative fault geometries, initial stress orientation and magnitude, fault strength, faulting mechanisms, and off-fault plasticity parametrization. The sensitivity of our results to additional complexity, such as attenuation, 3D velocity structure, scattering, local heterogeneities in the initial stress state due to squeezing of the elastic asperity of the two self-affine planes constituting the fault (Schmittbuhl et al, 2006), should also be analyzed in future studies.

5.6 Conclusion

Using 3D dynamic rupture modeling, we investigate the potential scale dependence of fault roughness effects. Our models allow identifying an overall (affecting similarly all length scales) dependence of roughness effects on the rupture process zone width. Models featuring a larger rupture process zone width tend to have more coherent rupture fronts and a more uniform rupture speed distribution. We also observe a systematic change in the spectral fall-off rate of the peak slip rate distribution at the length scale posed by the process zone width, which suggests that such length scale plays a critical role in modulating fault roughness dynamic effects. On the other hand, the spectral content of the fault slip and the rupture speed is consistently fractal over all scales, suggesting that such critical behavior is not an intrinsic characteristic of fault roughness effects.

Secondly, we develop a novel hybrid approach that allows emulating the dynamic behavior of rupture across finely sampled rough faults, using a coarser geometric fault representation. Guided by the first part of the study, we propose to filter the reference fault at wavelengths smaller than the process zone width estimate. The roughness is then effectively meshed only to a given wavelength, while the smallest wavelengths are accounted for by traction heterogeneities, used as a proxy for fault roughness effects. The hybrid approach offers an interesting compromise between computational efficiency and accuracy, especially for high-order numerical schemes based on a low-order mesh.

We study the near-field ground motion generated by the dynamic rupture models. Ruptures on both low-pass filtered and reference fault yield high-frequency (up to about 10 Hz) ground motion with a high degree of similarity statistically. This may be explained by the fact that the smaller-scale fluctuations of the peak slip rate are relatively well captured by the hybrid model, because only wavelengths below the estimated process zone width have been filtered.

Altogether, these results advance the understanding of fault roughness effects and should offer avenues for conducting efficiently physics-based seismic hazard characterization, integrating the synthetics of thousands of dynamic rupture simulation on rough faults.

5.7 Acknowledgements

We thank Prof. Martin Mai and Prof Jean-Paul Ampuero for fruitful discussions and detailed comments.

The authors acknowledge funding from the Volkswagen Foundation (project “ASCETE”, grant no. 88479), the European Union’s Horizon 2020 research and innovation programme (ChEESE project, grant agreement No. 823844; TEAR ERC Starting grant no. 852992), the German Research Foundation (DFG) (projects KA 2281/4-1, GA 2465/2-1, GA 2465/3-1), by KAUST-CRG (GAST, grant no. ORS-2016-CRG5-3027 and FRAGEN, grant no. ORS-2017-CRG6 3389.02), by KONWIHR – the Bavarian Competence Network for Technical and Scientific High Performance Computing (project NewWave), and by BayLat – the Bavarian University Centre for Latin America. Computing resources were provided by the Institute of Geophysics of LMU Munich Oeser et al (2006) and the Leibniz Supercomputing Centre (LRZ, projects no. h019z, pr63qo, and pr45fi).

Appendix

5.A Appendix

5.A.1 Roughness power spectrum

The roughness of a surface can be characterized by the roughness power spectrum C(k) defined by:

$$C(\mathbf{k}) = \frac{1}{(2\pi)^2} \int < h(x)h(0) > e^{-i\mathbf{k}x} \, \mathrm{d}x^2 \tag{5.4}$$

where $\mathbf{k}$ is the wavenumber, $x = (x, y)$ is the position on the surface and $h(x)$ is the associated height measured from the average surface plane. The ensemble average operator <...>is obtained by averaging the quantity bracketed over a set of surfaces presenting similar statistical properties. The power spectrum can also be identified as the Fourier transform of the pair correlation function <h(x)h(0)>.

The power spectrum of a self-affine surface follows a power-law behaviour (e.g., Persson et al, 2004):

$$C(\mathbf{k}) \sim k^{-2(H+1)} \tag{5.5}$$

where $k = |\mathbf{k}|$ and H, the Hurst index, characterizes the fall-off rate of the power-law.

5.A.2 Root-mean-square roughness

The power spectrum is fully characterized by H and by the amplitude to wavelength ratio α, the ratio between the root-mean-square roughness h_{rms} and the fault length. h_{rms} is indeed dominated by the longest wavelength of the roughness range for self-affine surfaces:

$$\begin{aligned} h_{\mathrm{rms}}^2 =< h^2 >= 2\pi \int_{k_0}^{k_1} C(k) k \mathrm{d}k \sim \int_{k_0}^{k_1} k^{-2H-1} \mathrm{d}k \\ h_{\mathrm{rms}}^2 \sim (k_0^{-2H} - k_1^{-2H}) \sim k_0^{-2H} \end{aligned} \tag{5.6}$$

which can we written more simply as:

$$h_{\mathrm{rms}} = \alpha L^H \tag{5.7}$$

with L the fault length.

5.A.3 Root-mean-square slope

The average root-mean-square slope s_{rms} of a fractal surface can be derived as in eq. 5.6 by adding a factor k^2 to the power spectral function, related to the spatial derivation.

$$\begin{aligned} s_{\mathrm{rms}}^2 = 2\pi \int_{k_0}^{k_1} C(k) k^3 \mathrm{d}k \sim \int_{k_0}^{k_1} k^{-2H+1} \mathrm{d}k \\ s_{\mathrm{rms}}^2 \sim (k_0^{-2(H-1)} - k_1^{-2(H-1)}) \sim k_1^{-2(H-1)} \text{ for } H < 1 \\ s_{\mathrm{rms}}^2 \sim \ln(k_1/k_0) \text{ for } H = 1 \end{aligned} \tag{5.8}$$

5.A.4 Estimating the rupture process zone width

The effective breakdown-zone width L_0 can be estimated in the simulations from the rupture time t_r, the dynamic weakening time t_d and the rupture velocity v_r.

$$L_0 = v_r(t_d - t_r) \tag{5.9}$$

t_r is defined as the time where the slip rate exceeds $0.01\,\mathrm{m/s^2}$. t_d is the time where the fault slip reaches D_c. v_r is calculated as the inverse of the slowness, which itself is calculated from the spatial derivatives of t_r.

Fig. 5.A.1 presents the distribution of rupture process zone width estimated for our reference dynamic rupture model, with D_c=0.5 m.

5.A.5 Power spectral density

In this study, we study the spectral properties of various rupture parameters using the amplitude spectral density, while it is more usual to use the power spectral density. In fact, we find that the amplitude spectral density is more sensitive and therefore more suitable than the power spectral density for identifying subtle changes in the fractal properties of the rupture dynamic properties distribution. In this section, we plot the power spectral density distribution of all studied models (Fig. 5.A.2, 5.A.3, and 5.A.4) for comparison with the amplitude spectral density plots (Fig. 5.4, 5.5, and 5.7).

5.A.6 Small-scale spatial variations of the source properties

Here we show a zoomed-in view (Fig. 5.A.5) of the rupture properties for the reference model, the model based on a coarser fault and the model based on the hybrid approach developed in this study, which allows identifying the loss of the small-scale heterogeneity of some source parameters when using a coarser rough fault representation.

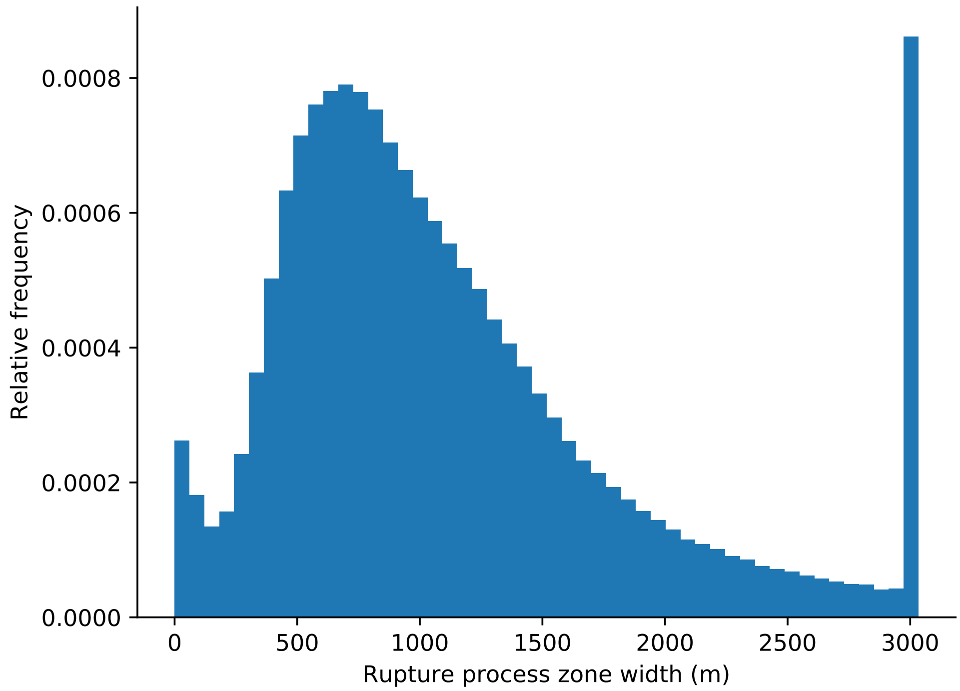

Figure 5.A.1: Histogram of the estimated rupture process zone width in the reference simulation featuring D_c=0.5 m and fault roughness in the range 200 m to 50 km. The large bin at 3000 m corresponds to all rupture process zone width greater than 3000 m.

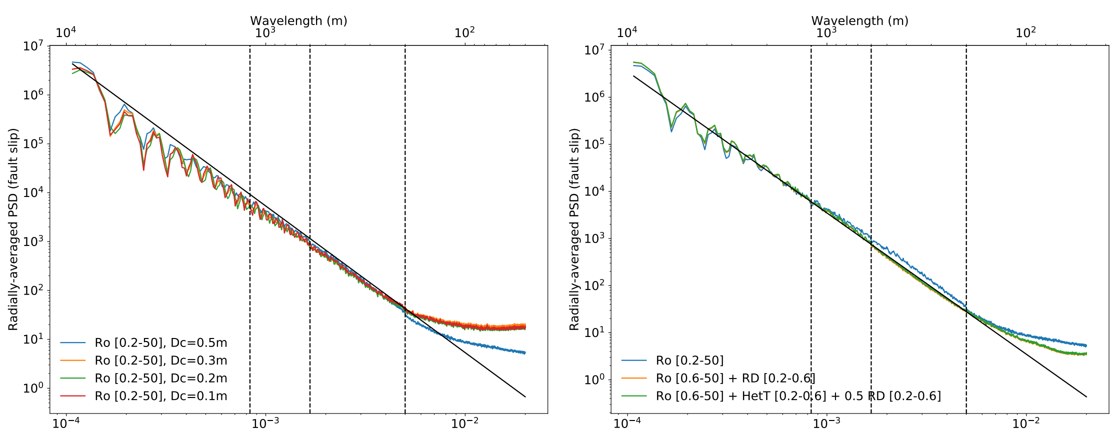

Figure 5.A.2: Radially-averaged power spectral density of the fault final slip. The black line illustrates the fall-off of a self-similar model. See caption of Fig. 5.3 for more details about a) and b).

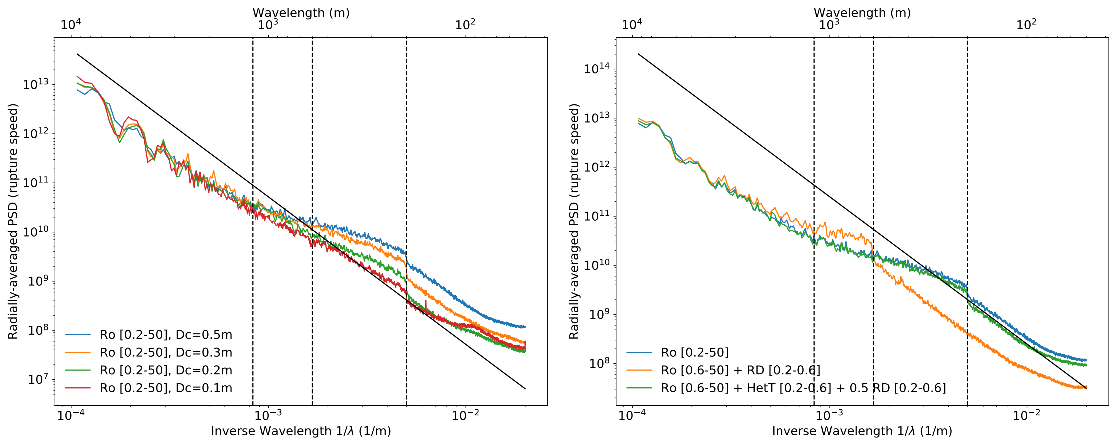

Figure 5.A.3: Radially-averaged power spectral density of the rupture velocity. See caption of Fig. 5.3 for more details about a) and b)

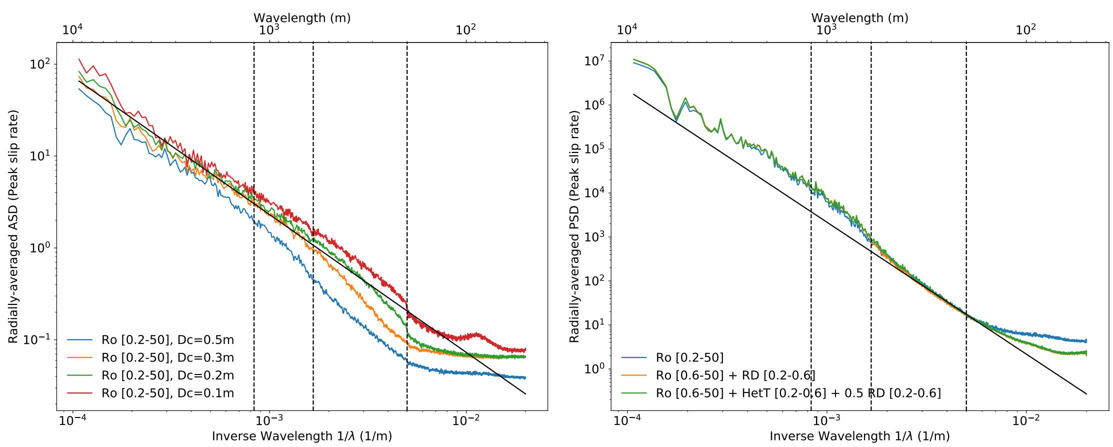

Figure 5.A.4: Radially-averaged power spectral density of the peak slip rate. See caption of Fig. 5.3 for more details about a) and b)

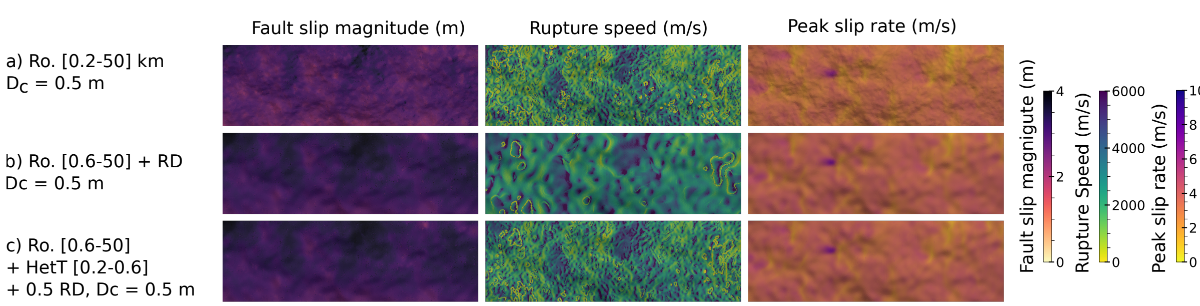

Figure 5.A.5: Source properties of simulated earthquake ruptures: final slip magnitude (first column, m), rupture speed (second, column, m/s) and peak slip rate (third column, m/s). The simulations (a) to (c) are detailed in the caption of Fig. 5.8. This figure offers zoomed-in snapshots of some of plots of Fig. 5.2.

6 Conclusion

In this thesis, I use 3D dynamic rupture modeling to understand the dynamics of previous large earthquakes and, more generally, to advance the physical understanding of coseismic processes on natural faults.

I first focus on the dynamics of the 2016 M_w 7.8 Kaikōura earthquake, which is arguably considered the most complex rupture observed to date. It caused surface rupture of at least 21 segments of the Marlborough fault system. I present a 3D dynamic rupture scenario of the event, which combines an unprecedented degree of realism, including a modern laboratory-based friction law, off-fault inelasticity, seismological estimates of regional stress, a realistic fault network geometry model, a 3D subsurface velocity model, and high-resolution topography and bathymetry. The model reproduces key characteristics of the event and constrains puzzling features including a large gap separating surface rupture traces, the possibility of significant slip on the subduction interface, the non-rupture of the Hope fault, and slow apparent rupture speed. The dynamic rupture model sheds light on the physical mechanisms of cascading ruptures in complex fault systems. The observed rupture cascade is dynamically consistent with regional stress estimates and a crustal fault network geometry inferred from seismic and geodetic data under the assumption of low apparent friction.

I then present a coupled, physics-based scenario of the 2018 Palu, Sulawesi earthquake and tsunami, constrained by rapidly available observations. The proposed 3D dynamic rupture scenario of the earthquake, featuring sustained supershear rupture propagation, matches key observed earthquake characteristics, including the moment magnitude, rupture duration, fault plane solution, teleseismic waveforms and inferred horizontal ground displacements. The model predicts strike-slip faulting with a normal slip component within the Palu Bay. Such a normal-faulting component, resulting from transtension, prevailing in this region, and the fault system geometry, produces a vertical step across the submarine fault segment of 1.5 m on average within the Bay, which is sufficient to produce reasonable tsunami amplitude and inundation elevations. This suggests that the primary tsunami source, a key riddle of the event, may have been coseismically generated vertical displacements.

Next, I explore the dynamics of the 2004, M_w 9.1 - 9.3 Sumatra-Andaman earthquake. Very large-scale dynamic rupture models of the event, combined with tsunami models, allow identifying controlling mechanisms of the event's unexpected kinematics and dynamics and studying the effect of dynamic 3D on- and off-fault deformation on tsunami genesis. The dynamic rupture scenario I develop incorporates a 3D structural model of the subduction region, high-resolution bathymetry, and topography combined with observational inferred regional tectonic stresses, rigidity, frictional strength, fluid pressure, and convergence rates. The earthquake scenario matches key observed characteristics, including the moment magnitude release, rupture duration, fault plane solutions, teleseismic waveforms, and ground displacements. It suggests that along-depth variation of trench sediments, including off-fault plastic yielding, as well as along-arc variations of regional stresses and tectonic convergence rates are the dominant factors controlling the event's dynamics and kinematics.

Finally, I investigate the scale-dependence of fault roughness effects on earthquake kinematics, dynamics, and ground motion. 3D dynamic rupture models allow identifying an overall (affecting similarly all length scales) dependence of roughness effects on the rupture process zone width. Models featuring a larger rupture process zone width tend to have more coherent rupture fronts and a more uniform rupture speed distribution. I also identify a systematic change in the spectral fall-off rate of the peak slip rate distribution at the length scale posed by the process zone width, which suggests that such length scale plays a critical role in modulating fault roughness dynamic effects. On the other hand, the spectral content of the fault slip and the rupture speed is consistently fractal over all scales. This suggests that such critical behavior is not an intrinsic characteristic of fault roughness effects. Guided by the first part of the study, I then propose a strategy to capture fault roughness effects on coarser geometric fault representations. This hybrid approach, in which the smallest roughness wavelengths are accounted for by traction heterogeneities, offers an interesting compromise between computational efficiency and accuracy.

Overall, this work demonstrates that realistic multi-physics earthquake simulations accounting for the complex geometry of the fault system can complement state-of-the-art data-driven imaging techniques at better characterizing and understanding the rupture process of earthquakes. Physics-based dynamic-rupture modeling can be especially insightful for studying complex and/or poorly instrumented earthquakes. Dynamic rupture modeling allows assessing the mechanical viability of competing hypotheses proposed to explain puzzling observations.

This work advances our physical understanding of the coseismic processes on natural faults. In particular, it allows better characterizing the conditions leading to such events, and more generally to understand how fault systems operate. The model of the Kaikōura earthquake suggests that its complex fault network operates at low apparent friction thanks to the combined effects of overpressurized fluids, low dynamic friction and stress concentrations induced by deep fault creep. In particular, it allows assessing the contribution of each ingredient to the apparent weakness. The Kaikōura model also suggests that stress concentrations induced by deep fault creep can facilitate rupture cascade over a complex fault system. Both Kaikōura and Palu rupture cascades are facilitated by a complex stress regime, acknowledging transpression or transtension. Such stress regimes, which favor various styles of faulting on differently oriented segments, indeed offer more possibilities of rupture continuation compared to a pure-shear stress regime, favoring only strike-slip faulting.

This work contributes to advancing the current state-of-the-art of modeling earthquake source dynamics. I introduce new procedures to constrain the initial fault stress and relative strength, based on observations and simple theoretical analysis. Such procedures, which rely on static analysis and only a few trial simulations are superior to the common trial-and-error approach and contribute to efficiently reducing the non-uniqueness in dynamic modeling. My modeling of the Sumatra-Andaman earthquake demonstrates that 3D dynamic rupture modeling of megathrust earthquakes is now feasible and is critical to understanding the interplay of subduction mechanics, megathrust earthquakes and tsunami genesis, particularly when observations are sparse.

Finally, this work demonstrates that high-performance computing empowered dynamic rupture modeling can produce well-constrained studies integrating source observations and earthquake physics very quickly after an event occurs. Dynamic rupture modeling can be integrated synergistically with data inversion efforts within the first days following the occurrence of an earthquake, making physics-based interpretations an important part of the rapid earthquake response toolset.

6.1 Perspectives

The new procedures I developed to constrain the initial fault stress and relative strength, based on observations and simple theoretical analysis are now routinely applied for constraining the initial condition of recent puzzling earthquakes. In particular, we build on the experience gained at modeling complex strike-slip earthquakes to develop a realistic scenario of the recent 2019 Ridgequest earthquake sequence (Taufiqurrahman et al, 2019). This earthquake sequence is characterized by a rare variety and amount of quality data. In particular, the SCEC (Southern California Earthquake Center) community models characterize the 3D regional stress regime and velocity structures to a rare level of detail. Also, the dense seismic network and the high-quality satellite data allow mapping the fault network geometry to an unprecedented level of detail. All together, this should allow building a highly realistic model of the earthquake which should teach us much about coseismic processes on natural faults.

The dynamic rupture scenario I developed, based on the known large-scale geometric features of the fault network, may be strongly affected by the incorporation of small-scale fault roughness effects. Introducing small-scale stochastic fault complexity using self-affine statistical models in the geometry of our model is straightforward. Nevertheless, such models can be highly computationally intensive depending on the minimum wavelength of the roughness considered. Therefore, such a follow-up study considering rupture on a network of rough faults will benefit from the results of the study presented in the chapter 5 of this dissertation. In particular, the strategies to efficiently capture fault roughness effects on rupture kinematics and ground motion should allow designing less computationally intensive models. By simulating rupture propagating on complex fault networks, I aim to better understand under which conditions earthquakes can dynamically link on such networks. Such modeling should allow identifying potential implications for seismic hazard assessment. Fig. 6.1 illustrates a modeled rupture on a rough fault network derived from our Kaikōura scenario. In this model, the moderate fault roughness incorporated (amplitude to wavelength ratio α=3×10^{-3}) does not affect much the rupture front overall coherency but perturbs rupture transfers between individual segments.

In future work, I also aim to better account for stress and/or strength variations due to, for example, variations in tectonic loading or stress changes from previous earthquakes. The introduction of self-consistent, physics-based stress and strength states could be obtained by coupling to geodynamic seismic cycle models. Seismic cycle models able to account for 3D complex fault networks are available (e.g., Luo et al, 2017; Aagaard et al, 2008) and will be coupled to SeisSol in the future to achieve more realistic initial conditions.

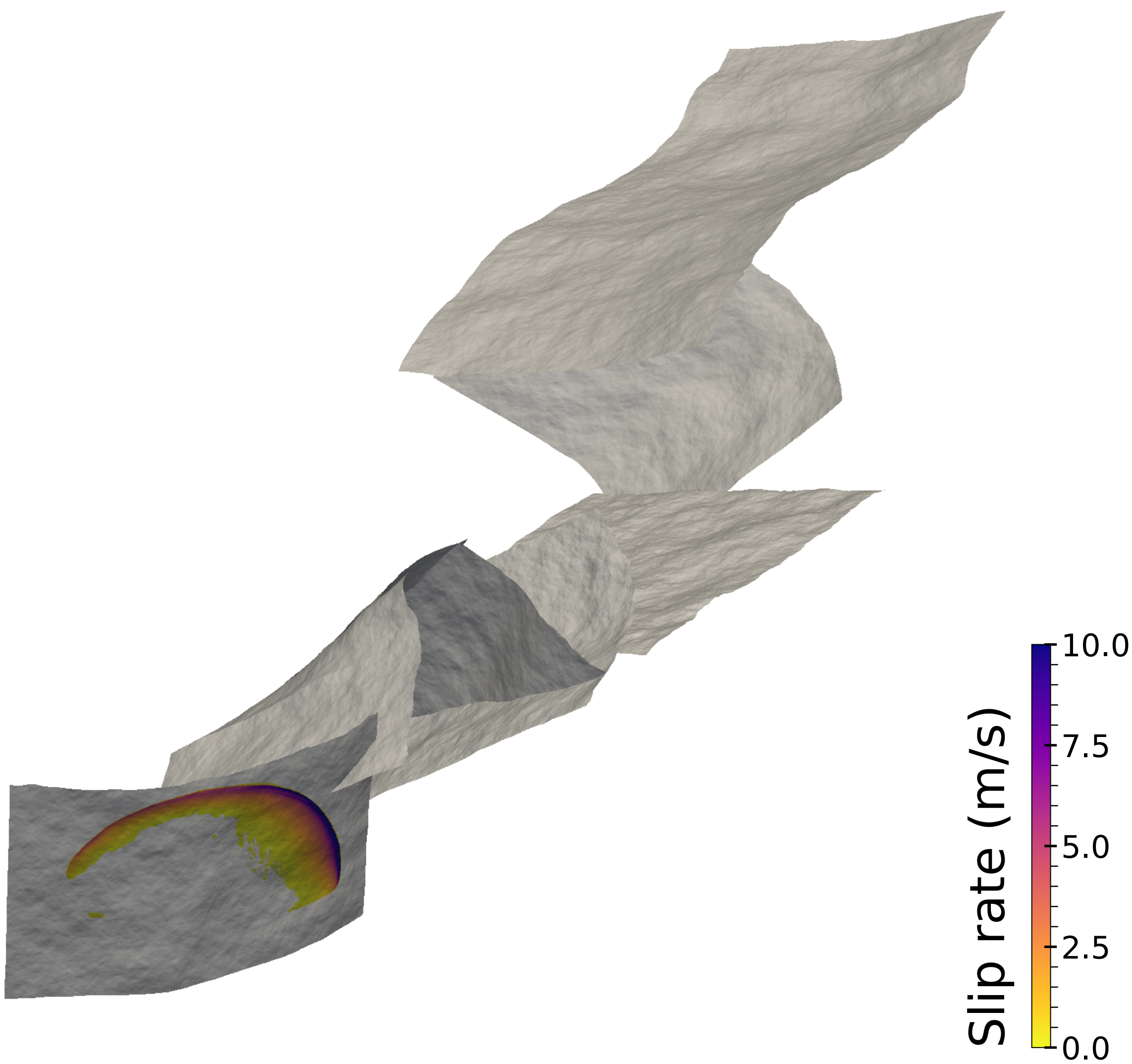

Figure 6.1: Modeled rupture on a the Kaikōura fault network including small-scale roughness. Snapshots of the absolute slip rate are shown at a rupture time of 5 s.

Bibliography

Aagaard B, Williams C, Knepley M (2008) Pylith: A finite-element code for modeling quasi-static and dynamic crustal deformation. Eos Trans AGU 89(53)

Ader T, Avouac JP, Liu-Zeng J, Lyon-Caen H, Bollinger L, Galetzka J, Genrich J, Thomas M, Chanard K, Sapkota SN, Rajaure S, Shrestha P, Ding L, Flouzat M (2012) Convergence rate across the Nepal Himalaya and interseismic coupling on the Main Himalayan Thrust: Implications for seismic hazard. Journal of Geophysical Research: Solid Earth 117(B4), DOI 10.1029/2011JB009071

Akkar S, Bommer JJ (2010) Empirical Equations for the Prediction of PGA, PGV, and Spectral Accelerations in Europe, the Mediterranean Region, and the Middle East. Seismological Research Letters 81(2):195–206, DOI 10.1785/gssrl.81.2.195

Ammon CJ, Ji C, Thio HK, Robinson D, Ni S, Hjorleifsdottir V, Kanamori H, Lay T, Das S, Helmberger D, Ichinose G, Polet J, Wald D (2005) Rupture Process of the 2004 Sumatra-Andaman Earthquake. Science 308(5725):1133–1139, DOI 10.1126/science.1112260

Ampuero JP, Ben-Zion Y (2008) Cracks, pulses and macroscopic asymmetry of dynamic rupture on a bimaterial interface with velocity-weakening friction. Geophysical Journal International 173(2):674–692, DOI 10.1111/j.1365-246X.2008.03736.x

Andrews D (1976) Rupture velocity of plane strain shear cracks. Journal of Geophysical Research 81(32):5679–5687, DOI 10.1029/JB081i032p05679

Andrews D (1985) Dynamic plane-strain shear rupture with a slip-weakening friction law calculated by a boundary integral method. Bulletin of the Seismological Society of America 75(1):1–21

Andrews DJ (2002) A fault constitutive relation accounting for thermal pressurization of pore fluid. Journal of Geophysical Research: Solid Earth 107(B12):ESE 15–1–ESE 15–8, DOI 10.1029/2002JB001942

Andrews DJ (2005) Rupture dynamics with energy loss outside the slip zone. Journal of Geophysical Research: Solid Earth 110(B1), DOI 10.1029/2004JB003191

Aochi H, Ide S (2011) Conceptual multi-scale dynamic rupture model for the 2011 off the Pacific coast of Tohoku Earthquake. Earth, Planets and Space 63(7):761–765, DOI 10.5047/eps.2011.05.008

Aochi H, Madariaga R (2003) The 1999 Izmit, Turkey, earthquake: Nonplanar fault structure, dynamic rupture process, and strong ground motion. Bulletin of the Seismological Society of America 93(3):1249–1266, DOI 10.1785/0120020167

Aochi H, Ulrich T (2015) A Probable Earthquake Scenario near Istanbul Determined from Dynamic Simulations. Bulletin of the Seismological Society of America 105(3):1468–1475, DOI 10.1785/0120140283

Aochi H, Cushing M, Scotti O, Berge-Thierry C (2006) Estimating rupture scenario likelihood based on dynamic rupture simulations: the example of the segmented Middle Durance fault, southeastern France. Geophysical Journal International 165(2):436–446, DOI 10.1111/j.1365-246X.2006.02842.x

Aochi H, Douglas J, Ulrich T (2017) Stress accumulation in the Marmara Sea estimated through ground-motion simulations from dynamic rupture scenarios. Journal of Geophysical Research: Solid Earth 122(3):2219–2235, DOI 10.1002/2016JB013790

Argus DF, Gordon RG, DeMets C (2011) Geologically current motion of 56 plates relative to the no-net-rotation reference frame. Geochemistry, Geophysics, Geosystems 12(11), DOI 10.1029/2011GC003751

Awaliah WO, Yudistira T, Nugraha AD (2018) Identification of 3-d shear wave velocity structure beneath sulawesi island using ambient noise tomography method. In: 10th ACES International Workshop, URL http://quaketm.bosai.go.jp/~shiqing/ACES2018/abstracts/aces_abstract_awaliah.pdf

Bai K, Ampuero JP (2017) Effect of Seismogenic Depth and Background Stress on Physical Limits of Earthquake Rupture Across Fault Step Overs. Journal of Geophysical Research: Solid Earth 122(12):10,280–10,298, DOI 10.1002/2017JB014848

Bai Y, Lay T, Cheung KF, Ye L (2017) Two regions of seafloor deformation generated the tsunami for the 13 November 2016, Kaikoura, New Zealand earthquake. Geophysical Research Letters 44(13):6597–6606, DOI 10.1002/2017GL073717

Banerjee P, Pollitz F, Nagarajan B, Burgmann R (2007) Coseismic Slip Distributions of the 26 December 2004 Sumatra-Andaman and 28 March 2005 Nias Earthquakes from GPS Static Offsets. Bulletin of the Seismological Society of America 97(1A):S86–S102, DOI 10.1785/0120050609

Bao H, Ampuero JP, Meng L, Fielding EJ, Liang C, Milliner CWD, Feng T, Huang H (2019) Early and persistent supershear rupture of the 2018 magnitude 7.5 Palu earthquake. Nature Geoscience 12(3):200–205, DOI 10.1038/s41561-018-0297-z

Bauer A, Scheipl F, Küchenhoff H, Gabriel AA (2017) Modeling spatio-temporal earthquake dynamics using generalized functional additive regression. In: Proceedings of the 32nd International Workshop on Statistical Modelling, vol 2, pp 146–149

Behr WM, Platt JP (2014) Brittle faults are weak, yet the ductile middle crust is strong: Implications for lithospheric mechanics. Geophysical Research Letters 41(22):8067–8075, DOI 10.1002/2014GL061349

Behrens J, Bader M (2009) Efficiency considerations in triangular adaptive mesh refinement. Phil Trans R Soc A 367(1907):4577–4589, DOI 10.1098/rsta.2009.0175

Behrens J, Rakowsky N, Hiller W, Handorf D, Läuter M, Päpke J, Dethloff K (2005) amatos: Parallel adaptive mesh generator for atmospheric and oceanic simulation. Ocean Modelling 10(1–2):171–183, DOI 10.1016/j.ocemod.2004.06.003

Bellier O, Sébrier M, Seward D, Beaudouin T, Villeneuve M, Putranto E (2006) Fission track and fault kinematics analyses for new insight into the Late Cenozoic tectonic regime changes in West-Central Sulawesi (Indonesia). Tectonophysics 413(3-4):201–220, DOI 10.1016/j.tecto.2005.10.036

Beyreuther M, Barsch R, Krischer L, Megies T, Behr Y, Wassermann J (2010) ObsPy: A Python Toolbox for Seismology. Seismological Research Letters 81(3):530–533, DOI 10.1785/gssrl.81.3.530

Bilek SL, Lay T (1999) Rigidity variations with depth along interplate megathrust faults in subduction zones. Nature 400(6743):443–446, DOI 10.1038/22739

Bilham R, Engdahl R, Feldl N, Satyabala SP (2005) Partial and Complete Rupture of the Indo-Andaman Plate Boundary 1847-2004. Seismological Research Letters 76(3):299–311, DOI 10.1785/gssrl.76.3.299

Bird P (2003) An updated digital model of plate boundaries. Geochemistry, Geophysics, Geosystems 4(3), DOI 10.1029/2001GC000252

Bizzarri A, Cocco M (2006) A thermal pressurization model for the spontaneous dynamic rupture propagation on a three-dimensional fault: 1. Methodological approach. Journal of Geophysical Research: Solid Earth 111(B5), DOI 10.1029/2005JB003862

Bletery Q, Sladen A, Jiang J, Simons M (2016) A Bayesian source model for the 2004 great Sumatra-Andaman earthquake. Journal of Geophysical Research: Solid Earth 121(7):5116–5135, DOI 10.1002/2016JB012911

Boore DM, Stewart JP, Seyhan E, Atkinson GM (2014) NGA-West2 Equations for Predicting PGA, PGV, and 5% Damped PSA for Shallow Crustal Earthquakes. Earthquake Spectra 30(3):1057–1085, DOI 10.1193/070113EQS184M

Bormann P, Baumbach M, Bock G, Grosser H, Choy GL, Boatwright J (2002) Seismic sources and source parameters. IASPEI New Manual of Seismological Observatory Practice 1:1–94

Borrero JC, Legg MR, Synolakis CE (2004) Tsunami sources in the southern California bight. Geophysical Research Letters 31:L13,211, DOI 10.1029/2004GL020078

Bradley BA, Razafindrakoto HNT, Polak V (2017) Ground-Motion Observations from the 14 November 2016 M_{w} 7.8 Kaikoura, New Zealand, Earthquake and Insights from Broadband Simulations. Seismological Research Letters 88(3):740–756, DOI 10.1785/0220160225

Breuer A, Heinecke A, Rettenberger S, Bader M, Gabriel AA, Pelties C (2014) Sustained Petascale Performance of Seismic Simulations with SeisSol on SuperMUC. In: Supercomputing. ISC 2014. Lecture Notes in Computer Science, vol 8488, Springer, Cham, pp 1–18, DOI 10.1007/978-3-319-07518-1_1

Breuer A, Heinecke A, Bader M (2016) Petascale Local Time Stepping for the ADER-DG Finite Element Method. In: 2016 IEEE International Parallel and Distributed Processing Symposium (IPDPS), IEEE, Chicago, IL, USA, pp 854–863, DOI 10.1109/IPDPS.2016.109

Bruhat L, Segall P (2017) Deformation rates in northern Cascadia consistent with slow updip propagation of deep interseismic creep. Geophysical Journal International 211(1):427–449, DOI 10.1093/gji/ggx317

Bruhat L, Fang Z, Dunham EM (2016) Rupture complexity and the supershear transition on rough faults. Journal of Geophysical Research: Solid Earth 121(1):210–224, DOI 10.1002/2015JB012512

Bruhat L, Klinger Y, Vallage A, Dunham EM (2019) Influence of fault roughness on surface displacement: from numerical simulations to coseismic slip distributions. preprint, EarthArXiv, DOI 10.31223/osf.io/cnksh

Burridge R (1973) Admissible speeds for plane-strain self-similar shear cracks with friction but lacking cohesion. Geophysical Journal International 35(4):439–455, DOI 10.1111/j.1365-246X.1973.tb00608.x

Byerlee J (1978) Friction of rocks. Pure and Applied Geophysics 116(4-5):615–626, DOI 10.1007/BF00876528

Candela T, Renard F, Klinger Y, Mair K, Schmittbuhl J, Brodsky EE (2012) Roughness of fault surfaces over nine decades of length scales. Journal of Geophysical Research: Solid Earth 117(B8), DOI 10.1029/2011JB009041

Carvajal M, Araya-Cornejo C, Sepúlveda I, Melnick D, Haase JS (2019) Nearly Instantaneous Tsunamis Following the Mw 7.5 2018 Palu Earthquake. Geophysical Research Letters 46(10):5117–5126, DOI 10.1029/2019GL082578

Cesca S, Zhang Y, Mouslopoulou V, Wang R, Saul J, Savage M, Heimann S, Kufner SK, Oncken O, Dahm T (2017) Complex rupture process of the Mw 7.8, 2016, Kaikoura earthquake, New Zealand, and its aftershock sequence. Earth and Planetary Science Letters 478:110–120, DOI 10.1016/j.epsl.2017.08.024

Chauhan APS, Singh SC, Hananto ND, Carton H, Klingelhoefer F, Dessa JX, Permana H, White NJ, Graindorge D, SumatraOBS Scientific Team (2009) Seismic imaging of forearc backthrusts at northern Sumatra subduction zone. Geophysical Journal International 179(3):1772–1780, DOI 10.1111/j.1365-246X.2009.04378.x

Chiou BJ, Youngs RR (2008) An NGA Model for the Average Horizontal Component of Peak Ground Motion and Response Spectra. Earthquake Spectra 24(1):173–215, DOI 10.1193/1.2894832

Chlieh M, Avouac JP, Hjorleifsdottir V, Song TRA, Ji C, Sieh K, Sladen A, Hebert H, Prawirodirdjo L, Bock Y, Galetzka J (2007) Coseismic Slip and Afterslip of the Great Mw 9.15 Sumatra–Andaman Earthquake of 2004. Bulletin of the Seismological Society of America 97(1A):S152–S173, DOI 10.1785/0120050631

Chlieh M, Avouac JP, Sieh K, Natawidjaja DH, Galetzka J (2008) Heterogeneous coupling of the Sumatran megathrust constrained by geodetic and paleogeodetic measurements. Journal of Geophysical Research 113(B5):B05,305, DOI 10.1029/2007JB004981

Clark K, Nissen E, Howarth J, Hamling I, Mountjoy J, Ries W, Jones K, Goldstien S, Cochran U, Villamor P, Hreinsdóttir S, Litchfield N, Mueller C, Berryman K, Strong D (2017) Highly variable coastal deformation in the 2016 MW7.8 Kaikōura earthquake reflects rupture complexity along a transpressional plate boundary. Earth and Planetary Science Letters 474:334–344, DOI 10.1016/j.epsl.2017.06.048

Cockburn B, Shu CW (1998) The Runge-Kutta discontinuous Galerkin method for conservation laws V: Multidimensional systems. Journal of Computational Physics 141(2):199–224, DOI 10.1006/jcph.1998.5892

Conrad CP, Lithgow-Bertelloni C (2002) How Mantle Slabs Drive Plate Tectonics. Science 298(5591):207–209, DOI 10.1126/science.1074161

Copley A (2018) The strength of earthquake-generating faults. Journal of the Geological Society 175(1):1–12, DOI 10.1144/jgs2017-037

Curray JR (2005) Tectonics and history of the Andaman Sea region. Journal of Asian Earth Sciences 25(1):187–232, DOI 10.1016/j.jseaes.2004.09.001

D'Acquisto M, Dal Zilio L, van Dinther Y, Molinari I, Gerya T, Kissling E (2018) Modelling tectonics and seismicity due to slab retreat along the northern apennines thrust belt. In: AGU Fall Meeting 2018, URL https://agu.confex.com/agu/fm18/meetingapp.cgi/Paper/431867

Dal Zilio L, van Dinther Y, Gerya T, Pranger C (2018) Seismic behaviour of mountain belts controlled by plate convergence rate. Earth and Planetary Science Letters 482:81–92, DOI 10.1016/j.epsl.2017.10.053

Dal Zilio L, van Dinther Y, Gerya T, Avouac J (2019) Bimodal seismicity in the himalaya controlled by fault friction and geometry. Nature Communications 10:48, DOI 10.1038/s41467-018-07874-8

Daryono MR (2018) Paleoseismologi Tropis Indonesia (Dengan Studi Kasus Di Sesar Sumatra, Sesar Palukoro-Matano, Dan Sesar Lembang). URL http://docplayer.info/111161004-Paleoseismologi-tropis-indonesia-dengan-studi-kasus-di-sesar-sumatra-sesar-palukoro-matano-dan-sesar-lembang-disertasi.html

Day SM, Dalguer LA, Lapusta N, Liu Y (2005) Comparison of finite difference and boundary integral solutions to three-dimensional spontaneous rupture. Journal of Geophysical Research 110(B12), DOI 10.1029/2005JB003813

De Michele M (2019) Subpixel offsets of copernicus sentinel 2 data, related to the displacement field of the sulawesi earthquake (2018, M_w 7.5). DOI 10.5281/zenodo.2573936

DeDontney N, Rice JR (2012) Tsunami Wave Analysis and Possibility of Splay Fault Rupture During the 2004 Indian Ocean Earthquake. Pure and Applied Geophysics 169(10):1707–1735, DOI 10.1007/s00024-011-0438-4

DeMets C, Gordon RG, Argus DF, Stein S (1994) Effect of recent revisions to the geomagnetic reversal time scale on estimates of current plate motions. Geophysical Research Letters 21(20):2191–2194, DOI 10.1029/94GL02118

DeMets C, Gordon RG, Argus DF (2010) Geologically current plate motions. Geophysical Journal International 181(1):1–80, DOI 10.1111/j.1365-246X.2009.04491.x

DEMNAS (2018) DEMNAS – seamless digital elevation model (DEM) dan batimetri nasional. Badan Informasi Geospasial, URL http://tides.big.go.id/DEMNAS

DesRoches R, Comerio M, Eberhard M, Mooney W, Rix GJ (2011) Overview of the 2010 Haiti Earthquake. Earthquake Spectra 27(S1):S1–S21, DOI 10.1193/1.3630129

Di Toro G, Han R, Hirose T, De Paola N, Nielsen S, Mizoguchi K, Ferri F, Cocco M, Shimamoto T (2011) Fault lubrication during earthquakes. Nature 471(7339):494–498, DOI 10.1038/nature09838

Dieterich JH (1979) Modeling of rock friction: 1. Experimental results and constitutive equations. Journal of Geophysical Research 84(B5):2161, DOI 10.1029/JB084iB05p02161

Dieterich JH, Smith DE (2009) Nonplanar Faults: Mechanics of Slip and Off-fault Damage. Pure and Applied Geophysics 166(10-11):1799–1815, DOI 10.1007/s00024-009-0517-y

van Dinther Y, Gerya T, Dalguer L, Mai P, Morra G, Giardini D (2013) The seismic cycle at subduction thrusts: insights from seismo-thermo-mechanical models. Journal Geophysical Research 118:6183–6202, DOI 10.1002/2013JB010380 van Dinther Y, Mai PM, Dalguer LA, Gerya TV (2014) Modeling the seismic cycle in subduction zones: the role and spatiotemporal occurrence of off-megathrust events. Geophysical Research Letters 41(4):1194–1201, DOI 10.1002/2013GL058886

van Dongeren A, Vatvani D, van Ormondt M (2018) Simulation of 2018 tsunami along the coastal areas in the palu bay. In: AGU Fall Meeting 2018, URL https://agu.confex.com/agu/fm18/meetingapp.cgi/Session/66627

Douilly R, Aochi H, Calais E, Freed AM (2015) Three-dimensional dynamic rupture simulations across interacting faults: The Mw7.0, 2010, Haiti earthquake. Journal of Geophysical Research: Solid Earth 120(2):1108–1128, DOI 10.1002/2014JB011595

Duarte JC, Schellart WP, Cruden AR (2015) How weak is the subduction zone interface? Geophysical Research Letters 42(8):2664–2673, DOI 10.1002/2014GL062876

Dumbser M, Käser M (2006) An arbitrary high-order discontinuous Galerkin method for elastic waves on unstructured meshes – II. the three-dimensional isotropic case. Geophysical Journal International 167(1):319–336, DOI 10.1111/j.1365-246X.2006.03120.x

Dunham EM (2007) Conditions governing the occurrence of supershear ruptures under slip-weakening friction. Journal of Geophysical Research: Solid Earth 112(B7), DOI 10.1029/2006JB004717

Dunham EM, Belanger D, Cong L, Kozdon JE (2011a) Earthquake Ruptures with Strongly Rate-Weakening Friction and Off-Fault Plasticity, Part 1: Planar Faults. Bulletin of the Seismological Society of America 101(5):2296–2307, DOI 10.1785/0120100075

Dunham EM, Belanger D, Cong L, Kozdon JE (2011b) Earthquake Ruptures with Strongly Rate-Weakening Friction and Off-Fault Plasticity, Part 2: Nonplanar Faults. Bulletin of the Seismological Society of America 101(5):2308–2322, DOI 10.1785/0120100076

Duputel Z, Rivera L (2017) Long-period analysis of the 2016 Kaikoura earthquake. Physics of the Earth and Planetary Interiors 265:62–66, DOI 10.1016/j.pepi.2017.02.004

Duru K, Dunham EM (2016) Dynamic earthquake rupture simulations on nonplanar faults embedded in 3d geometrically complex, heterogeneous elastic solids. Journal of Computational Physics 305:185–207, DOI 10.1016/j.jcp.2015.10.021

Eberhart-Phillips D, Reyners M, Bannister S, Chadwick M, Ellis S (2010) Establishing a Versatile 3-D Seismic Velocity Model for New Zealand. Seismological Research Letters 81(6):992–1000, DOI 10.1785/gssrl.81.6.992

England P (2018) On Shear Stresses, Temperatures, and the Maximum Magnitudes of Earthquakes at Convergent Plate Boundaries. Journal of Geophysical Research: Solid Earth 123(8):7165–7202, DOI 10.1029/2018JB015907

Fang Z, Dunham EM (2013) Additional shear resistance from fault roughness and stress levels on geometrically complex faults. Journal of Geophysical Research: Solid Earth 118(7):3642–3654, DOI 10.1002/jgrb.50262

Fichtner A, van Herwaarden DP, Afanasiev M, Simute S, Krischer L, Cubuk-Sabuncu Y, Taymaz T, Colli L, Saygin E, Villasenor A, Trampert J, Cupillard P, Bunge HP, Igel H (2018) The Collaborative Seismic Earth Model: Generation 1. Geophysical Research Letters 45(9):4007–4016, DOI 10.1029/2018GL077338

Field EH, Arrowsmith RJ, Biasi GP, Bird P, Dawson TE, Felzer KR, Jackson DD, Johnson KM, Jordan TH, Madden C, Michael AJ, Milner KR, Page MT, Parsons T, Powers PM, Shaw BE, Thatcher WR, Weldon RJ, Zeng Y (2014) Uniform California Earthquake Rupture Forecast, Version 3 (UCERF3)–The Time-Independent Model. Bulletin of the Seismological Society of America 104(3):1122–1180, DOI 10.1785/0120130164

Fletcher JM, Oskin ME, Teran OJ (2016) The role of a keystone fault in triggering the complex El Mayor-Cucapah earthquake rupture. Nature Geoscience 9(4):303–307, DOI 10.1038/ngeo2660

Fujii Y, Satake K (2007) Tsunami Source of the 2004 Sumatra-Andaman Earthquake Inferred from Tide Gauge and Satellite Data. Bulletin of the Seismological Society of America 97(1A):S192–S207, DOI 10.1785/0120050613

Fujiwara T, Kodaira S, No T, Kaiho Y, Takahashi N, Kaneda Y (2011) The 2011 Tohoku-Oki Earthquake: Displacement Reaching the Trench Axis. Science 334(6060):1240–1240, DOI 10.1126/science.1211554

Gabriel AA, Ampuero JP, Dalguer LA, Mai PM (2012) The transition of dynamic rupture styles in elastic media under velocity-weakening friction. Journal of Geophysical Research: Solid Earth 117(B9), DOI 10.1029/2012JB009468

Gabriel AA, Ampuero JP, Dalguer LA, Mai PM (2013) Source properties of dynamic rupture pulses with off-fault plasticity. Journal of Geophysical Research: Solid Earth 118(8):4117–4126, DOI 10.1002/jgrb.50213

Gabriel AA, Behrens J, Bader M, van Dinther Y, Gunawan T, Madden EH, Rannabauer L, Rettenberger S, Ulrich T, Uphoff C, Vater S, Wollherr S, van Zelst I (2018) S21E-0492: Coupled seismic cycle - Earthquake dynamic rupture - Tsunami models. In: AGU Fall Meeting 2018, Washington, D.C., URL https://agu.confex.com/agu/fm18/meetingapp.cgi/Paper/453669

Gahalaut VK, Gahalaut K (2007) Burma plate motion. Journal of Geophysical Research 112(B10):B10,402, DOI 10.1029/2007JB004928

Gallovič F, Valentová L, Ampuero J, Gabriel A (2019a) Bayesian Dynamic Finite-Fault Inversion: 1. Method and Synthetic Test. Journal of Geophysical Research: Solid Earth p 2019JB017510, DOI 10.1029/2019JB017510

Gallovič F, Valentová L, Ampuero J, Gabriel A (2019b) Bayesian Dynamic Finite-Fault Inversion: 2. Application to the 2016 M_w 6.2 Amatrice, Italy, Earthquake. Journal of Geophysical Research: Solid Earth p 2019JB017512, DOI 10.1029/2019JB017512

Galvez P, Ampuero JP, Dalguer LA, Somala SN, Nissen-Meyer T (2014) Dynamic earthquake rupture modelled with an unstructured 3-D spectral element method applied to the 2011 M9 Tohoku earthquake. Geophysical Journal International 198(2):1222–1240, DOI 10.1093/gji/ggu203

GEBCO (2015) The GEBCO_2014 Grid, version 20150318

Geist EL, Parsons T (2005) Triggering of tsunamigenic aftershocks from large strike-slip earthquakes: Analysis of the November 2000 New Ireland earthquake sequence. Geochemistry, Geophysics, Geosystems 6(10), DOI 10.1029/2005GC000935

Giraldo FX, Warburton T (2008) A high-order triangular discontinuous galerkin oceanic shallow water model. International Journal for Numerical Methods in Fluids 56(7):899–925

de Groot-Hedlin CD (2005) Estimation of the rupture length and velocity of the Great Sumatra earthquake of Dec 26, 2004 using hydroacoustic signals. Geophysical Research Letters 32(11):L11,303, DOI 10.1029/2005GL022695

Guatteri M (2004) A Pseudo-Dynamic Approximation to Dynamic Rupture Models for Strong Ground Motion Prediction. Bulletin of the Seismological Society of America 94(6):2051–2063, DOI 10.1785/0120040037, URL https://pubs.geoscienceworld.org/bssa/article/94/6/2051-2063/147063

Guilbert J (2005) Use of hydroacoustic and seismic arrays to observe rupture propagation and source extent of the $M_w = 9.0$ Sumatra earthquake. Geophysical Research Letters 32(15):L15,310, DOI 10.1029/2005GL022966

Gupta S, Borah K, Saha G (2016) Continental like crust beneath the Andaman Island through joint inversion of receiver function and surface wave from ambient seismic noise. Tectonophysics 687:129–138, DOI 10.1016/j.tecto.2016.09.013

Hamling IJ, Hreinsdóttir S, Clark K, Elliott J, Liang C, Fielding E, Litchfield N, Villamor P, Wallace L, Wright TJ, D'Anastasio E, Bannister S, Burbidge D, Denys P, Gentle P, Howarth J, Mueller C, Palmer N, Pearson C, Power W, Barnes P, Barrell DJA, Van Dissen R, Langridge R, Little T, Nicol A, Pettinga J, Rowland J, Stirling M (2017) Complex multifault rupture during the 2016 M_w 7.8 Kaikōura earthquake, New Zealand. Science 356(6334):eaam7194, DOI 10.1126/science.aam7194

Hardebeck JL (2012) Coseismic and postseismic stress rotations due to great subduction zone earthquakes. Geophysical Research Letters 39(21), DOI 10.1029/2012GL053438

Hardebeck JL (2015) Stress orientations in subduction zones and the strength of subduction megathrust faults. Science 349(6253):1213–1216, DOI 10.1126/science.aac5625

Hardebeck JL, Hauksson E (2001) Crustal stress field in southern California and its implications for fault mechanics. Journal of Geophysical Research: Solid Earth 106(B10):21,859–21,882, DOI 10.1029/2001JB000292

Hardebeck JL, Loveless JP (2018) Creeping subduction zones are weaker than locked subduction zones. Nature Geoscience 11(1):60–64, DOI 10.1038/s41561-017-0032-1

Harig S, Chaeroni, Pranowo WS, Behrens J (2008) Tsunami simulations on several scales: Comparison of approaches with unstructured meshes and nested grids. Ocean Dynamics 58:429–440, DOI 10.1007/s10236-008-0162-5

Harris RA, Day SM (1997) Effects of a low-velocity zone on a dynamic rupture. Bulletin of the Seismological Society of America 87(5):1267–1280

Harris RA, Barall M, Andrews D, Duan B, Ma S, Dunham E, Gabriel AA, Kaneko Y, Kase Y, Aagaard B, et al (2011) Verifying a computational method for predicting extreme ground motion. Seismological Research Letters 82(5):638–644, DOI 10.1785/gssrl.82.5.638

Harris RA, Barall M, Aagaard B, Ma S, Roten D, Olsen K, Duan B, Liu D, Luo B, Bai K, Ampuero J, Kaneko Y, Gabriel A, Duru K, Ulrich T, Wollherr S, Shi Z, Dunham E, Bydlon S, Zhang Z, Chen X, Somala SN, Pelties C, Tago J, Cruz-Atienza VM, Kozdon J, Daub E, Aslam K, Kase Y, Withers K, Dalguer L (2018) A Suite of Exercises for Verifying Dynamic Earthquake Rupture Codes. Seismological Research Letters 89(3):1146–1162, DOI 10.1785/0220170222

Hayes G (2018) Slab2 - A Comprehensive Subduction Zone Geometry Model. DOI 10.5066/F7PV6JNV, URL https://www.sciencebase.gov/catalog/item/5aa1b00ee4b0b1c392e86467, type: dataset

Hayes GP, Briggs RW, Sladen A, Fielding EJ, Prentice C, Hudnut K, Mann P, Taylor FW, Crone AJ, Gold R, Ito T, Simons M (2010) Complex rupture during the 12 January 2010 Haiti earthquake. Nature Geoscience 3(11):800–805, DOI 10.1038/ngeo977

Hayes GP, Wald DJ, Johnson RL (2012) Slab1.0: A three-dimensional model of global subduction zone geometries. Journal of Geophysical Research: Solid Earth 117(B1), DOI 10.1029/2011JB008524

Heaton TH (1990) Evidence for and implications of self-healing pulses of slip in earthquake rupture. Physics of the Earth and Planetary Interiors 64(1):1–20, DOI 10.1016/0031-9201(90)90002-F

Heidarzadeh M, Muhari A, Wijanarto AB (2019) Insights on the Source of the 28 September 2018 Sulawesi Tsunami, Indonesia Based on Spectral Analyses and Numerical Simulations. Pure and Applied Geophysics 176(1):25–43, DOI 10.1007/s00024-018-2065-9

Heidbach O, Rajabi M, Cui X, Fuchs K, Müller B, Reinecker J, Reiter K, Tingay M, Wenzel F, Xie F, Ziegler MO, Zoback ML, Zoback M (2018) The World Stress Map database release 2016: Crustal stress pattern across scales. Tectonophysics 744:484–498, DOI 10.1016/J.TECTO.2018.07.007

Heinecke A, Breuer A, Rettenberger S, Bader M, Gabriel AA, Pelties C, Bode A, Barth W, Liao XK, Vaidyanathan K, Smelyanskiy M, Dubey P (2014) Petascale High Order Dynamic Rupture Earthquake Simulations on Heterogeneous Supercomputers. In: SC14: International Conference for High Performance Computing, Networking, Storage and Analysis, IEEE, New Orleans, LA, USA, pp 3–14, DOI 10.1109/SC.2014.6

Hirose H, Obara K (2005) Repeating short- and long-term slow slip events with deep tremor activity around the Bungo channel region, southwest Japan. Earth, Planets and Space 57(10):961–972, DOI 10.1186/BF03351875

Hok S, Fukuyama E, Hashimoto C (2011) Dynamic rupture scenarios of anticipated Nankai-Tonankai earthquakes, southwest Japan. Journal of Geophysical Research 116(B12), DOI 10.1029/2011JB008492

Holden C, Kaneko Y, D'Anastasio E, Benites R, Fry B, Hamling IJ (2017) The 2016 Kaikōura Earthquake Revealed by Kinematic Source Inversion and Seismic Wavefield Simulations: Slow Rupture Propagation on a Geometrically Complex Crustal Fault Network. Geophysical Research Letters 44(22):11,320–11,328, DOI 10.1002/2017GL075301

Hollingsworth J, Ye L, Avouac JP (2017) Dynamically triggered slip on a splay fault in the M_w 7.8, 2016 Kaikoura (New Zealand) earthquake. Geophysical Research Letters 44(8):3517–3525, DOI 10.1002/2016GL072228

Huang Y, Ampuero JP (2011) Pulse-like ruptures induced by low-velocity fault zones. Journal of Geophysical Research 116(B12), DOI 10.1029/2011JB008684

Hughes KL, Masterlark T, Mooney WD (2010) Poroelastic stress-triggering of the 2005 M8.7 Nias earthquake by the 2004 M9.2 Sumatra–Andaman earthquake. Earth and Planetary Science Letters 293(3-4):289–299, DOI 10.1016/j.epsl.2010.02.043

Iaffaldano G, Bunge HP (2009) Relating rapid plate-motion variations to plate-boundary forces in global coupled models of the mantle/lithosphere system: Effects of topography and friction. Tectonophysics 474(1-2):393–404, DOI 10.1016/j.tecto.2008.10.035

Ida Y (1972) Cohesive force across the tip of a longitudinal-shear crack and Griffith's specific surface energy. Journal of Geophysical Research 77(20):3796–3805, DOI 10.1029/JB077i020p03796

Ide S, Aochi H (2013) Historical seismicity and dynamic rupture process of the 2011 Tohoku-Oki earthquake. Tectonophysics 600:1–13, DOI 10.1016/j.tecto.2012.10.018

IPGP (2018) URL http://geoscope.ipgp.fr/index.php/en/catalog/earthquake-description?seis=us1000h3p4

Ishii M, Shearer PM, Houston H, Vidale JE (2005) Extent, duration and speed of the 2004 Sumatra–Andaman earthquake imaged by the Hi-Net array. Nature 435(7044):933, DOI 10.1038/nature03675

Ito Y, Hino R, Kido M, Fujimoto H, Osada Y, Inazu D, Ohta Y, Iinuma T, Ohzono M, Miura S, Mishina M, Suzuki K, Tsuji T, Ashi J (2013) Episodic slow slip events in the Japan subduction zone before the 2011 Tohoku-Oki earthquake. Tectonophysics 600:14–26, DOI 10.1016/j.tecto.2012.08.022

Jade S, Ananda M, Kumar PD, Banerjee S (2005) Co-seismic and post-seismic displacements in andaman and nicobar islands from gps measurements. Current Science pp 1980–1984

Jeschke A, Pedersen GK, Vater S, Behrens J (2017) Depth-averaged non-hydrostatic extension for shallow water equations with quadratic vertical pressure profile: Equivalence to Boussinesq-type equations. International Journal for Numerical Methods in Fluids 84(10):569–583, DOI 10.1002/fld.4361

Kaiser A, Balfour N, Fry B, Holden C, Litchfield N, Gerstenberger M, D'Anastasio E, Horspool N, McVerry G, Ristau J, Bannister S, Christophersen A, Clark K, Power W, Rhoades D, Massey C, Hamling I, Wallace L, Mountjoy J, Kaneko Y, Benites R, Van Houtte C, Dellow S, Wotherspoon L, Elwood K, Gledhill K (2017) The 2016 Kaikōura, New Zealand, Earthquake: Preliminary Seismological Report. Seismological Research Letters 88(3):727–739, DOI 10.1785/0220170018

Kanamori H (2006) Lessons from the 2004 Sumatra–Andaman earthquake. Philosophical Transactions of the Royal Society A: Mathematical, Physical and Engineering Sciences 364(1845):1927–1945, DOI 10.1098/rsta.2006.1806

Kaneko Y, Fukuyama E, Hamling IJ (2017) Slip-weakening distance and energy budget inferred from near-fault ground deformation during the 2016 M_w 7.8 Kaikōura earthquake. Geophysical Research Letters 44(10):4765–4773, DOI 10.1002/2017GL073681

Kato N (2012) Fracture energies at the rupture nucleation points of large interplate earthquakes. Earth and Planetary Science Letters 353-354:190–197, DOI 10.1016/j.epsl.2012.08.015

Klinger Y (2010) Relation between continental strike-slip earthquake segmentation and thickness of the crust. Journal of Geophysical Research 115(B7):B07,306, DOI 10.1029/2009JB006550

Klinger Y, Okubo K, Vallage A, Champenois J, Delorme A, Rougier E, Lei Z, Knight EE, Munjiza A, Satriano C, Baize S, Langridge R, Bhat HS (2018) Earthquake Damage Patterns Resolve Complex Rupture Processes. Geophysical Research Letters 45(19):10,279–10,287, DOI 10.1029/2018GL078842

Kolecka N, Kozak J (2014) Assessment of the Accuracy of SRTM C- and X-Band High Mountain Elevation Data: a Case Study of the Polish Tatra Mountains. Pure and Applied Geophysics 171(6):897–912, DOI 10.1007/s00024-013-0695-5

Krischer L, Hutko AR, van Driel M, Stähler S, Bahavar M, Trabant C, Nissen-Meyer T (2017) On-demand custom broadband synthetic seismograms. Seismological Research Letters 88(4):1127–1140, DOI 10.1785/0220160210

Kyriakopoulos C, Oglesby DD, Funning GJ, Ryan KJ (2017) Dynamic Rupture Modeling of the M 7.2 2010 El Mayor-Cucapah Earthquake: Comparison With a Geodetic Model. Journal of Geophysical Research: Solid Earth 122(12):10,263–10,279, DOI 10.1002/2017JB014294

Lamb S, Arnold R, Moore JDP (2018) Locking on a megathrust as a cause of distributed faulting and fault-jumping earthquakes. Nature Geoscience 11(11):871–875, DOI 10.1038/s41561-018-0230-5

Laske G, Masters G, Ma Z, Pasyanos M (2013) Update on crust1. 0—a 1-degree global model of earth's crust. In: Geophys. Res. Abstr, EGU General Assembly Vienna, Austria, vol 15, p 2658

Lay T, Kanamori H (2011) Insights from the great 2011 Japan earthquake. Physics Today 64(12):33–39, DOI 10.1063/PT.3.1361

Lay T, Kanamori H, Ammon CJ, Koper KD, Hutko AR, Ye L, Yue H, Rushing TM (2012) Depth-varying rupture properties of subduction zone megathrust faults. Journal of Geophysical Research: Solid Earth 117(B4), DOI 10.1029/2011JB009133

Legg MR, Borrero JC (2001) Tsunami potential of major restraining bends along submarine strike-slip faults. In: Proceedings of the International Tsunami Symposium 2001, NOAA/PMEL, 1, pp 331–342

Legg MR, Borrero JC, Synolakis CE (2003) Tsunami hazards from strike-slip earthquakes. American Geophysical Union, Fall Meeting 2003, abstract id OS21D-06 URL http://adsabs.harvard.edu/abs/2003AGUFMOS21D..06L

Liang C, Fielding EJ (2017) Interferometry with ALOS-2 full-aperture ScanSAR data. IEEE Transactions on Geoscience and Remote Sensing 55(5):2739–2750

Liang Q, Marche F (2009) Numerical resolution of well-balanced shallow water equations with complex source terms. Advances in Water Resources 32:873–884, DOI 10.1016/j.advwatres.2009.02.010

Lin JY, Le Pichon X, Rangin C, Sibuet JC, Maury T (2009) Spatial aftershock distribution of the 26 December 2004 great Sumatra-Andaman earthquake in the northern Sumatra area. Geochemistry, Geophysics, Geosystems 10(5), DOI 10.1029/2009GC002454 de Linage C, Rivera L, Hinderer J, Boy JP, Rogister Y, Lambotte S, Biancale R (2009) Separation of coseismic and postseismic gravity changes for the 2004 Sumatra-Andaman earthquake from 4.6 yr of GRACE observations and modelling of the coseismic change by normal-modes summation. Geophysical Journal International 176(3):695–714, DOI 10.1111/j.1365-246X.2008.04025.x

Litchfield N, Van Dissen R, Sutherland R, Barnes P, Cox S, Norris R, Beavan R, Langridge R, Villamor P, Berryman K, Stirling M, Nicol A, Nodder S, Lamarche G, Barrell D, Pettinga J, Little T, Pondard N, Mountjoy J, Clark K (2014) A model of active faulting in New Zealand. New Zealand Journal of Geology and Geophysics 57(1):32–56, DOI 10.1080/00288306.2013.854256

Litchfield N, Benson A, Bischoff A, Hatem A, Barrier A, Nicol A, Wandres A, Lukovic B, Hall B, Gasston C (2017) 14th November 2016 M7. 8 Kaikoura Earthquake. Summary surface fault rupture traces and displacement measurements. GNS Science

Liu PLF, Barranco I, Fritz HM, Haase JS, Prasetya GS, Qiu Q, Sepulveda I, Synolakis C, Xu X (2018) What we do and don't know about the 2018 Palu Tsunami – A future plan. In: AGU Fall Meeting 2018, URL https://agu.confex.com/agu/fm18/meetingapp.cgi/Paper/476669

Lotto GC, Dunham EM, Jeppson TN, Tobin HJ (2017a) The effect of compliant prisms on subduction zone earthquakes and tsunamis. Earth and Planetary Science Letters 458:213–222, DOI 10.1016/j.epsl.2016.10.050

Lotto GC, Nava G, Dunham EM (2017b) Should tsunami simulations include a nonzero initial horizontal velocity? Earth, Planets and Space 69(1):117, DOI 10.1186/s40623-017-0701-8

Lotto GC, Jeppson TN, Dunham EM (2018) Fully Coupled Simulations of Megathrust Earthquakes and Tsunamis in the Japan Trench, Nankai Trough, and Cascadia Subduction Zone. Pure and Applied Geophysics pp 1–33, DOI 10.1007/s00024-018-1990-y

Løvholt F, Hasan H, Lorito S, Romano F, Brizuela B, Piatanesi A, Pedersen GK (2018) Multiple source sensitivity study to model the 28 September Sulawesi tsunami – landslide and strike slip sources. In: AGU Fall Meeting 2018, Washington, DC, URL https://agu.confex.com/agu/fm18/meetingapp.cgi/Paper/476627

Lund B, Townend J (2007) Calculating horizontal stress orientations with full or partial knowledge of the tectonic stress tensor. Geophysical Journal International 170(3):1328–1335, DOI 10.1111/j.1365-246X.2007.03468.x

Luo Y, Ampuero J, Galvez P, Van den Ende M, Idini B (2017) Qdyn: A quasi-dynamic earthquake simulator (v1. 1). URL: https://github com/ydluo/qdyn

Ma S (2012) A self-consistent mechanism for slow dynamic deformation and tsunami generation for earthquakes in the shallow subduction zone. Geophysical Research Letters 39(11), DOI 10.1029/2012GL051854

Ma S, Nie S (2019) Dynamic Wedge Failure and Along-Arc Variations of Tsunamigenesis in the Japan Trench Margin. Geophysical Research Letters 46(15):8782–8790, DOI 10.1029/2019GL083148

Ma S, Custódio S, Archuleta RJ, Liu P (2008) Dynamic modeling of the 2004 M $_w$ 6.0 Parkfield, California, earthquake. Journal of Geophysical Research: Solid Earth 113(B2), DOI 10.1029/2007JB005216

Madariaga R (1977) High-frequency radiation from crack (stress drop) models of earthquake faulting. Geophysical Journal International 51(3):625–651, DOI 10.1111/j.1365-246X.1977.tb04211.x

Madariaga R, Olsen KB (2000) Criticality of Rupture Dynamics in 3-D. Pure and Applied Geophysics 157(11):1981–2001, DOI 10.1007/PL00001071

Maeda T, Furumura T (2013) FDM Simulation of Seismic Waves, Ocean Acoustic Waves, and Tsunamis Based on Tsunami-Coupled Equations of Motion. Pure and Applied Geophysics 170(1-2):109–127, DOI 10.1007/s00024-011-0430-z

Mai PM (2019) Supershear tsunami disaster. Nature Geoscience 12(3):150–151, DOI 10.1038/s41561-019-0308-8

Mai PM, Schorlemmer D, Page M, Ampuero JP, Asano K, Causse M, Custodio S, Fan W, Festa G, Galis M, et al (2016) The earthquake-source inversion validation (SIV) project. Seismological Research Letters 87(3):690–708, DOI 10.1785/0220150231

Mai PM, Galis M, Thingbaijam KKS, Vyas JC, Dunham EM (2017) Accounting for Fault Roughness in Pseudo-Dynamic Ground-Motion Simulations. Pure and Applied Geophysics 174(9):3419–3450, DOI 10.1007/s00024-017-1536-8, URL http://link.springer.com/10.1007/s00024-017-1536-8

Mansinha L, Smylie DE (1971) The displacement fields of inclined faults. Bull Seis Soc Am 61(5):1433–1440

Massonnet D, Feigl KL (1998) Radar interferometry and its application to changes in the Earth's surface. Reviews of Geophysics 36(4):441–500, DOI 10.1029/97RG03139

McAdoo BG, Richardson N, Borrero J (2007) Inundation distances and run-up measurements from ASTER, QuickBird and SRTM data, Aceh coast, Indonesia. International Journal of Remote Sensing 28(13-14):2961–2975, DOI 10.1080/01431160601091795

McCaffrey R (2009) The Tectonic Framework of the Sumatran Subduction Zone. DOI 10.1146/annurev.earth.031208.100212

Meister O, Rahnema K, Bader M (2016) Parallel, memory efficient adaptive mesh refinement on structured triangular meshes with billions of grid cells. ACM Transactions on Mathematical Software 43(3):19:1–19:27, DOI 10.1145/2947668

Melgar D, Hayes GP (2017) Systematic Observations of the Slip Pulse Properties of Large Earthquake Ruptures. Geophysical Research Letters 44(19):9691–9698, DOI 10.1002/2017GL074916

Meltzner AJ, Sieh K, Abrams M, Agnew DC, Hudnut KW, Avouac JP, Natawidjaja DH (2006) Uplift and subsidence associated with the great Aceh-Andaman earthquake of 2004. Journal of Geophysical Research: Solid Earth 111(B2), DOI 10.1029/2005JB003891

Mena B, Mai PM, Olsen KB, Purvance MD, Brune JN (2010) Hybrid Broadband Ground-Motion Simulation Using Scattering Green's Functions: Application to Large-Magnitude Events. Bulletin of the Seismological Society of America 100(5A):2143–2162, DOI 10.1785/0120080318, URL https://pubs.geoscienceworld.org/bssa/article/100/5A/2143-2162/325193

Mikumo T, Olsen KB, Fukuyama E, Yagi Y (2003) Stress-Breakdown Time and Slip-Weakening Distance Inferred from Slip-Velocity Functions on Earthquake Faults. Bulletin of the Seismological Society of America 93(1):264–282, DOI 10.1785/0120020082

Mildon ZK, Roberts GP, Faure Walker JP, Iezzi F (2017) Coulomb stress transfer and fault interaction over millennia on non-planar active normal faults: the Mw 6.5–5.0 seismic sequence of 2016–2017, central Italy. Geophysical Journal International 210(2):1206–1218, DOI 10.1093/gji/ggx213

Miller MM (2002) Periodic Slow Earthquakes from the Cascadia Subduction Zone. Science 295(5564):2423–2423, DOI 10.1126/science.1071193

Mitchell JS, Mackay KA, Neil HL, Mackay EJ, Pallentin A, Notman P (2012) Undersea New Zealand, 1: 5,000,000. NIWA chart, miscellaneous series (92)

Muhari A, Imamura F, Arikawa T, Hakim AR, Afriyanto B, Ministry of Marine Affairs and Fisheries Jl Medan Merdeka Timur No16, Jakarta, Indonesia, International Research Institute of Disaster Sciences (IRIDeS), Tohoku University, Miyagi, Japan, Chuo University, Tokyo, Japan, Botram Ocean Technology Research and Management, Bandung, Indonesia (2018) Solving the Puzzle of the September 2018 Palu, Indonesia, Tsunami Mystery: Clues from the Tsunami Waveform and the Initial Field Survey Data. Journal of Disaster Research 13(Scientific Communication):sc20181,108, DOI 10.20965/jdr.2018.sc20181108

Müller RD, Roest WR, Royer JY, Gahagan LM, Sclater JG (1997) Digital isochrons of the world's ocean floor. Journal of Geophysical Research: Solid Earth 102(B2):3211–3214

Nanayama F, Satake K, Furukawa R, Shimokawa K, Atwater BF, Shigeno K, Yamaki S (2003) Unusually large earthquakes inferred from tsunami deposits along the Kuril trench. Nature 424(6949):660–663, DOI 10.1038/nature01864

Nicol A, Khajavi N, Pettinga JR, Fenton C, Stahl T, Bannister S, Pedley K, Hyland-Brook N, Bushell T, Hamling I, Ristau J, Noble D, McColl ST (2018) Preliminary Geometry, Displacement, and Kinematics of Fault Ruptures in the Epicentral Region of the 2016 Mw 7.8 Kaikōura, New Zealand, Earthquake. Bulletin of the Seismological Society of America 108(3B):1521–1539, DOI 10.1785/0120170329

Noda H, Dunham EM, Rice JR (2009) Earthquake ruptures with thermal weakening and the operation of major faults at low overall stress levels. Journal of Geophysical Research: Solid Earth 114(B7), DOI 10.1029/2008JB006143

Oeser J, Bunge HP, Mohr M (2006) Cluster design in the earth sciences: Tethys. In: International conference on high performance computing and communications, Springer, pp 31–40

Oglesby DD (2005) The Dynamics of Strike-Slip Step-Overs with Linking Dip-Slip Faults. Bulletin of the Seismological Society of America 95(5):1604–1622, DOI 10.1785/0120050058

Okada Y (1985) Surface deformation due to shear and tensile faults in a half-space. Bulletin of the Seismological Society of America 75(4):1135

Okal EA, Fritz HM, Synolakis CE, Borrero JC, Weiss R, Lynett PJ, Titov VV, Foteinis S, Jaffe BE, Liu PLF, Chan Ic (2010) Field Survey of the Samoa Tsunami of 29 September 2009. Seismological Research Letters 81(4):577–591, DOI 10.1785/gssrl.81.4.577

Okuda T, Ide S (2018) Hierarchical rupture growth evidenced by the initial seismic waveforms. Nature Communications 9(1):3714, DOI 10.1038/s41467-018-06168-3

Okuwaki R, Yagi Y, Shimizu K (2018) rokuwaki/2018paluindonesia: v2.0. DOI 10.5281/zenodo.1469007

Olsen KB, Madariaga R, Archuleta RJ (1997) Three-Dimensional Dynamic Simulation of the 1992 Landers Earthquake. Science 278(5339):834–838, DOI 10.1126/science.278.5339.834

Olsen KB, Day SM, Dalguer LA, Mayhew J, Cui Y, Zhu J, Cruz-Atienza VM, Roten D, Maechling P, Jordan TH, Okaya D, Chourasia A (2009) ShakeOut-D: Ground motion estimates using an ensemble of large earthquakes on the southern San Andreas fault with spontaneous rupture propagation. Geophysical Research Letters 36(4), DOI 10.1029/2008GL036832

Omira R, Dogan GG, Hidayat R, Husrin S, Prasetya G, Annunziato A, Proietti C, Probst P, Paparo MA, Wronna M, Zaytsev A, Pronin P, Giniyatullin A, Putra PS, Hartanto D, Ginanjar G, Kongko W, Pelinovsky E, Yalciner AC (2019) The September 28th, 2018, Tsunami In Palu-Sulawesi, Indonesia: A Post-Event Field Survey. Pure and Applied Geophysics 176(4):1379–1395, DOI 10.1007/s00024-019-02145-z

Osei Tutu A, Sobolev SV, Steinberger B, Popov AA, Rogozhina I (2018) Evaluating the Influence of Plate Boundary Friction and Mantle Viscosity on Plate Velocities. Geochemistry, Geophysics, Geosystems 19(3):642–666, DOI 10.1002/2017GC007112

Pelinovsky E, Yuliadi D, Prasetya G, Hidayat R (1997) The 1996 Sulawesi Tsunami. Natural Hazards 16(1):29–38, DOI 10.1023/A:1007904610680

Pelties C, de la Puente J, Ampuero JP, Brietzke GB, Käser M (2012) Three-dimensional dynamic rupture simulation with a high-order discontinuous Galerkin method on unstructured tetrahedral meshes. Journal of Geophysical Research: Solid Earth 117(B2), DOI 10.1029/2011JB008857

Pelties C, Gabriel AA, Ampuero JP (2013) Verification of an ADER-DG method for complex dynamic rupture problems. Geoscientific Model Development Discussions 6:5981–6034, DOI 10.5194/gmdd-6-5981-2013

Pelties C, Gabriel AA, Ampuero JP (2014) Verification of an ADER-DG method for complex dynamic rupture problems. Geoscientific Model Development 7(3):847–866, DOI 10.5194/gmd-7-847-2014

Persson B, Albohr O, Tartaglino U, Volokitin A, Tosatti E (2004) On the nature of surface roughness with application to contact mechanics, sealing, rubber friction and adhesion. Journal of Physics: Condensed Matter 17(1):R1

Pettinga JR, Yetton MD, Van Dissen RJ, Downes G (2001) Earthquake source identification and characterisation for the Canterbury region, South Island, New Zealand

Peyrat S, Olsen K, Madariaga R (2001) Dynamic modeling of the 1992 Landers earthquake. Journal of Geophysical Research: Solid Earth 106(B11):26,467–26,482, DOI 10.1029/2001JB000205

Platt JP (1993) Mechanics of oblique convergence. Journal of Geophysical Research 98(B9):16,239, DOI 10.1029/93JB00888

Poisson B, Oliveros C, Pedreros R (2011) Is there a best source model of the Sumatra 2004 earthquake for simulating the consecutive tsunami? Geophysical Journal International 185(3):1365–1378, DOI 10.1111/j.1365-246X.2011.05009.x

Power W, Clark K, King DN, Borrero J, Howarth J, Lane EM, Goring D, Goff J, Chagué-Goff C, Williams J, Reid C, Whittaker C, Mueller C, Williams S, Hughes MW, Hoyle J, Bind J, Strong D, Litchfield N, Benson A (2017) Tsunami runup and tide-gauge observations from the 14 November 2016 M7.8 Kaikōura earthquake, New Zealand. Pure and Applied Geophysics 174(7):2457–2473, DOI 10.1007/s00024-017-1566-2

Power WL, Tullis TE (1991) Euclidean and fractal models for the description of rock surface roughness. Journal of Geophysical Research 96(B1):415, DOI 10.1029/90JB02107

Prasetya GS, De Lange WP, Healy TR (2001) The Makassar Strait Tsunamigenic region, Indonesia. Natural Hazards 24(3):295–307, DOI 10.1023/A:1012297413280

Preuss S, Herrendörfer R, Gerya T, Ampuero JP, Dinther Y (2019) Seismic and aseismic fault growth lead to different fault orientations. Journal of Geophysical Research: Solid Earth DOI 10.1029/2019JB017324

Pribadi S, Nugraha J, Susanto E, Chandra, Gunawan I, Haryono T, Hery I (2018) Laporan pendahuluan gempabumi dan tsunami donggala-palu 2018 (*Preliminary report on the Donggala-Palu 2018 earthquake and tsunami*). Pers. comm.

Puente Jdl, Ampuero JP, Käser M (2009) Dynamic rupture modeling on unstructured meshes using a discontinuous Galerkin method. Journal of Geophysical Research: Solid Earth 114(B10), DOI 10.1029/2008JB006271

Quantum GIS (2013) Development team. Quantum GIS geographic information system. Open Source geospatial foundation project

Reid HF (1911) The elastic-rebound theory of earthquakes. Univ Calif Publ Bull Dept Geol 6(19):413–444

Rettenberger S, Meister O, Bader M, Gabriel AA (2016) Asagi: A parallel server for adaptive geoinformation. In: Proceedings of the Exascale Applications and Software Conference 2016, ACM, New York, NY, USA, EASC '16, pp 2:1–2:9, DOI 10.1145/2938615.2938618

Rhie J, Dreger D, Bürgmann R, Romanowicz B (2007) Slip of the 2004 Sumatra–Andaman Earthquake from Joint Inversion of Long-Period Global Seismic Waveforms and gps Static Offsets. Bulletin of the Seismological Society of America 97(1A):S115–S127, DOI 10.1785/0120050620

Rice JR (2006) Heating and weakening of faults during earthquake slip. Journal of Geophysical Research: Solid Earth 111(B5), DOI 10.1029/2005JB004006

Rikitake T (1976) Recurrence of great earthquakes at subduction zones. Tectonophysics 35(4):335–362, DOI 10.1016/0040-1951(76)90075-5

Ripperger J, Ampuero JP, Mai PM, Giardini D (2007) Earthquake source characteristics from dynamic rupture with constrained stochastic fault stress. Journal of Geophysical Research: Solid Earth 112(B4), DOI 10.1029/2006JB004515

Rogers G (2003) Episodic Tremor and Slip on the Cascadia Subduction Zone: The Chatter of Silent Slip. Science 300(5627):1942–1943, DOI 10.1126/science.1084783

Rosen PA, Gurrola E, Sacco GF, Zebker H (2012) The insar scientific computing environment. In: Synthetic Aperture Radar, 2012. EUSAR. 9th European Conference on, VDE, pp 730–733

Ross ZE, Meier M, Hauksson E, Heaton TH (2018) Generalized Seismic Phase Detection with Deep Learning. Bulletin of the Seismological Society of America 108(5A):2894–2901, DOI 10.1785/0120180080

Ross ZE, Idini B, Jia Z, Stephenson OL, Zhong M, Wang X, Zhan Z, Simons M, Fielding EJ, Yun SH, Hauksson E, Moore AW, Liu Z, Jung J (2019) Hierarchical interlocked orthogonal faulting in the 2019 Ridgecrest earthquake sequence. Science 366(6463):346–351, DOI 10.1126/science.aaz0109

Roten D, Olsen KB, Day SM, Cui Y (2018) Quantification of Fault-Zone Plasticity Effects with Spontaneous Rupture Simulations. In: Dalguer LA, Fukushima Y, Irikura K, Wu C (eds) Best Practices in Physics-based Fault Rupture Models for Seismic Hazard Assessment of Nuclear Installations, Springer International Publishing, Cham, pp 45–67, DOI 10.1007/978-3-319-72709-7_5

Ruff L, Kanamori H (1980) Seismicity and the subduction process. Physics of the Earth and Planetary interiors 23(3):240–252

Ruina A (1983) Slip instability and state variable friction laws. Journal of Geophysical Research: Solid Earth 88(B12):10,359–10,370, DOI 10.1029/JB088iB12p10359

Ryan KJ, Geist EL, Barall M, Oglesby DD (2015) Dynamic models of an earthquake and tsunami offshore Ventura, California. Geophysical Research Letters 42(16):6599–6606, DOI 10.1002/2015GL064507

Saito T, Furumura T (2009) Three-dimensional simulation of tsunami generation and propagation: Application to intraplate events. Journal of Geophysical Research 114(B2):B02,307, DOI 10.1029/2007JB005523

Samoa Gitlab (2019) URL https://gitlab.lrz.de/samoa/samoa

Sassa S, Takagawa T (2019) Liquefied gravity flow-induced tsunami: first evidence and comparison from the 2018 indonesia sulawesi earthquake and tsunami disasters. Landslides 16(1):195–200, DOI 10.1007/s10346-018-1114-x

Schmedes J, Archuleta RJ, Lavallée D (2013) A kinematic rupture model generator incorporating spatial interdependency of earthquake source parameters. Geophysical Journal International 192(3):1116–1131, DOI 10.1093/gji/ggs021, URL http://academic.oup.com/gji/article/192/3/1116/807260/A-kinematic-rupture-model-generator-incorporating

Schmittbuhl J, Chambon G, Hansen A, Bouchon M (2006) Are stress distributions along faults the signature of asperity squeeze? Geophysical Research Letters 33(13), DOI 10.1029/2006GL025952

SeisSol GitHub (2019) URL https://github.com/SeisSol/SeisSol

SeisSol website (2019) URL www.seissol.org

Sepulveda I, Haase JS, Liu PLF, Xu X, Carvajal M (2018) On the contribution of co-seismic displacements to the 2018 palu tsunami. In: AGU Fall Meeting 2018, URL https://agu.confex.com/agu/fm18/meetingapp.cgi/Paper/476717

Sevilgen V, Stein RS, Pollitz FF (2012) Stress imparted by the great 2004 Sumatra earthquake shut down transforms and activated rifts up to 400 km away in the Andaman Sea. Proceedings of the National Academy of Sciences 109(38):15,152–15,156, DOI 10.1073/pnas.1208799109

Shearer P, Bürgmann R (2010) Lessons Learned from the 2004 Sumatra-Andaman Megathrust Rupture. DOI 10.1146/annurev-earth-040809-152537

Shi Z, Day SM (2013) Rupture dynamics and ground motion from 3-D rough-fault simulations. Journal of Geophysical Research: Solid Earth 118(3):1122–1141, DOI 10.1002/jgrb.50094

Shimizu K, Yagi Y, Okuwaki R, Fukahata Y (2019) Development of an inversion method to extract information on fault geometry from teleseismic data. DOI 10.31223/osf.io/q58t7

Sibuet J, Rangin C, Lepichon X, Singh S, Cattaneo A, Graindorge D, Klingelhoefer F, Lin J, Malod J, Maury T (2007) 26th December 2004 great Sumatra–Andaman earthquake: Co-seismic and post-seismic motions in northern Sumatra. Earth and Planetary Science Letters 263(1-2):88–103, DOI 10.1016/j.epsl.2007.09.005

Simons WJ, Riva R, Pietrzak J, et al (2018) Tsunami potential of the 2018 Sulawesi earthquake from GNSS constrained source mechanism. In: AGU Fall Meeting 2018, Washington, D.C., URL https://agu.confex.com/agu/fm18/meetingapp.cgi/Paper/476730

Singh SC, Carton H, Tapponnier P, Hananto ND, Chauhan APS, Hartoyo D, Bayly M, Moeljopranoto S, Bunting T, Christie P, Lubis H, Martin J (2008) Seismic evidence for broken oceanic crust in the 2004 Sumatra earthquake epicentral region. Nature Geoscience 1(11):777–781, DOI 10.1038/ngeo336

Singh SC, Hananto N, Mukti M, Robinson DP, Das S, Chauhan A, Carton H, Gratacos B, Midnet S, Djajadihardja Y, Harjono H (2011) Aseismic zone and earthquake segmentation associated with a deep subducted seamount in Sumatra. Nature Geoscience 4(5):308–311, DOI 10.1038/ngeo1119

Socquet A, Simons W, Vigny C, McCaffrey R, Subarya C, Sarsito D, Ambrosius B, Spakman W (2006) Microblock rotations and fault coupling in SE Asia triple junction (Sulawesi, Indonesia) from GPS and earthquake slip vector data. Journal of Geophysical Research 111(B8), DOI 10.1029/2005JB003963

Socquet A, Hollingsworth J, Pathier E, Bouchon M (2019) Evidence of supershear during the 2018 magnitude 7.5 Palu earthquake from space geodesy. Nature Geoscience 12(3):192–199, DOI 10.1038/s41561-018-0296-0

Song X, Zhang Y, Shan X, Liu Y, Gong W, Qu C (2019) Geodetic Observations of the 2018 *Mw* 7.5 Sulawesi Earthquake and Its Implications for the Kinematics of the Palu Fault. Geophysical Research Letters 46(8):4212–4220, DOI 10.1029/2019GL082045

Stadler G, Gurnis M, Burstedde C, Wilcox LC, Alisic L, Ghattas O (2010) The Dynamics of Plate Tectonics and Mantle Flow: From Local to Global Scales. Science 329(5995):1033–1038, DOI 10.1126/science.1191223

Stein S, Okal EA (2005) Speed and size of the Sumatra earthquake. Nature 434(7033):581–582, DOI 10.1038/434581a

Stirling MW, Litchfield NJ, Villamor P, Van Dissen RJ, Nicol A, Pettinga J, Barnes P, Langridge RM, Little T, Barrell DJA (2017) The Mw 7.8 2016 Kaikōura earthquake: Surface fault rupture and seismic hazard context. Bull New Zeal Soc Earthq Eng (2):73–84

Subarya C, Chlieh M, Prawirodirdjo L, Avouac JP, Bock Y, Sieh K, Meltzner AJ, Natawidjaja DH, McCaffrey R (2006) Plate-boundary deformation associated with the great Sumatra–Andaman earthquake. Nature 440(7080):46, DOI 10.1038/nature04522

Suppe J (2014) Fluid overpressures and strength of the sedimentary upper crust. Journal of Structural Geology 69:481–492, DOI 10.1016/j.jsg.2014.07.009

Sutherland R, Townend J, Toy V, Upton P, Coussens J, Allen M, Baratin LM, Barth N, Becroft L, Boese C, Boles A, Boulton C, Broderick NGR, Janku-Capova L, Carpenter BM, Célérier B, Chamberlain C, Cooper A, Coutts A, Cox S, Craw L, Doan ML, Eccles J, Faulkner D, Grieve J, Grochowski J, Gulley A, Hartog A, Howarth J, Jacobs K, Jeppson T, Kato N, Keys S, Kirilova M, Kometani Y, Langridge R, Lin W, Little T, Lukacs A, Mallyon D, Mariani E, Massiot C, Mathewson L, Melosh B, Menzies C, Moore J, Morales L, Morgan C, Mori H, Niemeijer A, Nishikawa O, Prior D, Sauer K, Savage M, Schleicher A, Schmitt DR, Shigematsu N, Taylor-Offord S, Teagle D, Tobin H, Valdez R, Weaver K, Wiersberg T, Williams J, Woodman N, Zimmer M (2017) Extreme hydrothermal conditions at an active plate-bounding fault. Nature 546(7656):137–140, DOI 10.1038/nature22355

Synolakis CE, Bernard EN, Titov VV, Kânoğlu U, González FI (2007) Standards, criteria, and procedures for NOAA evaluation of tsunami numerical models. Tech. Rep. NOAA Technical Memorandum OAR PMEL-135, NOAA/OAR/PMEL

Tanioka Y, Satake K (1996) Tsunami generation by horizontal displacement of ocean bottom. Geophysical Research Letters 23(8):861–864, DOI 10.1029/96GL00736

Tanioka Y, Yudhicara, Kususose T, Kathiroli S, Nishimura Y, Iwasaki SI, Satake K (2006) Rupture process of the 2004 great Sumatra-Andaman earthquake estimated from tsunami waveforms. Earth, Planets and Space 58(2):203–209, DOI 10.1186/BF03353379

Taufiqurrahman, Gabriel AA, Li B, Li D, Wirp AS, Ulrich T, Palgunadi KH, Verdecchia A, Carena S, Mildon ZK (2019) S31g-0487: High-resolution integrated dynamic rupture modeling of the 2019 m6.4 searles valley and m7.1 ridgecrest earthquakes. In: AGU Fall Meeting 2019, San Francisco, URL https://agu.confex.com/agu/fm19/meetingapp.cgi/Paper/614871

Templeton EL, Rice JR (2008) Off-fault plasticity and earthquake rupture dynamics: 1. Dry materials or neglect of fluid pressure changes. Journal of Geophysical Research 113(B9), DOI 10.1029/2007JB005529

Townend J, Sherburn S, Arnold R, Boese C, Woods L (2012) Three-dimensional variations in present-day tectonic stress along the Australia–Pacific plate boundary in New Zealand. Earth and Planetary Science Letters 353-354:47–59, DOI 10.1016/j.epsl.2012.08.003

Tsai VC, Nettles M, Ekström G, Dziewonski AM (2005) Multiple CMT source analysis of the 2004 Sumatra earthquake. Geophysical Research Letters 32(17), DOI 10.1029/2005GL023813

Ulrich T, Gabriel AA, Ampuero JP, Xu W (2019a) Dynamic viability of the 2016 Mw 7.8 Kaikōura earthquake cascade on weak crustal faults. Nature Communications 10(1):1213, DOI 10.1038/s41467-019-09125-w

Ulrich T, Vater S, Madden EH, Behrens J, van Dinther Y, van Zelst I, Fielding EJ, Liang C, Gabriel AA (2019b) Coupled, Physics-Based Modeling Reveals Earthquake Displacements are Critical to the 2018 Palu, Sulawesi Tsunami. Pure and Applied Geophysics DOI 10.1007/s00024-019-02290-5

Uphoff C, Rettenberger S, Bader M, Madden E, Ulrich T, Wollherr S, Gabriel AA (2017) Extreme scale multi-physics simulations of the tsunamigenic 2004 sumatra megathrust earthquake. In: Proceedings of the International Conference for High Performance Computing, Networking, Storage and Analysis, SC 2017, DOI 10.1145/3126908.3126948

USGS (2015) URL https://earthquake.usgs.gov/earthquakes/eventpage/official20041226005853450_30/moment-tensor

USGS (2018a) URL https://earthquake.usgs.gov/earthquakes/eventpage/us1000h3p4/moment-tensor

USGS (2018b) URL https://earthquake.usgs.gov/earthquakes/eventpage/us1000h3p4/finite-fault

Uyeda S, Kanamori H (1979) Back-arc opening and the mode of subduction. Journal of Geophysical Research: Solid Earth 84(B3):1049–1061, DOI 10.1029/JB084iB03p01049

Valkaniotis S, Ganas A, Tsironi V, Barberopoulou A (2018) A preliminary report on the M7.5 Palu 2018 earthquake co-seismic ruptures and landslides using image correlation techniques on optical satellite data. DOI 10.5281/zenodo.1467128, report submitted to EMSC

Vallee M (2007) Rupture Properties of the Giant Sumatra Earthquake Imaged by Empirical Green's Function Analysis. Bulletin of the Seismological Society of America 97(1A):S103–S114, DOI 10.1785/0120050616

Vallée M, Charléty J, Ferreira AMG, Delouis B, Vergoz J (2011) SCARDEC: a new technique for the rapid determination of seismic moment magnitude, focal mechanism and source time functions for large earthquakes using body-wave deconvolution. Geophysical Journal International 184(1):338–358, DOI 10.1111/j.1365-246X.2010.04836.x

Van Puymbroeck N, Michel R, Binet R, Avouac JP, Taboury J (2000) Measuring earthquakes from optical satellite images. Applied Optics 39(20):3486, DOI 10.1364/AO.39.003486

Vater S, Behrens J (2014) Well-balanced inundation modeling for shallow-water flows with Discontinuous Galerkin schemes. In: Fuhrmann J, Ohlberger M, Rohde C (eds) Finite Volumes for Complex Applications VII – Elliptic, Parabolic and Hyperbolic Problems, Springer Proceedings in Mathematics & Statistics, vol 78, pp 965–973, DOI 10.1007/978-3-319-05591-6_98

Vater S, Beisiegel N, Behrens J (2015) A limiter-based well-balanced discontinuous galerkin method for shallow-water flows with wetting and drying: One-dimensional case. Advances in Water Resources 85:1–13, DOI 10.1016/j.advwatres.2015.08.008

Vater S, Beisiegel N, Behrens J (2017) Comparison of wetting and drying between a RKDG2 method and classical FV based second-order hydrostatic reconstruction. In: Cancès C, Omnes P (eds) Finite Volumes for Complex Applications VIII - Hyperbolic, Elliptic and Parabolic Problems, Springer, pp 237–245, DOI 10.1007/978-3-319-57394-6_26

Vater S, Beisiegel N, Behrens J (2019) A limiter-based well-balanced discontinuous Galerkin method for shallow-water flows with wetting and drying: Triangular grids. International Journal for Numerical Methods in Fluids DOI 10.1002/fld.4762

Vigny C, Perfettini H, Walpersdorf A, Lemoine A, Simons W, van Loon D, Ambrosius B, Stevens C, McCaffrey R, Morgan P, et al (2002) Migration of seismicity and earthquake interactions monitored by GPS in SE Asia triple junction: Sulawesi, Indonesia. Journal of Geophysical Research: Solid Earth 107(B10):ETG–7, DOI 10.1029/2001JB000377

Waldhauser F, Schaff DP, Diehl T, Engdahl ER (2012) Splay faults imaged by fluid-driven aftershocks of the 2004 Mw 9.2 Sumatra-Andaman earthquake. Geology 40(3):243–246, DOI 10.1130/G32420.1

Walpersdorf A, Rangin C, Vigny C (1998) GPS compared to long-term geologic motion of the north arm of Sulawesi. Earth and Planetary Science Letters 159(1):47–55, DOI 10.1016/S0012-821X(98)00056-9

Wang T, Wei S, Shi X, Qiu Q, Li L, Peng D, Weldon RJ, Barbot S (2018) The 2016 Kaikōura earthquake: Simultaneous rupture of the subduction interface and overlying faults. Earth and Planetary Science Letters 482:44–51, DOI 10.1016/j.epsl.2017.10.056

Watkinson IM, Hall R (2017) Fault systems of the eastern Indonesian triple junction: evaluation of Quaternary activity and implications for seismic hazards. Geological Society, London, Special Publications 441(1):71–120, DOI 10.1144/SP441.8

Weatherall P, Marks KM, Jakobsson M, Schmitt T, Tani S, Arndt JE, Rovere M, Chayes D, Ferrini V, Wigley R (2015) A new digital bathymetric model of the world's oceans. Earth and Space Science 2(8):331–345, DOI 10.1002/2015EA000107

Wells DL, Coppersmith KJ (1994) New empirical relationships among magnitude, rupture length, rupture width, rupture area, and surface displacement. Bulletin of the Seismological Society of America 84(4):974–1002

Wesnousky SG (2006) Predicting the endpoints of earthquake ruptures. Nature 444(7117):358–360, DOI 10.1038/nature05275

White RS (1988) The Earth's Crust and Lithosphere. Journal of Petrology Special_Volume(1):1–10, DOI 10.1093/petrology/Special_Volume.1.1

Widiyanto W, Santoso PB, Hsiao SC, Imananta RT (2019) Post-event Field Survey of 28 September 2018 Sulawesi Earthquake and Tsunami. Natural Hazards and Earth System Sciences Discussions pp 1–23, DOI 10.5194/nhess-2019-91

Williams CA, Eberhart-Phillips D, Bannister S, Barker DHN, Henrys S, Reyners M, Sutherland R (2013) Revised Interface Geometry for the Hikurangi Subduction Zone, New Zealand. Seismological Research Letters 84(6):1066–1073, DOI 10.1785/0220130035

Withers KB, Olsen KB, Day SM, Shi Z (2019a) Ground Motion and Intraevent Variability from 3d Deterministic Broadband (0–7.5 Hz) Simulations along a Nonplanar Strike-Slip Fault. Bulletin of the Seismological Society of America 109(1):229–250, DOI 10.1785/0120180006

Withers KB, Olsen KB, Shi Z, Day SM (2019b) Validation of Deterministic Broadband Ground Motion and Variability from Dynamic Rupture Simulations of Buried Thrust Earthquakes. Bulletin of the Seismological Society of America 109(1):212–228, DOI 10.1785/0120180005

Wollherr S, Gabriel AA, Uphoff C (2018) Off-fault plasticity in three-dimensional dynamic rupture simulations using a modal Discontinuous Galerkin method on unstructured meshes: implementation, verification and application. Geophysical Journal International 214(3):1556–1584, DOI 10.1093/gji/ggy213

Wollherr S, Gabriel A, Mai PM (2019) Landers 1992 ”Reloaded”: Integrative Dynamic Earthquake Rupture Modeling. Journal of Geophysical Research: Solid Earth DOI 10.1029/2018JB016355

Xu W, Feng G, Meng L, Zhang A, Ampuero JP, Bürgmann R, Fang L (2018) Transpressional Rupture Cascade of the 2016 M $_w$ 7.8 Kaikoura Earthquake, New Zealand. Journal of Geophysical Research: Solid Earth 123(3):2396–2409, DOI 10.1002/2017JB015168

Yalciner AC, Hidayat R, Husrin S, Prasetya G, Annunziato A, Doğan GG, Zaytsev A, Omira R, Proietti C, Probst P, Paparo MA, Wronna M, Pronin P, Giniyatullin A, Putra PS, Hartanto D, Ginanjar G, Kongko W, Pelinowski E (2018) The 28th September 2018 Palu earthquake and tsunami ITST 07-11 November 2018 post tsunami field survey report (short). Report, Middle East Technical University (and others), Ankara, Turkey, URL http://itic.ioc-unesco.org/images/stories/itst_tsunami_survey/itst_palu/ITST-Nov-7-11-Short-Survey-Report-due-on-November-23-2018.pdf

Yang H, Yao S, He B, Newman AV (2019) Earthquake rupture dependence on hypocentral location along the Nicoya Peninsula subduction megathrust. Earth and Planetary Science Letters 520:10–17, DOI 10.1016/j.epsl.2019.05.030

Yomogida K (1988) Crack-like rupture processes observed in near-fault strong motion data. Geophysical Research Letters 15(11):1223–1226, DOI 10.1029/GL015i011p01223

van Zelst I, Wollherr S, Gabriel AA, Madden E, van Dinther Y (2019) Modelling coupled subduction and earthquake dynamics. DOI 10.31223/osf.io/f6ng5

Zhang H, Koper KD, Pankow K, Ge Z (2017) Imaging the 2016 M_w 7.8 Kaikoura, New Zealand, earthquake with teleseismic P waves: A cascading rupture across multiple faults. Geophysical Research Letters 44(10):4790–4798, DOI 10.1002/2017GL073461

Zhao JX (2006) Attenuation Relations of Strong Ground Motion in Japan Using Site Classification Based on Predominant Period. Bulletin of the Seismological Society of America 96(3):898–913, DOI 10.1785/0120050122

Zielke O, Galis M, Mai PM (2017) Fault roughness and strength heterogeneity control earthquake size and stress drop. Geophysical Research Letters 44(2):777–783, DOI 10.1002/2016GL071700, URL https://onlinelibrary.wiley.com/doi/abs/10.1002/2016GL071700

Zoback MD, Zoback ML, Mount VS, Suppe J, Eaton JP, Healy JH, Oppenheimer D, Reasenberg P, Jones L, Raleigh CB, Wong IG, Scotti O, Wentworth C (1987) New Evidence on the State of Stress of the San Andreas Fault System. Science 238(4830):1105–1111, DOI 10.1126/science.238.4830.1105